UNIVERSITAT DE BARCELONA

Disentangling the formation path of lenticular galaxies

José Luis Tous Mayol

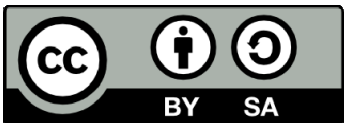

TESI DOCTORAL

DISENTANGLING THE FORMATION PATH OF LENTICULAR GALAXIES

JOSÉ LUIS TOUS MAYOL

DIRECTORS

Dr. José M. Solanes Majúa

Dr. Jaime D. Perea Duarte

UNIVERSITAT DE BARCELONA

Disentangling the formation path of lenticular galaxies

Memòria presentada per optar al grau de doctor per la Universitat de Barcelona

Programa de doctorat en Física

AUTOR
José Luis Tous Mayol

DIRECTORS
Dr. José M. Solanes Majúa
Dr. Jaime D. Perea Duarte

TUTOR
Dr. Alberto Manrique Oliva

DEPARTAMENT DE FÍSICA QUÀNTICA I ASTROFÍSICA

Barcelona, 23 de desembre de 2023

UNIVERSITAT DE BARCELONA

DECLARATION

This thesis is presented following the regulations of the University of Barcelona (Approved by the CdG in the session of 16 March 2012 and modified by the CdG on 9 May and 19 July 2012, 29 May and 3 October 2013, 17 July 2014, 16 July 2015, 15 June and 21 November 2016, 5 December 2017, 4 May 2018, 15 May and 22 July 2019, 7 October 2020, and 14 of July 2021). The listed regulations allow for the presentation of a PhD thesis as a compendium of published articles. According to the regulations, the thesis must contain a minimum of three published or accepted articles. This thesis contains the published version of four articles, which is sufficient to allow its presentation. It also contains one additional article, submitted but not yet accepted for publication at the moment of thesis presentation.

Barcelona, 23 de desembre de 2023

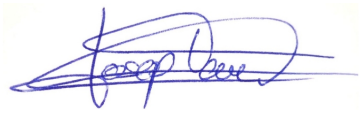

José Luis Tous Mayol

Als meus pares, la meva germana i la Marta. També, al Marujito.

ACKNOWLEDGEMENTS

Quiero empezar con los agradecimientos a mis directores. Josep Maria, Jaime, creo que soy muy afortunado de haber ido a parar con vosotros, no es fácil encontrar un entorno tan acogedor como el que me habéis dado. Gracias por acompañarme de principio a fin en este proceso, que no siempre ha sido fácil. Me he sentido muy mimado porque nunca os ha costado encontrar tiempo para dedicarme y siempre habéis confiado en mí, dándome mucha autonomía. Y es gracias a esto que he disfrutado cada día de mi trabajo. Me habéis enseñado que no hace falta ser un grupo grande para hacer ciencia de calidad y estoy muy orgulloso de nuestro trabajo. No cambiaría nada de estos últimos años a vuestro lado.

A continuación van mis directoras no oficiales. Gracias Chony por tus conocimientos extragalácticos. También por tu hospitalidad durante todas mis visitas al IAA. Gracias a ti, a Isa, a Pepa, a Sara, y a toda la gente del Instituto que he conocido a través de vosotras, Granada ya es casi como mi segunda casa. Helena, mi otra directora no oficial, debo decir que desde el momento en el que decidí usar vuestro catálogo morfológico, uno de mis objetivos era conocer a su autora principal. Hoy me hace feliz poder decir que esta autora se ha convertido en colaboradora y amiga.

Vull donar les gràcies també a la gent de casa. Començaré pel Jorge, el Dani, la Maite i tot el grup del TFRM. Vosaltres em vau ensenyar el que és treballar en un observatori i molt més. Sempre recordaré les campanyes al Montsec que, malgrat la son i el fred, també van estar plenes de bons moments i moltes anècdotes. Al Gerard, la Cristina i la Francesca, a qui he tingut la sort de conèixer i poder col·laborar-hi. També a tots els meus companys de doctorat. Als meus companys de despatx, antics i actuals, Xiying, Dani, Arnau, Helena, gràcies per fer tan fàcil la convivència; als Gaiers Marcel, Juan i Óscar (sobretot per salvar-me de la vespa gegant!); a la presidenta júnior, Mar, pel seu afecte i el seu català amb accent canari, a l'Elina i la seva generositat. Gràcies als gravitòlegs de la planta 3: Quim, Ana i Jordi; també al Toni, al Carlos, al Julien, l'Emanuele i al Sergi per les bones estones al balcó, als PhD meetings i a les calçotades. També als que ja fa temps que vau marxar de postdoc: Edgar, Sam, Ali, Pau, Alfred i Nico; i als nouvinguts: Marc, Judith, Elena, Chloé, Grace i Marie (segurament m'estigui deixant noms). No em puc oblidar, però, del JR, el mag del departament, que segueix fent que tot rutlli inclús des de la planta 1. Gràcies, thank you!

Vull acabar donant les gràcies a les persones més importants de totes, a la meva família per sempre ser al meu costat, especialment

en els moments més difícils. Papà, mamà, gràcies al vostre amor avui soc aquí, vosaltres sempre m'heu animat a lluitar pels meus projectes i m'heu ensenyat que és important saber gaudir també de la vida professional. Carla (Tos), la millor consellera del món, m'has donat la confiança quan més l'he necessitat. I Marta, crec que no puc expressar amb paraules la sort que tinc d'haver compartit els anys de la tesi (i uns quants més!) amb tu, al teu costat mai hi haurà foscor.

RESUM EN CATALÀ

Els astrònoms coneixen de l'existència de galàxies lenticulars (S0s) gairebé des que saben que hi ha altres galàxies més enllà de la Via Làctia. Mentre que s'accepta que les galàxies espirals sorgeixen del col·lapse de núvols gegants primordials de gas i que, quan es fusionen, sovint donen lloc a galàxies el·líptiques, l'origen de les galàxies S0 encara es continua debatent. Una clara bimodalitat en les propietats d'aquestes galàxies, les quals són relativament abundants en entorns de baixa i alta densitat, suggereix que podrien intervenir diversos mecanismes en la seva formació. En el camp o en petits grups, les galàxies S0 poden evolucionar a partir de fusions. En canvi, s'espera que les interaccions hidrodinàmiques transformin les espirals en S0 dins de grups grans de galàxies.

Aquesta tesi està dedicada a revisar les principals propietats de les galàxies classificades com a S0. El nostre objectiu és recopilar informació abundant i, sobretot, robusta sobre els paràmetres més rellevants d'aquest tipus morfològic poc entès i la seva possible dependència en l'entorn, per tal d'acotar els seus camins de formació. Per primera vegada, explorem tot l'espectre òptic d'aquestes galàxies, cercant pistes per inferir la seva evolució.

Comencem l'exploració amb espectres de fibra única de l'SDSS d'una mostra de gairebé 70.000 S0s properes i les seves propietats globals. Fem servir una anàlisi de components principals (PCA) per reduir la gran complexitat de les dades espectrals mitjançant les seves projeccions a un espai de baixa dimensionalitat, facilitant així una classificació basada en aprenentatge automàtic sense biaixos de les galàxies. El procediment revela que la població S0 es compon de dues classes principals amb propietats diferents. Mentre que la classe majoritària està formada per lenticulars passives amb espectres inactius, l'altra es caracteritza per galàxies actives que, malgrat la seva morfologia de tipus primerenc, mostren ritmes de formació estel·lar que poden arribar a ser similars als observats en espirals de tipus tardà. La font principal d'ionització de les galàxies actives és la formació d'estrelles. Tanmateix, en els sistemes S0 de tipus Seyfert i LINER detectats en ràdio i raigs X, l'activitat ve dominada, respectivament, per acreció nuclear i estrelles post-AGB.

Aplicada a espectres resolts espacialment de MaNGA, la PCA pot ser utilitzada per estudiar la configuració radial de l'activitat a les galàxies. L'extensió de la PCA a aquests espectres ens porta a identificar anells de formació estel·lar en galàxies S0, normalment associats a un gradient d'activitat positiu, i a crear el catàleg més gran d'aquests objectes mai identificat mitjançant aquest tipus de dades.

L'avaluació dels anells indica que són relativament abundants (~ 30%) en S0s completament formades, amb una freqüència que augmenta amb la massa dels amfitrions, però que no es correlaciona amb l'entorn. Els anells són dues vegades més freqüents entre els membres de la classe passiva que en els actius i probablement es nodreixen de gas residual del disc. Aquests resultats vinculen els anells amb la captura per les S0s de petits satèl·lits nans que orbiten estretament al seu voltant. Finalment, examinem els perfils d'activitat radials de les S0s en funció de les seves propietats. La comparació revela que el gradient d'activitat radial d'aquestes galàxies està estretament relacionat amb les seves classificacions PCA i BPT, i l'estat de formació estel·lar. La classe passiva sovint mostra perfils d'activitat de baix nivell i plans, mentre que els seus equivalents actius generalment tenen gradients d'activitat negatius, típicament associats amb un elevat ritme específic de formació estel·lar.

En conjunt, els nostres resultats donen suport a un escenari on les fusions menors podrien jugar un paper actiu en l'evolució recent de les galàxies S0 rejovenint-les, mentre que els cúmuls operen en sentit contrari, apagant la seva activitat. La metodologia que hem desenvolupat proporciona una imatge unificada de l'activitat a les galàxies S0 en el domini òptic. En combinació amb quantitats físiques i diagrames de línies, demostra ser una eina valuosa per interpretar tendències globals i radials clau en les galàxies lenticulars que hauria de ser aplicable a altres morfologies.

ABSTRACT

Astronomers have known of the existence of lenticular galaxies (S0) almost as long as they have known that there are other galaxies besides the Milky Way. While it is accepted that spiral galaxies emerge from the collapse of primordial vast clouds of gas and that when they merge they often give place to elliptical galaxies, the origin of S0 galaxies is still subject to debate. A clear bimodality in the properties of these galaxies, which are relatively abundant in low- and high-density environments, suggests that multiple formation mechanisms may be at play. In the field or in small groups, S0 galaxies can evolve from mergers. In contrast, hydrodynamic interactions are expected to transform spirals into S0s within large galaxy aggregations.

This thesis is devoted to reviewing the main properties of galaxies classified as S0. Our goal is to gather abundant and, above all, robust information about the most relevant parameters of this poorly understood morphological type and their possible dependence on the environment to constrain their formation pathways. For the first time, we explore the entire optical spectrum of these galaxies, seeking clues to infer their evolution.

We start the exploration with single-fibre spectra from the SDSS of a sample of nearly 70,000 nearby S0s and their global properties. A principal component analysis (PCA) is used to reduce the high complexity of the spectral data through its projections into a low-dimensional space, thereby facilitating a bias-free, machine-learning-based classification of the galaxies. The procedure reveals that the S0 population consists of two main classes with statistically inconsistent physical properties. While the bulk population is made by passive lenticulars with inactive spectra, the other is characterized by active galaxies that, despite their early-type morphology, show star formation rates that can be similar to those observed in late-type spirals. The main ionisation source of the active galaxies is star formation. However, in the Seyfert and LINER S0 systems detected in radio and X-ray, activity is driven, respectively, by nuclear accretion and post-AGB stars.

Applied to spatially resolved spectra from MaNGA, the PCA can be used to study the radial configuration of activity in the galaxies. The extension of the PCA to these spectra leads us to identify star-forming rings in S0 galaxies typically associated with a positive activity gradient, and assemble the largest catalogue of these objects ever identified through this kind of data. Assessment of the rings indicates that they are relatively abundant ($\sim$ 30%) in fully-formed S0s with a frequency that sharply increases with the mass of the hosts, but are uncorrelated

with the environment. The rings are twice more frequent among the members of the passive class than in the active, and likely feed on residual gas from the disc. These results link the rings with the capture by the S0s of tiny dwarf satellites that closely orbit them. Finally, we examine the radial activity profiles of S0s as a function of their properties. The comparison reveals that the radial activity gradient of these galaxies is tightly related to their PCA classification, BPT designation, and star formation status. The passive class often shows low-level, flat activity profiles, while their active counterparts generally have negative activity gradients, usually associated with high specific star formation rates.

Altogether, our results support a scenario where minor mergers could actively play a rejuvenation role in the recent evolution of S0 galaxies, while clusters operate in the opposite direction by quenching their activity. The framework we have developed in this thesis provides a unified picture of activity in S0 galaxies in the optical domain. In combination with physical quantities and line diagnostics, the framework is a valuable tool for interpreting key global and radial trends in lenticular galaxies that should be transferable to other morphologies.

PUBLICATIONS

Complete list of publications at the moment of thesis deposit.

Published and submitted articles included in the main body of this thesis

- **Tous, J. L.**, Solanes, J. M., Perea, J. D. & Domínguez-Sánchez, H. (2023). The local Universe in the era of large surveys-III. Radial activity profiles of S0 galaxies. Submitted to MNRAS
- **Tous, J. L.**, Domínguez-Sánchez, H., Solanes, J. M., & Perea, J. D. (2023). The origin of star-forming rings in S0 galaxies. ApJ, 942(1), 48
- Jiménez-Palau, C., Solanes, J. M., Perea, J. D., del Olmo, A., & **Tous, J. L.** (2022). The local universe in the era of large surveys-II. multi-wavelength characterization of activity in nearby S0 galaxies. MNRAS, 515(3), 3956-3974
- **Tous, J. L.**, Solanes, J. M., & Perea, J. D. (2020). The local Universe in the era of large surveys–I. Spectral classification of S0 galaxies. MNRAS, 495(4), 4135-4157

Published articles included in the appendix of this thesis

- Navó, G., **Tous, J. L.**, & Solanes, J. M. (2019). A statistical method for the identification of stars enriched in neutron-capture elements from medium-resolution spectra. A&A, 631, A93

Other published articles (not included in this thesis)

- Solanes, J. M., Perea, J. D., Valentí–Rojas, G., del Olmo, A., Márquez, I., Almeida, C. R., & **Tous, J. L.** (2019). Intrinsic and observed dual AGN fractions from major mergers. A&A, 624, A86

CONTENTS

1

INTRODUCTION

After the Big Bang, the baryons in the Universe began to arrange into giant gas clouds within dark matter haloes. The collapse of these clouds and subsequent gas-rich mergers gave place, after billions of years of evolution, to the galaxies that we observe today. The fact that most galaxies in the nearby Universe exhibit regular shapes led Hubble (1926) to introducing a morphological classification based on a scheme that we now know as the Hubble tuning fork diagram.

As suggested by its name, the diagram features three branches (Fig. 1). The one on the left encompasses spheroidal systems, from rounder to flatter, which we call elliptical galaxies. On the right, there are two parallel branches encompassing unbarred and barred spiral galaxies with arms that become progressively less tightly wound. All the objects that fit within the latter description are known as late type galaxies (LTGs). Just at the centre of the diagram, where the two spiral-galaxy branches and the elliptical branch join, lies a morphological class characterized by transition galaxies with a central bulge component surrounded by a disc devoid of spiral arms. These galaxies were first introduced as a hypothetical S0 class by Hubble (1926) himself and were later identified with the gas-poor lenticular galaxies frequently observed in rich clusters (Sandage 1961). Together with the ellipticals, we acknowledge lenticulars as early type galaxies (ETGs).

The observation that in the nearby Universe spiral galaxies are preferentially segregated to the low-density general field, while lenticulars dominate in the densest cluster regions, was soon interpreted as evidence of a possible evolutionary sequence among disc galaxies, in which spirals are transformed into lenticulars within galaxy aggregations. At the beginning, Spitzer & Baade (1951) proposed that

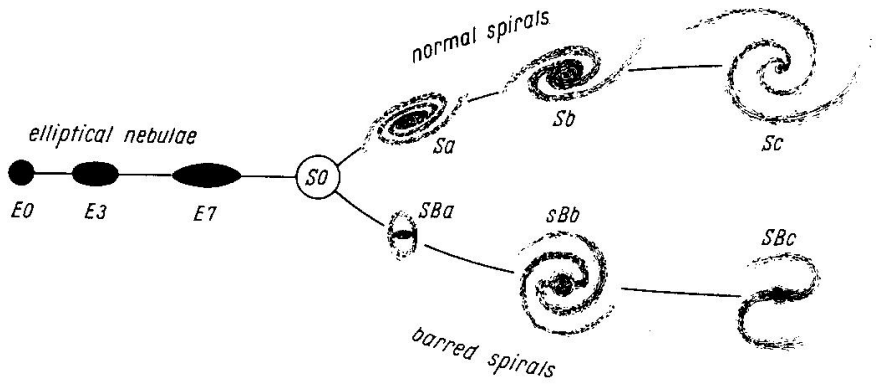

Figure 1: The tuning fork diagram as published in Hubble (1936).

lenticulars were, in fact, spirals that had been transformed through direct collisions with other companion cluster galaxies. This scenario was later refined by Gunn & Gott (1972), who showed that, in such dense environments, the ram pressure stripping (RPS) produced by the intracluster medium (ICM) upon the disc of infalling spiral galaxies could effectively remove the gas from these systems and induce the morphological transformation.

A series of subsequent observations reinforced the idea that spirals can be transformed into lenticular galaxies within clusters. On one hand, the prevalence of blue, star-forming galaxies within moderately high-redshift clusters ($z \sim 0.4 - 0.5$) with respect to the nearby ones (Butcher & Oemler 1978). In terms of morphology, this effect translates into a decrease in the fraction of S0 galaxies with z with a commensurate increase in the fraction of spirals, while the abundance of elliptical galaxies remains essentially constant (Couch et al. 1994; Dressler et al. 1997; Couch et al. 1998; Poggianti et al. 1999; Fasano et al. 2000). On the other hand, the observation that in virialized galaxy clusters, the fraction of lenticular galaxies increases with the local projected density at the expense of the fraction of spiral plus irregular galaxies, an effect commonly known as the morphology-density relation (Dressler 1980; Postman & Geller 1984; Giovanelli et al. 1986; Goto et al. 2003; Cappellari et al. 2011b; Houghton 2015). Taken together, these findings strongly suggest that clusters must have played a significant role in shaping the present-day morphological fraction.

Still, a considerable fraction of the S0 population ($\sim 20 - 30\%$) is found in small groups or even isolated in the low-density general field, where the intergalactic medium (IGM) is not dense enough to enable the hydrodynamic mechanisms that work efficiently within clusters. Besides, we know that S0 galaxies cannot escape the group and cluster potentials to populate the general field. Thus, other mechanisms are required to explain the presence of these galaxies outside these aggregations. Numerical simulations of galaxy interactions suggest that the S0s we observe in low-density environments may come from mergers, either minor in which a disc galaxy captures a small satellite, or major between pairs of galaxies involving at least one gas-rich spiral (Querejeta et al. 2015; Tapia et al. 2017; Eliche-Moral et al. 2018).

All in all, among the different Hubble types, S0 is special because it encompasses galaxies that, despite showing the same shape, might have evolved following radically different channels that could have left their distinctive imprint on the properties of these objects. This challenges a naive notion where a common shape implies a single origin. The main motivation of this thesis is, precisely, to seek for differences in the properties of S0 galaxies that can be used to identify specific formation pathways.

1.1 THE PRESENT-DAY LENTICULAR GALAXIES IN THE ERA OF LARGE SURVEYS

The study of the origin of S0 galaxies has undergone a remarkable transformation in recent years, essentially thanks to two cornerstones. One is the advent of large galaxy surveys that, since the beginning of the century, have been gathering homogeneous data for an unprecedented amount of extragalactic sources, permitting a solid statistical investigation of this population of galaxies. The other is the development of the artificial intelligence, essential to deal with the gigantic volume of data produced by these surveys.

1.1.1 *The surveys*

In the optic, a significant revolution came upon the implementation of the multi-object spectroscopy (MOS) in surveys such as the Sloan Digital Sky Survey (SDSS; York et al. 2000). This technique consists in connecting the spectrograph by fibre optic cables to small holes in a plate placed at the telescope's focal plane. By doing so, an exponential jump in the number of spectra that can be obtained per run is produced, from a single one in the traditional long-slit observations to several hundreds that, besides, are observed and reduced under virtually identical conditions. However, the increase in the numbers comes at the expense of losing spatial resolution: the spectrum obtained is the integral of all the light captured by a single fibre. The main galaxy sample (MGS) of the Sloan Legacy Survey (Strauss et al. 2002) consists of integrated optical spectra and photometric images in five bands for nearly a million galaxies with a median redshift of $z = 0.1$.

The next step was the development of the integral field spectroscopy (IFS). First, it was implemented on a "one object per run" basis in surveys such as the Calar Alto Legacy Integral Field Area (Sánchez et al. 2012) that produced spatially resolved spectra for several hundreds of galaxies. Then, this technique evolved with projects like the Mapping Nearby Galaxies at Apache Point Observatory (MaNGA; Bundy et al. 2015) or the Sydney-AAO (Australian Astronomical Observatory) Multi-object Integral field spectrograph (SAMI; Allen et al. 2015), in which a MOS philosophy was adopted to obtain this type of data for multiple sources at once. To this end, the single fibre optic cables were replaced by fibre bundles closely packed into hexagonal integral field units plugged into the plates.

Along with the development of these optical surveys, the full electromagnetic spectrum was being exploited, enabling a multi-wavelength approach to investigate the evolution of galaxies. For example, at longer wavelengths, the Very Large Array Faint Images of the Radio Sky at Twenty centimetres Survey (Becker et al. 1995) was de-

signed to overlap with the SDSS, covering a large area of the radio sky over the north and south galactic caps. The Two Micron All Sky Survey (Skrutskie et al. 2006) and the Wide-field Infrared Survey Explorer (Wright et al. 2010) mapped the entire sky in several near- and mid-infrared broad bands, respectively. In the ultraviolet, the Galaxy Evolution Explorer survey gathered photometry for hundreds of million sources, and low-resolution spectra for over a hundred thousand of them (Bianchi et al. 2017). At higher energies, the Chandra Source Catalogue (Evans et al. 2020) contains fluxes in five bands from 0.5 to 70 keV and broad-band master fluxes that cover the entire range of photon energies for 317,167 unique sources. There is also the XMM-Newton serendipitous catalogue of X-ray sources (Webb et al. 2020) which, in its latest version, contains X-ray fluxes of 656,997 unique sources detected in the range of 0.2 to 12 keV with the XMM-Newton telescope (Jansen et al. 2001).

Other surveys especially designed to address cosmological questions, such as the Baryon Oscillation Spectroscopic Survey (BOSS; Eisenstein et al. 2011) and its extended version (Dawson et al. 2016), the Dark Energy Survey (DES; The Dark Energy Survey Collaboration 2005), the Dark Energy Spectroscopic Instrument (DESI Collaboration et al. 2016), or the upcoming surveys from the Euclid mission (Euclid Collaboration et al. 2022), allow us to follow the evolution of galaxies across larger cosmic times.

1.1.2 *Morphology identification*

Having this wealth of information without an objective and reliable visual morphological classification of galaxies would have been simply useless to address the formation and evolution of the different Hubble types. Well aware of that, Nair & Abraham (2010) released a catalogue of detailed visual classifications for 14,034 galaxies in the fourth SDSS data release (DR4; Adelman-McCarthy et al. 2006). Far from being a complete classification of the main sample of SDSS galaxies, it represented a one order of magnitude increase in size compared to existing catalogues produced by expert morphologists. Earlier, a first attempt of classifying a considerable fraction of the SDSS MGS came with the Galaxy Zoo citizen science project (Lintott et al. 2008). In its first version, volunteers were asked to classify nearly 900,000 galaxies through a user-friendly web interface. However, the outcome was a simple division into three categories: ETGs, LTGs and mergers.

The biggest and most detailed classification of galaxies in the nearby Universe we have to date is the one by Domínguez Sánchez et al.

(2018)[1]. These authors used convolutional artificial neural networks trained with colour images from both the Galaxy Zoo 2 (Willett et al. 2013) and Nair & Abraham's catalogue to determine the morphology of about 671,000 galaxies from the SDSS-DR7 (Abazajian et al. 2009). Subsequent versions of this catalogue include the classification of MaNGA targets from improved training models (Fischer et al. 2019; Domínguez Sánchez et al. 2021). Compared to former visual classifications, these automated determinations of the Hubble type are objective and at least as accurate, primarily due to the ability of computers to detect subtle variations in image brightness that may elude the human eye.

Thus, the combination of extensive and reliable morphological classifications, along with large volumes of homogeneous spectroscopic and photometric data, provides a unique opportunity to study the formation and evolution of S0 galaxies using a statistical approach that fully harnesses the wealth of information present in their light.

1.1.3 *A Hubble type with heterogeneous properties*

It is becoming widely accepted that the population of present-day lenticular galaxies exhibits some heterogeneity in its properties, suggesting that at least two different classes of galaxies hide under the same morphological designation. In this section, I review some of the recent works that have exposed bimodalities in different properties of the S0 population.

In Xiao et al. (2016), the SDSS spectra of 583 lenticulars were used to classify the galaxies based on the presence, or lack, of strong emission lines. Emission line S0s were then further subclassified through the standard Baldwin, Phillips & Terlevich (1981; BPT) diagram that relies on the [NII]λ6584/Hα and OIIIλ5007/Hβ flux ratios directly measured from their spectra. In agreement with previous results (e. g. Helmboldt et al. 2008), the authors found that emission line lenticulars prefer low-density environments. Furthermore, the study revealed that the star-forming (SF) S0s have bulges characterized by rather low Sérsic indices ($n < 2$) which, in some cases, are bluer than the disc, and that a remarkable fraction (8%) of these SF galaxies are one order of magnitude less massive than the other S0s of their sample.

Along the same line are the results in Gavazzi et al. (2018) from the study of 147 ETGs with kinematic and morphological information from the ATLAS^{3D} survey (Cappellari et al. 2011a). Combining these data with narrow-band observations centred on the Hα line, these authors found that 14% of the S0s in their sample show strong emission characterized by an Hα equivalent width (EW) greater or equal to 5

1 While there are larger catalogues, like those of Vega-Ferrero et al. (2021) or Cheng et al. (2021) for galaxies from DES, they only distinguish ETGs from LTGs, or ellipticals from spirals, and do not specifically identify the class of S0 galaxies.

Å. As compared to lenticulars with weak (1 Å$\leqslant$ EW(Hα)$<$ 5 Å) or undetected emission, the active S0s have lower stellar mass and gas-rich discs associated with a healthy star formation.

Fraser-McKelvie et al. (2018) carried out an analysis of the bulge and disc components in a sample of 279 S0 galaxies using spatially resolved spectra from the MaNGA product launch 5. They measured light-weighted Lick indices on both regions and compared them with the outcomes of single stellar population (SSP) model predictions to infer the age and metallicity of each component in their galaxies. Their analysis uncovered a bimodality driven by the stellar mass that is also reflected in the stellar populations of both structural components but is unrelated to the environment. Furthermore, in line with the results obtained in the multi-wavelength study by Barway et al. (2013), they found that low stellar mass ($M_* < 10^{10}\,M_\odot$) lenticulars host younger and more metal-poor stars than their massive counterparts. Studied apart, the bulges of the low-mass lenticulars typically concentrate younger stars than their discs and show low Sérsic indices, while the massive lenticulars follow the opposite configuration. They concluded that the low-mas, galaxy population could come from faded spirals, while an evolution driven by mergers would explain the properties observed in the high-mass population.

Other authors have used the kinematics of the stellar component of S0 galaxies to probe their evolutionary history based on measurements of the ordered (and/or disordered) motion of the stars. In this sense, the work of Fraser-McKelvie et al. was complemented in Domínguez Sánchez et al. (2020) making, in addition, an optimal use of the spatial resolution offered by the IFS. In the latter work, the spectra of 410 S0 galaxies from the MaNGA-DR15 were used to derive characteristic age and metallicity radial profiles. Likewise, Lick indices were measured from high signal-to-noise ratio (S/N) stacked spectra of galaxies with similar absolute luminosity and central velocity dispersion at different galactocentric distances, and were compared with SSP models. The results they obtained indicate that low-mass lenticulars exhibit strong, negative metallicity gradients (i. e., metallicity increases outside in) but rather flat age profiles. Instead, the massive counterparts show negative age gradients but flat metallicity profiles.

The stellar and gas kinematics of a sample of 219 S0 galaxies was investigated in Deeley et al. (2020) using data cubes from SAMI. These authors used the ratio of observed line of sight stellar velocity, v, to velocity dispersion, σ, to split the sample and compare the properties of the pressure supported (i. e., $v/\sigma < 0.5$) against the rotationally supported (i. e., $v/\sigma \geqslant 0.5$) lenticulars. The comparison revealed that the former galaxies tend to be more compact and dominate in the field and in low-mass galaxy groups ($< 10^{11}\,M_\odot$), and a number of them exhibit misaligned stellar and gas components. In contrast, the

rotationally supported lenticulars of their sample tend to be within high-mass groups ($> 10^{13}$ $M_\odot$) and exhibit ellipticity and Sérsic index distributions that are more compatible with the properties observed in spiral galaxies with similar stellar masses. This work came to confirm previous findings from the pilot study of the stellar populations and kinematics of 21 S0 galaxies by Coccato et al. (2020), combining dedicated observations with the Multi-Unit Spectroscopic Explorer (Bacon et al. 2010) and archival data from the ATLAS^{3D} survey.

More recently, in Coccato et al. (2022) two classes of S0 galaxies were defined based on the distributions of age, kinematics, size, Sérsic index, stellar mass, and bulge-to-total light ratio. A KMeans clustering algorithm was applied to find the two classes from these parameters of a sample of 329 S0s from MaNGA and SAMI, and then study the distribution of both classes within different environments. By comparing the two classes, they found that one is composed of galaxies that, on average, are less massive, smaller, younger, more rotationally supported, have lower Sérsic indices and smaller bulge-to-total light ratios than the galaxies of the other class. They attributed all the characteristics of the less massive lenticulars to the expected outcome of faded spiral galaxies, including any gas consumption or gas removal mechanism not related with gravitational encounters, while the properties of the more massive ones could be those of lenticulars formed through galaxy mergers. Furthermore, according to the authors, these descriptions match with the observation of an increase in the fraction of galaxies that belong to the less massive class with both the local density of the environment and the halo mass of the host group at the expense of the more massive lenticulars.

With all this evidence, it is clear that different classes of S0 galaxies exist and that they can be identified from the properties of both the stellar and gas components. Nevertheless, if we want to associate any attribute of these objects with a specific formation pathway, we first need to understand the expected outcomes in each component produced by the different mechanisms capable of driving their transformation.

1.2 THE FORMATION PATHWAYS OF LENTICULAR GALAXIES

The range of properties observed in lenticular galaxies certainly calls for more than one formation pathway. As stated at the beginning of this chapter, at least two classes of external mechanisms, not necessarily mutually exclusive, are needed to explain the observed characteristics of these galaxies in the nearby Universe. These mechanisms are hydrodynamic interactions and gravitational encounters. In addition, I will also discuss the role of internal, secular processes in the transformation of late-type spirals into lenticulars. The premise of this thesis is to explore the idea that the radically different physical processes

involved in each case should leave some imprint on the properties of the galaxies on which they act.

1.2.1 *Evolution driven by hydrodynamics*

Hydrodynamic mechanisms are thought to drive the transformation of spiral galaxies into S0s within galaxy aggregations. Galaxy clusters are specially favourable places for this sort of interactions because the density ($n_{ICM} \sim 10^{-3} - 10^{-1}$ cm^{-3}) and temperature ($T \sim 10^{7} - 10^{8}$ K) of the ICM (Peterson & Fabian 2006) are high enough to interact with interstellar medium (ISM) of the galaxies that move through it at high relative velocities that in some cases exceed 1000 km/s. The RPS (Gunn & Gott 1972), probably assisted by transport processes such as continuous turbulent viscous stripping (Nulsen 1982; Roediger & Hensler 2005), is one of the primary mechanisms of this type. The ram pressure of the ICM can remove the cold atomic gas in the disc of galaxies in about one cluster crossing time ($\sim 10^{9}$ yr, Merluzzi et al. 2016; Lotz et al. 2019). Nevertheless, hydrodynamic simulations show that the efficiency of these mechanisms can be even higher depending on factors such as the inclination of the discs relative to the trajectory (Abadi et al. 1999) or the presence of multiphase structures in the ISM and gaps on its spatial distribution (Quilis et al. 2000). Consequently, a considerable fraction of the total gas reservoir can be stripped even on shorter timescales of about 10^{8} yr. Only massive galaxies with a strong enough gravitational field will be able to retain some gas in their central regions, where star formation will be progressively quenched by a low-rate star formation activity. Additionally, the RPS can "strangulate" or "starve" galaxies by removing from their dark matter haloes the reservoir of hot gas, preventing its subsequent cooling and disc replenishment (Larson et al. 1980). All this should translate into an outside-in quenching of the star formation activity in galaxies (see Boselli et al. 2022 and the references therein).

Unlike the gas, which is collisional, the stars of the galaxies undergoing RPS remain unaffected by the interaction. Therefore, it is expected that the stellar kinematics of S0 galaxies that have evolved primarily through hydrodynamic interactions will resemble those of their spiral ancestors and still be dominated, essentially, by rotation. In other words, it is expected that these lenticulars exhibit more elongated shapes and higher angular momenta than those that could have acquired their early-type morphology by other means (Rizzo et al. 2018; Deeley et al. 2020).

1.2.2 *Evolution driven by gravity*

Galaxy mergers operate effectively in the low-density general field or within small groups, where the peculiar velocities of galaxies are sim-

ilar to the internal velocities of their stars. Hydrodynamic simulations such as those run by Hopkins et al. (2013) show that these interactions often result in the inflow of gas towards the galaxy's central region, where it is compressed, giving place to starbursts. This description is supported by the observation of extended star formation enhancements in galaxies that exhibit signs of recent interactions, such as the double-peak galaxies studied by Maschmann et al. (2020; 2022). The kinematic misalignment between gas and stellar components has been extensively used to identify galaxies that have undergone recent accretion events (e. g., Bertola et al. 1992; Kannappan & Fabricant 2001; Sarzi et al. 2006; Davis et al. 2011; Deeley et al. 2020). Indeed, in Chen et al. (2016) the presence of counterrotating gas in galaxies is linked to intense, nuclear (< 1 kpc) star formation. The accreted gas is thought to exchange angular momentum with the pre-existing gas of the galaxy and cause an inflow towards the central region, fuelling both star formation and accretion into the supermassive black hole (Raimundo et al. 2023). Hydrodynamic simulations also show that mergers – especially minor – can produce long-lived ($\sim 1 - 6 \times 10^9$ years), SF, rings in the primary galaxies (Mapelli et al. 2015; Deeley et al. 2021). In addition, mergers not only affect the ISM but also leave their imprint on the stellar kinematics by contributing to making discs with smaller ellipticities and slightly more pressure support than those of typical spiral galaxies (Querejeta et al. 2015). The fact that all these features are frequently observed in fully-formed lenticulars (e. g., Comerón et al. 2014; Deeley et al. 2020; Maschmann et al. 2020; Rathore et al. 2022), suggests a scenario where mergers play an important role in shaping the properties of these galaxies.

Hydrodynamic interactions and gravitational encounters can also operate together. For instance, within groups and clusters, galaxies are "harassed" through multiple high-speed encounters with companion galaxies (Moore et al. 1996) and/or with the group/cluster potential. Chemodynamical simulations, such as those analysed in Bekki & Couch (2011), show that repetitive gravitational encounters can trigger starbursts in the bulge of galaxies, especially during the group stage in which the spiral galaxies are pre-processed before falling into a cluster. These interactions may produce outcomes similar to galaxy mergers on the properties of S0 galaxies.

1.2.3 *Secular evolution*

Some S0s could have also evolved secularly from strangulated spiral galaxies. In Peng et al. (2015), strangulation is proposed as the primary mechanism of galaxy quenching. Its authors determined the stellar metallicity in 26,000 nearby galaxies and found that, for a stellar mass smaller than $10^{11}\,M_\odot$, quenched galaxies are more metal rich than SF galaxies of a similar mass. They argue that the higher

metallicity in a quenched galaxy results from enrichment through uninterrupted star formation activity without low-metallicity gas replenishment. In the absence of SF regions dissipating the excess of energy through gas collisions, the instabilities in the disc of a quiescent spiral galaxy grow out of control. As a consequence, the system heats up and may eventually lose the spiral arms, transforming into a S0 galaxy.

This scenario in which the supply of cold gas to the galaxy is halted but star formation continues within the galaxy, increasing the metallicity, cannot be driven by RPS. As discussed in Section 1.2.1, apart from removing the gas reservoir that galaxies may still keep in their cropped haloes, the latter mechanism would also strip the gas that feeds star formation in the disc on a relatively short timescale, so a substantial further star formation-driven enrichment would be impossible. It is more likely, as some authors suggest, that the outflows associated with active galactic nuclei (AGN) and stellar feedback can cause the strangulation, since the injection of energy into the halo may prevent the gas from cooling down and being accreted (van de Voort et al. 2016; Brownson et al. 2019). Both types of feedback can be fuelled by secular processes. For instance, disc instabilities such as spiral arms and bars may increase the efficiency of both star formation and nuclear accretion by transporting gas to the central region and enhancing its density (Vera et al. 2016; Silva-Lima et al. 2022). However, while supernova explosions and stellar winds associated with stellar feedback operate over the whole galaxy, they may be insufficient to prevent the re-accretion of the expelled gas by massive galaxies with a strong gravitational field (Muratov et al. 2015; Chisholm et al. 2017). And while it is true that massive galaxies usually host luminous AGN associated with powerful outflows, still the injection of energy is anisotropic and the influence is limited in most cases to the central region of galaxies (King & Pounds 2015; Fluetsch et al. 2019).

Therefore, it seems more likely that secular processes only play a secondary role, assisting the morphological transformation driven by external mechanisms. Indeed, the relative importance of the different mechanisms here discussed, has been recently explored with the aid of cosmological hydrodynamic simulations. The study of the formation history of S0-like galaxies in the IllustrisTNG-100-1 simulation (Springel et al. 2018) by Deeley et al. (2021), suggests that only six per cent of these objects would have evolved without experiencing major interactions. Instead, gas stripping and merger events would be, according to these simulations, the two main pathways for S0 formation.

1.3 THESIS OVERVIEW

The main objective of this thesis is to study the properties of the gaseous and stellar components of lenticular galaxies to gain further insight into their formation pathways. The main novelty of our approach is that the focus is directly placed on the full optical spectrum of these galaxies, and the samples investigated have an unprecedented size. In addition, spectra are analysed through machine learning techniques, so the results are fully independent of any physical model of the gas and stellar components.

The thesis is divided in four parts with different chapters. In the first two, each chapter corresponds to a publication produced as part of the investigation. The last part before the appendix (Part iii), contains the summary of the main results and conclusions of this thesis, and provides a brief outline on how I want to expand this investigation.

Part i is devoted to the study of single-fibre spectra of S0 galaxies. In Tous et al. (2020; Chapter 2), we present the identification of two main classes of S0, and a third one with a few objects with intermediate properties, from the PCA applied to a sample of ~ 68,000 spectra of these galaxies from the SDSS-DR12 (Alam et al. 2015). The two classes are characterized in terms of their typical spectral features and both internal and external properties. In Jiménez-Palau et al. (2022b; Chapter 3) we investigate the main ionization sources in these classes through the comparison of the PCA-based classification with well established activity diagnosis from the literature at different regions of the electromagnetic spectrum.

In Part ii the PCA methodology is extended to study spatially resolved spectra from the MaNGA survey. First, the methodology is applied on a sample of 532 lenticulars from the preliminary release contained in the SDSS-DR15 (Aguado et al. 2019) to characterize the activity gradient in these objects. The exercise reveals that SF, inner rings are relatively common among lenticular galaxies and the origin of these disc instabilities is discussed in Tous et al. (2023; Chapter 4). Finally, in Tous et al. (submited; Chapter 5), the methodology is used on data from the final release of MaNGA (Abdurro'uf et al. 2022) to explore the correlation between the radial activity structure and the processes of quenching and rejuvenation in 1072 S0 galaxies.

In the appendix of this thesis (Part iv), I have also included Navó et al. (2019; Appendix A), where the stacking technique employed in Part ii is introduced for the first time, and the complete catalogue of SF rings (Appendix B) built in Tous et al. (2023).

Part I

INSIGHTS FROM SINGLE-FIBRE SPECTRA

2 SPECTRAL CLASSIFICATION

Galaxy spectra are a wealthy source of information about the baryonic content of the Universe. However, the high complexity of these multidimensional data makes of its interpretation a difficult task. PCA is an extremely useful information compression technique that can be used in this situation. In Tous et al. (2020), we present its application in the classification of optical spectra of present-day S0 galaxies. It is the first step to investigating the evolution of these galaxies from a new perspective that puts the focus directly on the spectra and uses physical quantities to interpret the outcome of the classification.

The representation of nearly 70,000 integrated SDSS-DR12 spectra of S0 in the plane defined by their first two principal components (PCs)[1], allows identifying three regions where galaxies cluster depending on their activity level (star formation/AGN and quiescence). The most populated region, which we call the passive sequence (PS), is a compact strip that contains systems conforming to the traditional view of "red and dead" galaxies. Instead, another quarter of the local S0 population resides in an extended active cloud (AC), formed by systems with significant nebular emission. Both areas of the diagram are separated by a narrow dividing zone that constitutes the transition region (TR), inhabited by a small fraction of lenticular galaxies with intermediate spectral properties.

Statistical assessment of the characteristics of each class reveals that the differences extend to the properties of both the gas and the stellar components. Compared to the PS spectral class, the galaxies in the AC tend to be slightly less massive, more luminous with less concentrated light profiles, have a younger, bluer, and metal-poorer stellar component, and avoid high-galaxy-density regions. Consistently with their emission line spectra, the galaxies of the AC class show star formation rates (SFRs) that can be comparable to those observed in Milky Way-like spirals. Our results provide solid evidence that star formation in S0 galaxies is not a rare phenomenon and raise the possibility of identifying these active systems with plausible progenitors of their quiescent counterparts.

In addition, the rigorous tests presented in the first appendix of this paper demonstrate that our spectral classification is unaffected by the inclination of galaxies, neither by the finite aperture of the fibres used to decompose their light.

1 The first five principal components are publicly available in https://cdsarc.cds.unistra.fr/viz-bin/cat/J/MNRAS/515/3956 (Jimenez-Palau et al. 2022a).

Monthly Notices
of the
ROYAL ASTRONOMICAL SOCIETY

MNRAS **495,** 4135–4157 (2020)
Advance Access publication 2020 May 21

doi:10.1093/mnras/staa1408

The local Universe in the era of large surveys – I. Spectral classification of S0 galaxies

J. L. Tous [1,2★] J. M. Solanes[1,2] and J. D. Perea[3]

[1]*Departament de Física Quàntica i Astrofísica, Universitat de Barcelona, C. Martí i Franquès 1, E-08028 Barcelona, Spain*
[2]*Institut de Ciències del Cosmos (ICCUB), Universitat de Barcelona., C. Martí i Franquès 1, E-08028 Barcelona, Spain*
[3]*Departamento de Astronomía Extragaláctica, Instituto de Astrofísica de Andalucía, IAA–CSIC, Glorieta de la Astronomía s/n, E-18008 Granada, Spain*

Accepted 2020 May 18. Received 2020 May 18; in original form 2020 February 26

ABSTRACT

This is the first paper in a series devoted to review the main properties of galaxies designated S0 in the Hubble classification system. Our aim is to gather abundant and, above all, robust information on the most relevant physical parameters of this poorly understood morphological type and their possible dependence on the environment, which could later be used to assess their possible formation channel(s). The adopted approach combines the characterization of the fundamental features of the optical spectra of 68 043 S0 with heliocentric $z \lesssim 0.1$ with the exploration of a comprehensive set of their global attributes. A principal component analysis is used to reduce the huge number of dimensions of the spectral data to a low-dimensional space facilitating a bias-free machine-learning-based classification of the galaxies. This procedure has revealed that objects bearing the S0 designation consist, despite their similar morphology, of two separate subpopulations with statistically inconsistent physical properties. Compared to the absorption-dominated S0, those with significant nebular emission are, on average, somewhat less massive, more luminous with less concentrated light profiles, have a younger, bluer, and metal-poorer stellar component, and avoid high-galaxy-density regions. Noteworthy is the fact that the majority of members of this latter class, which accounts for at least a quarter of the local S0 population, show star formation rates and spectral characteristics entirely similar to those seen in late spirals. Our findings suggest that star-forming S0 might be less rare than hitherto believed and raise the interesting possibility of identifying them with plausible progenitors of their quiescent counterparts.

Key words: galaxies: elliptical and lenticular, cD – galaxies: evolution – galaxies: formation – galaxies: general – galaxies: stellar content.

1 INTRODUCTION

Hubble (1936) introduced in his book, The Realm of Nebulae, a hypothetical class of S0 galaxies that were supposed to have intermediate characteristics between those of E (elliptical) and S (spiral) galaxies. Later works by Hubble himself and other eminent morphologists (see, e.g. the review on the early history of galaxy classification by Sandage 2005) indicated that the lens-shaped galaxies that were often found in galaxy aggregations had to be identified as the S0 postulated by Hubble. This identification seemed reasonable because (typical) lenticular galaxies (from now on, the terms S0 and lenticular will be used indifferently) contain both a significant spheroidal central component and a disc component. Although these two structural elements are present to a greater or lesser extent in most spirals – the exception being some bulgeless discs – the main difference between them and lenticulars is that the objects of the latter class host thick and smooth discs, without a spiral structure, and consist mainly of aging stars.

Fifteen years later, the observation that S0, unlike in the field, comprise the dominant population in the central regions of many rich clusters of galaxies led Spitzer & Baade (1951) to suggest that such objects were, in fact, spirals from which the interstellar gas has been removed by collisions with other galaxies, quenching the star formation in the discs. It would take 21 more years to realize that it was much more likely that the gas-sweeping mechanism operating in these large structures is actually the ram pressure produced by the intracluster medium upon the discs as galaxies move through the cluster (Gunn & Gott 1972).

The view that the cluster environment can drive the transformation of S into S0 is supported by several pieces of observational evidence. One of the most important is the morphology–density relation in rich clusters (Dressler 1980; Postman & Geller 1984; Giovanelli, Haynes & Chincarini 1986; Goto et al. 2003; Cappellari

★ E-mail: jtous@fqa.ub.edu

et al. 2011; Houghton 2015), which convincingly demonstrates that in such systems the number fraction of S0 rises with local projected density at the same pace that the S + Irr (irregular) fraction diminishes. Yet, the most direct evidence that late-type galaxies (LTGs) may evolve in dense environments to become S0 is what is generically known as the Butcher–Oemler effect (Butcher & Oemler 1978) consisting of the observation that a number of moderately high-redshift ($z \sim 0.4$–0.5) clusters contain a higher proportion of blue, star-forming objects, as well as a factor of 2 lower S0 and E fractions than local galaxy associations (e.g. Couch et al. 1994,1998; Dressler et al. 1997; Poggianti et al. 1999; Fasano et al. 2000; Treu et al. 2003).

In spite of being the dominant constituent in the inner regions of many rich clusters, S0 also occur, albeit less frequently – in terms of the relative population fractions, but not necessarily in terms of global numbers – in small groups and even in the general field, where one can hardly expect that hydrodynamic interactions between the interstellar medium (ISM) and the much more tenuous intergalactic gas account for their formation. The presence of bulge-enhanced, spiral-less disc galaxies in lower density environments is explained instead by invoking close gravitational interactions between pairs of late-type objects that may lead to their merger (Barnes 1999; Querejeta et al. 2015; Eliche-Moral et al. 2018), since this sort of transformation mechanism is most effective when the relative speeds of the galaxies are low and similar to the internal velocities of their stars.

We are therefore confronted with the possibility that galaxies that fit into Hubble's S0 class may have followed at least two distinct formation pathways: some could be descendants of evolved S and/or Irr whose gaseous component is swept by the dense intracluster medium and their shapes altered by tidal interactions either with the global cluster potential, or with other cluster members, or both (Moore et al. 1996), while other, in good agreement with the standard hierarchical scenario of structure formation, could be the result of the merger of smaller disc systems (note that in both cases, the ancestors must always be objects of late type).

Past efforts to understand S0 and their origin have focused essentially on studying the gross properties of these objects inferred from photometric data in one or more broad wavelength bands, from radio to X-rays. There have been works devoted to analyse, for instance, either the luminosities and sizes of the bulge component (Solanes, Salvador-Solé & Sanromà 1989; Barway et al. 2007; Mishra, Barway & Wadadekar 2017), the global luminosity function (Burstein et al. 2005), or the Tully–Fisher relation, both standard (Hinz, Rieke & Caldwell 2003; Bedregal, Aragón-Salamanca & Merrifield 2006; Williams, Bureau & Cappellari 2010; Davis et al. 2016) and baryonic (den Heijer et al. 2015). Such investigations have often produced mixed results regarding the parentage of S0 galaxies, which have led to the proposal of multiple formation theories (see, e.g. van den Bergh 2009) whose imprints in the observable properties of the remnants are, nevertheless, difficult to discriminate.

However, it is quite rare to find statistical studies focusing on the stellar content of S0 that deal with the wealth of information that is revealed when the emitted light is divided into its component wavelengths. The main reason is the much longer time-scales required to get a single usable data element, i.e. a spectrum pixel with a sufficiently high signal-to-noise ratio (S/N), compared to photometric observations which measure light over much broader wavelength bands. Fortunately, this situation has gradually changed over the course of this century, thanks to the advent of multiobject spectrographs that allow multiple galaxies to be observed in a single exposure, increasing the census of spectra available to the astronomical community by 10–50 times. One of the most paradigmatic examples of these groundbreaking surveys is perhaps the Sloan Digital Sky Survey (SDSS; York et al. 2000), which, over the last 17 years, has obtained optical single-fibre spectra for nearly a million galaxies in approximately 8000 deg^2 of the sky as regards only the nearby Universe ($z \lesssim 0.25$).

This is precisely the approach taken by Xiao et al. (2016), who have investigated the nuclear activities of a sample of 583 nearby S0 galaxies observed with the SDSS spectrograph with high S/N. After dividing their data set into galaxies with and without significant nebular emissions, these authors used the BPT diagnostic diagram (Baldwin, Phillips & Terlevich 1981) which determines the ionization mechanism from the flux ratios of four main emission lines, to classify their emission-line objects into star-forming galaxies, composite galaxies, Seyfert galaxies, and low-ionization nuclear emission-line region. Like previous studies have found, their analysis revealed that star-forming S0 have lower stellar masses and luminosities, and bluer global colours than the rest, while a more detailed analysis based on photometric 2D bulge-disc decomposition of a subset of their data reveals that these galaxies also have central regions with a low ($n < 2$) Sérsic index that, in a substantial number of cases, are bluer than the discs. These results, which agree with photometric studies that also hinted at the existence of two subclasses of S0 (e.g. Barway et al. 2013), support a picture in which star-forming S0 form through the accretion of gas from an external source – a gas-rich dwarf or a cosmological cold-gas filament – into a progenitor disc galaxy that leads to a short-lived burst of final star formation.[1] Besides, Xiao et al. also find evidences that activity and environment are related, since they observe that S0 with obvious signs of star formation and/or of hosting active galactic nuclei (AGN) reside essentially in low-density regions, while S0 with low-level emission lines (S/N $<$ 3) or with classic absorption-line spectra populate environments with a broader range of densities. In an earlier work, Helmboldt, Walterbos & Goto (2008) reached similar conclusions regarding the typical masses and local environments of actively star-forming early-type galaxies.

The spectral analyses of galaxies have recently broken newer ground with the measurement of spectra at multiple points in the same object using fibre bundles closely packed into hexagonally shaped integral field units. The Mapping of Nearby GAlaxies survey (MaNGA; Bundy et al. 2015) is a large-scale integral field spectroscopy (IFS) galaxy census included in the ongoing core projects of the fourth SDSS phase (Blanton et al. 2017), that is, using the two BOSS spectrographs to provide spatially resolved spectral information on thousands of nearby objects. In a recent work, Fraser-McKelvie et al. (2018) have investigated the stellar populations of both the bulge and disc components of a subset of 279 S0 galaxies selected from a partial release of MaNGA's observations. They extract four Lick indices from the spectral datacubes and use them to measure light-weighted stellar ages, metallicities, and α-enhancement parameters. When represented graphically, the index–index diagrams and the implied stellar age–metallicity plots for both regions show bimodal distributions strongly correlated with the stellar mass. The clear bimodality revealed by the spectroscopic data leads these authors to conclude that they are observing two

[1]Formation driven by dissipative processes may also explain the ubiquity of S0 with counter-rotating gas and stars (see, e.g. Tapia et al. 2017, and references therein).

distinct populations of S0 galaxies: one that is old, massive, and metal-rich, and that possesses bulges that are predominantly older than their discs, and the other that comprises a younger stellar population that is less massive and more metal-poor, and that has bulges with more recent star formation than the discs. In agreement with Xiao et al. (2016), the correlations inferred are found to extend to the light profiles and colours of the central regions, with low-mass galaxies harbouring a larger fraction of what they call pseudo-bulges and being more star forming, while the opposite is true for higher mass galaxies. This duality in the structural relations of the S0 galaxies points, according to the estimates by Fraser-McKelvie et al., to separate formation sequences that would be independent of the environment: the low-mass S0 would be the outcome of fading spirals, while their higher mass counterparts would preferentially arise from mergers. Nonetheless, because nearby cluster S0 are underrepresented in the MaNGA's galaxy sample used, it is also emphasized that this conclusion cannot be extrapolated to regions of high galaxy density.

This is the first paper in a series dedicated to investigate the physical properties of the galaxies classified as S0 within the local Universe ($z \lesssim 0.1$). Our aim is increasing our understanding of the members of this special morphological class that connects the two extremes of the Hubble sequence and, ultimately, identifying the formation channels that they may have followed. In Section 2, we give the details of the different data bases adopted for this study, which takes as its core data the several tens of thousands optical integrated spectra retrieved from the Main Galaxy Sample (MGS) of the Sloan Legacy Survey (Strauss et al. 2002), a magnitude-limited spectroscopic catalogue that was completed during the original SDSS observing plan, which ran from 2000 to 2008. The single-fibre SDSS spectra are cross-matched with several public photometric data sets, including the recently published catalogue by Domínguez Sánchez et al. (2018) of morphologies for MGS galaxies inferred using Deep Learning algorithms and our own determination of the galaxy local density. The adequate exploitation of this large body of data demands the use of automated diagnostic tools capable of extracting as much objective information as possible on the properties of the galaxies. Besides, we want to take advantage of all the information contained in the full range of wavelengths covered by the spectra instead of using just a few spectral lines. To satisfy both requirements, we apply in Section 3 the well-known exploratory technique of principal component analysis (PCA; e.g. Ronen, Aragon-Salamanca & Lahav 1999, and references therein), which provides an optimal representation of the data in terms of a few mutually-orthogonal linear variables that discriminate most effectively among the galaxy spectra. After discussing the outcome of the PCA in Section 4, we carry in Section 5 a detailed analysis of the physical characteristics of the major spectral classes into which the S0 population can be subdivided within the subspace defined by the projection of their spectra on the first and second principal components. Finally, in Section 6, we summarize this work, discuss its main findings, and present our conclusions. Three Appendices provide evidence of the statistical soundness of our results and complete the information given in the main text.

2 THE DATA BASE

2.1 Target selection

The source of galaxy spectra is the version of the MGS data base included in Data Release 12 of the SDSS (SDSS-DR12; Alam et al. 2015). The MGS provides reduced spectroscopic observations for extended objects (galaxies) that are essentially complete for extinction-corrected *r*-band Petrosian magnitudes below $r_{\rm lim} \simeq 17.7$. MGS spectra have been collected from two digital detectors (blue and red) mounted in the same telescope. They consist of 3800 spectral bins that cover a joint wavelength range of 3800–9200 Å with a spectral resolution R ranging from 1850 to 2200. This gives an average instrumental dispersion of 69 km s^{-1} per pixel and a velocity resolution of ∼90 km s^{-1}. The aperture diameter of the fibres collecting the spectra is 3 arcsec. This is a generally small radius within nearby galaxies, meaning that aperture effects could take on certain relevance, especially for the nearest objects. However, as it is empirically demonstrated in Appendix A1, the main conclusions derived from this work will not be affected by this potential shortcoming. The global incompleteness of the MGS is small, about 6 per cent (Strauss et al. 2002), so no action will be taken to compensate it. Similarly, we will ignore the additional incompleteness that arises in SDSS spectroscopy at very low redshifts ($z < 0.05$) for very bright galaxies due to blending with saturated stars, as it is negligible, less than 0.5 per cent according to Strauss et al..

Galaxy morphologies are retrieved from the catalogue by Domínguez Sánchez et al. (2018) that lists this information for ∼671 000 galaxies from the SDSS-DR7, covering most of the MGS. The classification of such a huge number of objects is obtained thanks to Deep Learning algorithms that use Convolutional Neural Networks trained with colour images from both the Galaxy Zoo 2 (Willett et al. 2013) and the visual classification catalogue of Nair & Abraham (2010). Compared to traditional visual determinations of the Hubble type, this automated classification is more reliable, more objective, and provides a more accurate identification of the structural elements needed to distinguish among the different galaxy classes. Thanks to these characteristics, the morphological identifications extend to up to the limits of the MGS and, therefore, are applied to a very large number of objects covering a wide dynamical range of physical properties.

Domínguez Sánchez et al.'s morphologies are based on the training with the Nair & Abraham's data set. They are provided in terms of a continuous numerical parameter that we convert into the classical discrete T-type classification (see, e.g. de Vaucouleurs 1977 and references therein) by simply taking the nearest integer to the reported values. According to these authors, the average scatter of Deep Learning morphological classifications is only $\sigma = 1.1$ and their performance, in terms of accuracy, completeness, and contamination, comparable or even better than that of expert classifier intercomparisons. To efficiently distinguish between pure E and S0 galaxies, they also provide the probability of being S0 ($P_{\rm S0}$) for objects with $T \leq 0$. We will consider any galaxy with $T \leq 0$ and $P_{\rm S0} > 0.7$ to be an S0. Such a conservative value for the probability has been chosen to prioritize the purity of the S0 sample while preserving a sufficient number of objects for the analysis. Possible contamination by the roundest E, which are difficult to distinguish from relatively face-on S0, or by undetected spiral structure in highly inclined discs is in all likelihood minimal, thanks to the strict selection criterion adopted and, especially, due to the fact that computers are far better than humans at detecting subtle variations in the brightness of the images (see also the statements by Fischer, Domínguez Sánchez & Bernardi 2019 as regards the identification of S0 classified using the same methodology). Visual inspection of the images of a random subset of our data has reassured us that we are dealing with genuine representatives of this population. We provide some examples in Appendix B.

Although the spectroscopic MGS observations span a relatively broad range of redshifts, we deal only with those S0 galaxies lying within $0.01 \leq z \leq 0.1$. The upper limit, which encompasses the peak of the MGS, is set to select a homogeneous sample of lenticular objects representative of the local Universe over which the effects of *K*-corrections, curvature, and cosmic evolution are negligible. The lower redshift limit excludes those (few) galaxies with most uncertain measurements due to their closeness or large apparent brightness. Although their number is also very small, we have also excluded galaxies with apparent magnitudes from elliptical Petrosian *r*-band fluxes brighter than 12.0 to eliminate objects with unrealistically high absolute luminosities in the surveyed volume. The application of all these constraints allows us to obtain a magnitude-limited sample of 68 043 integrated spectra from S0 galaxies, which will be hereafter referred to as the Main Local Sample of S0 (MLSS0).

The upper redshift adopted for the MLSS0 has also the characteristic of maximising the number of MGS galaxies that can be included in a volume-limited subset of it. By taking into account the redshift and magnitude limitations commented above, we define a volume-limited sample of 32 188 S0, the VLSS0 hereafter, that includes galaxies with Petrosian *r*-band absolute magnitude $M_r \lesssim -20.5$. Note that the sizes of the two collections of galaxies that we have just defined are approximately two orders of magnitude larger than that of any set of integrated S0 spectra used in previous studies and have no parallel either in the scale of S0 samples recently extracted from IFS surveys, which, at the time of the writing of this work, are still insufficient to draw conclusions with a high statistical power.

2.2 Spectrophotometric data

A great deal of the measurable properties required for this and forthcoming studies are selected mainly from the v1_0_1 of the NASA-Sloan Atlas (NSA) catalogue (Blanton et al. 2011). The NSA data set includes virtually all galaxies with known redshifts out to about $z < 0.15$ within the coverage of the SDSS-DR11 (an internal bookkeeping release). This catalogue is built around the SDSS optical/NIR properties, which are completed with observational data from the ultraviolet *Galaxy Evolution Explorer* (*GALEX*) survey (Boselli et al. 2011), the 21-cm Arecibo Legacy Fast ALFA (ALFALFA) survey (Giovanelli et al. 2005) – of which we also have the 21-cm linewidths and masses of neutral hydrogen (H I) of its final version (Haynes et al. 2018) – as well as with some measurements from the CfA Redshift Catalogue (ZCAT; Huchra, Geller & Corwin 1995), the 2dF Galaxy Redshift Survey (2dFGRS; Colless et al. 2001), the 6dF Galaxy Survey (6dFGS; Jones et al. 2004), and the NASA/IPAC Extragalactic Database (NED). However, not all the data in the NSA catalogue have been used. Some information, such as its estimation of the stellar mass, has been replaced with measurements retrieved from the latest version of the GALEX-SDSS-WISE Legacy Catalogue (GSWLC-2; Salim et al. 2016; Salim, Boquien & Lee 2018), which has led us to recalculate the mass-to-*r*-band-light ratio (unless otherwise stated, we use elliptical Petrosian aperture photometric data). We have also taken from this latter catalogue the estimates of the star formation rate (SFR) which, like the stellar mass, is based on joint UV + optical + mid-IR SED fitting, as well as the values of dust attenuation in different bands that we use to study the effects of internal extinction in our galaxies. In addition, the Portsmouth stellar kinematics and emission-line flux measurements of Thomas et al. (2013) have been chosen as a source for stellar velocities, fluxes, and equivalent width measurements of the most important recombination lines from SDSS spectra, whilst mass-weighted stellar population ages and metallicities calculated using a Chabrier-MILES fit of the stellar population parameters are retrieved from the eBOSS Firefly Value-Added Catalogue (Comparat et al. 2017). All these data have been further augmented with the information about group membership listed in the catalogue by Tempel et al. (2017). Finally, for galaxies belonging to the VLSS0, the information on the physical properties has been completed with our own determination of the number density of their environment (see the next section).

Unless otherwise stated, all cosmology-dependent variables involved in the present investigation have been scaled to a standard flat Friedmann–Robertson–Walker world model with matter energy density $\Omega_{\rm m} = 0.3$, dark energy density $\Omega_\Lambda = 0.7$, and Hubble constant $H_0 = 100h$ km s^{-1} Mpc^{-1} with $h = 0.7$.

2.3 Local densities

The proxy for environment we use is our own estimate of the local density of galaxies within narrow redshift slices. Extinction-corrected galaxy densities have been calculated exclusively for all the members of our volume-limited sample that belong to the Northern Galactic cap of the MGS, since in this region of the sky the sampling of galaxies is more exhaustive than in the Southern Galactic cap.

For a given galaxy, the density of its local environment is computed using an optimized version of the *k*-nearest-neighbour Bayesian estimator (cf. Casertano & Hut 1985) :

$$\mu_5 = C(\Delta m) \left(R^2 \sum_{i=1}^{5} d_i^2 \right)^{-1} , \quad (1)$$

where $R \approx cz/H_0$ is the radial distance to that galaxy and d_i is the angular separation between it and its *i*th closest neighbour selected among those galaxies with a recessional velocity within 1000 km s^{-1} from the target. Note that the use of the distances to all five neighbours notably improves the precision of density estimates compared to the traditional *k*-nearest-neighbour metric, which only considers the distance to the farthest companion. Besides, we have also included in equation (1) a correction factor,

$$C(\Delta m) = A \times 10^{0.6\Delta m} , \quad (2)$$

to account for the effect of Galactic extinction on the observed densities (Solanes, Giovanelli & Haynes 1996), something we consider necessary given the vast area of the sky probed by the sample. In equation (2), Δm is the extinction in the *r*-band at the position of the target, which we retrieve from the SDSS photometry, and A is a normalization constant that is set to 1, as we are only interested in ranking the local densities. Note also that by limiting the search of neighbours to galaxies lying within thin shells in recessional velocity around the target galaxy, equation (1) becomes, in practice, a 3D local density estimator.

We have avoided calculating densities for objects near the edges of the data set, as they may be underestimated. For this, we have first computed the probability density function of the angular distances to the fifth neighbour of all the Northern Galactic cap members of our volume-limited subset. Then, we have taken three times the scale (that is, the standard deviation) of this distribution to establish the thickness of the band around the edges of the survey in which the density calculation has not been performed – the galaxies lying in this peripheral region have nonetheless been used in the calculation of the densities of objects lying further inside. Likewise, the edge

effects in the density estimates of the nearest and furthest galaxies have been taken care of by increasing by 1000 km s^{-1} the radial coordinate of our data set at both ends, discarding afterwards the galaxies included in the resulting extra volume.

3 PRINCIPAL COMPONENT ANALYSIS

Because we are dealing with spectra of galaxies at distances that range over several hundreds of Mpc, their total fluxes and wavelength coverage are not directly comparable. It is therefore necessary to preprocess all the spectra to put them on an equal basis. We firstly start by shifting each spectrum to the laboratory rest frame. Since the binning in wavelength has a constant logarithmic dispersion, this correction is given by $\log \lambda_r = \log \lambda_o - \log(1 + z)$, where λ_r is the rest-frame wavelength and λ_o is the observed one. After applying this correction, we re-bin the flux and its error, interpolating into pixels with a constant logarithmic spacing of 0.0001, so the resolution of the original spectra is preserved along the full visible range.[2]

We have also taken care of spectral bins affected by sky lines or bad data by blacking out those pixels whose errors are set to infinity as well as those that have the mask bit BRIGHTSKY activated.[3] Any spectrum containing more than 10 per cent of troublesome pixels according to this criterion is fully discarded.

The spectra that pass our quality filter are then normalized. We have followed Dobos et al. (2012) and rescaled each individual spectrum to have the average value of the flux in several intervals representative of the continuum level, which is set equal to 1. We use the following expression:

$$f_{ij}^{n} = f_{ij} \left(\sum_{k} \frac{f_{kj}}{N_j} \right)^{-1} , \tag{3}$$

where f_{ij} is the flux at spectral bin i of galaxy j and the sum runs over the N_j bins conforming the following four wavelength intervals devoid of strong lines: 4200 – 4300, 4600 – 4800, 5400 – 5500, and 5600 – 5800 Å. Note that N_j may differ from one galaxy to another depending on the number of pixels with bad data that fall on these continuum regions. Spectra with more than 20 per cent of defective pixels within such intervals are also discarded.

The removal of problematic pixels introduces null values in the array of normalized fluxes, thus preventing the proper performance of the PCA. To solve this problem, we employ the PCA-based algorithm described by Yip et al. (2004) to fill such gaps. A brief summary of the algorithm's functioning would be that, on a first stage, it fills the gaps by linear interpolation and then uses a linear combination of the eigenspectra (ES from now on), derived from the full data set, to substitute the missing data and re-fill the gaps with more realistic flux values (Connolly & Szalay 1999). This second step is iterated until the reconstructed fluxes from the empty pixels converge. With this stage completed, the spectra are corrected for Galactic dust reddening calculated by means of the extinction PYTHON module (https://extinction.readthedocs.io/en/latest/), which relies on the standard Fitzpatrick (1999) dust extinction model. The A_V coefficient per object is obtained from the Galactic extinction in the g band included in the NSA catalogue, assuming a fixed R_V of 3.1.

[2] http://www.sdss.org/dr12/spectro/spectro_basics/.

[3] According to the SDSS spectral mask criteria; http://www.sdss.org/dr12/algorithms/bitmasks/#SPPIXMASK.

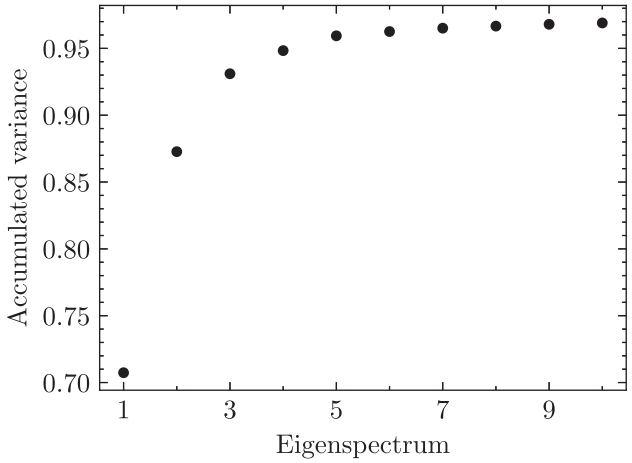

Figure 1. Accumulated fractional variance from the first 10 ES of the training sample.

Following preprocessing, we proceed to define the subset of the MGSS0, formed by the 6477 S0 galaxies whose spectra have S/N $\geq$ 30, as the training sample for the computation of the PCA. This restriction of the original sample to the galaxies with highest S/N is adopted to guarantee that the different dimensions inferred from the PCA decomposition are entirely physically motivated and not affected by noisy data. On the other hand, the threshold applied in the S/N maximizes the amount of variance explained by the different components, i.e. optimizes the dimensionality reduction, allowing us to work with the smallest possible set of ES, while still dealing with a training subset sufficiently large to ensure that these eigenvectors, also called principal components, are representative of the whole data set. As shown in Fig. 1, the first three ES already account for more than 90 per cent of the variance of the training sample, whilst only four ES are required to achieve the 95 per cent of it (had we derived the ES using the whole volume-limited sample, the number of dimensions required to account for these fractions of the variance would have been substantially larger). Besides, we have verified that the ES from this training sample are capable of reconstructing the specific spectrum of any S0 that belongs to the parent MGSS0 data set. This can be seen in the different panels of Fig. B1 in Appendix B, where we show, using arbitrary examples of S0 spectra, that the linear combination of the mean spectrum (top panel of Fig. 2) with the first 10 ES – the latter weighted by the coefficients that result from projecting the individual spectra on the corresponding ES – gives rise to reconstructed spectra nearly indistinguishable from the input ones. These projections of the spectral data vectors on the new orthogonal basis defined by the principal components are hereafter labelled PC1, PC2, etc.

4 S0 EIGENSPECTRA

The results of the previous section tell us that it should be possible to obtain a good insight on the main physical characteristics of the S0 population in the local Universe by plotting their spectral data projected on a low-dimensional space whose orthogonal axes are formed by the first three ES.

Fig. 2 depicts the mean of the ∼6500 training spectra along with the first three ES. The typical S0 spectrum, depicted in the top panel, is basically characterized by a red continuum that in the violet part shows a relatively strong 4000 Å break ($D4000$) and conspicuous H and K absorption lines corresponding to the fine

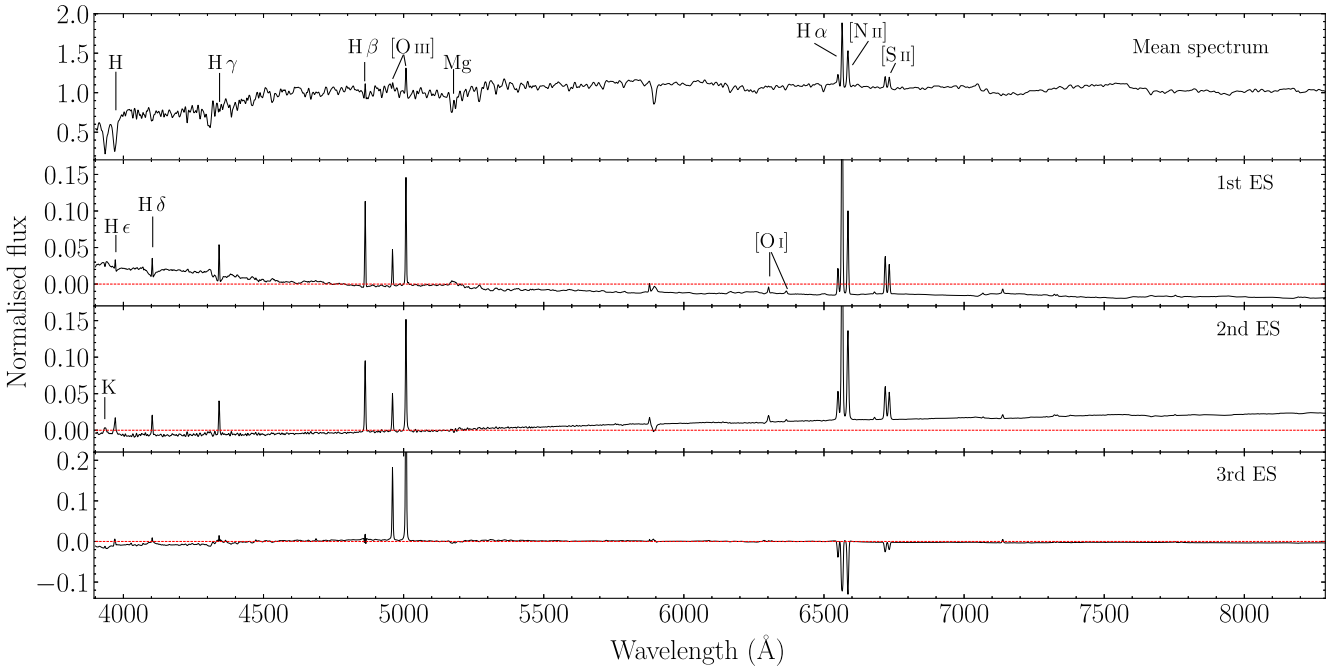

Figure 2. From the top to bottom: mean spectrum and first three ES of the 6477 S0 galaxies included in the training sample. The zero level of the ES is highlighted with a horizontal red dashed line. Some of the most important lines of the mean spectrum, also visible in the other panels, are labelled. Lines such as [O I], H δ, and H ϵ, which are blended with the Ca II H line, appear in emission in the first two ES, but not in the mean spectrum, whilst the other member of the Ca II doublet, the K line, is seen, also in emission, only in the second ES. Note, however, that the true emission/absorption nature of these lines is determined in practice by the sign of the weight factor multiplying each ES. The variance of the training sample explained by the first, second, and third ES is 71, 17, and 6 per cent, respectively, out of a total of 93 per cent.

structure splitting of the singly ionized calcium (Ca II) at $\lambda = 3935$ (K) and 3970 Å (H).[4] The average spectrum also shows a moderately strong H α emission line at 6565 Å and other, weaker, nebular lines that are labelled in the figure. The second panel from the top shows the first ES, which accounts for 71 per cent of the variation in the training sample. This mode combines a blue continuum with particularly strong emission lines that include the Balmer series from H α to H ϵ, as well as forbidden emission lines from both low-ionization species such as [S II], [N II], and [O I], and one, [O III], which is highly ionized (bear in mind, however, that the lines in the ES may act in practice either as emission lines or as absorption lines, depending on the sign of the weight factor applied to them). The second ES (third panel from the top), which accounts for 17 per cent of the variation in the training sample, has a similar appearance to the former spectra in terms of the emission lines. However, it differs basically in two aspects, the most important being that in this ES the continuum is red, whilst the other difference concerns the presence of the Ca II doublet in emission. It is also evident that the two components of this doublet behave somewhat differently, almost certainly due to the close proximity between the H line of Calcium and the Balmer H ϵ line, whose strengths are also often anticorrelated. This second component may play a role in the regulation of the strength of the emission and absorption lines present in the average spectrum. The third ES, shown in the bottom panel, accounts for only 6 per cent of the total variation, meaning that its features provide only a relatively fine tuning to the spectra reconstructed from the two lower order ES. In this mode, the continuum plays virtually no role – it is basically null except at wavelengths $\lesssim$4500 Å, where it slightly drops towards negative flux values – the most important characteristics being two strong [O III] emission lines, at 4960 and 5008 Å, and the H α + [N II] + [S II] complex, which is now observed in absorption. Other lines such as [O I], higher order Balmer lines, and the H line of Ca II are also present, although they are all very weak. As in the case of H α and the adjacent [N II] and [S II] lines, the [O III] λ5008 emission line is not just a star-forming indicator but also a good tracer of AGN activity (see, e.g. Trouille & Barger 2010; Suzuki et al. 2016, and references therein). This is because although this forbidden emission line originates from high-ionization states caused by both hot, young massive stars and AGN, it has been observed to be relatively weak in metal-rich, star-forming galaxies. Indeed, thanks to these characteristics, the third principal component is, despite its relative low weight, a useful diagnostic tool for activity in S0 galaxies (Tous et al., in preparation).

In Fig. 3, we portray the pairwise scatter plots that result from plotting the first three PC of the S0 galaxies in the MLSS0 against each other. As shown in the top panel, the PCA results delineate three distinct areas in the PC1–PC2 subspace, which point to the existence of two different subpopulations (from a spectral point of view) of S0 galaxies. A large number of points appear concentrated in a crowded narrow band that crosses the diagram diagonally defining a zone in this plane in which the values of the first two transformed predictors show a strong linear correlation indeed. This tilted band has a sharply defined edge on its left-hand side setting the boundary of a forbidden region in this subspace (see Section 5), whilst it extends on the right-hand side into a substantially less populated and much more scattered cloud of points where the projected values conform to the expectation of being linearly uncorrelated. The

[4]Rest-frame wavelength values are expressed in vacuum throughout this paper.

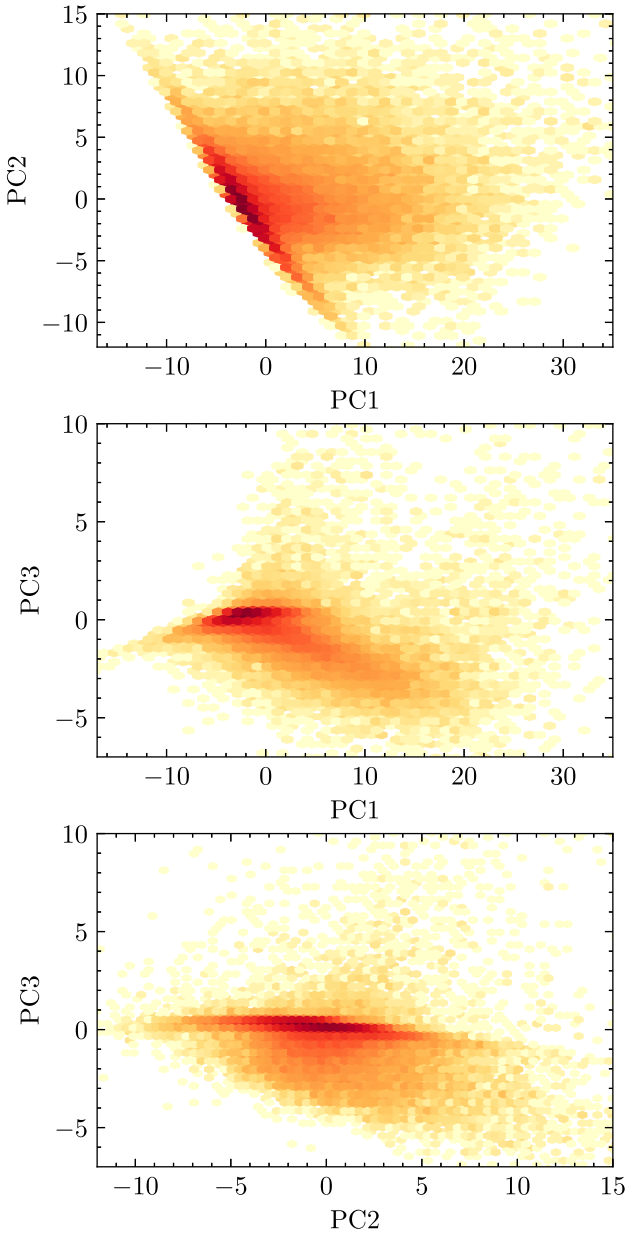

Figure 3. Projections of the S0 spectra in the MLSS0 on the three planes defined by the first three principal components. Data points have been grouped in hexagonal bins where the intensity of the colour scales with the logarithm of their number density. From the top to bottom, the panels portray the PC1–PC2, PC1–PC3, and PC2–PC3 subspaces.

compartmentalization of space observed in the PC1–PC2 diagram is not preserved in the other two 2D subspaces represented in the middle and bottom panels of Fig. 3 that involve the projections on to the third principal component. The distributions of data points in the PC1–PC3 and PC2–PC3 diagrams are certainly reminiscent of that in the top panel, but show a lower degree of organization. It can be seen that the galaxies whose spectra delineate the diagonal strip observed in the PC1–PC2 subspace are still strongly clustered, now forming in both planes an approximately horizontal strip around the PC3 = 0 coordinate. The rest of the data distribute unevenly both above and below this band, with the largest fraction showing negative values of PC3 and, at the same time, values of the PC1 and PC2 predictors that are positive in a good measure, an inherent feature of galaxies with a high Hα/[O III] flux ratio. Whichever the case, in the last two subspaces, the boundary of the forbidden region is much less clearly defined. Also note the fact that the peaks of the point clouds of the three 2D projections fall near the origin of the coordinate system, which indicates that the spectra of a good number of S0 galaxies must be quite similar to the mean spectrum reported in Fig. 2.

5 THE PC1–PC2 SUBSPACE

In the remainder of this paper, we will focus mainly on the definition and analysis of the major spectral classes into which the S0 population can be subdivided within the PC1–PC2 subspace, while the projections of the S0 spectra on the third principal component that, as mentioned in the previous section, bear information on the SFRs and nuclear activity of these galaxies, will be investigated in future work. For simplicity, in this and the following sections, the discussions involving the principal components will be dealt with using their observed values, since the correction of the aperture and inclination biases outlined in Appendix A lead to only small differences in the results that do not alter the conclusions of this work in a significant way.

5.1 Relationship with spectrophotometric observables

We have just seen that a great deal of the information about the variance of the S0 spectra is contained on the first two eigenvectors, which are dominated by strong emission lines but show continua with slopes of opposite sign (see Fig. 2). These two ES, when combined with the mean spectrum, must reproduce the general spectral features characteristic of completely passive galaxies with no detectable emission lines (this requires both ES to have negative weight factors; see, e.g. panel c in Fig. B1), as well as of galaxies showing star formation/starburst/AGN signatures, either on top of a red or blue continuum [the latter requires PC1 > 0, PC2 < 0, or both; see, e.g. panels (h), (i), and (k) of Fig. B1]. Thus, although there is no guarantee a priori that the new dimensions provided by a PCA – they are mutually orthogonal linear combinations of the input variables – have any physical meaning, it is sensible to expect in this particular case that the main spectral predictors we have inferred are closely connected to parameters that inform about the star formation history of the galaxies.

A thorough review of the different spectrophotometric properties included in our final data base has shown that the direction of the maximum variance in the strength of the Hα emission line, given by its equivalent width, EW(Hα), is essentially contained in the PC1–PC2 subspace. Besides, it is nearly perfectly orthogonal to the direction delineated by the tilted band identified in the top panel of Fig. 3, as illustrated in the top panel of Fig. 4. Actually, the EW(Hα) is the parameter of our catalogue that shows the strongest positive linear correlation with the first PC, whilst it also shows a weak positive correlation with PC2: According to the annotated heatmap depicted in Fig. 5, the corresponding Pearson correlation coefficients are r[EW(Hα), PC1] = 0.85 and r[EW(Hα), PC2] = 0.32, respectively. Besides, Fig. 4 allows one to see that the sharp lower left-hand boundary of the data cloud is the locus of S0 galaxies with no emission in the Hα line. This sensibility of the PC1–PC2 subspace to a specific spectral line may come as a surprise as PCA is known not to do a good job detecting differences in narrow spectral features. However, the fact that the Hα line is the strongest emission line in the mean spectrum and that it is flanked by two [N II] lines that are also rather strong (see

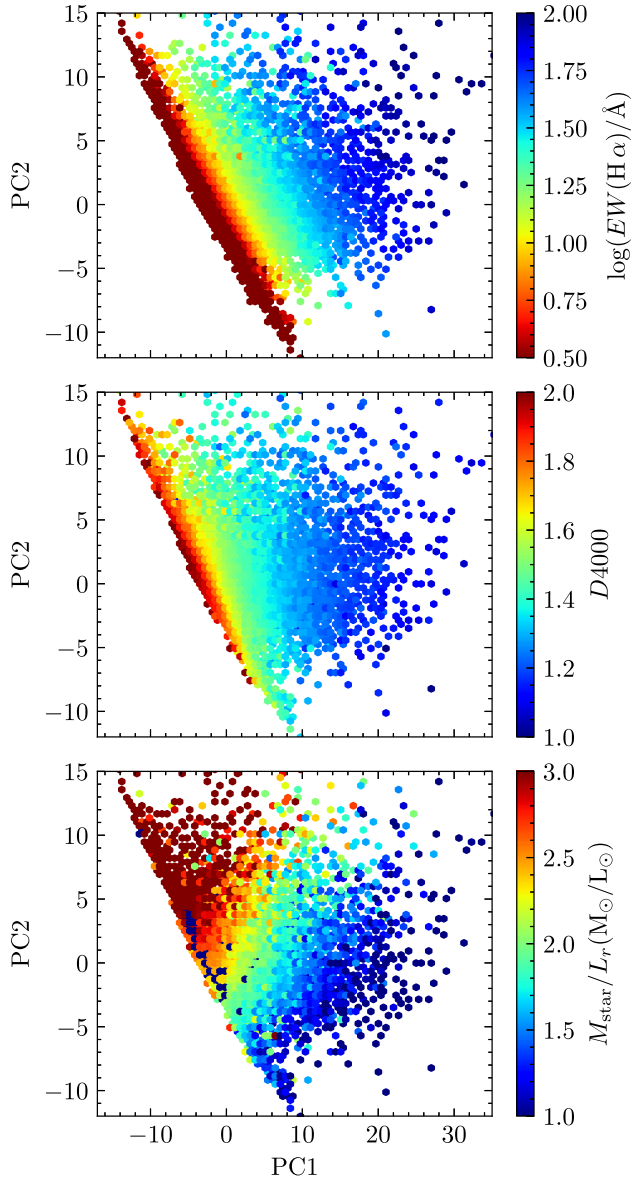

Figure 4. Same representation as in the upper panel of Fig 3 but using colour as a third dimension to indicate the mean equivalent width of the H α line at each hexagonal bin (top panel), the mean $D4000$ break (middle panel), and the mean stellar mass-to-light ratio $M_{\rm star}/L_r$ (bottom panel).

Fig. 2) make the H α–[N II] complex a remarkable classification feature within any optical galaxy spectrum. Nor must we forget that the H α emission can be closely related to quantities that are sensitive to the past and present star formation of the galaxies, such as the $D4000$ break, integrated colours, and SFR, both global and per unit mass, which involve more significant portions of the flux contained within the optical window. Indeed, we find that these latter parameters are also contained in the PC1–PC2 plane in good measure (see, e.g. the middle panel of Fig. 4) and, similarly to the EW(H α), they show a moderate to strong correlation with PC1 and a substantially feeble relationship with PC2. Actually, the correlations between all the physical properties investigated and the second predictor – which, in general, are positive – are found to be weak at best (all Pearson's coefficients are <0.5). As shown in Fig. 5, the stellar mass-to-light ratio $M_{\rm star}/L_r$ whose variance, like that of the colour – with which is known to be closely related – is also largely encapsulated into the PC1 axis (see the bottom panel of Fig. 4), is the parameter that shows the most evident connection with PC2 ($r[M_{\rm star}/L_r, {\rm PC2}] = 0.46$). For completeness, we have also included in Fig. 5 measures of the strength of the linear association between the physical variables and PC3. They behave much like those involving PC1, but are somewhat weaker (the strengths are similar to those involving PC2) and have opposite signs. All these results confirm that the most relevant predictors derived from our characterization of the S0 spectra encode information about the secular evolution of the stellar population of these galaxies.

5.2 Main spectral classes

As we have already pointed out, the cloud of S0 points in the PC1–PC2 plane shows obvious signs of being distributed into two regions (Fig. 3), whose natural divider appears to be a straight line orthogonal to the direction that maximizes the variation of the EW(H α) (see the top panel of Fig. 4). However, although the existence of a thin, lens-shaped zone consisting essentially of the S0 galaxies without significant H α emission is undeniable, it is not at all obvious to find the best place where to put the divider between said narrow band and the much more extended and scattered region dominated by the S0 with emission lines. Thus, rather than attempting to split the data by eye, and in line with the general approach adopted in this work, we have considered more adequate using a supervised machine learning classifier to split the distribution of S0 data points in this subspace into two different classes.

After exploring several binary classification algorithms, we have found that, for the sort of distribution we are dealing with, a logistic regression offers the best performance as it yields the highest accuracy, which is evaluated as the ratio of correctly classified objects over the total members of the training sample. The classification has been directly implemented in the PC1–PC2 plane and not in a subspace of higher dimension. Apart from a matter of simplicity, we have proceeded in this way mainly because we have verified that the outcome of the process is insensitive to the amount of PC involved. We have employed as training data set a sample of 400 S0 spectra selected from bonafide members of the two main groups we want the algorithm to come up with, tagging the galaxies falling into the narrow, lens-shaped region with ones and with zeros those outside it. Basically, what the algorithm does is, first, to fit a logistic model to the training set according to the labels assigned to each point and the positions they occupy in the PC1–PC2 subspace. Then, the model is used to assign to each galaxy in the whole data set a probability of belonging to the most compact mode, $P_{\rm PS}$. The outcome of this procedure is the extreme bimodal distribution shown in the histogram depicted in the left-hand panel of Fig. 6, where the data are essentially grouped in two large spikes around either end of the probability distribution, leaving only a few values between them. To unambiguously separate the galaxies that belong to each spike, we have applied a non-parametric binary classification scheme inspired on Otsu's method (Otsu 1979) – a 1D discrete analogue of Fisher's discriminant analysis – that in its simplest form splits the data into two classes by maximising the inter-class variance. Specifically, we have adopted the 95 per cent of the maximum inter-class variance as the upper limit of this parameter that defines the ranges of values of $P_{\rm PS}$, which should be associated with each main spectral mode of the S0 galaxies, represented by the red and blue histograms.

This mapping in the PC1–PC2 plane, which, as we have discussed above, is intimately connected to spectral parameters that inform

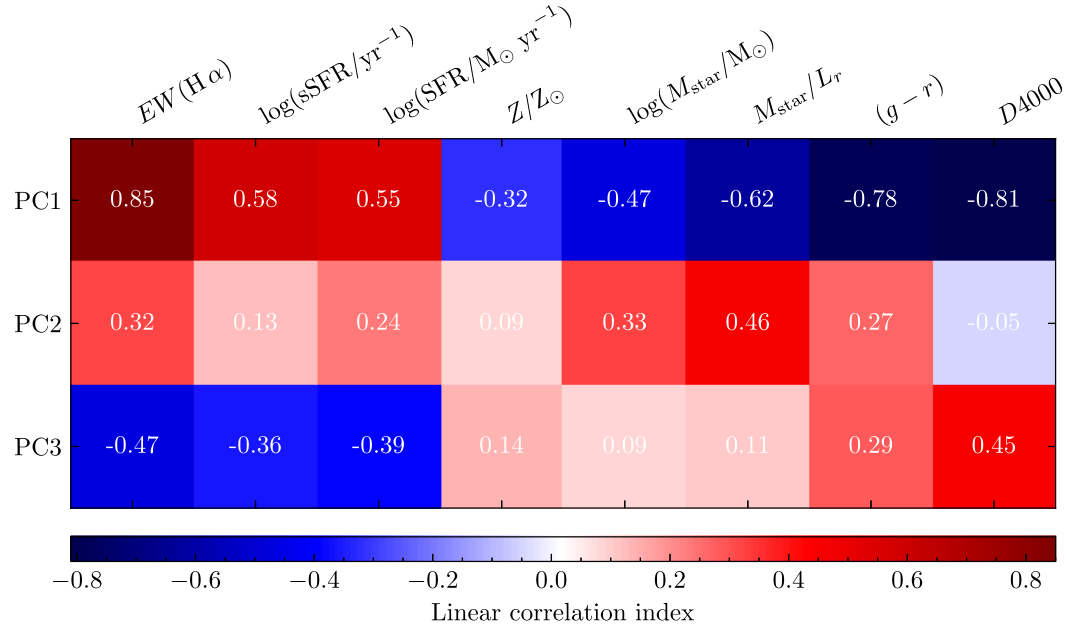

Figure 5. Linear pairwise correlations between the first three principal components of the spectra of S0 galaxies and the eight spectrophotometric properties in our data base more closely related to them. Cells are colour-coded according to the values of the Pearson's correlation statistic calculated from the VLSS0, which are also annotated.

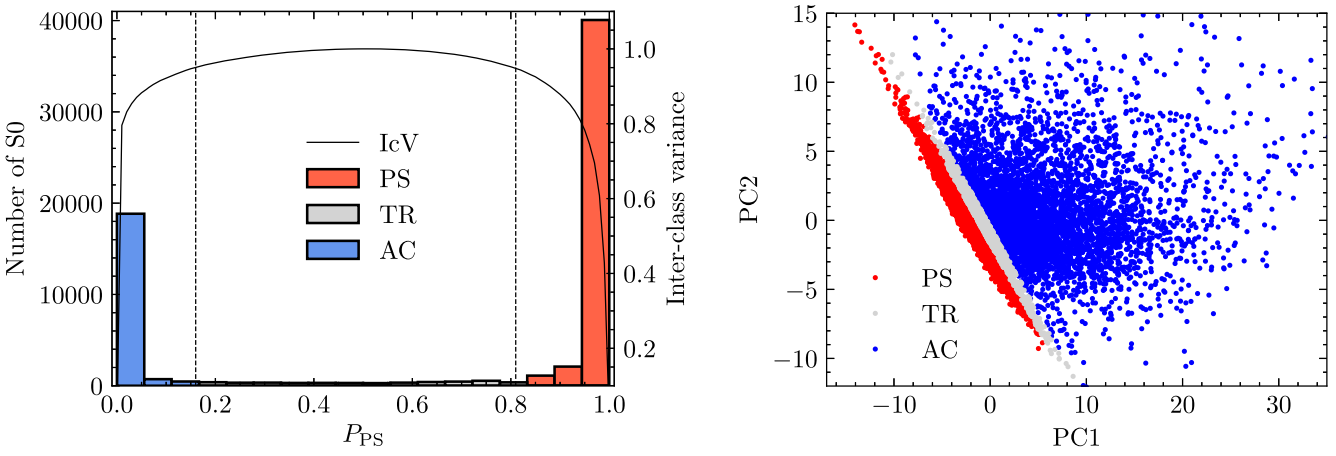

Figure 6. Left-hand panel: histogram showing the probability distribution that an S0 belongs to the Passive Sequence (PS), P_PS, which results from the application of the logistic regression to the whole MLSS0 in the PC1–PC2 subspace. The black curve indicates the fractional inter-class variance (IcV). We choose a value of 0.95 of this parameter to split the original data set into PS objects (S0 with $P_\mathrm{PS} \geq 0.81$), shown in red, and Active Cloud (AC) members (S0 with $P_\mathrm{PS} < 0.16$), which are shown in blue. S0 galaxies with values of P_PS outside these two extreme ranges, identified in the plot by two vertical dashed lines, are assigned to the Transition Region (TR) and are expected to show spectral characteristics intermediate between those of the PS and AC objects. Right-hand panel: similar to the top panel Fig. 3 but, instead of binning the data points into hexagons, here we represent a random 20 per cent of the original sample (to avoid overcrowding) with the different features of the PC1–PC2 diagram highlighted in colour: PS (red), AC (blue), and TR (grey).

on the activity of galaxies, bears some obvious similarities with the bimodal distribution into red and blue sequences shown by the general galaxy population in the colour–magnitude diagrams of optical broad-band photometric studies (see, e.g. Blanton & Moustakas 2009, and references therein). This has prompted us to designate the thin, compact band delineated in the PC1–PC2 subspace by the S0 which essentially lack Hα emission (shown in red colour too in the right-hand panel of Fig. 6) as the *Passive Sequence* (hence the PS subscript), whilst the name *Active Cloud* (AC) is used to denote the much more disperse area encompassed by the objects with star formation signatures (identified with blue colour in Fig. 6). Likewise, the narrow strip of the PC1–PC2 subspace, which houses the few S0 that fall in the deep valley separating the two main modes of P_PS because of their in-between spectral characteristics (represented in grey in Fig. 6), has been named the *Transition Region* (TR).

The suitability of the naming adopted to identify the different spectral classes detected in the PC1–PC2 subspace becomes evident when examining the mean spectrum of each group. In Fig. 7 we show, from the top to bottom, the mean optical spectral flux distributions of the galaxies classified as PS (red spectrum), TR (grey), and AC (blue). The lack of emission lines, the deep $D4000$ Å break and the rather red continuum seen in the mean spectrum of the PS are well-known characteristics of absorption-dominated

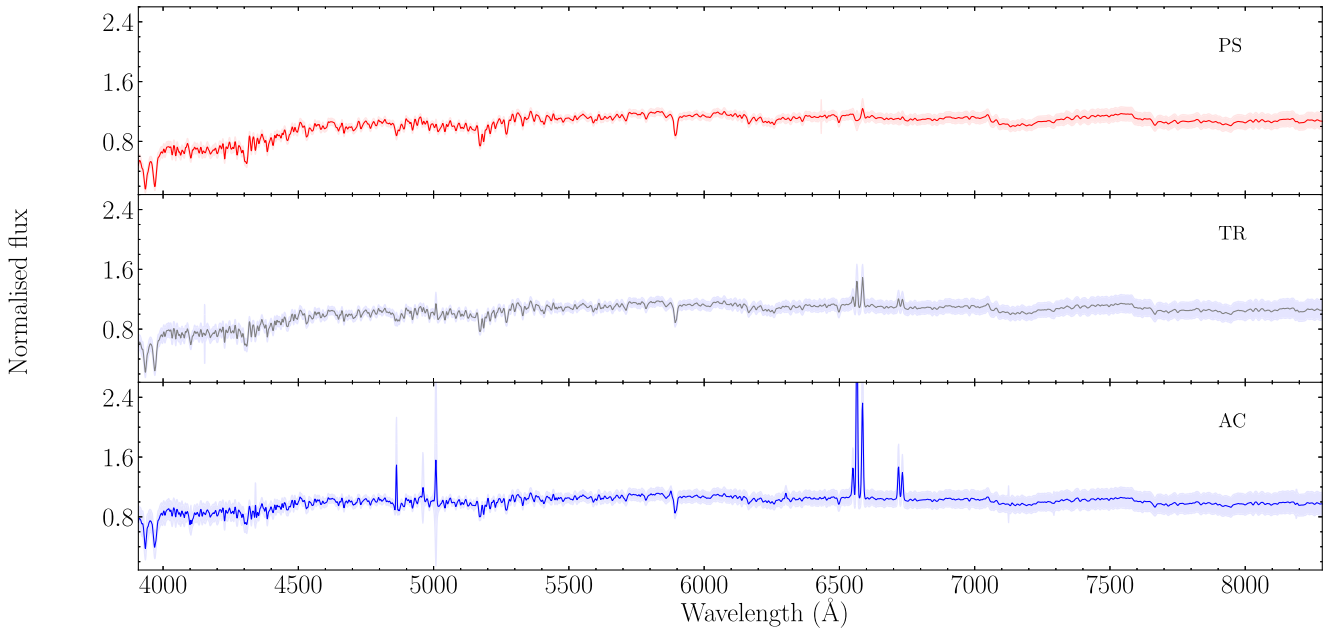

Figure 7. Mean spectra of the spectral classes of S0 determined from the first two principal components inferred in the PCA of our VLSS0 data set. From the top to bottom: the PS in red colour, the TR in grey, and the AC in blue. The shaded areas around the solid curves represent the 1σ variations about the average.

galaxies, whereas the relatively strong emission lines, the shallower $D4000$-Å break, and the somewhat bluer continuum are traits that warrant our classification of the AC galaxies as objects with a significant level of activity, which seems to be mainly related to star formation (see the next section). Note that the average spectrum of the latter class does not fit well within the classic picture of S0 galaxies, which are better represented by a spectrum similar to that of a typical PS object.

In a similar vein, we confirm the expectation that the characteristics of the mean spectrum of TR objects are intermediate with respect to those of the two main classes, with a relatively significant H α emission line, but with other emission lines from metals absent or rather weak. Fig. 7 also shows that the TR and AC spectral classes have 1σ uncertainties about the average (represented by the shaded areas surrounding the mean fluxes), bigger than that of the PS class, which reveal the greater variability shown by their spectra.

5.3 Physical properties of the spectral classes

The total numbers and corresponding fractions of objects of the VLSS0 that make up the two main S0 subpopulations, PS and AC, identified by our classification scheme are listed in the second and third rows of Table 1. The values in parentheses provide the same information for the whole MLSS0 data set. It follows that about two-thirds of the brightest S0 in the local Universe are members of the PS and show spectral characteristics which would agree with the classic image that is expected for these early-type galaxies. Nevertheless, we also have found that a quarter of the local S0 population belongs to the AC class[5] and hence presents a richer spectra with relatively strong emission lines, which demonstrates that not all S0 are necessarily quiescent objects.

Table 1 also summarizes for each main spectral class the median values of the probability distribution functions (PDFs) and their associated uncertainties, given in terms of interquartile ranges, of the eight properties most tightly correlated with the first principal components. The properties listed are (see also Section 5.1): the equivalent width of the H α line, (row 5 in Table 1), specific SFR (row 6), global SFR (row 7), stellar metallicity, represented by Z (row 8), total stellar mass (row 9), stellar mass-to-r-band-light ratio (row 10), $(g - r)$ colour index (row 11), and $D4000$-Å break (row 12). A more detailed inter-class comparison of these parameters is provided in Appendix C, where we display their full PDF in the form of violin plots.

It becomes clear from both the summary statistics reported in Table 1, and the symmetric density plots of Fig. C1 that the two subpopulations of lenticulars show many important differences on their typical physical parameters. This is confirmed by the application of a two-sample Kolmogorov–Smirnov (KS) test to the eight pairs of PDF, which has produced p-values $\ll 0.05$ in all cases, indicating that there is a very small likelihood that the two types of S0 come from the same parent population.

A further distinctive feature between the PDF of both spectral classes is that for PS objects, the distributions of some of the properties investigated, especially the two SFRs, Z, and, to a lesser extent, EW(H α), tend to be right-skewed and heavy-tailed (i.e. to have longer and heavier right tails), while the AC's distributions are more symmetric. Our examination of the robustness of the results rules out the possibility that this asymmetry obeys to a misclassification of highly inclined AC members as PS galaxies. Therefore, this could point to the existence of a subclass within the PS lenticulars that would have escaped detection.

To facilitate a more direct comparison between our results and those of previous studies of S0 galaxies that rank them according to some measurable global property, we plot in Fig. 8 the histograms of the two S0 classes detected in our VLSS0 as a function of stellar

[5]Given that the galaxies with emission lines appear to have bigger difficulties than quiescent objects in passing the filtering applied to select high-quality spectra (see Section 3), we cannot exclude the possibility that we are underestimating the true AC fraction somewhat.

Table 1. Amount of galaxies of the VLSS0 within each main spectral class, as well as medians and lower and upper quartiles of several of their most important physical properties.

S0 subpopulation	Passive Sequence			Active Cloud		
N (in MLSS0)	22 067 (43 579)			7933 (20 024)		
% (in MLSS0)	69 (64)			25 (29)		
Summary statistics	Q_1	Median	Q_4	Q_1	Median	Q_4
$\log(\mathrm{EW}(\mathrm{H}\alpha)/\text{Å})$	−0.516	−0.157	0.108	0.944	1.164	1.401
$\log(\mathrm{sSFR/yr^{-1}})$	−12.317	−11.934	−11.409	−10.600	−10.327	−10.033
$\log(\mathrm{SFR/M_\odot\ yr^{-1}})$	−1.557	−1.167	−0.584	0.133	0.376	0.603
$Z/Z_\odot$	1.259	1.498	1.717	0.820	1.012	1.199
$\log(M_{\mathrm{star}}/\mathrm{M_\odot})$	10.645	10.762	10.910	10.530	10.665	10.818
M_{star}/L_r ($\mathrm{M_\odot}/L_\odot$)	2.238	2.506	2.805	1.653	2.027	2.464
$(g-r)$	0.713	0.740	0.766	0.587	0.641	0.687
$D4000$	1.804	1.877	1.940	1.322	1.425	1.521

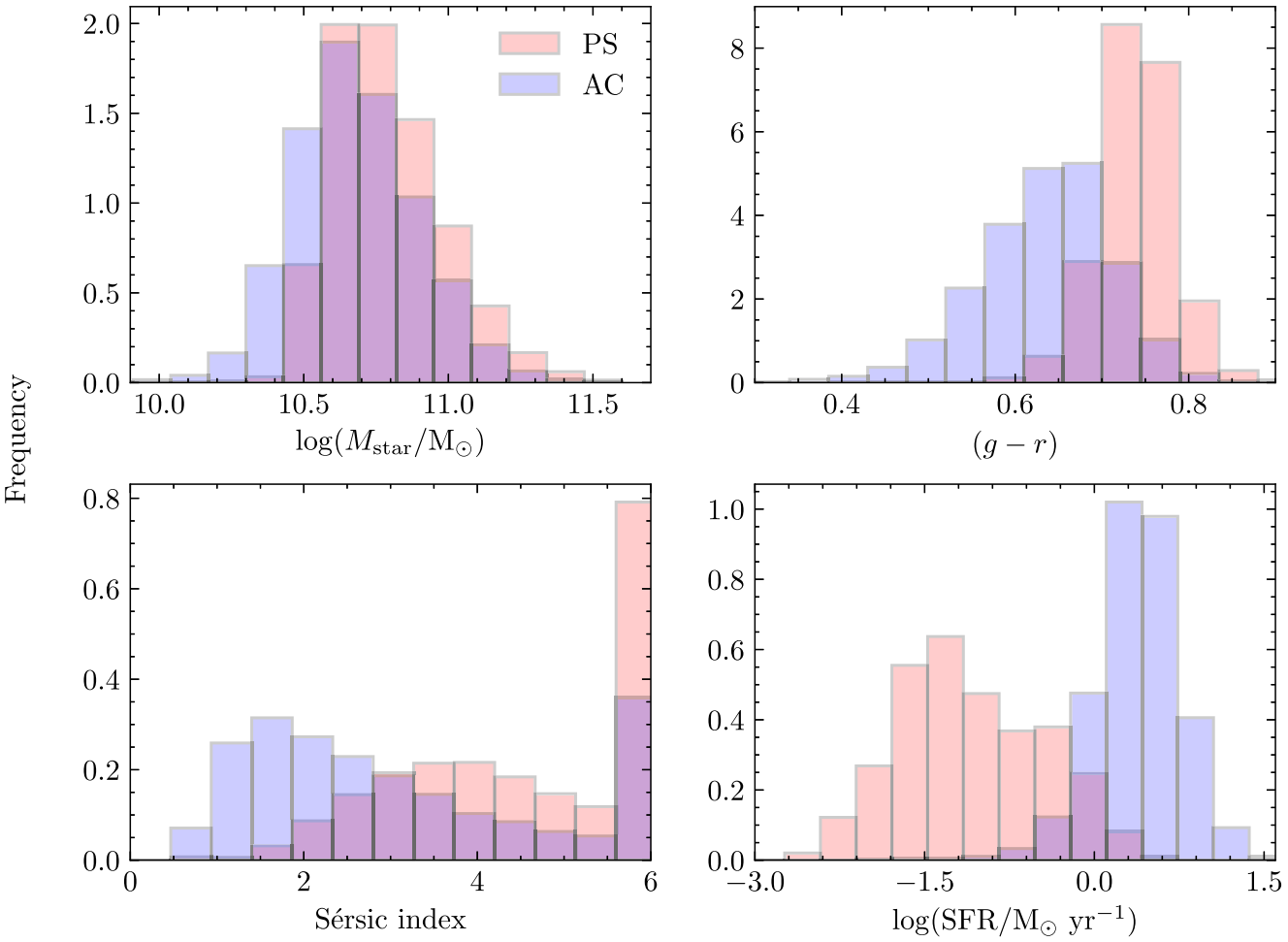

Figure 8. From the left to right and top to bottom: histograms of the stellar mass, $(g-r)$ colour, global Sérsic index, and SFR of lenticulars split by their spectral class. Red is used for PS objects and blue for members of the AC. According to a two-sample KS test, the two spectral classes show statistically significant differences on all these properties (the p-values are all $\ll 0.05$). The very high peaks of the Sérsic index at the right end of the distributions are unphysical, as they arise from an artificial limitation in the calculation of this parameter to values lower than 6.

mass (top left-hand panel), $(g-r)$ colour (top right-hand panel), global Sérsic index (bottom left-hand panel), and SFR (bottom right-hand panel), respectively. Likewise, in Fig. 9, we provide for these same galaxies number density contours showing the bivariate distribution of their stellar ages and metallicities and plotting also some data points colour-coded by stellar mass. The histograms, in particular, allow one to better appreciate the different discriminant capabilities of various spectrophotometric measurements when assessing membership in one of the S0 subpopulations that we have identified. The most unambiguous division of the spectral classes would be provided by the SFR (or its per-unit-mass counterpart, sSFR), which is capable of separating the two main modes within

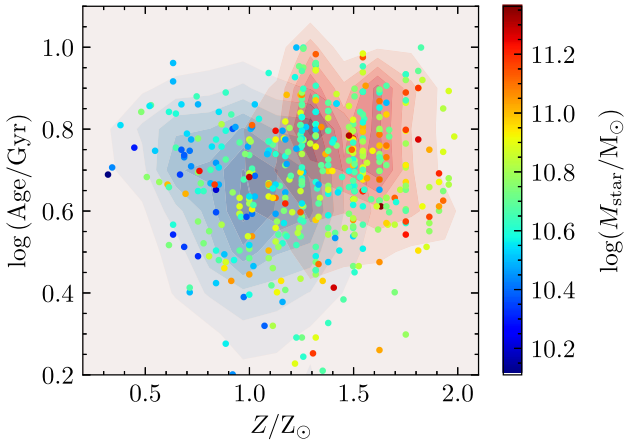

Figure 9. Contour plots showing the bivariate distribution of stellar ages and metallicities for galaxies in the VLSS0 partitioned into PS (red) and AC (blue) members; the darker the colour, the higher the density. Three per cent of the data points in this sample, to avoid overcrowding, have also been included, colour-coded by their stellar mass. The graph shows that our spectral classification of the S0 is reasonably correlated with both the age and the metallicity of the stellar population of these galaxies. However, there is no evidence of a substantial correlation with stellar mass.

much of the dynamic range of this property, proving almost as effective as our PCA-based technique. This is to be expected, given the relatively direct bearing that our automated classification method has with those physical parameters more intimately related to star formation (indeed a very similar result would have also been obtained by using the EW(Hα) or the $D4000$ break). For its part, the $(g-r)$ colour would perform well as divider on the extremes of its dynamic range, but could not resolve membership on its central part where the two S0 spectral modes show a substantial overlap. In contrast, the two subpopulations of S0 identified in our sample produce similar distributions of the global Sérsic index and, especially, of the total stellar mass – despite the long-recognized close relationship of the latter with the star formation history of galaxies (e.g. Gavazzi & Scodeggio 1996) – which would make these two properties unsuitable as discriminants of the two spectral modes. Recall, however, that in all the four cases, the differences between the PS and AC distributions are highly significant according to the two-sample KS test.

As regards the characteristic values of the properties assigned to each spectral class, our results are largely consistent with the outcomes by Xiao et al. (2016) and Fraser-McKelvie et al. (2018), who, using samples significantly smaller than ours, find that star-forming S0 galaxies are less massive, bluer,[6] and possess shallower, i.e. less concentrated, central light profiles, with a possible prevalence of pseudo-bulge-like components since a large proportion of them are best fitted by Sérsic profiles of index $n < 2$ (see also the results of an early study of E + S0 galaxies by Helmboldt et al. 2008). On top of that, our analysis reveals the existence of a good number of S0, *both active and passive*, with measurable SFRs. Among the latter, the observed values are certainly low and, when divided by the luminous mass of the parent galaxy, perfectly consistent with the sSFR values typical of the so-called 'non-star-forming red sequence of galaxies' (see, e.g. Kennicutt & Evans 2012, and references therein). Thus, despite they all have ongoing star formation, its reduced intensity has not prevented these galaxies from being assigned the passive status. On the other hand, the majority of the S0 belonging to the AC show SFR that are comparable or higher than the current rate of the Milky Way and that translate into values of the sSFR that are just as strong as those found in actively star-forming late spirals of the same mass. These high levels of star formation move this class of lenticulars largely away from the traditional view of quiescent galaxies.

The only discrepancy with respect to the former studies is the relevance attributed to the stellar mass, which is seen as the main driver of the division of lenticulars into two subpopulations associated with the degree of star formation (see, e.g. also Barway et al. 2013, who use as a divider the K-band luminosity) – and by extension of the formation pathway taken,[7] whilst, as noted above, it plays a lesser role in our investigation. Fig. 9, which is similar to fig. 5 of Fraser-McKelvie et al. (2018), supports further this conclusion, showing that, in contrast with those findings, in our data set, the stellar mass provides a division between the older, metal-rich PS objects and the younger, metal-poor AC counterparts, which is less clear. Differences in the mass ranges encompassed by the data sets analysed – unlike the other studies, ours deals with a volume-limited sample that for this reason contains lenticulars of relatively high mass – could explain the inconsistency.

By way of a summary, one can conclude that the S0 belonging to the AC subpopulation differ from their PS counterparts in that the former:

(i) are only slightly less massive on average, although somewhat more luminous, so they have lower $M_{\rm star}/L$ ratios;
(ii) have a younger, bluer stellar population, which is ostensibly poorer in metals;
(iii) have lower global Sérsic indices that follow a more asymmetric, positively skewed distribution of modal value $n \lesssim 2$;
(iv) are almost entirely actively star-forming systems with average SFRs, of about 2 $M_\odot\,{\rm yr}^{-1}$, which are more than one order of magnitude higher.

5.4 Relationship with the environment

One key factor when it comes to understanding galaxy properties is the environment in which these objects reside. We have chosen to characterize it by means of the Galactic-extinction-corrected 3D galaxy number density estimator, μ_5, defined in Section 2.3. In Fig. 10, we show the evolution in the number fraction of AC lenticulars with local density for all our VLSS0 galaxies, with the colour and size of the data points informing, respectively, about the corresponding change in the average equivalent width of the Hα line and in the average SFR of the whole population. This plot reveals that while PS lenticulars are present in all kind of environments, the abundance of AC objects decreases linearly with increasing $\log(\mu_5)$, going from fractions above 40 per cent at the lowest densities probed by our sample to being virtually absent in the densest regions of the local volume. (As in the case of their intrinsic physical properties, we find that the differences in the PDF of the local density for the two main spectral classes of lenticulars are statistically very significant, with a two-sample KS test returning $p \ll 0.05$.) Accordingly, the average values of the EW(Hα) and SFR for the S0 population are also steadily reduced with local projected density (they follow a roughly linear decrement with $\log(\mu_5)$ as

[6]Fraser-McKelvie et al. (2018) use *Wide-Field Survey Explorer* (*WISE*) mid-infrared colours as indicators of recent star formation activity.

[7]To us, it makes more sense to think of S0 mass as the *consequence* of the formation pathway followed and not as the cause.

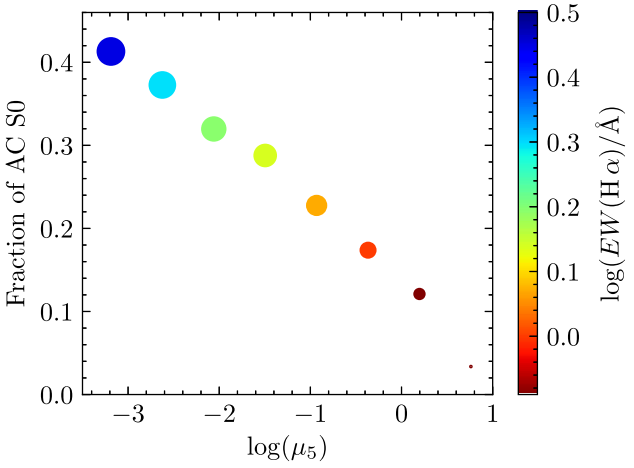

Figure 10. Number fraction of AC lenticulars as a function of the logarithm of the local density for all the galaxies in our VLSS0. The colour of the data points indicates the average value of log(EW(H α)) for the whole sample, whilst their size is proportional to the mean log (SFR). This plot illustrates the dramatic impact the environment has on the activity of S0 galaxies.

well), suggesting that the denser the environment, the more severe is the quenching of the star formation activity in S0 galaxies.

Once again, our results show a good level of consensus with the outcomes of the studies mentioned in the previous section, as well as consistency with expectations for the general galaxy population (Rines et al. 2005). This is the case of Xiao et al. (2016), who claim that active S0 are mainly located in the sparse environment, whilst quiescent lenticulars or with low-level star formation and/or AGN activity reside preferentially in the dense environment. Helmboldt et al. (2008) also arrive at a similar conclusion with their samples of star-forming early-type and K + A galaxies, finding that both types of objects reach higher fractions among all galaxies in lower density environments. Only Fraser-McKelvie et al. (2018) seem to have an apparently discordant view when, from an analysis based on two environmental indicators – one that measures the strength of the local tidal perturbations from neighbours and another that evaluates the large-scale structure in terms of the projected density to the fifth nearest neighbour – find no significant evidences of a connection between the stellar masses, ages, and metallicities of MaNGA's lenticulars and their environment. These same authors, however, warn that their conclusion is based on an incomplete version of the MaNGA data set in which the statistically rare cluster members are missing. Indeed, in contrast with the stellar mass, it can be observed that while our density measurements span over about four orders of magnitude and encompass the most extreme environments, the spatial spectroscopy data used in the former study, apart from being much fewer, sample a significantly narrower range of densities. Thus, it appears that the widely documented systematic differences observed in the (star formation) activity between late-type spirals in rich environments and those in the field (see, e.g. Boselli et al. 2016, and references therein) are not exclusive to this end of the Hubble sequence, but they can actually be extended to all disc galaxies. This suggests that the physical properties of S0 galaxies are not detached from the environment in which they find themselves.

6 SUMMARY AND DISCUSSION

In this work we have applied several Machine Learning techniques to analyse a sample of 68 043 optical spectra of S0 galaxies in the local Universe ($0.01 < z \lesssim 0.1$), by much the largest data set of any kind ever assembled for this galaxy population. Our aim has been to investigate the physical properties of this type of objects in a more objective and informative way using their whole optical spectra, instead of the classical diagnostics based exclusively on photometric measurements or on a few specific spectral lines. Our analysis relies on both the spectra measured in the SDSS Legacy Survey and the morphological information listed in the recently published catalogue of automatically classified galaxies by Domínguez Sánchez et al. (2018). These data have been complemented with a variety of spectrophotometric parameters gathered from further external sources, including several parameters taken from the NSA and other well-known and much used SDSS-based catalogues. The final data base has been completed with our own estimation of the local density corrected for the effects of Galactic interstellar extinction in a volume-limited subset of 32 188 S0 galaxies with $M_r \lesssim -20.5$ mag.

We have used a PCA to extract the most relevant features of the S0 optical spectra. This objective and a priori-free technique has enabled us to reduce the highly multidimensional spectral data – the number of pixels per spectrum is about 3800 for the SDSS-I/II spectra – to a low-dimensional space that is optimal for this purpose. This is because it relies on the most important projections along a few new orthogonal axes, the ES (also known as the principal components), which maximize the variance and, hence, minimize information loss.

The fact that we can explain with only three ES nearly 95 per cent of the variance shown by a training sample of S0 spectra is an indication that all the physics of the local population of S0 galaxies should be essentially contained in a few dimensions, probably not more than two if we stick to their passive representatives, due to the strong correlation shown by the first two principal components of this ensemble (see below). The first two ES, which already explain about 90 per cent of the variance, are characterized by the presence of strong emission lines, notably the H α + [N II] + [NS II] complex, a few lines from highly ionized species such as [O III], and higher order Balmer lines up to H ϵ. The most important differences lie in the continuum, blue for the first ES and red for the second, and in the presence of the Ca II H + K doublet in emission in the latter. Many of these lines are also visible in the third ES, some of them now in absorption, which shows an essentially flat continuum. Preliminary analyses have revealed that this component, which only embodies 6 per cent of the spectral variance, is, however, a key diagnostic element for the identification of nuclear activity in S0 galaxies, an issue that we have left for future research.

The projections of the S0 spectra on the bivariate plane defined by the first two ES, denoted PC1 and PC2, have unveiled the existence of two main regions: a crowded narrow band with a sharply defined left edge that crosses the diagram diagonally, defining a zone in this plane in which the values of the first two predictors show a strong linear correlation, and a substantially less populated and much more scattered cloud of points that runs from the right of this band, where the PC scores are linearly uncorrelated. We have used a combination of a logistic regression and Otsu's method to perform an optimal separation of all galaxies in our data set into two main classes according to their location in the PC1–PC2 subspace. The resulting spectral subsets have been, respectively, called the 'Passive Sequence' and the 'Active Cloud', as they include subpopulations of S0 with spectra representative of passive and active galaxies. In between these two distributions, we have defined a narrow dividing zone that we have named the 'Transition Region', which contains objects with intermediate spectral characteristics. This classification

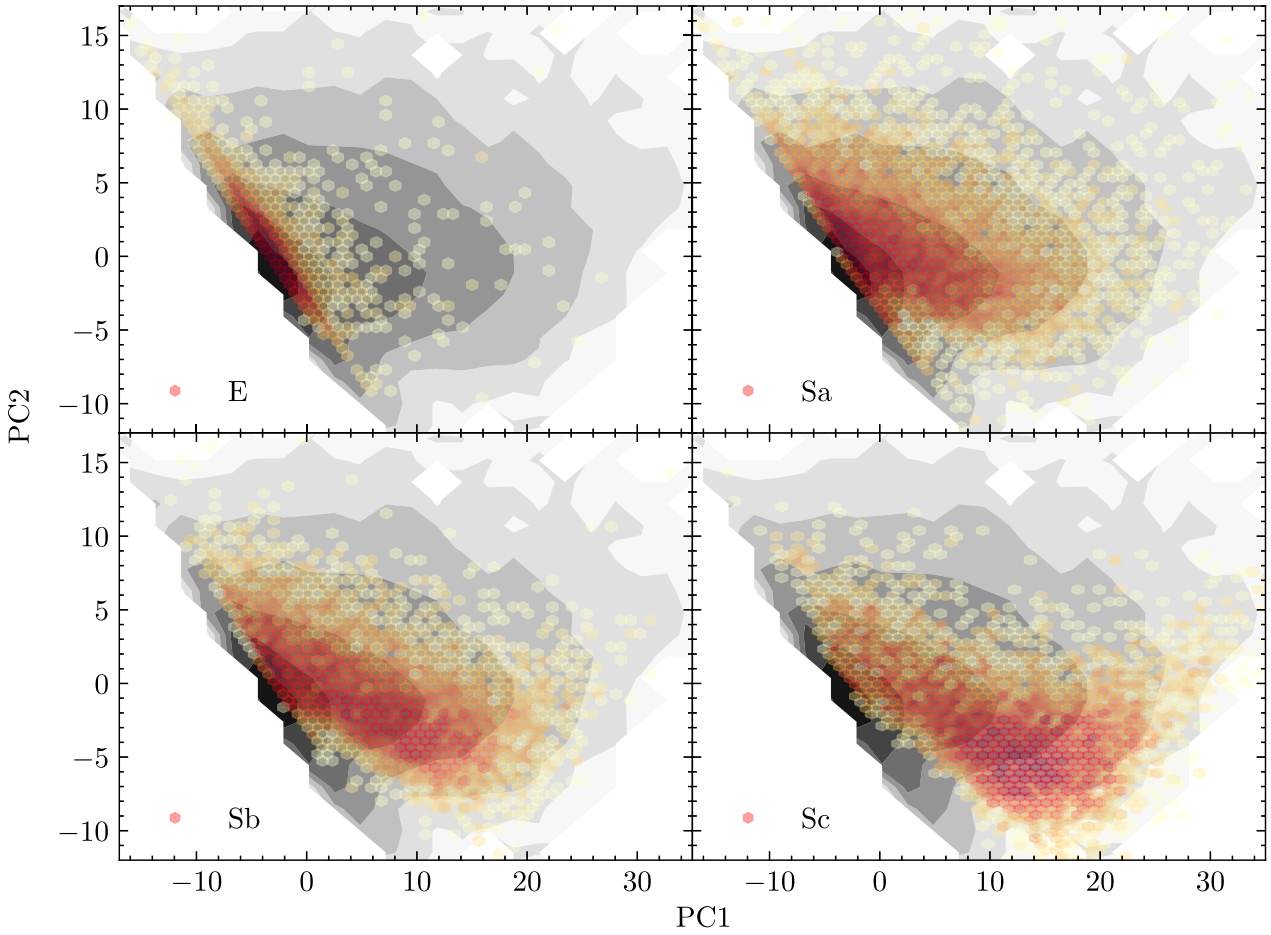

Figure 11. Number density distributions of galaxies of the main Hubble types in the PC1–PC2 plane defined by the S0. The background grey-scale contours represent equally spaced logarithmic densities for the lenticular population. Overlaid on the top are the density distributions of E, Sa, Sb, and Sc galaxies calculated in this same subspace from arbitrary samples of ∼10 000 spectra of each type (the morphologies are from the catalogue by Domínguez Sánchez et al. 2018). The colour intensity of the hexagonal cells is also graduated on a logarithmic scale, with the darker ones identifying the most populated bins. Note how the density distributions of bright galaxies change from being fundamentally in the PS to occupy mostly the bluest portion of the AC (see Fig. 4) as the Hubble type goes from E to Sc. Note also that just as there are hardly any E distributed across the AC region, Sc galaxies are virtually absent from the PS.

of the S0 is markedly reminiscent of the 'Red Sequence/Green Valley/Blue Cloud' features of the well-known colour–magnitude diagram used to classify the entire galaxy population, thus the names adopted. Investigation of the potential biases that the fixed aperture of fibres and the inclination of galaxies (basically related to their internal extinction) could entail has shown that the changes induced by these factors on the S0 spectra, and hence also on their PC scores, have, however, a negligible impact on their classification.

The differences in the spectra of each subpopulation of S0 galaxies are also reflected in their different physical properties. Most of the intrinsic parameters analysed show a clear bimodality that correlates with the spectral division, giving weight to the notion that the two types of lenticulars that we have identified may have followed different evolutionary paths. This is especially evident for those attributes directly related to star formation, such as the SFR, sSFR, EW(H α), and $D4000$. However, it is remarkable that we do not see a stark separation in stellar mass, a property that some past studies (e.g. Fraser-McKelvie et al. 2018) have identified as the main driver of the division in lenticular subpopulations. We attribute this apparent inconsistency to the different mass ranges encompassed by the respective samples, since unlike these other studies, in this work, we have used a volume-limited subset of S0 galaxies that, for this reason, contains objects of relatively high mass. In any event, we have found that, for all the quantities investigated, the comparison between the PDF associated with each subpopulation has always produced statistically significant differences.

As regards the values of the properties assigned to each spectral class, our findings are, in general, in good agreement with the outcomes from most of the previous studies of this kind. Using a volume-limited subset of spectra, we have found that the members of the AC class tend to be slightly less massive than their passive counterparts, more luminous though with less concentrated light profiles, and to have a somewhat younger, bluer stellar component that is poorer in metals. Besides, while PS lenticulars are present in all kind of environments, AC objects inhabit preferentially sparser regions showing abundances that anticorrelate with the local density of galaxies. However, the most striking results are that virtually all AC lenticulars are actively star-forming systems, with average SFR comparable to those seen in late spiral galaxies – in fact, they lie in the upper-mass range of the star-forming main sequence – together with the observation that such systems may constitute, at least, a quarter of the S0 population in the local volume.

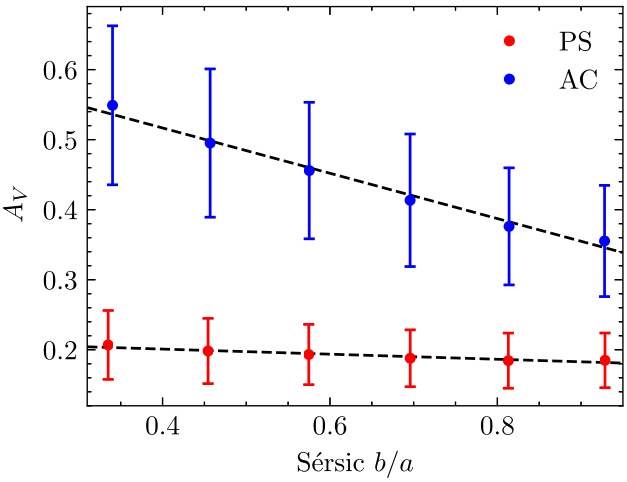

Figure 12. Inclination dependence of the total internal extinction in the photometric *V* band for the two main spectral classes of S0. The data points and bars represent, respectively, the means and 1σ errors of A_V. The axial ratio *b*/*a* derived by the SDSS from 2D, single-component Sérsic fits in the *r* band is used as a proxy for inclination. The adopted range of values for this observational parameter takes into account the results by Masters et al. (2010), who find that the intrinsic *b*/*a* of S0 galaxies is 0.23.

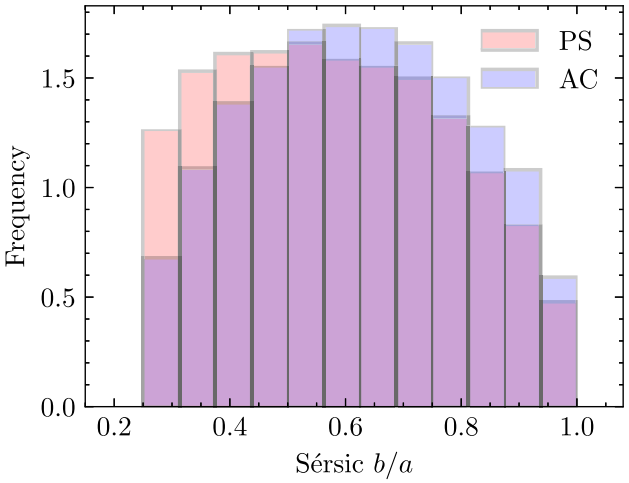

Figure 13. Observed distribution of inclinations for the two main spectral subpopulations of lenticulars in the MLSS0.

Indeed, by reducing the optical spectra of the other Hubble types to the most fundamental features inferred for the S0, one can see that the concordance between the AC lenticulars and late-type disc galaxies is not solely confined to their similar levels of star formation. Thus, as shown in Fig. 11, the projections of the spectra of the E galaxies in the same PC1–PC2 plane defined by the S0, occupy essentially the narrow, lens-shaped region delineated by the PS spectral class, whilst the projections of the spectra of the different spiral classes progressively move towards higher values of PC1 and lower values of PC2, gradually shifting the peak of the corresponding density distributions from the origin of the plane to the lower right-hand corner of the AC's region. Even so, it can be seen that, in addition to all the spectra of E and Sa, virtually all of the spectra of Sb and the vast majority of those of Sc remain in this subspace within the limits delineated by the lenticular population. All this can be taken as evidence that the traditional conception of present-day S0 as basically red and dead galaxies is not correct, and that this morphological group should increasingly be treated as an heterogeneous collection of objects (see also Welch & Sage 2003; Morganti et al. 2006; Crocker et al. 2010; Barway et al. 2013).

Implicit in the fact that one of the major distinguishing attributes of the two main spectral classes of lenticulars is the level at which they are currently forming stars, is the idea that one should expect important differences in their ISM too. A simple way of checking this would be to use the measurements of the H I content from the ALFALFA survey included in our data base. In practice, however, this is not feasible as the fraction of S0 that have 21-cm data available is very small (our data set contains just a few hundred H I observations for S0), mostly due to the substantially lower depth of ALFALFA ($z_{\rm hel} \lesssim 0.06$) and its only partial overlap with the SDSS footprint. Instead, we use another effective way of revealing the presence of diffuse matter in galaxies, such as their internal extinction of starlight, for which we do have abundant data. Fig. 12 demonstrates that our assessment on the ISM of lenticulars is correct. In this plot we compare the inclination dependence of the total internal extinction in the *V* (550 nm) band, A_V, for the two main S0 subpopulations. The differences are striking: while the PS galaxies show a mild, and essentially inclination-free, nebular extinction, the degree of extinction of AC members is significantly higher and grows linearly with inclination. The fact that we obtain such markedly different outcomes for the two types of S0 using a purely photometric parameter reinforces the reliability of our spectral classification.

The study of the ISM of S0 has been completed with the application of the statistical test by Jones, Davies & Trewhella (1996) geared towards the determination of the typical optical depth of a sample. This qualitative test consists of (i) inferring the observed distribution of inclinations, using the ratio of the semiminor to semimajor axes; (ii) comparing it with different expectations from simulated samples of disc galaxies affected by the same selection effects and that contain objects that are either completely optically thin or completely optically thick; and (iii) determining which theoretical distribution best corresponds to the actual data. We show in Fig. 13 the observed distributions of inclinations for the two spectral classes of lenticulars included in the whole MLSS0 data set, which is a magnitude-selected sample. Comparison of these distributions with fig. 1b of these authors reveals that the S0 can be considered, in general, galaxies with a relatively low opacity, although the AC's members appear to be, as expected, optically thicker than their PS counterparts, which behave as essentially transparent discs. The possible effects of internal extinction, as well as of the fixed aperture of the fibres, on the spectra of the S0 have been explored in detail on Appendix A, where we demonstrate that they have a marginal impact on our PCA-based classification of these objects.

At this point, we feel that it is still premature to start too detailed a discussion about the possible formation paths followed by the two subpopulations of lenticulars that we have uncovered. In relation to this issue, one of our most relevant results is the very significant segregation found between the intrinsic attributes of the two spectral classes of S0. The nature of the differences is such that prevents PS lenticulars to be the outcome of the internal secular evolution of AC objects, in the sense that the PDF of some properties, such as $M_{\rm star}$, are at odds with a closed-box transformation of the local AC into the quiescent S0. However, if one takes into account the downsizing paradigm in its appearance of the decline with time of

the typical mass of star-forming galaxies (e.g. Fontanot et al. 2009), then the PS members could well be the descendants of intermediate-z lenticulars with AC characteristics, which could even have also acted as progenitors of the spheroid-dominated post-starburst K + A galaxies that reside preferentially in the field. Implicit in this scenario is an increase of the AC/PS fraction with redshift. On the other hand, the clear anticorrelation found between the local density of the environment and the fractional abundance of actively star-forming S0, which obeys a nearly perfect power law, is another of the elements that could shed some light in our understanding of the physics involved in S0 formation. This relationship can be naturally explained in cluster regions where hydrodynamic interactions are expected to drive the connection of galaxy properties with the radial run of the density in these systems. However, it does not seem very likely that this sort of mechanisms are solely responsible for a correspondence that, as we have shown, extends from the densely populated regions of the local volume all the way down to the most sparse environment. There, we still see that the galaxies bearing the S0 designation are mostly absorption-dominated objects, which are unlikely to form from gas processes but rather through gravitational effects. It is even possible that these latter mechanisms do not even work in the emptiest parts of space, where the density of galaxies is too low for their mutual interactions to be really effective.

Taken as a whole, what all these results do indeed indicate is that the environment of S0 galaxies must play a pivotal role in the modulation of their star formation activity and, possibly, also of many other of their physical properties. But with the information we have gathered to date, we cannot answer yet the fundamental question of what are the specific environmental mechanisms involved and how have them played out in detail, without going too far into the territory of speculation. However, our study of the S0 populations is still in its infancy. Indeed, we will continue working in this area in the hope that our research may reveal new evidence in a not too distant future that allows us to draw well-founded and more specific conclusions about the possible formation scenarios of these fascinating objects.

ACKNOWLEDGEMENTS

The authors thank the reviewer for his/her detailed, insightful, and encouraging comments, which have enabled us to refine the focus of this paper. We acknowledge financial support from the Spanish Agencia Estatal de Investigación and European FEDER funds through the research project AYA2016-76682-C3. JLT was also partially supported by a collaboration scholarship from the Royal Academy of Sciences and Arts of Barcelona and the University of Barcelona. Additional funding for this work has been provided by the State Agency for Research of the Spanish Ministerio de Ciencia, Innovación y Universidades through the Centre of Excellence Severo Ochoa's award for the Instituto de Astrofísica de Andalucía under contract SEV-2017-0709. This research has made use of data from the following data bases: NASA-Sloan Atlas at http://nsatlas.org/, Morphological catalogue for SDSS galaxies by Domínguez Sánchez et al. (2018), GALEX-SDSS-WISE at http://pages.iu.edu/~salims/gswlc/, and both Portsmouth Stellar Kinematics and Emission Line Fluxes and eBOSS Firefly at https://www.sdss.org/dr15/data_access/value-added-catalogs/. We are grateful to all the people involved in the gathering, reduction, and processing of the data contained in all these catalogues, as well as the public and private institutions that have provided the necessary funding, resources and technical support to make possible both all these surveys and the release of their findings to the community.

REFERENCES

Alam S. et al., 2015, ApJS, 219, 12
Allen J. T. et al., 2015, MNRAS, 446, 1567
Baldwin J. A., Phillips M. M., Terlevich R., 1981, PASP, 93, 5
Barnes J. E., 1999, in Barnes J. E., Sanders D. B., eds, Proc. IAU Symp. 186, Galaxy Interactions at Low and High Redshift, Kluwer, Dordrecht, p. 137
Barway S., Kembhavi A., Wadadekar Y., Ravikumar C. D., Mayya Y. D., 2007, ApJ, 661, L37
Barway S., Wadadekar Y., Vaghmare K., Kembhavi A. K., 2013, MNRAS, 432, 430
Bedregal A. G., Aragón-Salamanca A., Merrifield M. R., 2006, MNRAS, 373, 1125
Blanton M. R., Moustakas J., 2009, ARA&A, 47, 159
Blanton M. R., Kazin E., Muna D., Weaver B. A., Price-Whelan A., 2011, AJ, 142, 31
Blanton M. R. et al., 2017, AJ, 154, 28
Boselli A. et al., 2011, A&A, 528, A107
Boselli A. et al., 2016, A&A, 596, A11
Bundy K. et al., 2015, ApJ, 798, 7
Burstein D., Ho L. C., Huchra J. P., Macri L. M., 2005, ApJ, 621, 246
Butcher H., Oemler A., Jr, 1978, ApJ, 219, 18
Cappellari M. et al., 2011, MNRAS, 416, 1680
Casertano S., Hut P., 1985, ApJ, 298, 80
Colless M. et al., 2001, MNRAS, 328, 1039
Comparat J. et al., 2017, preprint (arXiv:1711.06575)
Connolly A. J., Szalay A. S., 1999, AJ, 117, 2052
Couch W. J., Ellis R. S., Sharples R. M., Smail I., 1994, ApJ, 430, 121
Couch W. J., Barger A. J., Smail I., Ellis R. S., Sharples R. M., 1998, ApJ, 497, 188
Crocker A. F., Bureau M., Young L. M., Combes F., 2010, MNRAS, 410, 1197
Davis T. A., Greene J., Ma C.-P., Pand ya V., Blakeslee J. P., McConnell N., Thomas J., 2016, MNRAS, 455, 214
de Vaucouleurs G., 1977, Evolution of Galaxies and Stellar Populations. Yale Univ. Obser., New Haven, CT
den Heijer M. et al., 2015, A&A, 581, A98
Dobos L., Csabai I., Yip C.-W., Budavári T., Wild V., Szalay A. S., 2012, MNRAS, 420, 1217
Domínguez Sánchez H., Huertas-Company M., Bernardi M., Tuccillo D., Fischer J. L., 2018, MNRAS, 476, 3661
Dressler A., 1980, ApJ, 236, 351
Dressler A. et al., 1997, ApJ, 490, 577
Eliche-Moral M. C., Rodríguez-Pérez C., Borlaff A., Querejeta M., Tapia T., 2018, A&A, 617, A113
Fasano G., Poggianti B. M., Couch W. J., Bettoni D., Kjærgaard P., Moles M., 2000, ApJ, 542, 673
Fischer J. L., Domínguez Sánchez H., Bernardi M., 2019, MNRAS, 483, 2057
Fitzpatrick E. L., 1999, PASP, 111, 63
Fontanot F., De Lucia G., Monaco P., Somerville R. S., Santini P., 2009, MNRAS, 397, 1776
Fraser-McKelvie A., Aragón-Salamanca A., Merrifield M., Tabor M., Bernardi M., Drory N., Parikh T., Argudo-Fernández M., 2018, MNRAS, 481, 5580
Gavazzi G., Scodeggio M., 1996, A&A, 312, L29
Giovanelli R., Haynes M. P., Chincarini G. L., 1986, ApJ, 300, 77
Giovanelli R. et al., 2005, AJ, 130, 2598
Goto T., Yamauchi C., Fujita Y., Okamura S., Sekiguchi M., Smail I., Bernardi M., Gomez P. L., 2003, MNRAS, 346, 601
Graham A. W., 2014, in Seigar M. S., Treuthardt P., eds, ASP Conf. Ser. Vol. 480, Scaling Laws in Disk Galaxies. Astron. Soc. Pac., San Francisco, p. 185
Gunn J. E., Gott J., Richard I., 1972, ApJ, 176, 1
Haynes M. P. et al., 2018, ApJ, 861, 49
Helmboldt J. F., Walterbos R. A. M., Goto T., 2008, MNRAS, 387, 1537
Hinz J. L., Rieke G. H., Caldwell N., 2003, AJ, 126, 2622

Houghton R. C. W., 2015, MNRAS, 451, 3427
Hubble E. P., 1936, Realm of the Nebulae. Yale Univ. Press, New Haven
Huchra J. P., Geller M. J., Corwin, Harold G. J., 1995, ApJS, 99, 391
Jones H., Davies J. I., Trewhella M., 1996, MNRAS, 283, 316
Jones D. H. et al., 2004, MNRAS, 355, 747
Kennicutt R. C., Evans N. J., 2012, ARA&A, 50, 531
Masters K. L. et al., 2010, MNRAS, 404, 792
Mishra P. K., Barway S., Wadadekar Y., 2017, MNRAS, 472, L89
Moore B., Katz N., Lake G., Dressler A., Oemler A., 1996, Nature, 379, 613
Morganti R. et al., 2006, MNRAS, 371, 157
Nair P. B., Abraham R. G., 2010, ApJS, 186, 427
Otsu N., 1979, IEEE Trans. Syst. Man Cybern., 9, 62
Poggianti B. M., Smail I., Dressler A., Couch W. J., Barger A. J., Butcher H., Ellis R. S., Oemler A. J., 1999, ApJ, 518, 576
Postman M., Geller M. J., 1984, ApJ, 281, 95
Querejeta M. et al., 2015, A&A, 579, L2
Rines K., Geller M. J., Kurtz M. J., Diaferio A., 2005, AJ, 130, 1482
Ronen S., Aragon-Salamanca A., Lahav O., 1999, MNRAS, 303, 284
Salim S. et al., 2016, ApJS, 227, 2
Salim S., Boquien M., Lee J. C., 2018, ApJ, 859, 11
Sandage A., 2005, ARA&A, 43, 581
Solanes J. M., Salvador-Solé E., Sanromà M., 1989, AJ, 98, 798
Solanes J. M., Giovanelli R., Haynes M. P., 1996, ApJ, 461, 609
Spitzer L., Jr., Baade W., 1951, ApJ, 113, 413
Strauss M. A. et al., 2002, AJ, 124, 1810
Suzuki T. L. et al., 2016, MNRAS, 462, 181
Tapia T., Eliche-Moral M. C., Aceves H., Rodríguez-Pérez C., Borlaff A., Querejeta M., 2017, A&A, 604, A105
Tempel E., Tuvikene T., Kipper R., Libeskind N. I., 2017, A&A, 602, A100
Thomas D. et al., 2013, MNRAS, 431, 1383
Treu T., Ellis R. S., Kneib J.-P., Dressler A., Smail I., Czoske O., Oemler A., Natarajan P., 2003, ApJ, 591, 53
Trouille L., Barger A. J., 2010, ApJ, 722, 212
van den Bergh S., 2009, ApJ, 702, 1502
Welch G. A., Sage L. J., 2003, ApJ, 584, 260
Willett K. W. et al., 2013, MNRAS, 435, 2835
Williams M. J., Bureau M., Cappellari M., 2010, MNRAS, 409, 1330
Xiao M.-Y., Gu Q.-S., Chen Y.-M., Zhou L., 2016, ApJ, 831, 63
Yip C. W. et al., 2004, AJ, 128, 585
York D. G. et al., 2000, AJ, 120, 1579

APPENDIX A: TESTING THE DEPENDENCE OF THE RESULTS ON THE OBSERVATIONAL SET-UP

In this appendix, we investigate whether there are factors alien to the population of lenticulars that could be biasing their spectral properties and, hence, their classification and other outcomes of this work.

A1 Effects of aperture: central-to-total light contribution

Our analysis of nearby, bulge-enhanced S0 galaxies is based on SDSS optical galaxy spectra taken using single fibres. The relatively small diameter of these fibres (3 arcsec) and moderate depth of the selected data set imply that the flux distributions they collect do not come from the galaxies as a whole, but from their central regions. For the nearest lenticulars, this could cause the light entering the spectrograph to essentially come from their bulge component. Were it to be the case, and assuming bulges are generally a passive element no co-evolving with discs (but see Fraser-McKelvie et al. 2018), one might expect to see a correlation between the apparent size of the galaxies and their spectra. Therefore, it is not unreasonable to assume that our spectral classification into passive and active lenticulars could be affected by artefacts associated with the fixed fibre aperture, since the sampled physical scales vary significantly (from ∼0.405 to 1.85 kpc arcsec^{-1} for redshifts between 0.02 and 0.1, respectively).

To estimate the potential bias this may induce in the spectral classification, we have devised a strategy consisting first in quantifying the effects of the fixed fibre aperture on the spectra, or, equivalently, on the projections of such spectra on to the principal components. This has been done by calculating the dependence of PC1, PC2, and PC3, for the entire S0 population, on $\log(R_{50}/R_{\rm f})$, the logarithm of the ratio between the Petrosian-based estimate of the projected half-light radius in the *r*-band provided by the NSA photometry and the radius of the SDSS fibres. The inferred variations turn out to be very well approximated by linear laws. These simple relationships facilitate the derivation of a straightforward statistical correction to the data in the subspace of the main principal components to compensate for the aperture effects[8] (see below), while revealing that such compensation entails shifts of different magnitude in the PC values along a common direction.

As shown in the bottom panel of Fig. A1, the direction of those shifts is nearly parallel to the PS sequence. This plot depicts the median values of the first three PC scores per bin of aperture size after applying a clockwise rotation of ∼40° around the PC3 axis. This is the angle subtended by the observed PS ridge of the MLSS0 with the original PC2 axis (see the right-hand panel of Fig. 6), which has been inferred from an orthogonal regression fit to the data. In this new basis, the PS viewed along the direction of the PC3 axis adopts an upright position with the AC extending horizontally, so the names assigned to the new axes were $\mathrm{PC1}'_{\perp}$, $\mathrm{PC2}'_{\parallel}$, and PC3, respectively.[9] In the rotated frame of reference, the statistical correction of the aperture effects can be expressed in a vector form as

$$(\mathrm{PC1}'_{\perp}, \mathrm{PC2}'_{\parallel}, \mathrm{PC3})^{\rm cor} = (\mathrm{PC1}'_{\perp}, \mathrm{PC2}'_{\parallel}, \mathrm{PC3})^{\rm obs} + [\log(R_{50}/R_{\rm f})^{*} - \log(R_{50}/R_{\rm f})] \cdot (m_1, m_2, m_3)\ , \tag{A1}$$

where $\log(R_{50}/R_{\rm f})^{*}$ represents any arbitrary reference value that one wishes to adopt for this quantity – it could be, for instance, the value of the most populated bin – and $m_1 = 0.40$, $m_2 = 3.7$, and $m_3 = -0.30$ are the slopes of the fitted straight lines. As shown by the figure, the correction of the aperture effects would move the PC scores in a direction essentially parallel to the vertical axis that now is also the PS direction: it forms an angle of less than 6°! More specifically, we have calculated that the application of this correction would imply the reclassification of a tiny fraction (always less than 1 per cent) of the S0 galaxies between adjacent spectral classes, whereas there would not be a single case of change of status between PS and AC. Therefore, despite the evident effects of the fixed aperture of the fibres on the S0's

[8]Since any spectrum can be represented by an arbitrarily large linear combination of the ES weighted by the corresponding PC, this statistical correction could also be directly applied to the original spectra.
[9]We have permitted ourselves to abuse the language since arbitrary rotations do not preserve the PC condition, hence the prime superscript.

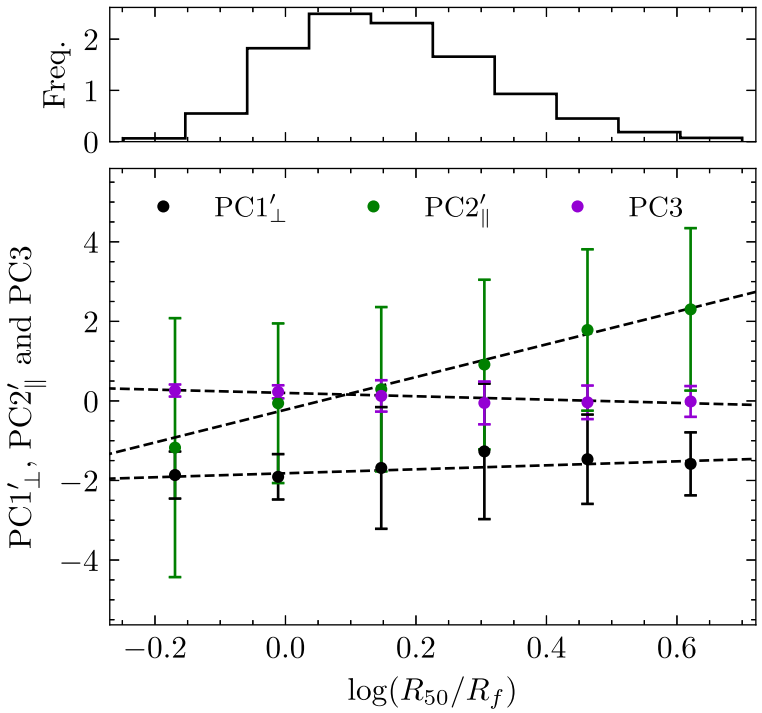

Figure A1. Top panel: frequency distribution of the observed apparent sizes of S0 galaxies with respect to the radius of the SDSS fibres. Bottom panel: median values and interquartile ranges of the three main PC scores for the MLSS0 in bins of $\log(R_{50}/R_f)$ rotated about the PC3 axis so that the PS for the MLSS0 becomes parallel to the *y*-axis (see the text for details). The dashed straight lines correspond to the linear laws fitted to the data points in the new base (black circles for the new abscissae, $PC1'_\perp$, green for the new ordinates, $PC2'_\parallel$, and purple for the unaffected PC3 values). They can be used to correct, from a statistical point of view, the S0's spectra for aperture effects. The nearly horizontal line associated with $PC1'_\perp$ demonstrates that this correction would move the PC scores along a direction essentially parallel to the PS.

spectra, it is clear that their impact on the PS/TR/AC classification is practically insignificant, so there is no need to take corrective actions in this regard.

The histogram in the upper panel of Fig. A1 provides another useful result related to this issue. According to the distribution of *B*/*D* flux ratios shown by S0 (see, e.g. the review by Graham 2014), the bulge-to-total light ratios for this population should range from ∼0.1 to ∼0.3, with the peak at 0.2. An eyeball estimation of the radius encompassing these light fractions that accounts for the typical differences in the bulge and disc light profiles indicates that one should expect the fibres to capture light essentially coming from the bulge component, even in highly inclined S0, for those galaxies on which $\log(R_{50}/R_f) \gtrsim 0.4$–$0.5$ (this is something that we have empirically confirmed). As illustrated by the histogram, there are very few objects verifying this condition. To give some figures by way of example, only a 3 percent of S0 have $\log(R_{50}/R_f) > 0.5$. This implies that nearly all the single-fibre spectra evaluated should contain some light coming from the disc component.

A2 Effects of inclination: internal dust reddening

The apparent inclination of the galaxies is another factor that might lead to their spectral misclassification. For a given galaxy at a fixed distance, it determines the relative contributions to the spectrum of the different structural components of the galaxy, which, in turn, are modulated by the degree of its internal extinction. In fact, the detection in this work of a substantial fraction of S0 with obvious signs of ongoing star formation, as well as the well-known fact that even lenticulars that have used up or lost most of their interstellar matter may retain significant dust in their discs, suggest that one may expect internal absorption in these objects to be not totally negligible, especially for highly inclined star-forming AC S0 (recall that we have already argued, based on Figs 12 and 13, that this subpopulation should be moderately opaque).

This possibility is confirmed by Fig. A2, where we show the results of applying the same procedure described in Appendix A1, which transforms the first three PC into a new base in which the PS becomes parallel to the *y*-axis, to the PS, TR, and AC spectral classes separately. This plot reveals that the values of the two main PC of the AC galaxies and of the second one of TR objects are the most sensitive to changes on inclination. It may also be observed that the strength of the bias tends to decrease with the order of the PC. At the other extreme, the impact of *b*/*a* on the spectra of PS members is negligible, which is consistent with our appraisal that the galaxies of this latter class should contain very small amounts of gas and dust.

As in the case of the aperture effects, the inclination dependencies of the transformed PC scores shown in the three panels of Fig. A2 are very well approximated by linear laws that can be used to derive a statistical correction to the S0 spectra, which compensates for this bias. But again, we find that the correction of the inclination would move the original PC values in directions away from the uncorrected PS ridge that form small angles with it: <2°, ∼2°, and ∼15°, respectively, for the PS, TR, and AC galaxies. This means that the only correction that

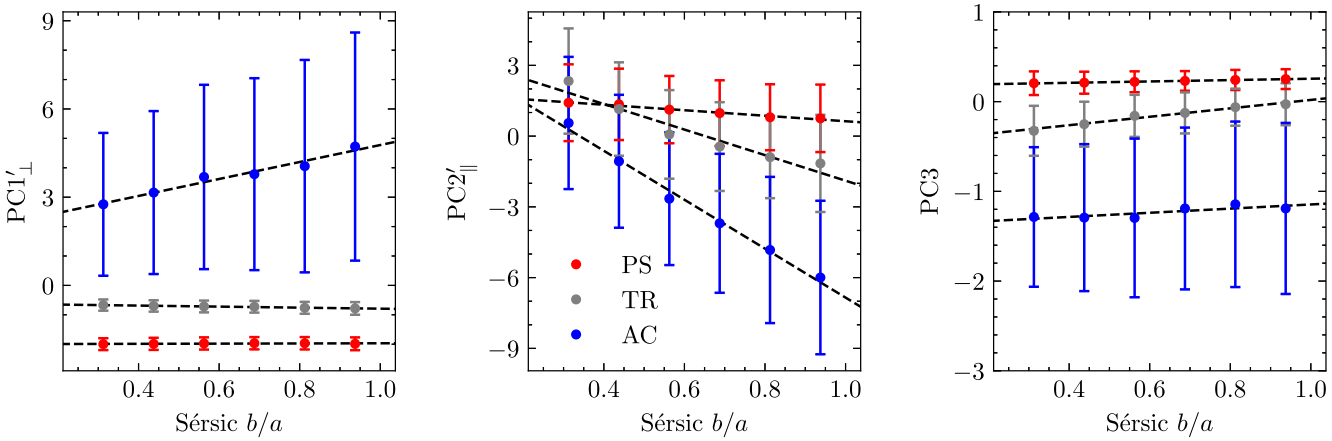

Figure A2. Median values and interquartile ranges of the three main PC scores for the PS (red circles), TR (grey circles), and AC (blue circles) galaxies of the MLSS0 in bins of the observed axial ratio *b*/*a*, with the latter inferred from 2D single-component Sérsic fits in the *r* band. We show, using separate panels, the values of the main three scores in the same rotated frame of reference used in Fig. A1. The dashed straight lines correspond to the linear laws fitted to the data points. They can be used to correct, from a statistical point of view, the S0's spectra for inclination effects. The plot illustrates an increasing sensibility of the spectral classes to inclination: being essentially null for the PS, mild for the TR, and somewhat more significant for the AC. As in other figures in which the ratio *b*/*a* is also used, the intrinsic axial ratio of S0 galaxies has been taken into account when introducing a lower limit on the observed inclination values.

could reasonably be expected to have some effect on the spectral classification of S0 galaxies would be that corresponding to the latter class. By taking the values of the face-on (i.e. $b/a = 1$) scores as the baseline, this correction in the rotated frame of reference is

$$(\mathrm{PC1}'_{\perp}, \mathrm{PC2}'_{\parallel}, \mathrm{PC3})^{\mathrm{cor}}_{\mathrm{AC}} = (\mathrm{PC1}'_{\perp}, \mathrm{PC2}'_{\parallel}, \mathrm{PC3})^{\mathrm{obs}}_{\mathrm{AC}} + (1 - b/a) \cdot (m_1, m_2, m_3) \,, \tag{A2}$$

where $m_1 = 2.9$, $m_2 = -10.4$, and $m_3 = 0.20$ are the slopes of the fitted straight lines to the AC data.[10] But much as with the aperture effects, the inclination biases translate in practice into misclassification frequencies between adjacent spectral classes that are very small (of a few per cent at most) and, most importantly, into a null probability that PS galaxies will become AC and vice versa. It can therefore be concluded that inclination effects, and their correction, do not have a significant impact on the main conclusions of this work. Note also that corrections of the sort outlined by equations (A1) and (A2) could be iterated if necessary until convergence.

Finally, it must be taken into account that the corrections reported above are specific to our sample. They must be recalculated for data sets of S0 spectra gathered with different selection rules, especially if they involve the use of other aperture sizes. In any case, the results of the present investigation suggest that, unless the differences in the observational constraints are dramatic, aperture and inclination effects present in single-fibre optical spectroscopic surveys of the local population of S0 galaxies appear to have a much more limited impact on their spectral classification than might be expected. Even so, the most efficient way to overcome these limitations is through IFS surveys, such as for instance the aforementioned MaNGA or the Sydney-AAO Multi-object Integral field spectrograph (SAMI) Galaxy Survey (Allen et al. 2015), both currently under way. Censuses like these provide full 2D spectral coverage of the galaxies and, once completed, will result in samples representative of the nearby Universe, which can easily be corrected to become volume-limited data sets.

[10]We are ignoring here the fact that *b*/*a* is not fully equivalent to cos *i* at high inclinations *i* due to the finite thickness of the lenticular galaxies.

APPENDIX B: EXAMPLES OF SPECTRA AND IMAGES OF MEMBERS OF THE TWO SPECTRAL CLASSES OF S0

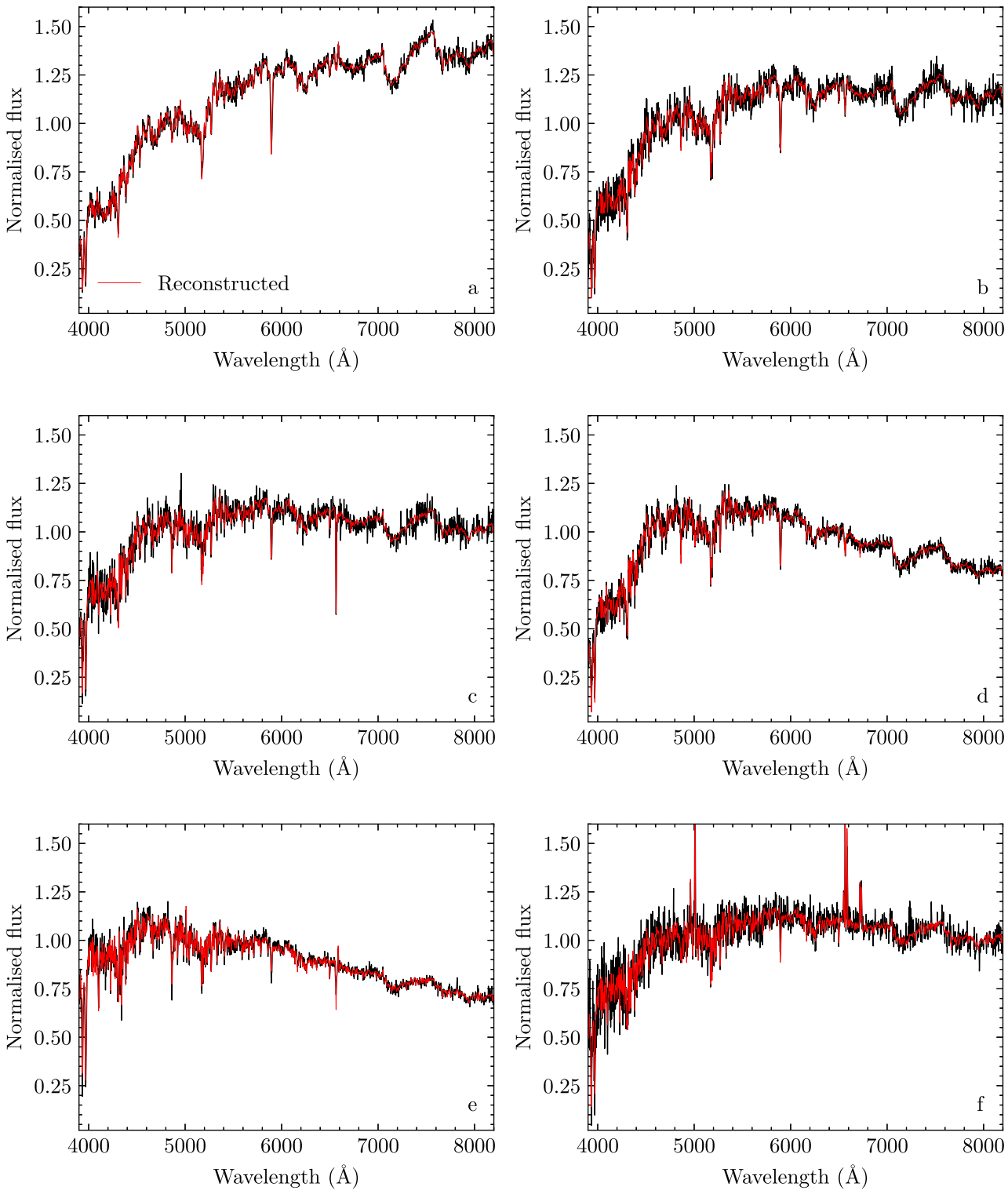

Figure B1. Random examples of individual S0 spectra at different positions of the PC1–PC2 subspace, marked in the last panel of this figure. Black curves are actual rest-frame shifted, re-binned, and normalized spectra of our main sample with gaps filled as explained in Section 3. The red curves on top show the reconstructed spectra obtained by combining the mean of the S0 spectra with the first 10 eigenspectra, which explain 97 per cent of the variance of the training sample (see Fig. 1). Panels (a)–(e) are for galaxies included in the class dubbed Passive Sequence (PS), whereas panels (f)–(k) are for members of the Active Cloud (AC). The colour images of the galaxies producing these spectra are shown in Fig. B2.

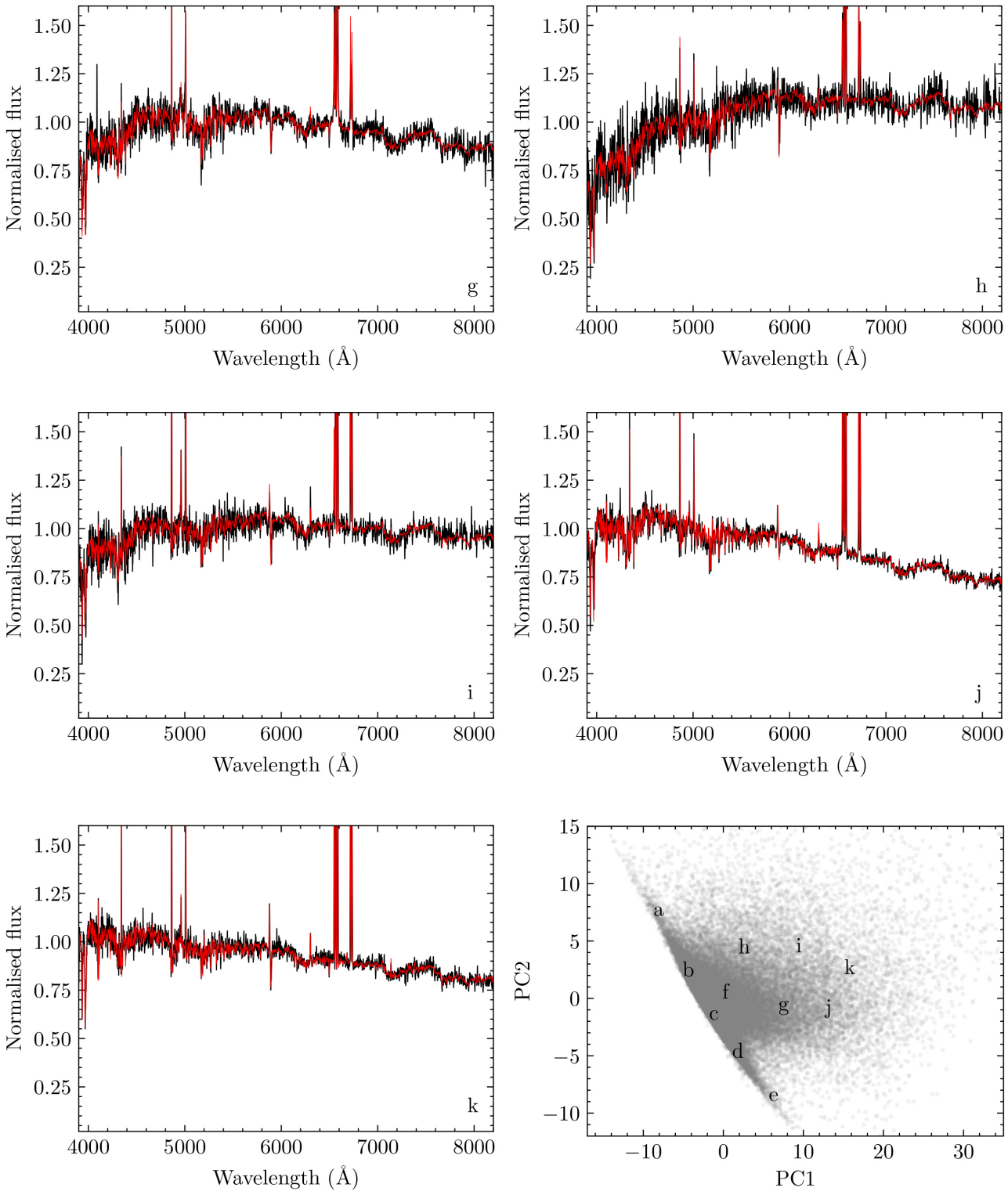

Figure B1 – *Continued.*

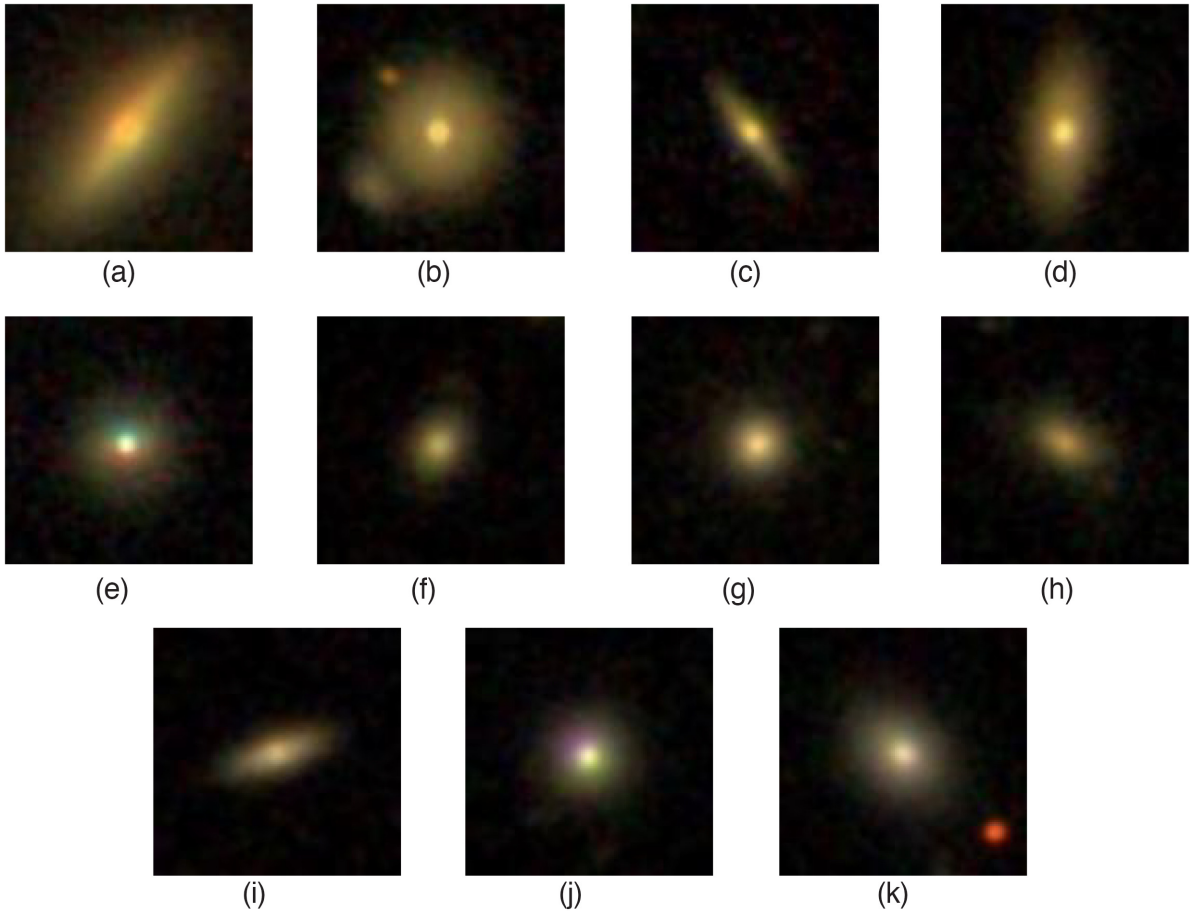

Figure B2. SDSS colour images of the S0 galaxies producing the spectra shown in Fig. B1.

APPENDIX C: PDF OF SOME PROPERTIES OF THE TWO SPECTRAL CLASSES OF S0

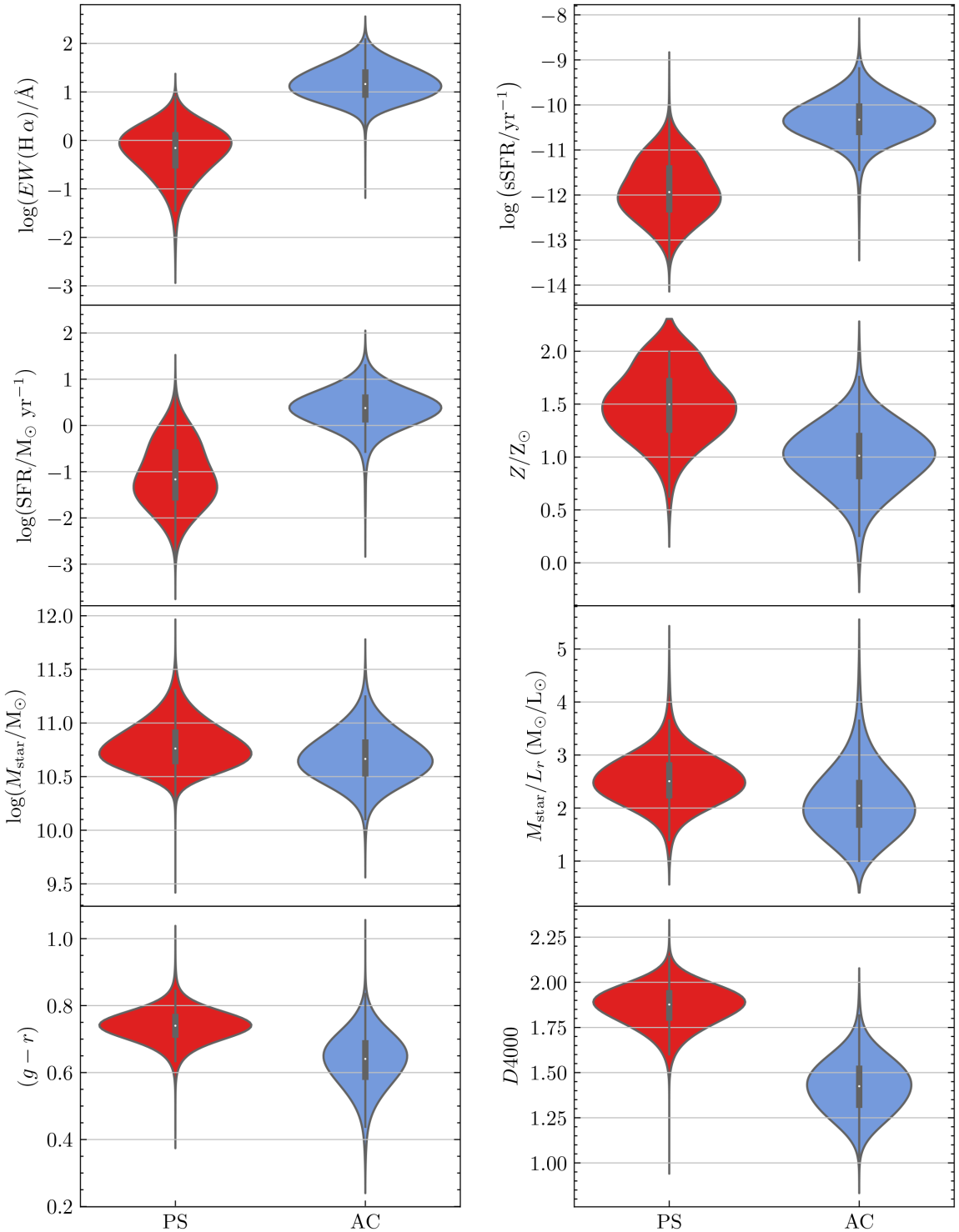

Figure C1. Violin plots showing for the members of the PS (red) and the AC (blue) in the VLSS0 their PDF for the eight spectrophotometric properties that are found to correlate most strongly with the first three PC. From the left to right and top to bottom: Hα equivalent width, specific star formation rate per unit stellar mass and per galaxy, metallicity and mass of the stellar population, stellar mass-to-r-band-light ratio, $(g - r)$ colour, and $D4000$ break. The central dots and boxes indicate, respectively, the medians and interquartile ranges of the distributions. In all cases, the two-sample KS test returns p-values $\ll 0.05$, indicating a very low likelihood that the two main S0 spectral classes come from the same parent population.

This paper has been typeset from a TEX/LATEX file prepared by the author.

3

ACTIVITY

In Jiménez-Palau et al. (2022b) we explore the relation between our classification scheme and well established classifiers from the literature commonly used in the identification of ionization sources, such as the BPT and WHAN (Cid Fernandes et al. 2010) diagrams. Furthermore, we extend the comparison to other conventional activity diagnostics defined in the radio, mid-infrared, and X-ray domains.

We demonstrate that our definition of the PCA spectral classes can be reduced to a single parameter, which is the distance of galaxies to the ridge line of the PS in the plane PC1–PC2,

$$\mathrm{PC2} = -1.162 \cdot \mathrm{PC1} - 2.932, \tag{1}$$

given by:

$$\Delta\mathrm{PS} = \log\left[2.913 + 0.758 \cdot \mathrm{PC1} + 0.652 \cdot \mathrm{PC2}\right]. \tag{2}$$

With the latter expression, the PCA taxonomy can be reduced to a one-dimensional classifier of activity that, in addition, strongly correlates with the EW of the Hα emission line. Comparison with the WHAN diagram, reveals that its horizontal dividers at 3 and 6 Å in EW(Hα) coincide with our constant values of ΔPS that mark the separation between the PS/TR/AC spectral classes, 0.23 and 0.44, respectively. Apart from providing our "mathematical" classification with physical meaning, this agreement is the seed of a unified framework that we are currently developing to characterize self-consistently activity in S0 galaxies, using exclusively the first three principal components (see Section 6.2).

Regarding the sources of ionization, we show that the AC class comprehends a mixture of SF galaxies, which are the majority, and, to a lesser extent, mostly weak AGN. In contrast, the hosts of low-ionization nuclear emission-line regions (LINERs) and retired galaxies prefer, respectively, the locations of the TR and PS in the plane PC1–PC2. We also find evidence that most of the nebular emission of Seyfert and LINER lenticular galaxies detected in radio and X-ray is not driven by star formation, and that the dominant ionizing radiation for many LINERs could come from post-asymptotic giant branch stars.

Monthly Notices of the ROYAL ASTRONOMICAL SOCIETY

MNRAS **515,** 3956–3974 (2022)
Advance Access publication 2022 June 20

https://doi.org/10.1093/mnras/stac1678

The local universe in the era of large surveys - II. multi-wavelength characterization of activity in nearby S0 galaxies

C. Jiménez-Palau [1★], J. M. Solanes,[1,2] J. D. Perea,[3] A. del Olmo[3] and J. L. Tous [1,2]

[1]*Institut de Ciències del Cosmos (ICCUB), Universitat de Barcelona, C. Martí i Franquès 1, E-08028 Barcelona, Spain*
[2]*Departament de Física Quàntica i Astrofísica, Universitat de Barcelona, C. Martí i Franquès 1, E-08028 Barcelona, Spain*
[3]*Departamento de Astronomía Extragaláctica, Instituto de Astrofísica de Andalucía, IAA-CSIC, Glorieta de la Astronomía s/n, E-18008 Granada, Spain*

Accepted 2022 June 14. Received 2022 June 14; in original form 2022 March 6

ABSTRACT

This is the second paper in a series using data from tens of thousands S0 galaxies of the local Universe ($z \lesssim 0.1$) retrieved from the NASA-Sloan Atlas. It builds on the outcomes of the previous work, which introduced a new classification scheme for these objects based on the principal component analysis (PCA) of their optical spectrum and its projections on to the first two eigenvectors or principal components (the PC1–PC2 diagram). We provide a comprehensive characterization of the activity of present-day S0s throughout both the broad-band PC1–PC2 spectral classifier and the conventional narrow-line BPT/WHAN ones, contrasting the different types of activity classes they define, and present an alternative diagram that exploits the concordance between WHAN and PCA demarcations. The analysis is extended to the mid-infrared, radio and X-ray wavelengths by crossmatching our core sample with data from the *WISE*, FIRST, *XMM–Newton*, and *Chandra* surveys. This has allowed us to carry out a thorough comparison of the most important activity diagnostics in the literature over different wavebands, discuss their similarities and differences, and explore the connections between them and with parameters related to star formation and black hole accretion. In particular, we find evidence that the bulk of nebular emission from radio and X-ray detected S0–Seyfert and LINER systems is not driven by star birth, while the dominant ionising radiation for a number of LINERs might come from post-AGB stars. These and other outcomes from the present work should be transferable to other morphologies.

Key words: galaxies: active – galaxies: elliptical and lenticular, cD – galaxies: star formation – infrared: galaxies – radio continuum: galaxies – X-rays: galaxies.

1 INTRODUCTION

Hubble (1936) presented in his book *The Realm of Nebulae* a morphological classification scheme for galaxies based on their visual appearance. It included a hypothetical S0 type of objects showing traits halfway between those of the major lines of early-type galaxies (ETG), whose main representatives were the football-shaped ellipticals (E), and of late-type galaxies (LTG), containing different classes of spirals (S) that resembled flat, swirling discs. Shortly after, this S0 class was identified with the lens-shaped, armless disc galaxies frequently found in large aggregates of these objects. This identification was drawn on the fact that lenticular galaxies (henceforth, the terms lenticular and S0 will be used interchangeably) possess the general disc/bulge morphology of S galaxies, combined with a baryonic content dominated mainly by old stars and in which the warm and cold nebular components are usually scarce, as is the case in E galaxies.

The S0 is also the only morphological type that is relatively abundant in both low- and high-density environments, as shown by the morphology-density relation, first inferred by Dressler (1980) for cluster regions and subsequently revised and extended to sparser environments by numerous authors (see e.g. Postman & Geller 1984, Giovanelli, Haynes & Chincarini 1986, Goto et al. 2003, Cappellari et al. 2011, and Houghton 2015, among others). Their dominance among the galaxies that populate the dense central regions of rich clusters led some to suggest that they were, in fact, the descendants of late-type progenitors whose gaseous interstellar medium (ISM) had been removed by direct collisions with other cluster members quenching their star formation (Spitzer & Baade 1951). This mechanism was later superseded by the more plausible ram pressure produced by the hot intracluster medium (ICM) on the ISM of spiral galaxies as they move through it (Gunn & Gott 1972), probably accompanied by structural changes induced in the discs by the frequent, short-lived gravitational interactions they experience with the global cluster potential, with other companions, or with both, known as galaxy harassment (Moore et al. 1996).

Among the most important pieces of evidence supporting this scenario of S0s formation there is the already mentioned morphology-density relation, which convincingly demonstrates that in rich clusters the number fraction of S0s rises with local projected galaxy density at roughly the same pace that the fraction of S decreases. Furthermore, the nurturing effects of high-density environments on disc galaxies are also manifested over the time dimension in the form of a factor $\gtrsim 3$ increase in the fraction of lenticular objects in clusters between $z \simeq 0.4$ and 0, accompanied by a commensurate decrease in the LTG fraction and an almost nil evolution of the abundance of ellipticals (e.g. Couch et al. 1994; Dressler et al. 1997; Couch et al. 1998; Poggianti et al. 1999; Fasano et al. 2000; Treu et al. 2003).

★ E-mail: cjimenezp@icc.ub.edu

Despite the body of evidence that substantiates the relevant role of clusters in the formation of S0, these galaxies are also found, albeit less frequently, in loose small groups and even in the general field – with relative population fractions of ∼20–30 per cent – where the much thinner intergalactic medium and low peculiar velocities hinder the efficient functioning of hydrodynamic mechanisms. The presence of S0s in these sparser environments must then be explained by invoking close gravitational interactions between galaxies, in which at least the largest one is a LTG, that lead to their merger (e.g. Querejeta et al. 2015). The reason is that this formation mechanism reaches its peak efficiency when the relative speeds involved in the collision are comparable to the internal stellar motions of the colliding objects. This makes S0 special among the other Hubble types, as it suggests that galaxies from a single morphological class may have followed two radically different formation pathways.

The uniqueness of S0 galaxies has motivated the publication in recent years of a series of works, both numerical and observational, specifically dedicated to investigating these objects that have further reinforced this trait. Most of the experimental studies have focused on demonstrating, through controlled simulations with a wide variety of initial conditions, the feasibility of mergers (both major and minor) as a mechanism for the formation of galaxy remnants with structural and dynamic characteristics in accordance with those observed in the local population of S0, even in gas-poor implementations (e.g. Borlaff et al. 2014; Mapelli, Rampazzo & Marino 2015; Querejeta et al. 2015; Eliche-Moral et al. 2018). More recently, Deeley et al. (2021) have used the publicly available data from the state-of-the-art IllustrisTNG-100 cosmological simulation (Nelson et al. 2019) to identify present-day S0 galaxies and investigate with unprecedented levels of detail their formation histories over cosmic time. This work shows that S0-like objects can, indeed, be produced by multiple mechanisms, with the main pathways of formation being by far merger events and the gas stripping that results from the infall of galaxy groups into larger units.

Observationally, the study of lenticular galaxies has begun to be approached through the analysis of large samples of optical spectra of these objects extracted either from single-fibre censuses or from the most recent surveys that use integral field spectroscopy. The former include research by Xiao et al. (2016), who have been among the first to analyse the local population of S0s and its relationship with evolutive processes from the point of view of activity classes. Based on the information provided by the Baldwin-Phillips-Terlevich (BPT) diagram (Baldwin, Phillips & Terlevich 1981; see also section 3.2), Xiao et al. were able to find evidence that activity and environment are closely related, noting that S0s with significant star formation and/or harbouring an AGN primarily reside in low-density regions (see also Davies et al. 2017), while those showing a standard absorption-line spectrum or one with emission lines of low signal-to-noise ratio (SNR < 3) are located in all kind of environments. More importantly, their results hinted at the existence of two types of S0s associated with different formation pathways. Although initially applied to the general galaxy population, the search of spectra with double-peak narrow emission lines by Maschmann & Melchior (2019) and Maschmann et al. (2020) can also be included within this category. These authors have found an important excess of S0s in samples of double-peak galaxies, accompanied by a systematic central excess of star formation. This and the fact that many of the double-peak lenticulars are isolated or located in poor groups has led them to suggest a scenario for these objects of bulge growth via multiple sequential minor mergers. For their part, spatially resolved spectroscopic measurements have also provided evidence of the existence of a subpopulation of field S0 galaxies that, compared to their classical counterparts located preferentially in groups and clusters, are less massive and show lower and flatter velocity dispersion profiles (Fraser-McKelvie et al. 2018; Domínguez-Sánchez et al. 2020), as well as less rotational support (Coccato et al. 2020; Deeley et al. 2020; Xu et al. 2022).

The duality in the properties of lenticular galaxies has been further confirmed by the extensive statistical study of a massive database of more than 68 000 single-fibre optical spectra of S0 galaxies in the local Universe ($z \lesssim 0.1$) led out recently by some of us (Tous, Solanes & Perea 2020, hereafter Paper I). In that work, we applied the principal component analysis (PCA) technique to reduce the large number of dimensions of the spectral data to the features encoded in the low-dimensional space defined by the first, most relevant eigenspectra (see Appendix A), while minimizing information loss. The projections of the S0 spectra on the axes of the bivariate subspace defined by the first two eigenvectors or principal components, denoted here by PC1 and PC2, explains about 90 per cent of the total variance and reveals the existence of two main regions outlined by subpopulations of lenticular galaxies with statistically inconsistent physical properties. We call these regions 'Passive Sequence' (PS) and 'Active Cloud' (AC), since they encompass sources whose spectra are representative, respectively, of passive and active galaxies. Compared to their absorption-dominated counterparts, S0s with significant nebular emission are, on average, somewhat less massive, more luminous with less concentrated light profiles, have a younger, bluer and metal-poorer stellar component, and avoid high-galaxy-density environments. A narrow dividing zone or 'Transition Region' (TR), formed by objects with intermediate spectral characteristics, separates the two main areas of the PC1–PC2 subspace and completes a novel classification for the S0s that is reminiscent of the well-known 'Red Sequence-Green Valley-Blue Cloud' division applied to the entire galaxy population in colour-magnitude diagrams. Interestingly, the analysis in Paper I also revealed that most of the S0s included in the AC class, which account for at least a quarter of the population of nearby lenticular galaxies, have star formation rates (SFRs) fully consistent with those observed in late spirals. This is in line with the findings of Kaviraj et al. (2007) from near-ultraviolet data. These results therefore indicate that present-day S0s with abundant star formation are not an isolated phenomenon and, consequently, that the traditional conception of these galaxies as basically red and passive stellar systems should be replaced by that of a class of objects that span a range of physical properties, can exhibit different levels of activity and, so it seems, also follow diverse formation channels (see also Welch & Sage 2003; Morganti et al. 2006; Crocker et al. 2011; Barway et al. 2013).

The present work aims to further deepen our understanding of the properties of the S0 population in the low-z Universe by carrying out an exhaustive characterization of the activity of these objects, as much linked to black hole accretion as to normal stellar processes. This effort is particularly relevant given the aforementioned confirmation of the existence of a significant fraction of lenticular galaxies with ongoing star formation. This fact, together with the higher fractional abundance of nuclear activity in galaxies with a strong bulge component (e.g. Overzier et al. 2003; Ho 2008) and the tendency of systems hosting an active central supermassive black hole (SMBH) to have global SFRs typical of pure star-forming galaxies (Rosario et al. 2013; Suh et al. 2019), make S0s ideal systems for ascertaining the extent to which nuclear activity and star formation are interrelated phenomena. Besides, both observations and theory suggest that there is a link between the activity of galaxies and the evolution of the global properties of their hosts, the similarity between the space density of quasars and the integrated star formation history of the

Universe being a good example (see e.g. Chen et al. 2022 and references therein). Therefore, a study of these characteristics can provide valuable information, also for the general population of galaxies, for a better understanding of the physical nature of this connection, as well as helping to determine whether it is direct or indirect.

This article is organized as follows. We begin by describing in section 2 the contents of the baseline data set used to carry out this endeavour. Section 3 is devoted to a thorough comparative statistical study of the various classes of activity into which lenticular galaxies can be subdivided according to the information contained in their optical spectra. We start by describing the recently introduced PCA-based spectral classification (section 3.1) and continue with the conventional BPT and WHAN schemes (sections 3.2 and 3.3). In section 3.4 a fourth alternative diagnostic of activity is introduced that uses elements from both the PCA and WHAN classifiers. Limiting the investigation of activity in galaxies to only the optical window can lead to incomplete and biased results due to obscuration by dust or mixed emission from different sources (see e.g. Satyapal et al. 2008, 2014; Suh et al. 2019). For this reason, we have extended our analysis to other wavebands by matching our optical data on S0s to mid-infrared (mid-IR) extragalactic sources (section 4), as well as to radio and X-ray measurements (section 5). Finally, we summarize our main findings in section 6, while the basic ideas behind our PCA treatment of the S0 spectral data are outlined in Appendix A. Given the breadth of this study, it has been considered convenient to postpone the discussion on the implications of the results obtained regarding the possible evolutionary scenarios of lenticular galaxies to the forthcoming papers in this series.

When necessary, it is assumed that we live in a standard concordant ΛCDM universe with cosmological parameters: $\Omega_{\rm m} = 0.3, \Omega_\Lambda = 0.7$ and $H_0 = 70\ {\rm km\,s^{-1}\,Mpc^{-1}}$.

2 BASELINE DATA ON PRESENT-DAY S0 GALAXIES

Our core database is an extensive share of the original sample used in Paper I. It consists of a compilation of spectrophotometric measurements for 56 008 S0 galaxies having elliptical r-band Petrosian magnitudes ≤ 17.77, heliocentric redshifts $0.01 \leq z \leq 0.1$ and good-quality optical spectra, extracted from the reprocessed Sloan Digital Sky Survey (SDSS; York et al. 2000) photometry listed in the `v1_0_1` version of the NASA-Sloan Atlas[1] (NSA; Blanton et al. 2011) and other public catalogs. SDSS measurements are complemented in the NSA with observations from the CfA Redshift Catalog (ZCAT; Huchra, Geller & Corwin 1995), the 2dF Galaxy Survey (2dFGRS; Colless et al. 2001), the 6dF Galaxy Survey (6dFGS; Jones et al. 2004) and the NASA/IPAC Extragalactic Database (NED), with the addition of ultraviolet data from the *Galaxy Evolution Explorer* (*GALEX*; Boselli et al. 2011) satellite and a small fraction of 21-cm measurements of the Arecibo Legacy Fast ALFA (ALFALFA; Giovanelli et al. 2005) survey in the overlapping regions. Among other properties, our database includes two numerical parameters derived by Domínguez-Sánchez et al. (2018) from deep learning models: the revised Hubble-type index, T (de Vaucouleurs 1977), and the probability that an ETG is an S0, $P_{\rm S0}$, which we use to robustly identify galaxies of S0 morphology by imposing the conditions $T \leq 0$ and a $P_{\rm S0} > 0.7$. For the stellar masses, M_*, we prefer the estimates listed in the GALEX-SDSS-WISE Legacy Catalog 2 (GSWLC-2; Salim, Boquien & Lee 2018), which also acts as the source for the SFRs used in this work, while fluxes and equivalent widths, EW, of the most important nebular emission lines, together with the BPT spectral classes (see section 3.2) are retrieved from the Portsmouth stellar kinematics and emission-line flux measurements by Thomas et al. (2013). All this information is completed with several parameters calculated in Paper I, such as two estimators of the local density, one based on the average distance to the first fifth neighbours in a volume-limited subset of our core database formed by all galaxies with $M_r < -20.5$, and one that ranks this same type of estimator according to the percentile that each galaxy gets in the deepest volume-limited subset that can be defined for it within this database (see Tous 2018 for details). Besides, we have the coefficients of the projections of the entire optical spectra of S0 galaxies into the first principal components (see also Appendix A), as well as their PCA-based activity classification (see section 3.1) inferred from the spectral analysis of this population carried out in Paper I.

[1]This data set is built around the Main Galaxy Sample (Strauss et al. 2002) of the SDSS, an essentially complete magnitude-limited subset of the Legacy Survey.

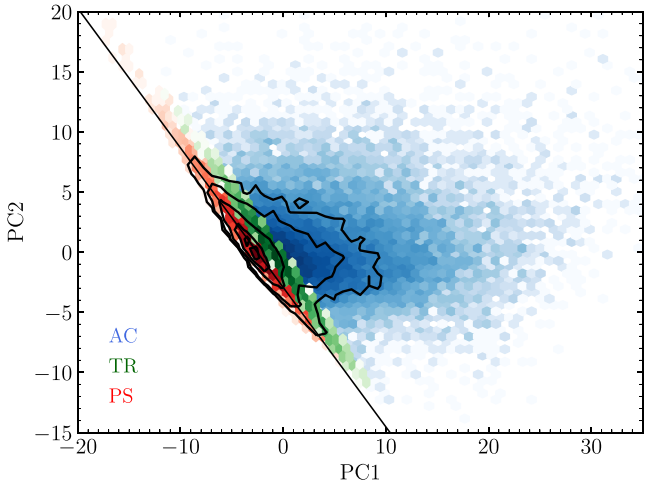

Figure 1. Projections of the optical spectra of our core sample of local S0 galaxies on their first two Principal Components defined in Paper I. The PC1–PC2 diagram is subdivided into three distinct regions corresponding to three different spectral classes throughout heat maps of different colours: PS (red), TR (green), and AC (blue). The intensity of all colours scales with the logarithm of the number density of points which are binned in hexagonal cells. The overlaid black contours correspond to global number densities 20, 40, 60, 80, and 90 per cent of the peak value drawn from a volume-limited subset of S0s taken from the full sample that includes galaxies with a Petrosian r-band absolute magnitude $M_r < -20.5$. The diagonal black straight line shows the PS ridge.

3 CLASSIFICATION OF PRESENT-DAY S0 GALAXIES FROM THEIR OPTICAL SPECTRA

In this section, we perform a comparative statistical analysis of the different classes of activity into which the population of nearby S0 galaxies can be subdivided by applying various treatments to the information contained in their optical spectra.

3.1 Spectral classes from the PCA of the full spectrum

As commented in the Introduction and shown in Fig. 1, the projections of the optical spectra of local S0 galaxies on their first two principal components enable their classification into three distinct

spectral classes: PS, formed by the members of the Pasive Sequence, the compact and densely populated narrow band that diagonally crosses the PC1–PC2 subspace (in red colours); AC, which comprises the galaxies located in the substantially less populated and much more scattered Active Cloud zone running from the right of the PS (blue); and TR, which contains the objects located in the slim Transition Region that separates the PS and AC areas (green). It can also be seen from Fig. 1 that the definition of the PCA spectral groups correlates very strongly with the projected distance of galaxies to the ridge line of the PS in the PC1–PC2 plane, which obeys the equation

$$\mathrm{PC2} = -1.162 \cdot \mathrm{PC1} - 2.932. \quad (1)$$

This distance, dubbed ΔPS, can be inferred from the function:

$$\Delta\mathrm{PS} = \log\left[2.913 + 0.758 \cdot \mathrm{PC1} + 0.652 \cdot \mathrm{PC2}\right], \quad (2)$$

whose dominion encompasses all physically plausible values of PC1 and PC2, which are essentially those in the half-plane to the right of the ridge line in Fig. 1 (see Paper I), and that reduces the PCA taxonomy to a one-dimensional classifier of activity. Much as with the traditional BPT and WHAN diagrams (see next sections), the spatial distribution shown by the broad-band spectral classes of S0 galaxies over this subspace provides a fairly faithful representation of the region spanned by the optical spectra of all Hubble types (see fig. 11 in Paper I), although in terms of occurrence most of the lenticulars are concentrated in the PS.

Fig. 2 shows two alternative versions of the PC1–PC2 diagram in which a colour scale is added to encode activity information. The extra dimension ΔMS in the top panel indicates the average distance to what is often referred to as the galaxies' Main Sequence (MS). This is a linear relationship in a log–log plot (but see Popesso et al. 2019) between the SFR and M_* obeyed by most present-day star-forming galaxies, used here to measure the level of activity shown by nearby S0s associated with the formation of new stars. This 'distance' is inferred through the difference between the observed SFR and that expected from a MS counterpart with the same M_*, via the equation

$$\Delta\mathrm{MS} = \log\left[\frac{\mathrm{SFR}}{\mathrm{M}_\odot\ \mathrm{yr}^{-1}}\right] - 0.76\log\left[\frac{M_*}{\mathrm{M}_\odot}\right] + 7.6, \quad (3)$$

where the expression providing the location of the MS ridge line for local objects has been taken from Renzini & Peng (2015). Note that due to the explicit dependence on M_*, this equation actually informs about variations in the specific SFR (SSFR).

Due to the lack of an equivalent way to isolate the contribution of the central SMBH to the global activity of galaxies, we have chosen to use in the lower panel of Fig. 2 the EW of the [O III]λ5007 Å emission line to encode the AGN-related activity. This is a spectral line excited primarily by electron collisions that is generally the strongest and least blended of the emission lines originated in the Narrow Line Region (NLR) of AGN-dominated galaxies, and that is often assumed to provide an unbiased measure of the ionising flux from the nucleus (e.g. Baskin & Laor 2005; Li et al. 2006; Comerford et al. 2009; Kauffmann & Heckman 2009; see also Trouille & Barger 2010 and references therein). Besides, the use of an EW measure makes it unnecessary to correct for NLR dust extinction. Note also that in order to provide clean maps we only show, in this and the remaining figures in this work involving spectral diagnostic diagrams, those galaxies with a good-quality optical spectrum, as defined in Paper I, and for which the emission lines used in the diagrams have values of the amplitude-over-noise parameter, AoN, greater than 1.5, which is the minimum condition for a reliable estimation of the line flux according to the Portsmouth catalog.

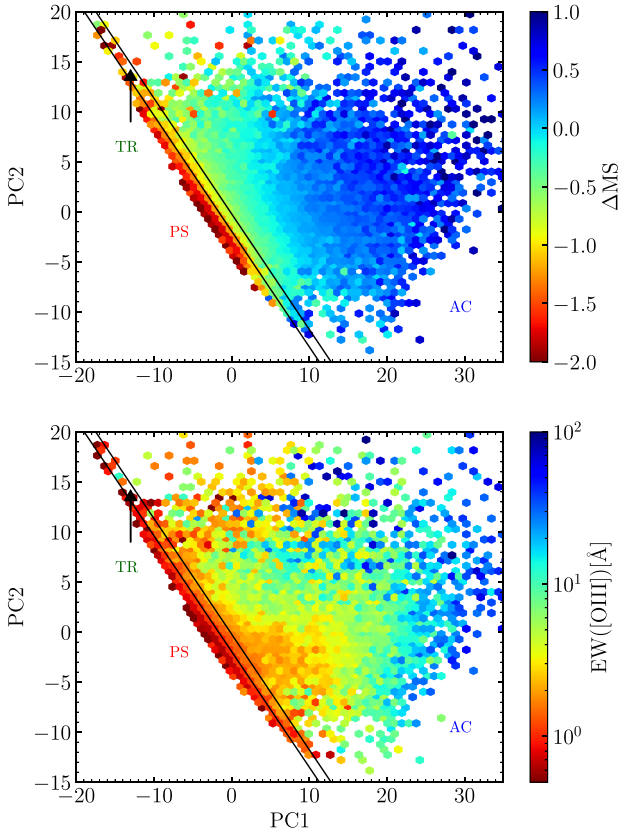

Figure 2. Alternative versions of the PC1–PC2 diagram for our core sample of nearby S0 galaxies. The scatter plots include a colour code that varies according to the mean value of ΔMS (equation (3); *top*) and the [O III]λ5007 Å EW (*bottom*) in each of the hexagonal cells in which the data has been grouped. Two parallel black straight lines show the best linear approximations to the PS/TR and TR/AC dividers. Note that the number of measurements used to build both plots is not exactly the same, since the data in the bottom panel obey the additional constraint AoN[O III] > 1.5 (see text).

Comparison of the two panels of Fig. 2 shows that the lowest values of both ΔMS and EW([O III]) are achieved around the PS region, which indicates that this spectral class mainly encompasses galaxies with null or depressed star formation and probably lacking nuclear activity. In contrast, the highest levels of activity normally occur in galaxies that inhabit the section of the AC region furthest from the PS. Nevertheless, the parameter ΔMS seems to be somewhat better correlated with the distance to such sequence (the colour scale runs more parallel to the PS ridge) than the EW([O III]).

In the top three panels of Fig. 3, we depict the distributions of the PCA spectral classes – conveniently renormalized, so they can be compared on an equal basis – in terms of what is probably the most fundamental global physical property of galaxies, M_*, and of two extrinsic parameters, z and a measure of the influence of environment given by the percentile rank associated with our nearest-neighbour-based local density estimator. As shown by these graphs, lenticular AC galaxies tend to be somewhat less massive than those belonging to the PS and TR classes, which exhibit fairly similar stellar mass distributions to each other. Likewise, the redshift distribution of this spectral class shows a mild bias towards low redshifts compared to those from the other two groups. For their part, the distributions of the PCA types according to our local environment descriptor

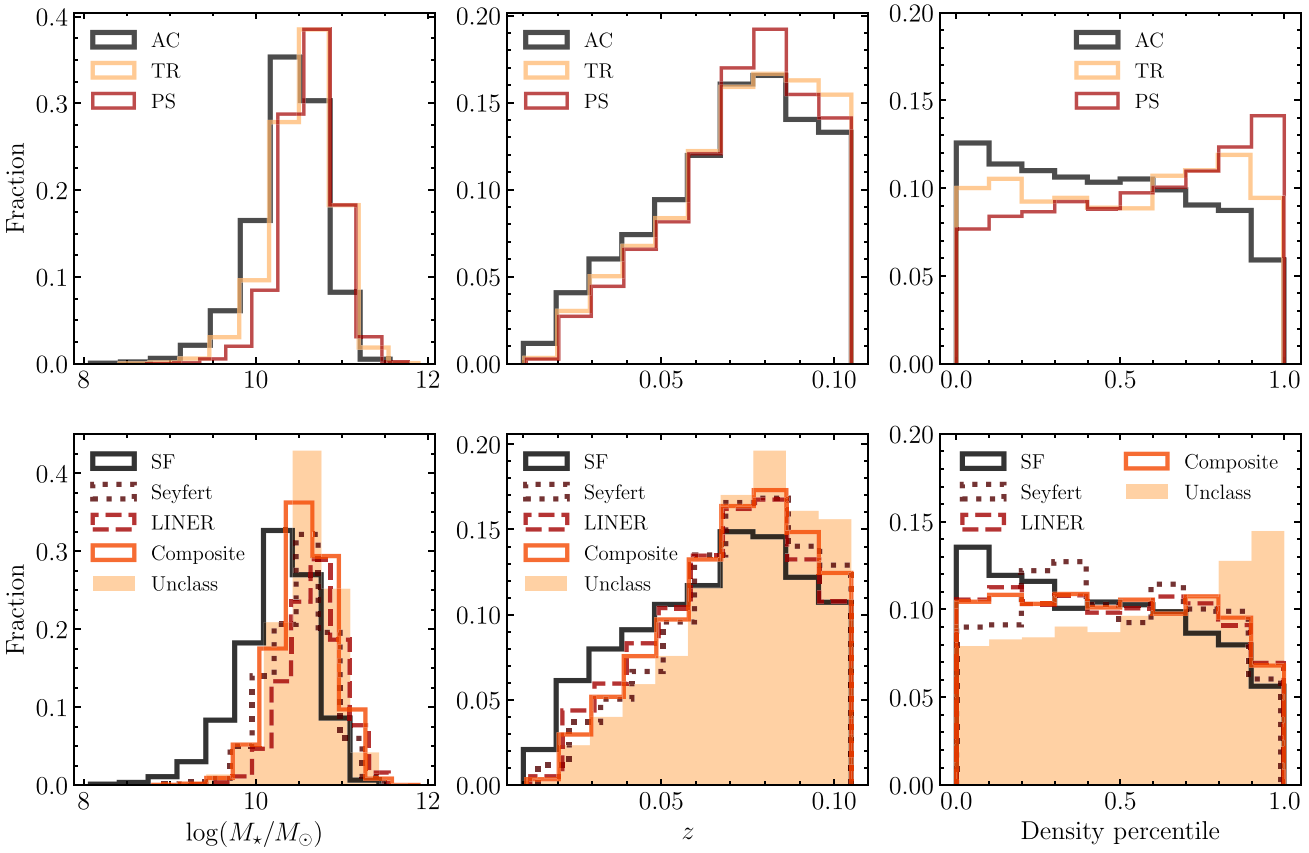

Figure 3. Distributions of stellar mass (*left*), heliocentric redshift (*middle*) and percentile rank of the density (*right*) for our sample of nearby S0 galaxies in terms of both the broad-band PCA (*top*) and narrow-line BPT (*bottom*) spectral classes. To facilitate intercomparison among these distributions, the total counts in all subsets have been normalized to sum to one, so the height of the histograms represents the proportion of a given class in each one of the bins defined on the *x*-axes.

reveal significant differences, with the S0 members of the PS and AC classes showing opposite tendencies, the latter being more abundant in regions devoid of galaxies and the former in the most crowded environments (see also fig. 10 in Paper I). In contrast, the distribution of the lenticulars of the TR class shows a roughly neutral behaviour with local density. Our data set contains 32 519, 4259 and 19 230 lenticular galaxies that are, respectively, bona fide members of the classes PS, TR and AC. So, not surprisingly, most of the nearby S0s are objects with a passive optical spectrum, although the number of their counterparts with signs of mild or substantial activity is by no means negligible.

3.2 Spectral classes from ratios of narrow emission lines

The BPT diagnostic diagrams are a well-known set of plots comparing pairs of narrow optical emission-line ratios designed to distinguish the ionisation mechanism of the gaseous component. They have become one of the benchmarks for the identification of the different classes of activity in galaxies. In Fig. 4, we show heatmaps of the most extensively used version of this classification scheme depicting the [N II]λ6584/Hα flux ratio against the [O III]λ5007/Hβ flux ratio (the BPT–NII diagram, see fig. 5 of Baldwin et al. 1981) for our sample of lenticular objects (top panel) and for an arbitrary sample of similar size of nearby galaxies extracted from the SDSS having an optical spectrum of good quality (see Paper I) and with morphologies evenly distributed in the range of Hubble types from E to Sc (bottom panel). The black curves in the diagrams mark the boundaries of the regions traditionally adopted to distinguish among the different activity classes: star-forming galaxies (SF), Seyfert galaxies, which host a considerable active galactic nucleus (AGN), low-ionisation nuclear emission-line region galaxies (LINER), encompassing true low-luminosity AGNs as well as galaxies whose LINER-like emission is inconsistent with ionisation by a nuclear source, and Composite sources that show mixed SF and AGN contributions.[2] The demarcations, summarized in Table 1, are the same used in the Portsmouth catalog, which is our reference source for the BPT classification. Comparison of both panels shows that the two galaxy samples define fairly similar 'seagull-shaped' loci in BPT–NII space, the biggest difference being a somewhat emptier upper half of the 'left wing' on the part of the S0, due to a lower presence of objects with intense star formation. Consequently, it is reasonable to conclude that, except for minor details, the spatial distribution of present-day lenticular galaxies in BPT–NII diagnostic diagrams bears a resemblance to that of the entire Hubble Sequence.

In Fig. 5, colour bars are added to the BPT–NII diagram to report, as in Fig. 2, on the mean values of the distance to the galaxies' MS,

[2]The Composite class is considered ill-defined by some authors, who therefore exclude it from their emission-line taxonomic paradigms of galaxies (e.g. Cid Fernandes et al. 2011). See also section 3.3.

Table 1. Demarcations of the spectral classes that can be defined in BPT–NII diagnostic diagrams.

Activity classes	Equation of divider	Reference	Acronym
Star-forming/Composite	$\log([\mathrm{O\,III}]/\mathrm{H}\beta) = 0.61/(\log([\mathrm{N\,II}]/\mathrm{H}\alpha) - 0.05) + 1.30$	Kauffmann et al. (2003)	K03
Composite/AGN	$\log([\mathrm{O\,III}]/\mathrm{H}\beta) = 0.61/(\log([\mathrm{N\,II}]/\mathrm{H}\alpha) - 0.47) + 1.19$	Kewley et al. (2001)	K01
Seyfert/LINER	$\log([\mathrm{O\,III}]/\mathrm{H}\beta) = 1.01\log([\mathrm{N\,II}]/\mathrm{H}\alpha) + 0.48$	Cid Fernandes et al. (2010)	C10

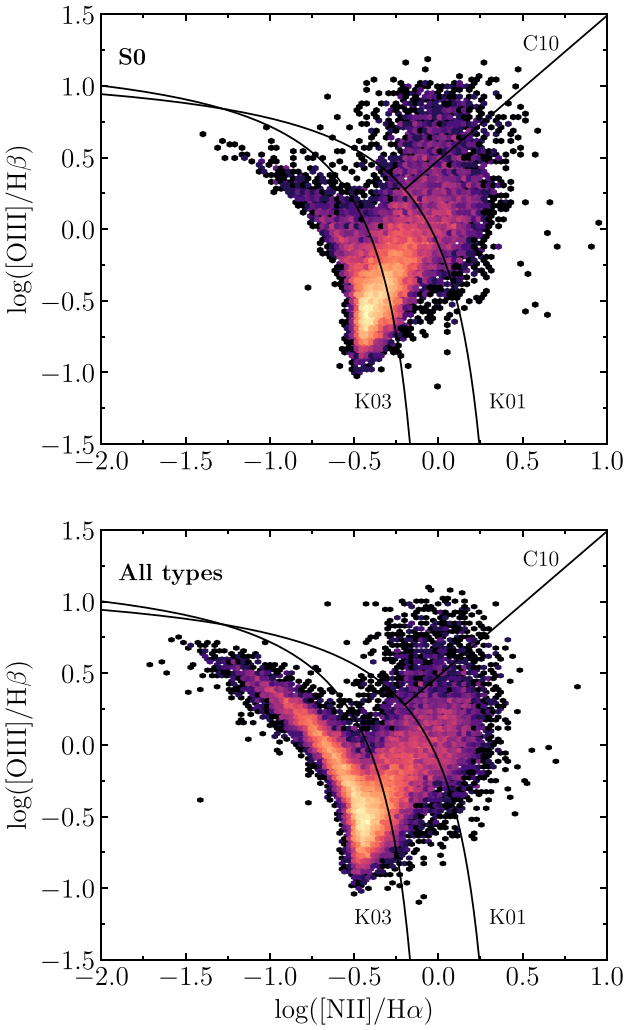

Figure 4. Heatmaps of the BPT–NII diagrams for our sample of nearby S0 galaxies (*top*) and for an arbitrary sample of ∼45 000 galaxies of all Hubble types with $z \leq 0.1$ (*bottom*). The latter has been assembled from ∼36 000 galaxies of types E, Sa, Sb, and Sc, plus about 9000 S0 galaxies randomly removed from the upper panel to guarantee that the figure compares two fully independent data sets. Only galaxies from the baseline data set having both a good-quality optical spectrum and values AoN > 1.5 for all four emission lines have been included in the diagrams. In both panels, colours scale with the logarithm of the number of points in each hexagonal cell, with darker colours corresponding to smaller values and lighter colours to larger ones. Black curves show the demarcation lines listed in Table 1.

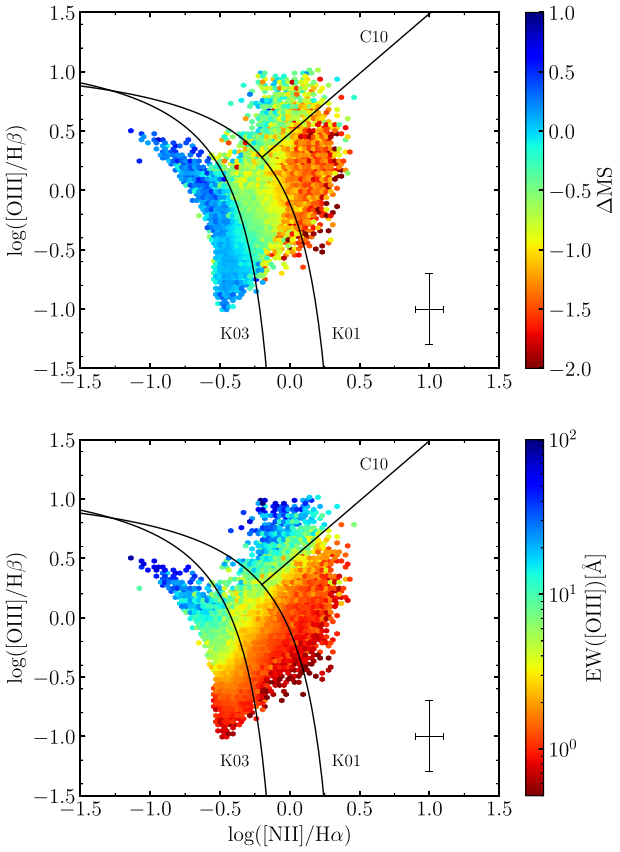

Figure 5. Same as in Fig. 2 but for the BPT–NII diagram. Black curves show the demarcation lines listed in Table 1. As in Fig. 4, we only plot galaxies whose parameters pass our quality filters. The error bars in the bottom-right corners of the panels show the medians of the errors in both axes.

ΔMS (top panel), and of the EW([O III]) (bottom panel). As would be expected, these two representations of the BPT–NII diagram show that the highest values of this parameter essentially populate the left-wing sequence associated with star-forming galaxies, whose right-upper boundary is very well outlined by the K03 demarcation. Although to a lesser extent, S0s with similarly high values of ΔMS are also present in the left half of the right wing, extending from the bottom of the diagram to the Seyfert's region (some blue data points can be seen protruding from the wing tip). This area of the BPT–NII diagram, however, brings together galaxies with vastly different SSFRs, which makes the ΔMS parameter show intermediate typical values across it. This dilution effect also affects the galaxies with the most depressed star-formation activity which, far from being restricted to the LINER region, also populate the lower part of the diagram. Such behaviours can be guessed by comparing these diagrams with the corresponding ones in the following section. For its part, the bottom panel shows that the [O III] EW decreases in a more or less orderly fashion towards the bottom-right of the diagram, following a direction nearly perpendicular to the C10 divisor. The fact that the highest values of this emission line are located at both the Seyfert and SF wingtips demonstrates that star-forming galaxies can also be strong [O III] emitters (e.g. Suzuki et al. 2016).

The distributions of the total stellar mass, redshift and density percentile for the BPT spectral classes are depicted in the bottom panels of Fig. 3. They are drawn from a total of 9490 SF lenticulars,

Table 2. Joint distribution of the PCA and BPT spectral classes for S0 galaxies with $z \leq 0.1$.

BPT class	PCA type		
	AC	TR	PS
Star-forming	9414	53	23
Seyfert	1073	75	23
LINER	631	625	2422
Composite	4971	1691	1797
Unclass[a]	3141	1815	28254

Note. ([a]) Encompasses galaxies with unreliable or absent BPT classification.

1171 Seyfert, 3678 LINER, and 8459 Composite. A fifth 'Unclass' type with 33 210 members has been added to this scheme to account for objects with either an unreliable BPT classification or none at all because they have one or more emission lines with a low contrast (i.e. small AoN) or a total lack thereof (see Table 2). As the first two panels show, the distributions of M_* and z behave quite similarly in most cases, the only exception being the SF class, whose members tend to be less massive and exhibit redshifts skewed towards lower values compared to those of the other spectral groups. This disparate behaviour is simply a present-epoch manifestation of downsizing – also latent in the histograms of the PCA classes since, as Table 2 shows, essentially all SF lenticulars (more than 99 per cent of this BPT group) are members of the AC class – combined with the fact that the different subsets of S0 galaxies behave largely as flux-limited samples (see e.g. the upper panel of fig. 1 from Gkini et al. 2021). This finding suggests that the signature of downsizing in the local Universe could also be preserved among individual Hubble types. Regarding the relationship with the local environment, Seyfert, LINER and Composite S0s display relatively uniform abundances for densities below the 90th percentile and an appreciable drop in the relative fractions in the last 10 per cent, while the SF lenticulars show a monotonous decrease in their abundance with increasing density percentile. Only the sources labelled Unclass, which are mainly passive galaxies with absorption spectra (see below), clearly favour high-density environments.

To complete this benchmarking exercise for the optical PCA and BPT spectral types of the S0 galaxies in the local Universe, we show in Table 2 their joint distribution. Practically all SF and Seyfert lenticulars belong to the AC, which also contains a substantial fraction of galaxies classified as Composite (∼30 per cent of the objects with a BPT tag). In contrast, the PS class is fully dominated by galaxies that lack a BPT classification (about 60 per cent of all the objects in our baseline S0 sample), showing that these sources can nevertheless be perfectly characterized by means of the PCA taxonomy. Most of the S0 LINERs are also members of the PS class, so while a good handful of them are found in the TR and AC regions (∼17 per cent each), it is clear that this class of galaxies sustains, in general, a low level of activity, of whatever type (see sections 3.3 and 5.3). Furthermore, S0s included in the Composite class live up to their name and are fairly more evenly distributed among the PS, TR and AC spectral types, roughly in a 20–20–60 ratio, respectively. The Composite group is indeed the most populated of the narrow-line activity classes that contribute to the TR broad-band spectral type, whereas the members of the SF and Seyfert classes tend to avoid this region (they represent, respectively, only ∼2 and 3 per cent of the TR objects with a reliable BPT assignment). These last two spectral types are also, by far, the less well represented BPT classes in the PS (∼0.5 per cent each), a role that is played by the LINER class among the members of the AC ($\lesssim$ 4 per cent).

3.3 WHAN diagram

According to Stasińska et al. (2008) one of the shortcomings of BPT diagrams is that they cannot discriminate between galaxies hosting a true weakly active nucleus (wAGN) – to avoid confusion Seyferts are renamed as strong AGNs (sAGN) – and 'retired galaxies' (RG) (see also, e.g. Singh et al. 2013; Stasińska et al. 2015). The latter are systems where star formation has stopped long ago, but when enough intergalactic gas is withheld, can show nebular emission lines arising from photoionisation by very hot low-mass evolved stars (HOLMES) during their short-lived post-AGB phase. The WHAN diagram proposed by Cid Fernandes et al. (2010), Cid Fernandes et al. (2011), which depicts the Hα EW versus the flux ratio [N II]/Hα, is intended to solve this issue. This scheme contains the same basic demarcations SF/AGN and Seyfert/LINER of the BPT–NII diagram, conveniently transposed to the new coordinates, while relying on theoretical arguments about the ionising photons budget to partition the LINER region into wAGN and RG. For the last group, Cid Fernandes et al. proposed an upper EW(Hα) = 3 Å boundary, regardless of the value of [N II]/Hα. Objects mainly ionised by HOLMES, in turn, are further subdivided according to the presence or absence of emission lines in their spectra into 'emission-line retired' (ELR) galaxies, if they have an EW(Hα) $\geq$ 0.5 Å, and 'line-less retired' (LLR) galaxies when the Hα line is weaker. However, for the present work we will consider RG as a single spectral group, since the distinction between ELR and LLR objects seems to obey more to limitations in the sensitivity of the detectors than to be physically motivated.[3]

As done previously with the PC1–PC2 and BPT diagrams, we show in Fig. 6 two representations of the WHAN diagnostic with colour gradients added to reveal any connection that may exist between the different spectral types and parameters ΔMS (top panel) and EW([O III]) (bottom panel). We also include black straight lines to show the demarcations between the different spectral types discussed in the previous paragraph. By examining the upper panel of this figure, one can see that ΔMS and EW(Hα) are closely related, with the most actively star-forming galaxies dominating the upper area of the diagram and the most passive systems concentrating in the lower RG region. More specifically, the WHAN diagram reveals the presence of objects that possess a high SSFR in both the SF and sAGN (Seyferts according to the BPT naming) regions, a result which comes to show that sources powered by BH accretion can also exhibit important star formation activity. Similarly, nearly all of the most quiescent objects are located below the upper boundary of the RG region, EW(Hα) = 3 Å, which concentrates ∼ 47 per cent of all the S0s included in this graph. The comparison of the upper panels of Figs 5 and 6 shows that these extreme values of ΔMS encompass significantly wider ranges of the variable log([N II]/Hα) (x-axis) in the WHAN diagram than in the BPT one. Therefore, the differences that both layouts show in terms of their relationship with the parameter ΔMS cannot be attributed to a possible reclassification of the activity of some galaxies. The most plausible explanation is the strong segregation of the SSFR imposed by the Hα EW, which prevents galaxies with very different values of ΔMS to intermingle, something that does happen, however, in the BPT–NII space.

In addition, there is the constraint AoN > 1.5, which is applied to the four fluxes involved in the BPT–NII diagram to eliminate those sources with the most doubtful classifications, while for the WHAN

[3]It is quite a standard procedure in the literature to assume that emission lines with EW < 0.5 Å are not convincingly detected (Herpich et al. 2016).

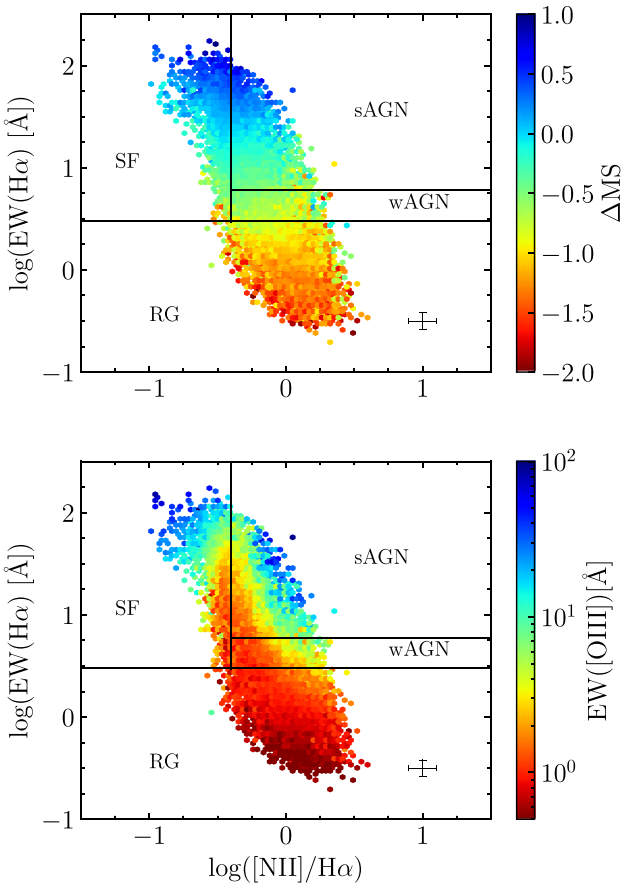

Figure 6. Same as in Fig. 2, but for the WHAN diagram. The horizontal black solid line at EW(Hα) = 6 Å represents the optimal transposition of the Kewley et al. (2006) divider between sAGN and LINER derived in Cid Fernandes et al. (2010). A second horizontal division line at EW(Hα) = 3 Å separates the LINER zone into wAGN and RG (see text), while the vertical black solid line at log([N II]/Hα]) = −0.4 mimics the divider between SF galaxies (on the left) and all AGNs (on the right) of Stasińska et al. (2006). The error bars in the bottom-right corners of the panels show the medians of the errors in both axes.

diagram only the significance of the [N II] and Hα emission-lines matters. This particular element allows us to classify another 15 319 S0 galaxies using the WHAN diagnostic, the majority of whom have weak emission lines (only $\sim$ 1/3 of the 17 893 galaxies of the RG class have a BPT type assigned). Furthermore, had we taken a look at the probability density function (PDF) of the EW(Hα) for the S0 galaxies designated SF on the BPT diagram, we would have seen that it follows a bimodal distribution, with the main mode centred on values characteriztic of MS objects and a much smaller secondary peak located below 3 Å and encompassing values typical of RG-class objects, for which star formation is essentially dead and that should therefore be excluded from the SF class (see e.g. Feldmann 2017).

On the other hand, the comparison of the bottom panels of these same figures shows that both the BPT and WHAN spaces feature distributions of the EW([O III]) variable that span an almost identical range with respect to the log([N II]/Hα) dimension. As regards the WHAN diagram, the highest values of this variable are attained in the upper-left and upper-right boundaries of the SF and sAGN regions, respectively, while the lowest values pile up mainly throughout the RG section. However, the correlation between the equivalent widths of [O III] and Hα is now very weak. In fact, we can observe in this latter activity classifier the existence of a wide wedge-shaped zone formed by objects with a very low [O III] emission that protrudes above the RG region along the SF/AGN divider extending up to EW(Hα) $\sim$ 50. It is not unreasonable to expect that this [O III]-devoid wedge, which covers a good part of the wAGN region and of the margins of the SF and sAGN regions closest to the Stasińska et al.'s (2006) divider, may comprise mainly galaxies whose activity is not necessarily related to the accretion into a central massive black hole. Interestingly, this would be consistent with the finding by Cazzoli et al. (2018) that AGN is the dominant mechanism of ionization for LINERs when their flux ratios [N II]/Hα are $\gtrsim$ 0.7. The implications of this result on the allocation of activity classes will be addressed in a separate work.

3.4 DPSN diagram

The WHAN diagram was introduced by Cid Fernandes et al. (2010) as an alternative to BPT diagrams with a diagnostic power equal to or even better and with an improved economy of measurements that reduces the dependence on the sensitivity of the instrumentation and, therefore, also the number of emission-line galaxies excluded from line quality cuts and the effects of the resulting bias. Another two-dimensional activity classifier that preserves these good qualities can be obtained using for the y-axis the distance to the PS, ΔPS, given by equation (2), and keeping the same horizontal dimension adopted in the WHAN and BPT–NII diagrams. This proposal is based on the fact that ΔPS, which is essentially linked to the global shape of the optical continuum of the stellar population of the host galaxy, is also very strongly correlated with EW(Hα), as already shown in Paper I. Since the PCA taxonomy can be reduced to a single component along the ΔPS axis, it is expected that this new diagram can also provide a suitable topological separation for both the WHAN and PCA spectral classes.

These expectations are fully confirmed by Fig. 7. In the left-hand panel, we show a WHAN diagram in which the data have been coloured according to the average values of ΔPS to corroborate that this parameter is strongly correlated with EW(Hα), whereas in the middle panel we employ number density contours of different colours to trace the regions populated by the three PCA modes of lenticular galaxies in the WHAN subspace. While it could be anticipated from the layout of colours on the left-hand panel that most of the PS lenticulars would lie within the RG region and that the bulk of the members of the AC class would fall above the EW(Hα) = 6 Å divider, i.e. in the SF + sAGN domains of the diagram, it is particularly telling that the distribution of TR members heavily sits within the boundaries of the wAGN section. Specifically, 95 per cent of the PS objects have EW(Hα) < 3 Å, 92 per cent of the ACs have EW(Hα) > 6 Å and 73 per cent of the TRs fall between the 3 and 6 Å divisors. Note that the smaller fractions of the TR class can be explained by the uncertainties affecting the flux and EW estimates of narrow emission lines causing some data spillover through the dividing lines of the diagram, especially down and to the right of the plot, which is critical for a narrow area like that assigned to the wAGN class. This coincidence between divisor lines that rely on completely different spectral elements is all the more noteworthy considering that the PS/TR/AC classification emerges from purely mathematical arguments derived from the analysis of the first principal components of the optical spectra, while the thresholds applied to the EW of the Hα line are empirical approximations to model-based and theoretically motivated physical frontiers. It can therefore be concluded that the taxonomic paradigm introduced in Paper I from S0 galaxies strengthens the suitability of the EW(Hα)-

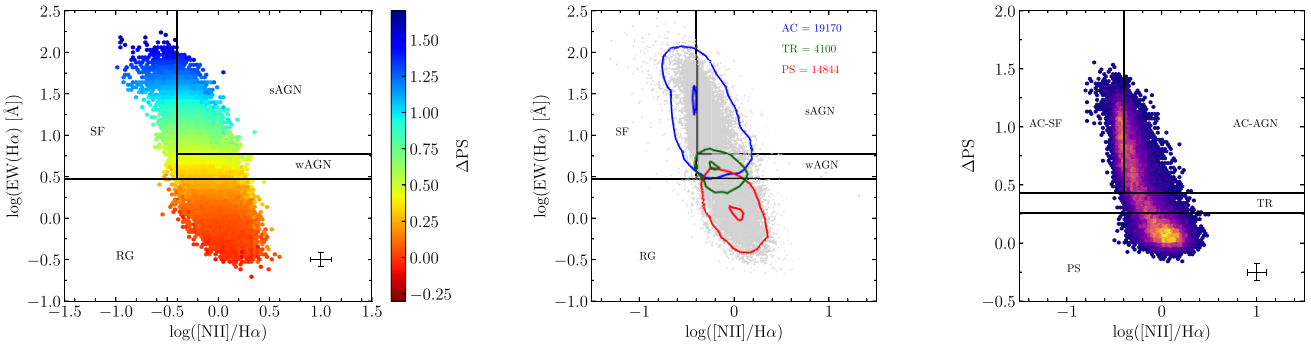

Figure 7. *Left:* Same as in Fig. 6, but using as third dimension the distance to the PS, ΔPS, to show that it strongly correlates with EW(Hα). *Middle*: Same WHAN diagram with coloured contours corresponding to number densities of 10 and 90 per cent of the peak value for the PS (red), TR (green), and AC (blue) broad-band spectral types, with the actual numbers of galaxies in each category being listed in the upper-right corner of the panel. One in every two galaxies of the whole subset are plotted as light grey points in the background for reference. *Right:* Heatmap of the DPSN diagram for our sample of nearby S0 galaxies. The vertical axis of the WHAN diagram is replaced in this new space by ΔPS and the best linear approximations to the PS/TR and TR/AC boundaries are transposed into the horizontal divisors ΔPS = 1.7 and 2.8, respectively. The SF/AGN vertical divider used by Stasińska et al. (2006) to separate these two spectral classes in terms of the ratio [N II]/Hα has been preserved. These three plots highlight the close correspondence that exists between the emission-line classification introduced by Cid Fernandes et al. (2011) for low-z SDSS galaxies of all Hubble types and that defined in Paper I from the PCA of the full optical spectra of the local S0 population.

based divisors proposed by Cid Fernandes et al. (2011) to distinguish wAGN from RG among the population of narrow emission-line galaxies. And vice versa, that the existence of dividers devised from the relative strength of the Hα emission provides a physical basis for the broad-band PS/TR/AC spectral types inferred in Paper I.

Based on the above considerations, we introduce in the right-hand panel of Fig. 7 a new activity diagnostic diagram, which we will call DPSN, using our sample of nearby S0 galaxies as a test bed. In this scheme, the PS/TR and TR/AC demarcations included in Figs 1 and 2 are converted, respectively, into the horizontal divisor lines ΔPS = 1.7 and 2.8, while the optimal SF/AGN vertical separation of Stasińska et al. (2006) is kept. The DPSN subspace, which essentially preserves the shape and relative locations of the SF, sAGN, wAGN, and RG areas from the WHAN diagnostic, maintains a similar discrimination ability in the vertical direction, but now makes it more resistant to measurement errors, since the location of the sources along this axis is set by a parameter that relies upon the flux contained in their entire optical spectra rather than on a single line. In addition, once the base of eigenvectors has been determined, something that must be done only once for a given spectroscopic galaxy sample, the calculation of the PC of the individual spectra, and hence of ΔPS, is relatively straightforward, making unnecessary using stellar synthesis analysis to subtract the continuum flux. Other advantages of using this latter parameter instead of EW(Hα) to measure activity are that the distribution of its values is barely affected, in a statistical sense, by both internal extinction and fixed aperture effects (see Paper I), and, although it does not have a practical impact on the census of galaxies qualifying for classification – the horizontal dimension continues to provide the strictest quality cut –, that it is possible to infer the distance to the PS for any object endowed with a good-quality optical spectrum, regardless of the host's level of activity. The latter is particularly useful for samples, such as the one we are studying here, in which galaxies with absorption spectra abound.

In the next two sections, we discuss the properties of the various spectral classes of local S0s in regions of the electromagnetic spectrum, other than the visible, using data drawn from some of the most important mid-IR, radio and X-ray wide-area surveys. We want thereby to increase our understanding of the different subpopulations of lenticular galaxies by examining them from different angles and, ultimately, unravel their origin.

4 INFRARED DETECTIONS OF PRESENT-DAY S0 GALAXIES

An important issue that affects any diagnostic diagram for galaxies that uses fluxes and/or EWs is that these parameters are aperture-dependent. This has led several authors (e.g. Herpich et al. 2016; Zewdie et al. 2020) to consider alternative classification paradigms that rely partially or totally on photometric data. This is justified on the basis that differences in the astrophysical sources driving galaxy evolution translate to differences in the SED and hence in the colours of the hosts.

It soon became clear that the mid-IR waveband was particularly suitable to search for such differences. One of the most powerful diagnostics currently available in this electromagnetic window are colours derived using photometry from the *Wide-Field Infrared Sky Explorer* (*WISE*; Wright et al. 2010) all-sky survey. This observatory has mapped the entire sky in four mid-IR broad bands W_1, W_2, W_3, and W_4 centred at 3.4, 4.6, 12, and 22 μm, respectively. Even though the study of AGNs was not among the main goals of *WISE*, this survey is really appropriate for that aim since its mid-IR detectors roughly cover one of the wavelength ranges in which AGNs can be clearly distinguished from SF galaxies (see e.g. fig. 1 in Hickox & Alexander 2018). In particular, *WISE* observations are useful in discovering AGNs whose emission in the UV-optical waveband has been obscured by the dust and gas within the torus surrounding the accretion disc of the SMBH and/or by dust in the galaxy (e.g. Stern et al. 2012; Mateos et al. 2013; Assef et al. 2013; see also the review on obscured AGNs by Hickox & Alexander 2018, as well as next section). However, it is important to remember that mid-IR observations are only sensitive to relatively luminous AGNs in which nuclear emission is strong enough to dominate over emission from other physical processes in the host galaxy, such as star formation, which in extreme cases (e.g. starbursts) can dilute or overwhelm the AGN output (Gürkan, Hardcastle & Jarvis 2014; Radcliffe et al. 2021). Another advantage of using colours to classify galaxies is that

Table 3. Joint distribution of the PCA and BPT spectral classes for S0 galaxies with $z \leq 0.1$ detected in the AllWISE catalog.

BPT class	PCA type		
	AC	TR	PS
Star-forming	1744	19	8
Seyfert	262	23	10
LINER	211	214	1024
Composite	1153	495	691
Unclass	495	375	5202

they can be inferred for any type of object, whether it has an emission spectrum or not.

Next, we focus on the S0s in our data set that are also detected in the AllWISE Source Catalog, which lists the most sensitive and accurate data released by the *WISE* survey, including, among other products, astrometry and photometry for over 747 million objects.

4.1 Crossmatch to AllWISE catalog

The AllWISE counterparts of our S0 galaxies have been extracted by selecting the closest pair within a search radius of 2 arcsec, a sensibly shorter distance than the 6.1 arcsec angular resolution of the W_1 band. Despite the strictness of the rule applied, we do not expect to miss a significant number of pairs, as a previous test demonstrated that the distribution of angular separations for matched sources is strongly skewed towards values < 1 arcsec. Besides, we have excluded AllWISE detections that are consistent with point sources, i.e. having an extended source flag parameter `ext_flg` $= 0$, to eliminate potential matches with stellar objects. In an effort to achieve a mid-IR sample of the highest quality, we have also demanded a minimum SNR of 5 in the W_1 and W_2 bands, and of 3 for the less sensitive W_3 magnitude.[4] Finally, only AllWISE counterparts with a good quality photometry, i.e. having `cc_flag` $= 0$ in the first three bands, have been considered.

After applying all the aforementioned constraints, we obtain a mid-IR sample with a total of 11 926 present-day S0 galaxies. While this figure represents an overall reduction of ∼5:1 from the size of the baseline optical database, the relative percentage abundances of the different activity groups barely register, in general, significant changes (see Table 3). Thus, in the *WISE* energy band the SF and Seyfert continue en masse being part of the AC region, maintaining percentages of around 99 and 90 per cent, respectively, with the LINER and Unclass type of lenticulars being mostly members of the PS, and the Composite the most evenly distributed BPT class within the PCA broad-band categories, while the global fraction of objects without a BPT classification drops slightly to 51 per cent.

4.2 Mid-IR colour–colour diagrams

The WHAN diagram (section 3.3), just like the proposed DPSN alternative (section 3.4), enable rather exhaustive descriptions of the activity exhibited by galaxies because they deal with a pair of the strongest emission lines in the optical window and have their vertical axes based on measurements that are scarcely affected by the quality of the data. However, such subspaces are not entirely free of sensitivity issues, specially regarding their horizontal dimension.

The WHAW diagram Herpich et al. (2016) constitutes one attempt to improve over the WHAN classification by replacing the x-axis coordinate with the $W_2 - W_3$ colour. Unlike emission line ratios, colours are global parameters applicable to galaxies of any kind and, in particular, $W_2 - W_3$ is expected to do a very good job at separating objects with a high SSFR from RG (e.g. Cluver et al. 2014; Orellana et al. 2017). However, such a change in the horizontal axis is not accompanied by a clear differentiation between SF and Seyfert galaxies, at least not as much as that provided by the BPT- and WHAN-like spaces. This has restricted the applicability of this type of hybrid diagnostic diagram that combines optical spectroscopy with mid-IR photometry, and might explain why it has been scarcely used in the literature.

A different approach for galaxy classification is provided by fully photometric schematics that, thanks to their insensitivity to aperture effects, enable the categorisation of all types of sources, including galaxies totally devoid of emission lines. *WISE* colour–colour plots keep the $W_2 - W_3$ colour of the horizontal axis used by the WHAW diagrams, but replace the vertical coordinate by the $W_1 - W_2$ colour to achieve a sound topological separation of sources that show certain levels of activity, such as AGNs and ultra-luminous infrared galaxies (ULIRGs).[5]

Fig. 8 displays the $W_1 - W_2$ versus $W_2 - W_3$ colour space for the subset of nearby S0s detected in AllWISE. As in previous figures, we have coloured the data points according to the value of parameters ΔMS (top panel) and EW([O III]) (bottom panel). The two plots reveal (see also Fig. 9) that most measurements are distributed over a narrow and slightly bent upwards strip that runs roughly parallel to the horizontal axis. The upper right part of this band connects with a sparsely populated region – outlined by hexagonal cells that typically contain a single data point – that extends across the reddest sectors of the plot and hosts a sizeable fraction of lenticulars with important levels of activity (see below). The much more crowded banana-shaped region encompasses roughly the same range of IR colours displayed by data sets of nearby galaxies spanning the entire Hubble Sequence. However, and not unexpectedly, the distribution shown by the S0s is predominantly consistent with those sectors of the diagram traditionally associated with early-type systems, lacking, for example, the deep gap in the range $W_2 - W_3 \approx 0.8 \div 2.4$ mag, deemed as the infrared transition zone (IRTZ), that appears in samples that contain ETGs and LTGs (see e.g. fig. 1c of Alatalo et al. 2014 for a detailed view of this area). Regarding the values of ΔMS, and hence of the SSFR, we find that they are strongly correlated with the $W_2 - W_3$ colour, so that all but five of our S0 systems with enhanced star formation, i.e. having $\Delta\text{MS} \gtrsim 0$, are housed in sectors redwards of the upper boundary of the IRTZ. Something similar happens to the values of EW([O III]), which also increase with the mid-IR colours of the *WISE* space, although in this case with a substantially larger dispersion that makes it pretty easy to find objects with strong [O III] emission (EW([O III]) $\gtrsim 10$ Å) within the IRTZ and that considerably intermingles the values of this parameter in said space. In contrast, those lenticulars that are passive in all respects cluster bluewards of the IRTZ – notice that the third dimension of the panels assigns them the reddest cells – and exhibit $W_2 - W_3$ colours near zero (Jarrett et al. 2011).

Among the S0s with enhanced $W_1 - W_2$ colour, we find 44 sources that verify the condition $W_1 - W_2 > 0.5$, the criterion adopted by Assef et al. (2013) to obtain highly reliable AGN samples (see

[4]We do not make use in this work of the much shallower and noisier W_4 band data.

[5]These objects are usually absent in data sets that, like the one that concerns us here, are based on optically selected galaxies.

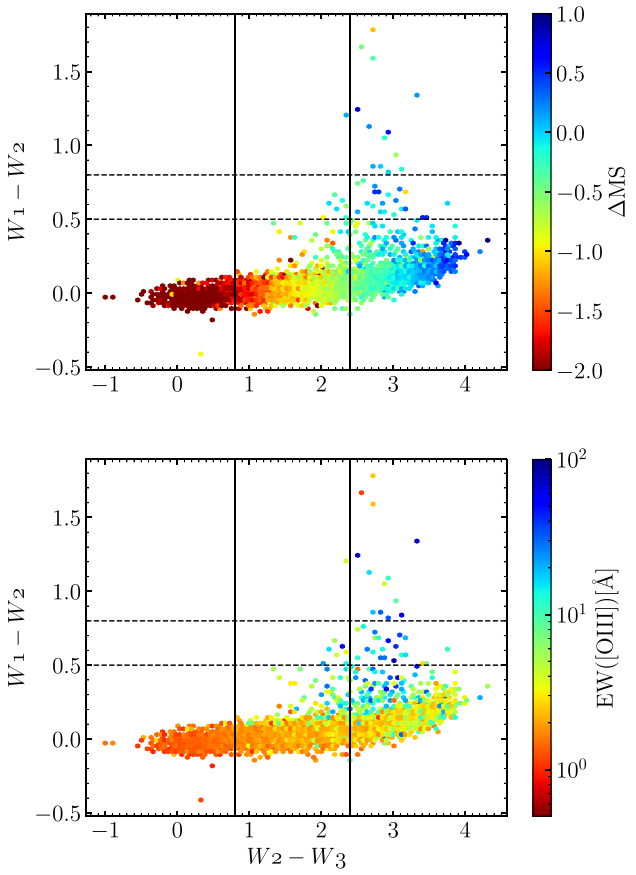

Figure 8. Same as in Fig. 2 but for the $W_1 - W_2$ versus $W_2 - W_3$ colour–colour diagram of the members of our S0 sample with a counterpart in the AllWISE catalog. The two vertical black solid lines demarcate the edges of *WISE*'s IRTZ defined to be $W_2 - W_3 \approx 0.8 \div 2.4$ by Alatalo et al. (2014), while the $W_1 - W_2 > 0.5$ and the stricter $W_1 - W_2 > 0.8$ colour cuts adopted, respectively, by Assef et al. (2013) and Stern et al. (2012) to select AGN sources, are shown as horizontal black dashed lines. Despite the important difference in sample sizes, we have kept the same ranges of the colour bars used in previous diagrams for ease of comparison.

also Stern et al. 2012 for a somewhat stricter threshold), whereas very few of them, three to be exact, show values of $W_1 - W_2 \gtrsim 1.6$ characteristic of obscured AGN. Forty of the galaxies above the Assef et al.'s (2013) colour cut (91 per cent of the total) belong to the AC class, 27 of them tagged as Seyfert (57 per cent) and only one as SF. It thus appears that the Assef et al.'s (2013) limit provides, at least for present-day S0 galaxies, not only a good criterion to obtain reliable samples of systems powered by nuclear SMBH, but also an upper boundary to the $W_1 - W_2$ colour that can be achieved by these objects when the principal source of activity comes from star formation.

Fig. 9 depicts the location of the spectral classes defined through the PCA and BPT diagnostics within the *WISE* diagram.[6] With regard to the PCA types, we find that AC lenticulars are primarily located to the right of the upper boundary of the IRTZ, in the lower right sector of the diagram, although we can also see an extended low-density belt going further into the IRTZ and upwards to the AGN region. The reddest divider of the IRTZ also acts as an upper limit for nearly all PS objects, which are essentially found to the left of it. In turn, a sizeable number of the TR members lie within both edges of the IRTZ, with the peak of their distribution at the red boundary of this region, reinforcing the idea that this spectral class encompasses objects evolving towards a quiescent state. In terms of the BPT classes, we find that S0–Seyferts occupy a region not unlike that of the AC members, albeit somewhat more extended along the vertical direction, covering the entire IRTZ and reaching redder $W_1 - W_2$ colours. While it is true that some of these objects also exhibit high values of ΔMS, the fact that the Seyfert spectral class shows a far larger spread in the $W_1 - W_2$ versus $W_2 - W_3$ colour space than the S0–SF – the largest of all spectral groups indeed – suggests that in a number of cases its members owe their mid-IR colours mainly to the presence of nuclear engines in the hosts (see also, e.g. Alatalo et al. 2014). Another BPT class of S0 galaxies that tends to scatter in the *WISE* colour space towards the more active areas of it (although less so than Seyferts and ACs), is the LINER, probably for the same reason that we have just commented. This class has also a good number of objects in common with the TR one (see Table 3), both spectral groups being the main dwellers of the IRTZ, but with the distribution of the former more centred in this area, which seems to indicate that the LINER class encompasses objects with somewhat lower activity levels. For its part, the few lenticular galaxies that are actively forming stars are preferentially found redwards of the upper edge of the IRTZ, although there is also a sparse tail that penetrates into this region up to $W_2 - W_3 \sim 1.5$ in accordance with the findings of Cluver et al. (2014) from the resolved sources of the Galaxy And Mass Assembly (GAMA) survey. This suggests that, in spite of their SF status, some members of this class are already beginning to see their SFR diminished. Generally speaking, we can conclude that the loci occupied by the different spectral classes of present-day lenticulars in the $W_1 - W_2$ versus $W_2 - W_3$ diagnostic diagram show a good agreement with those that can be inferred for the entire local population of galaxies (compare our Fig. 9 with e.g. fig. 7 in Zewdie et al. 2020), the most notable difference being that the *WISE* colours of our sample are bluer on average. This is unsurprising given the placement of S0 galaxies within the Hubble Sequence.

We shall end this section by discussing two lenticular galaxies that have come to our attention because in spite of their PS classification are found well past the upper limit of the IRTZ (red crosses in the PS panel of Fig. 9). Close inspection of the spectrophotometric data available for these two objects (`specObjID` = 1083174028455208960 and 395248620099627008) in the *SciServer* of the SDSS reveals that they have very red stellar continuum spectra, which explains their PCA classification as passive systems, while showing at the same time relatively prominent nebular emission lines. The red SDSS colours, which together with the high intrinsic brightness justify their selection as Luminous Red Galaxies, appear to be the result of a combination of closeness ($z \sim 0.03$), high inclination ($i \sim 60$ deg), and presence of relatively significant amounts of gas and dust. This last factor points to the existence of a certain level of star formation in these objects capable of generating emission lines, but whose main booster is most likely nuclear activity, since both S0s are cataloged in the literature as radio sources with post-starburst stellar populations, in agreement with their BPT rating as Seyfert and Composite, respectively. In any case, these seemingly contradictory spectral and photometric diagnoses can be perfectly understood, while their complementarity is revealed. More specific statements about the evolutionary status of these and other galaxies

[6]Although this and the next comparisons with the PCA types have been restricted for space reasons to the main BPT classes, they are also representative of the corresponding WHAN classes.

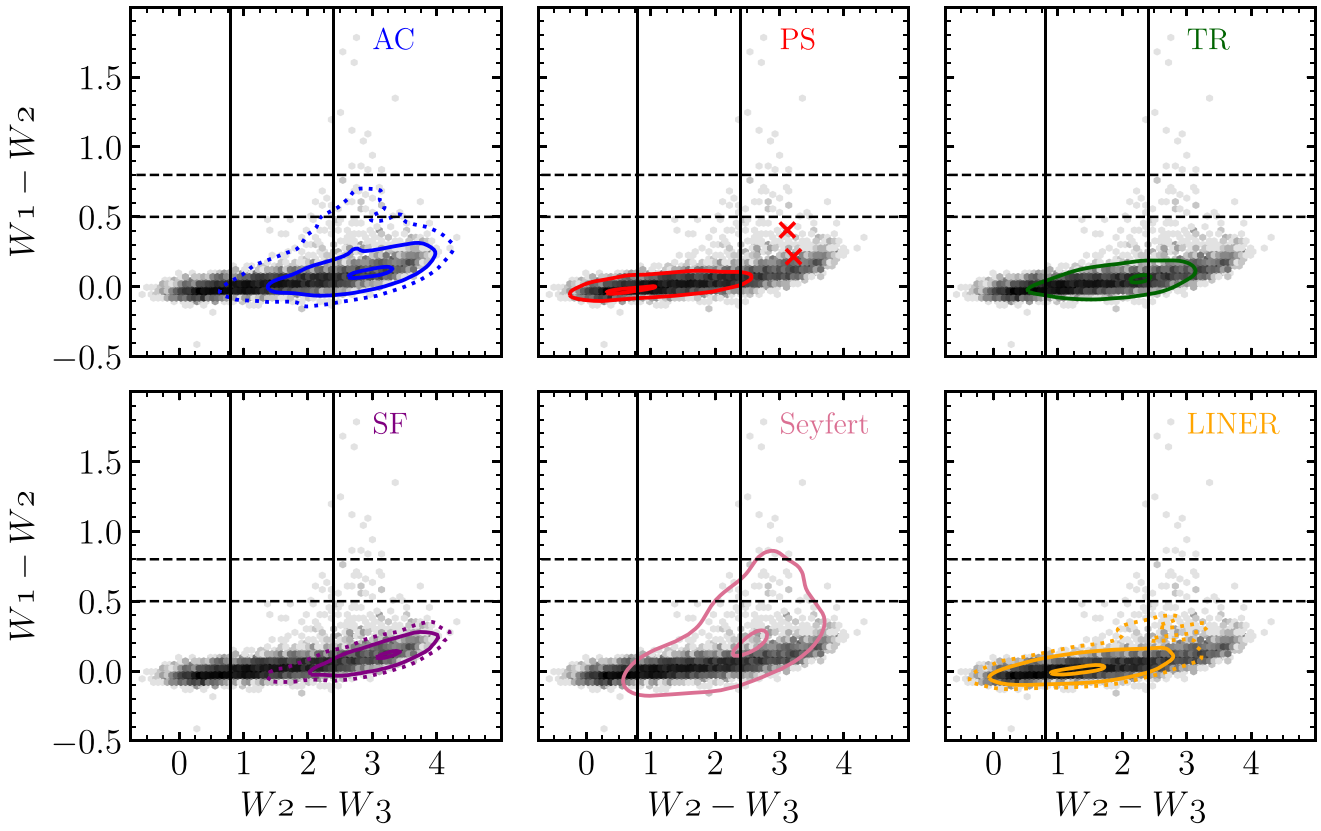

Figure 9. Mid-IR colour–colour diagrams for the main broad-band and narrow-band optical spectral classes of the nearby S0s included in AllWISE. From left to right and top to bottom: AC lenticulars (blue), PS (red), TR (green), SF (purple), Seyfert (pink), and LINER (orange). Contours in each panel are drawn at number densities 10 and 90 per cent of the peak value. Extra contours (dotted lines) are added to some panels at number densities one per cent (AC) and 3 per cent (SF and LINER) of the peak values to show better the total breadth of these distributions. Two PS galaxies with abnormally red $W_2 - W_3$ colours discussed in the text are marked with red crosses. In all panels, a heatmap of the full AllWISE S0 sample is shown in the background using a logarithmic greyscale. The vertical black solid lines are the limits of the IRTZ, while the horizontal black dashed lines show the lower $W_1 - W_2$ colour cuts adopted by Assef et al. (2013) (bottom) and Stern et al. (2012) (top) to select AGN sources.

included in our mid-IR S0 sample would require follow-up studies of their baryonic content that are beyond the scope of this paper.

5 RADIO AND X-RAY DETECTIONS OF PRESENT-DAY S0 GALAXIES

Radio wavelengths are widely used to characterise nuclear emission. In fact, AGNs were first discovered by their luminosity in the radio waveband. The emission in this regime from high-luminosity radio galaxies is dominated by non-thermal synchrotron radiation arising from processes related to the accretion disc around the central SMBH and/or powerful relativistic jets. These radio-loud sources comprise only a small fraction of the general AGN population, which is predominantly radio quiet (e.g. Zamfir, Sulentic & Marziani 2008; Kellermann et al. 2016, and references therein). Synchrotron emission by relativistic electrons, accelerated in this case in supernova shocks, is also one of the two main components of the radio continuum emission related to the evolution of massive stars. The other is thermal free–free radiation from ionised gas in the H II regions surrounding them (Condon 1992). Besides, the optical depth for radio emission is very low and so the 20-cm (1.4 GHz) radio continuum can be used to observe both the star formation rate in dusty galaxies and the most obscured AGNs that can escape detection in the optical, mid-IR and X-ray windows. To differentiate between non-thermal activity and that related to star formation one can require $L_{1.4\ \mathrm{GHz}} \gtrsim 10^{23}\ \mathrm{W\,Hz^{-1}}$, which is roughly the luminosity at which radio source counts switch from being largely dominated by star-forming galaxies to being dominated by powerful AGNs (see e.g. the radio luminosity function in fig. 11 of Best et al. 2005). Below this limit, AGNs cannot be reliably distinguished from SF on the basis of radio luminosity alone. However, by assuming that for local $L \gtrsim L^*$ galaxies non-thermal radio emission directly tracks their SFR, we can use the latter to calibrate the radio power at 1.4 GHz according to the empirical relation by Bell (2003)[7]

$$L^{\mathrm{SFR}}_{1.4\ \mathrm{GHz}} = 1.8 \cdot 10^{21} \left[\frac{\mathrm{SFR}}{\mathrm{M_\odot\ yr^{-1}}}\right]\ \mathrm{W\,Hz^{-1}}, \quad (4)$$

the scatter being a factor of around ± 0.26 dex on a galaxy-by-galaxy basis (see also Yun, Reddy & Condon 2001).

AGN activity can also be traced through X-ray emission and is believed to be produced by Comptonisation of optical/UV photons of the accretion disc by the corona of hot electrons that envelops it (e.g. Haardt & Maraschi 1991). These observations, however, can

[7]This calibration only considers the contribution of synchrotron emission from relativistic electrons associated with SN remnants which, according to the standard model of SF luminous galaxies, accounts for ∼90 per cent of the total radio continuum flux at 1.4 GHz (Condon 1992).

undergo some absorption, especially in thicker Compton sources with $N_{\rm H} > 10^{24}\,{\rm cm}^{-2}$ (e.g. Diamond-Stanic, Rieke & Rigby 2009; LaMassa et al. 2009). As in the radio domain, stellar processes related to diffuse gas and X-ray binaries in galaxies can also be a source of X-ray emission. A sensible criterion to disentangle the type of source that dominates the X-ray counts, AGN or stellar, is provided by the Ranalli et al.'s (2003) relation between SFR and hard (2–10 keV) X-ray luminosity calibrated for local samples (c.f. Trouille & Barger 2010):

$$L^{\rm SFR}_{2-10\ {\rm keV}} = 5 \cdot 10^{39} \left[\frac{\rm SFR}{{\rm M}_\odot\ {\rm yr}^{-1}}\right]\ {\rm erg\,s}^{-1}, \quad (5)$$

which implies that a SFR of at least 200 $M_\odot\,yr^{-1}$ is required to produce an X-ray luminosity greater than $10^{42}\,erg\,s^{-1}$ (Persic & Rephaeli 2007 and Vattakunnel et al. 2012 find similar relations between the X-ray hard luminosity and the SFR within a factor of ∼1.5 of equation 5). These huge SFRs are typical of ULIRGs, and we expect none in our S0 sample (see section 4.2). Therefore, any source in our data set more luminous than this limit would likely be an AGN on energetic grounds. Again, weak AGNs may not be correctly identified by just applying this constraint.

5.1 Crossmatch to FIRST and 4XMM-DR11/CSC 2.0 catalogs

The VLA Faint Images of the Radio Sky at Twenty centimetres (FIRST) Survey (Becker, White & Helfand 1995) covers 10 57 5deg^2 of the radio sky over the north and south galactic caps by using the Very Large Array in its B configuration. This results in a high image resolution of 5–6 arcsec and a source position accuracy of < 1 arcsec. The FIRST footprint was designed to overlap with the sky area surveyed by the SDSS, so ∼ 30 per cent of the sources have optical counterparts in the Sloan data. The sensitivity of the observations is also excellent, with a limiting flux density of about one mJy for point sources. We select from the FIRST catalog those objects with an S0 counterpart in our baseline data set within a fiducial radius of 8 arcsec, eliminating stellar sources (`SDSS_class == 's'`) and those that are likely spurious (`P(S) >0.1`). We also demand the ratio between the radial separation r and the R_{50} Petrosian radius of our S0 galaxies to be lower than 1 as a way of increasing the probability that we are selecting the same source in both data sets. With this procedure we obtain a total of 1586 matches, including 1176 unique and 410 multiple, for which we have chosen the narrowest pair.

For the crossmatch with X-ray data, we use two catalogs in an attempt to remedy somewhat the significantly poorer statistics offered by the shallow observations in this waveband. On the one hand, there is 4XMM-DR11 (Webb et al. 2020), the year 2020 version of the fourth generation of the catalog of Serendipitous X-ray sources from the *XMM–Newton* telescope (Jansen et al. 2001). Although not an all-sky survey, this is actually the largest X-ray catalog in existence, comprising 895 415 individual detections of 602 543 unique X-ray sources in the energy range from 0.2 to 12 keV distributed over 1239 deg^2 of the sky and with a median positional accuracy for the point source detections of < 1.57 arcsec. We have matched our S0 data set to sources in this catalog located at an angular separation of less than 10 arcsec and used the information listed in the detection flags to eliminate possible spurious and/or contaminated sources, producing a first subset of 298 S0 galaxies with measured X-ray fluxes.

On the other hand, we have also crossmatched our S0 with the final second major release of the *Chandra* X-ray observatory (Schwartz 2004). The Chandra Source Catalog (CSC 2.0; Evans et al. 2020) lists measured properties of 317 167 unique point and extended compact sources distributed across the entire sky (but not covering it) and observed with a position error of 0.71 arcsec (95 per cent confidence) for ∼ 90 per cent of them. *Chandra*'s Advanced CCD Imaging Spectrometer provides fluxes in five science energy bands from 0.5 to 7.0 keV, including the broad-band master fluxes that cover the entire range of photon energies. To carry out the pairing with *Chandra*'s data, we have taken advantage of the CSC 2.0-SDSS table of unambiguous matches that lists, among other parameters, the source type, the object identifier and coordinates from SDSS-DR15, the angular distance r between the matched sources, and the match probability. We accept as bona fide matches those with an equal `ObjID` as long as they are at a radial separation $r \leq 5$ arcsec and have a minimal match probability of 0.9. This has produced a second subset of 123 matches, less than half of those obtained with *XMM–Newton* catalog. After removing the 29 sources common to both subsets, we obtain a net total sample of 392 nearby X-ray emitting S0 galaxies, a quantity that, while not small, is well below the sizes reached by the samples inferred from the other bandwidths.

Table 4. Joint distribution of the PCA and BPT spectral classes for S0 galaxies with $z \leq 0.1$ detected in the FIRST catalog.

BPT class	PCA type		
	AC	TR	PS
Star-forming	594	0	0
Seyfert	160	2	1
LINER	139	25	24
Composite	458	11	8
Unclass	104	14	46

Table 5. Joint distribution of the PCA and BPT spectral classes for S0 galaxies with $z \leq 0.1$ detected in the 4XMM-DR11 and/or CSC 2.0 catalogs.

BPT class	PCA type		
	AC	TR	PS
Star-forming	66	0	0
Seyfert	44	1	0
LINER	31	12	29
Composite	65	14	11
Unclass	13	12	104

5.2 Characterisation of radio and X-ray detections

We show in Table 4 the bivariate distribution of FIRST S0 detections in terms of the PCA and BPT spectral classes, while in Table 5 we do the same for those S0s that are X-ray emitters. Not unexpectedly, most galaxies that appear in both tables are preferentially grouped into spectral classes associated with some type of activity. In the radio domain, objects of the SF class still dominate the statistics among the BPT spectral groups, with the most noticeable change with respect to the data listed in Table 2 corresponding to the LINERs. Within this group, sources simultaneously tagged AC are clearly more abundant (by more than a 5:1 ratio) than those belonging to the PS class, thus reversing the trend observed at visible wavelengths. This major shift is largely responsible for strongly skewing the membership of the PCA spectral groups towards the AC class, which now accounts for more than 90 per cent of all detections. Although these outcomes point to a greater prevalence, in relative terms, of galaxies with nuclear activity, we would not

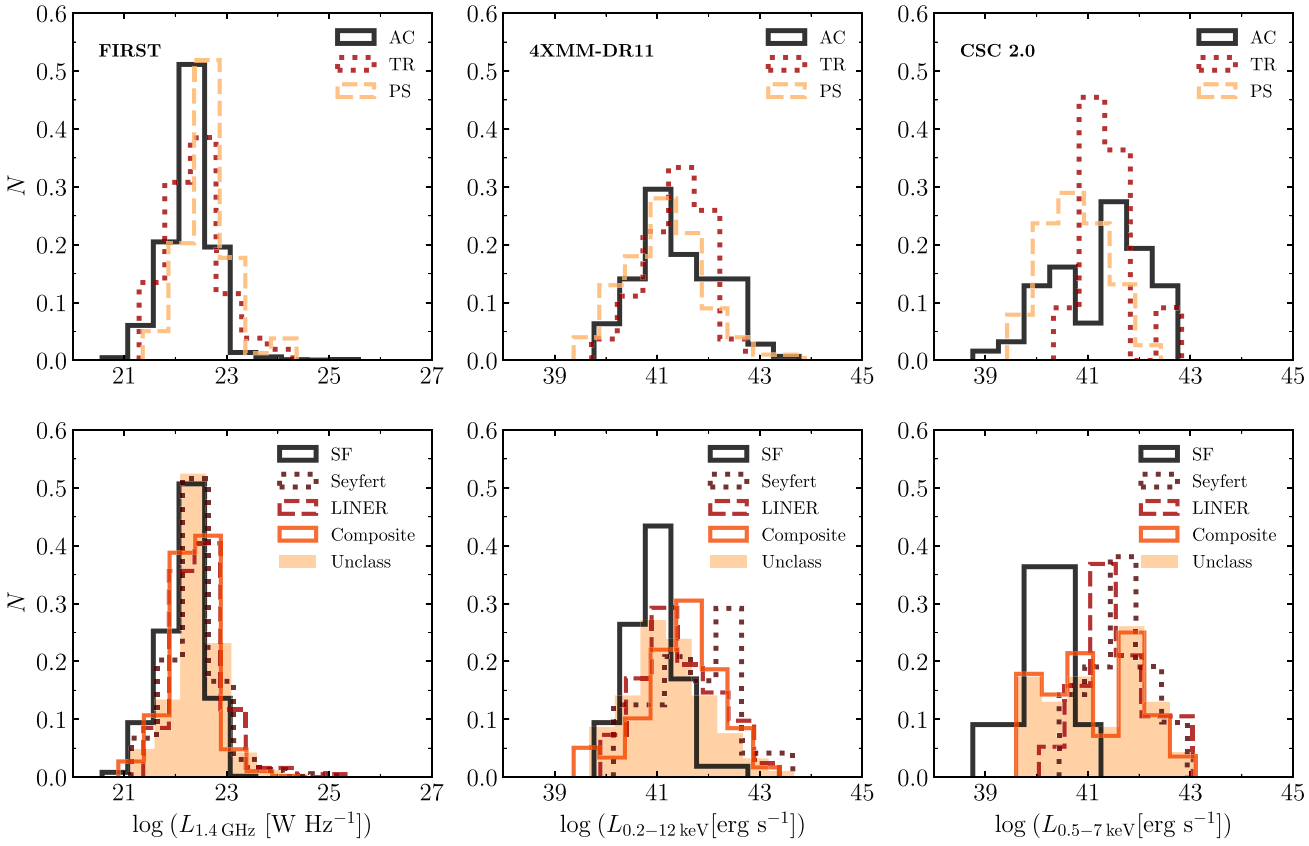

Figure 10. Radio and X-ray luminosity frequency distributions for the PCA (*top*) and BPT classes (*bottom*) of present-day S0 galaxies. The 1.4 GHz radio luminosities are inferred from the monochromatic flux integrated over the source listed in the FIRST catalog (*left*), while the X-ray luminosities have been calculated from the broad-band fluxes included in the 4XMM-DR11 (*middle*) and CSC 2.0 (*right*) catalogs. Both radio and X-ray luminosities are uncorrected for absorption; the low z of the sources also makes it unnecessary to apply rest-frame and other cosmological corrections. The height of the histograms represents the relative fraction of the members of a given spectral class in the different bins defined for each instrument in the x-axis.

be talking in any case about radio-loud AGN,[8] as can be deduced by observing that the distributions of the 1.4 GHz continuum radio luminosity of the various spectral classes reflected in the left-hand panels of Fig. 10 softly cap at $\sim 10^{23}$ W Hz^{-1}. Furthermore, the scant differences shown by these distributions could be considered to support claims that radio emission in radio-quiet AGNs is mainly due to star formation, and therefore that the radio power is also a good tracer of the SFR in galaxies of this spectral class (e.g. Bonzini et al. 2015). This automatically would imply that the vast majority of local S0–Seyferts are in hosts that are also actively forming stars; we return to this issue below.

The scarcity of sources with powerful nuclear emissions in the subset of X-ray detections is corroborated by the finding of a relatively small fraction (16.6 per cent) of galaxies whose broad-band luminosity exceeds 10^{42} erg s^{-1}, and that therefore does not seem to be solely the result of stellar processes (see the central and right-hand panels of Fig. 10). In this waveband, lenticular galaxies split quite evenly among the BPT types, something that does not happen with the PCA ones, where the AC class is again the most populated by far. Nevertheless, unlike the radio domain and despite poorer statistics, the relative frequency distribution of X-ray luminosities for this latter class shows obvious signs of bimodality arising from stark differences between the distributions corresponding to its major BPT contributors, SFs and Seyferts, which peak, respectively, around 10^{41} and 10^{42} erg s^{-1}, whereas S0–LINERs exhibit intermediate values. This dichotomy means that, irrespectively of the possibility that a substantial fraction of S0–Seyferts may reside in hosts with healthy star formation, the latter is totally insufficient to account for their X-ray emission.

5.3 Nature of the radio and X-ray emissions

In this section, we take a closer look at the source of the integrated radio and X-ray emissions of present-day lenticular galaxies. We have restricted our analysis exclusively to objects that belong to the main BPT spectral classes, since this type of classification schemes allows one to differentiate more clearly between AGN and star-formation related activity than broad-band diagnostics.

We begin by examining the distribution of the principal BPT types of our S0 galaxies in the plane of mid-IR and radio luminosities. We have applied the same strategy as Rosario et al. (2013), plotting in Fig. 11 the luminosity at 12 μm derived from the *WISE* W_3 band against the monochromatic 1.4 GHz radio power. Following these authors, we also add an eyeball straight line with positive slope across the middle of the diagram to split it into two branches or

[8]The generally low power of the sources in our sample warrants that the sizes of most of them are likely close to or below the resolution limit and therefore that their measured radio fluxes are accurate.

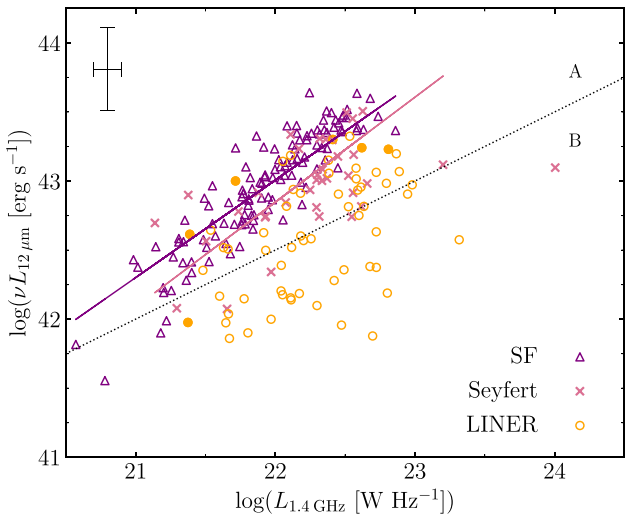

Figure 11. Observed mid-IR 12 μm luminosity versus monochromatic 1.4 GHz radio luminosity for the main BPT types of nearby S0 galaxies, SF (purple empty triangles), Seyfert (pink crosses) and LINER (orange empty circles), simultaneously detected in the SDSS, *WISE* and FIRST surveys. Filled symbols are used for the six LINERs that are also X-ray emitters. The dotted line, which divides the diagram in two sectors (letters A and B), is the same as in fig. 3 of Rosario et al. (2013). Also following these authors, we have used an ordinary-least-squares bisector algorithm to estimate the linear regression lines for the SF (purple line) and Seyferts on sector A (pink line). These lines are included in the plot for the sole purpose of allowing the mean trends of both subsets of objects to be compared at a glance. The error bars in the upper-left corner show the typical 1σ uncertainties of the data for both axes.

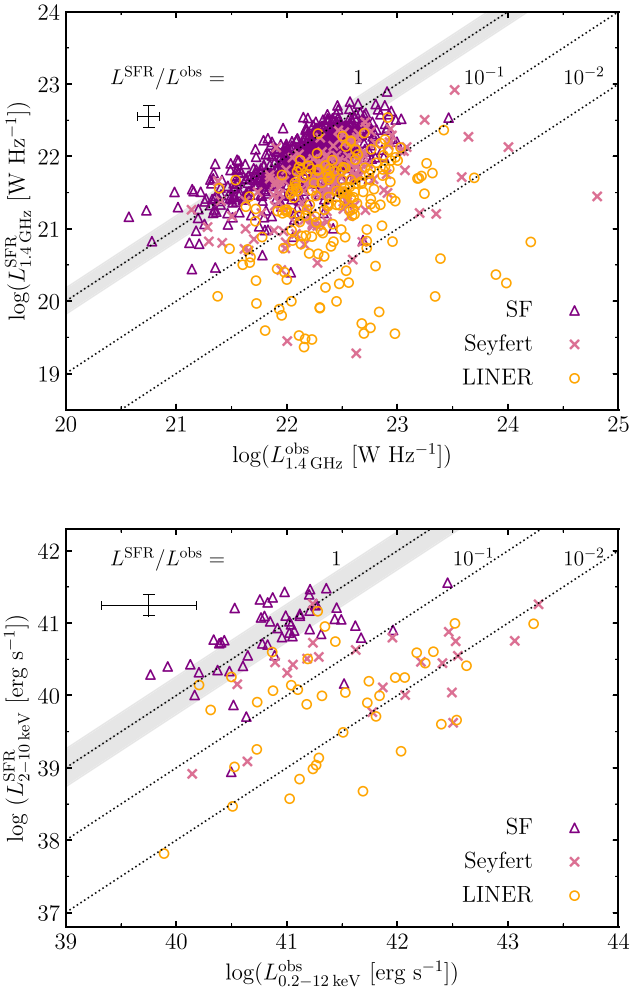

Figure 12. Monochromatic 1.4 GHz radio (*top*) and hard-band (2–10 keV) X-ray luminosities (*bottom*) predicted from the measured SFR, L^{SFR}, versus the observed values of these quantities, L^{obs} (in X-rays the broad-band $L_{0.2\text{-}12\,keV}$ is used as a proxy), for the main BPT types of nearby S0 galaxies. The SFR-calibrated radio and X-ray powers are evaluated using equations (4) and (5), respectively. The dotted lines in both panels correspond to L^{SFR}/L^{obs} of 1, 10^{-1} and 10^{-2}. The error bars displayed below the L^{SFR}/L^{obs} legends show the typical 1σ uncertainties of the data in both panels. The 1σ uncertainties of the L^{SFR} estimates are also represented by the semi transparent grey bands drawn on top of the $L^{SFR}/L^{obs} = 1$ lines. The colour and shape coding of the data points are the same as in Fig. 11.

sectors, A and B, located, respectively, above and below this divider. At this stage, it is no longer surprising to find out that our subset of S0s essentially reproduces the same basic patterns found by Rosario et al. from a considerably larger data set of narrow-line galaxies with diverse morphologies in the redshift range $0.02 < z < 0.15$ located above the K01 curve of the BPT–NII diagram. Thus, we see that the S0–Seyfert and LINER show substantially different mid-IR-to-radio properties, with the former clustering almost completely on sector A and the latter being quite evenly distributed over the diagram – except those detected in X-rays, which are mostly located in sector A. In this context, it has to be noted that the location of our Hα-weak and presumably not very dusty S0–LINER in this subspace appears difficult to explain by higher-than-average levels of AGN-heated dust in their hosts or shocks from radio jets. This makes it more plausible to think of an explanation for the radio emission of these objects linked to the diffuse UV field from post-AGB stars, although, as already stated in Section 3.3, this scenario might not apply to those LINERs with relatively high values of the [N II]/Hα flux ratio and/or that are X-ray emitters (González-Martín et al. 2009; Cazzoli et al. 2018; see also Fig. 11), which are likely powered by AGNs. For their part, the members of the SF class also lie almost exclusively on sector A, generally overlapping with the Seyferts but showing a higher coherence, as well as indications of a somewhat stronger mid-IR emission for a given radio luminosity. Although the variance in the mid-IR-to-radio properties is not statistically significant and, therefore, inconclusive regarding the connection that may exist between the radio emission of Seyferts and the SFR of their hosts, the addition of a second dimension to the radio photometry hints at the possibility that both factors may not necessarily be closely related in local S0 galaxies.

The direct calibration of the expected radio and X-ray fluxes in terms of the measured SFR confirms these suspicions. In Fig. 12, we plot for the subsets of SF, Seyfert and LINER lenticulars, the predicted monochromatic 1.4 GHz radio (top panel) and hard (2–10 keV) X-ray power (bottom panel), evaluated by replacing, respectively, in equations (4) and (5) the SFR reported in the GSWLC-2 catalog – and derived from UV-to-mid-IR SED fitting –, against the observed values of these quantities. Although these graphs are only exploratory due to the smallness and more than likely incompleteness of the samples involved, they reveal a clear displacement between SF and both Seyfert and LINER sources by about one to two orders of magnitude at a given observed luminosity. Thus, while the measured luminosity in both bands for most SF lenticulars is consistent within

the uncertainties with being essentially powered by the formation of new stars, the main contribution to the radio-continuum and X-ray emission for most of their counterparts classified as Seyfert and LINER is unrelated to star formation.

This turns out to be particularly true in the X-ray domain (bottom panel of Fig. 12), where the mean of $\log(L^{\rm SFR}/L^{\rm obs})$ for the subset of SF lenticulars is -0.089 ± 0.13 dex (95 per cent confidence interval) and the standard deviation 0.48 dex. In contrast, for the subsets of S0–Seyferts and LINERs the means are -1.4 ± 0.32 and -1.6 ± 0.25 dex, and the standard deviations 0.75 and 0.79 dex, respectively, which points to a generally very limited contribution of the SFR to the power radiated in this band by these two spectral classes. Note that only the 4XMM-DR11 data are shown in the plot, where we have approximated $L^{\rm obs}$ by the broad-band 0.2–12 keV luminosities, since there are no hard-band 2–10 keV values listed in this catalog. None the less, we have verified that restricting $L^{\rm obs}$ to the hardest band (4.5–12 keV) used in the 4XMM-DR11 data processing or approximating it by the total 0.5–7 keV band flux measured by *Chandra*'s instruments does not change our conclusions. It seems, therefore, that the intrinsic absorption and the possible thermal emission from gravitationally heated hot halo gas that can distort the SF-related X-ray emission at energies below $\lesssim 2$ keV do not introduce significant differences in the outcome of this diagnostic. This is in agreement with the finding by Ranalli, Comastri & Setti (2003) that for local star-forming galaxies the relationships between the SFR and both the hard and soft X-ray luminosities obey, in a log–log plot, linear laws with only a slight difference in the intercept.

The relationship between predicted and observed luminosities at 1.4 GHz for local S0s shown in the top panel of Fig. 12 follows a pattern very similar to that outlined by the X-ray data. Note, for example, that much as with the X-ray measurements, there are quite a few lenticulars classified as LINER in the upper panel of Fig. 12 for which the fraction of the radio luminosity attributable to the birth of new stars does not exceed one per cent at best. In this band, the estimates of the mean values, their 95 per cent confidence limits and the standard deviations of the random variable $\log(L^{\rm SFR}/L^{\rm obs})$ inferred from the subsets of SF, Seyfert and LINER lenticulars are, respectively, -0.21 ± 0.025 and 0.31 dex, -0.77 ± 0.085 and 0.55 dex, and -1.2 ± 0.11 and 0.77 dex (for these calculations we have used a linear regression model with errors in both variables).

This same test can also be easily reconverted into a diagnostic for potentially misclassified sources, by simply adopting the condition $\log(L^{\rm SFR}/L^{\rm obs}) > -0.3$ as the definition of an SF galaxy. Thus, by accounting for the uncertainties in both axes, the estimated contamination of the population of SF galaxies by sources whose observed fluxes are not actually related to stellar birth (Seyfert and LINER) is about 8 and 6 per cent in the radio and X-ray bands, respectively ($\sim$9 per cent for the X-rays had we used for $L^{\rm obs}$ the luminosity in the 4.5–12 keV band instead). Conversely, about two per cent of the radio fluxes from Seyfert and LINER sources could actually be explained by looking at their SFR, while according to the X-ray data there is a zero probability that members of these two spectral classes have been given an erroneous optical spectroscopic taxonomy. Although admittedly crude, these estimates serve to rule out that the conclusions of this work may suffer from misclassification issues.

6 SUMMARY

We have performed a comprehensive statistical study of the activity, both linked to normal stellar processes as to black hole accretion, of the S0 population in the local Universe ($z \lesssim 0.1$) on an unprecedented scale, not only with regard to the size of our sample of lenticular galaxies, the largest of its type thus far, but also by the number of energy ranges (optical, mid-IR, radio, and X-ray), and the typology (spectral and photometric) of measurements involved.

Building on the substantial data from the NASA-Sloan Atlas, we have first extensively reviewed a number of classification schemes used in the literature to divide our sample of S0 galaxies into physically motivated activity classes according to diagnostics based on specific features of their optical spectra. More specifically, we have characterised the degree and nature of activity of present-day S0 galaxies using the classification paradigm recently introduced by Tous et al. (2020), which is grounded on the PCA of the entire optical spectra, as well as the well-known BPT and WHAN diagrams, which rely on the strength of narrow emission lines. Additionally, we have harnessed the resemblance between the PCA and WHAN dividers to introduce a new activity diagnostic that combines both schemes. We have also carried out an intercomparison of various PDF from the objects belonging to the different spectral categories in order to characterise their properties (stellar mass, redshift) and gain insight on the role played by external factors (local density of neighbours) in determining membership to the different spectral classes. All this has been followed by an exploration of the origin of the mid-IR emission of the main BPT/WHAN and PCA classes in which our S0s are divided, using the photometric data from the *WISE* all-sky survey to further our knowledge on the connection between the spectroscopically-defined taxonomy and alternative, non-spectroscopic classification schemes, such as mid-IR colour–colour diagrams. Last but not least, we have used the FIRST 1.4 GHz photometry in combination with broad-band flux measurements from the *XMM–Newton* and *Chandra* observatories to investigate the interplay between the radio and X-ray luminosities of our S0 galaxies, characterise them according to the spectral type, and apply some straightforward empirical tests for the purpose of unveiling the relationship between the power emitted in these extreme wavebands and star formation.

We summarize below the main results obtained:

(i) The intercomparison of the stellar mass and redshift distributions of the various spectral classes of present-day S0 galaxies has evidenced that those with ongoing star formation tend to be less massive than the rest of their (both active and passive) counterparts, mimicking the behaviour observed in the general galaxy population. This manifestation of downsizing in the local Universe suggests that the imprint of this phenomenon could also be preserved among individual Hubble types.

(ii) We confirm previous findings that nearby S0 galaxies showing an active optical spectrum, particularly if they belong to the SF class, display a clear preference for residing in sparser environments of the local Universe, while objects with a fully passive character tend to be more abundant in crowded regions.

(iii) We have revealed the existence of strong parallels between the demarcations along the vertical axis of the WHAN diagram, based on the EW of the Hα line, and the PS/TR/AC boundaries inferred from the PCA of the entire optical spectrum recently introduced in the first paper of this series to classify S0 galaxies. The coincidence between dividers that depend on such different spectral elements emanates from the tight underlying correlation between the strength of the Hα, and other prominent nebular emission lines, and the shape of the continuum of the stellar component. This has led us to propose the replacement of the EW(Hα) in this diagram with the less-prone-to-errors distance to the PS ridge in the PC1–PC2 plane, adding robustness to the classification without altering the results.

(iv) The *WISE* mid-IR colours of our sample of nearby S0s validate their narrow-line and broad-band optical spectroscopic classifications. We have found that $W_2 - W_3$ is closely related to the distance to the MS of galaxies. This, and the substantial differences observed in the spatial distributions of the various spectral classes in *WISE* colour–colour plots, lend support to the idea that different physical mechanisms take part in their classification. The IR emission of local S0s also appears to rule out the existence of a sizeable fraction of obscured AGNs within this population, shows that members of the weakly active LINER and TR classes are preferentially located in the IRTZ, and, for the objects included in the Seyfert class, does not seem to be predominantly driven by star formation.

(v) The active members of our S0 sample faithfully replicate the markedly different trends followed in the mid-IR radio plane by LINER galaxies of all morphologies relative to their SF and Seyfert counterparts. The fact that such a strong segregation is maintained by the presumably gas- and dust-poor LINER lenticulars suggests that at least one part of the members of this class is neither illuminated by new stars nor by AGNs. Instead, the emission lines of these objects are probably generated by the diffuse UV field of evolved stars, as proposed by Cid Fernandes et al. (2011) and Singh et al. (2013), among others.

(vi) Several lines of evidence, among them, the calibration of the radio and X-ray integral luminosities of the active members of our S0 sample associated with their global SFRs published in the literature, indicate that in most of the current S0 classified as LINER, but also in much of those belonging to the Seyfert class, star birth is not driving their emission in these extreme wavebands. This finding seems to contradict previous claims (Bonzini et al. 2015) that radio luminosity in radio-quiet AGNs is mainly due to star-forming-heated emission, and therefore that the radio power is also a good tracer for the SFR of this type of galaxies. We note, however, that in this particular work the galaxy sample used is very different from ours, as it is dominated by systems with $z \sim 1 \div 2$, a time when the volume-averaged cosmic SFR was at its peak (e.g. Madau & Dickinson 2014). Thus, the discrepancy could simply mean that such an assertion cannot be extrapolated to galaxies in the local Universe.

Further confirmation of all these results may come from multi-wavelength studies working with a single galaxy sample made up of objects detected simultaneously in different energy ranges. This is something utterly impossible to do with the current data, since after applying to our baseline S0 data set all the quality filters established for each one of the four wavebands investigated, we are left with less than 10 sources verifying all constraints, a number totally insufficient to draw any valid conclusion. Finally, we want to highlight that the significant overlap between the spectral properties of current S0 galaxies and those of earlier and later morphologies, as well as the remarkable similarities that, as we have been emphasizing, show their respective spatial distributions in the different types of diagrams analysed, suggest that many of the findings of this work are exportable to other Hubble types.

ACKNOWLEDGEMENTS

We wish to thank an anonymous referee for his/her thorough review of the manuscript, which has helped us improve the presentation of the contents and better emphasize the results. We acknowledge financial support from the Spanish state agency MCIN/AEI/10.13039/501100011033 and by 'ERDF A way of making Europe' funds through research grants PID2019–106027GB–C41 and PID2019–106027GB–C43. MCIN/AEI/10.13039/501100011033 has also provided additional support through the Centre of Excellence Severo Ochoa's award for the Instituto de Astrofísica de Andalucía under contract SEV–2017–0709 and the Centre of Excellence María de Maeztu's award for the Institut de Ciències del Cosmos at the Universitat de Barcelona under contract CEX2019–000918–M. JLT acknowledges financial support by the PRE2020–091838 grant from MCIN/AEI/10.13039/501100011033 and by 'FSE Invests in your future'. We are also grateful to all the people involved in the gathering, reduction, and processing of the data sets listed in the Data Availability Statement below, as well as the public and private institutions that have provided the necessary funding, resources and technical support to make possible both the relevant surveys and the release of their measurements to the community. We equally acknowledge the use of the TOPCAT software package (written by Mark Taylor, University of Bristol) in the testing of the data from the various catalogs.

DATA AVAILABILITY

This research has made prominent use of the following databases in the public domain: the NASA-Sloan Atlas at http://nsatlas.org/, the Morphological catalog for SDSS galaxies at https://cdsarc.cds.unistra.fr/viz-bin/cat/J/MNRAS/476/3661, the Portsmouth Stellar Kinematics and Emission Line Fluxes at https://data.sdss.org/sas/dr12/boss/spectro/redux/galaxy/v1_1/, the AllWISE Data Release at https://wise2.ipac.caltech.edu/docs/release/allwise/, the FIRST Survey Catalog at http://sundog.stsci.edu/first/catalogs/readme.html, the 4XMM–DR11 at http://xmmssc.irap.omp.eu/Catalogue/4XMM-DR11/4XMM_DR11.html, as well as the Chandra Source Catalog Release 2.0 at https://cxc.cfa.harvard.edu/csc/.

REFERENCES

Alatalo K., Cales S. L., Appleton P. N., Kewley L. J., Lacy M., Lisenfeld U., Nyland K., Rich J. A., 2014, ApJ, 794, L13
Assef R. J. et al., 2013, ApJ, 772, 26
Baldwin J. A., Phillips M. M., Terlevich R., 1981, PASP, 93, 5
Barway S., Wadadekar Y., Vaghmare K., Kembhavi A. K., 2013, MNRAS, 432, 430
Baskin A., Laor A., 2005, MNRAS, 358, 1043
Becker R. H., White R. L., Helfand D. J., 1995, ApJ, 450, 559
Bell E. F., 2003, ApJ, 586, 794
Best P. N., Kauffmann G., Heckman T. M., Ivezić Ž., 2005, MNRAS, 362, 9
Blanton M. R., Kazin E., Muna D., Weaver B. A., Price-Whelan A., 2011, AJ, 142, 31
Bonzini M. et al., 2015, MNRAS, 453, 1079
Borlaff A. et al., 2014, A&A, 570, A103
Boselli A. et al., 2011, A&A, 528, A107
Cappellari M. et al., 2011, MNRAS, 416, 1680
Cazzoli S. et al., 2018, MNRAS, 480, 1106
Chen Z., He Z., Ho L. C., Gu Q., Wang T., Zhuang M., Liu G., Wang Z., 2022, Nature Astron., 6, 339
Cid Fernandes R., Stasińska G., Schlickmann M. S., Mateus A., Vale Asari N., Schoenell W., Sodré L., 2010, MNRAS, 403, 1036
Cid Fernandes R., Stasińska G., Mateus A., Vale Asari N., 2011, MNRAS, 413, 1687
Cluver M. E. et al., 2014, ApJ, 782, 90
Coccato L. et al., 2020, MNRAS, 492, 2955
Colless M. et al., 2001, MNRAS, 328, 1039
Comerford J. M. et al., 2009, ApJ, 698, 956
Condon J. J., 1992, ARA&A, 30, 575
Connolly A. J., Szalay A. S., Bershady M. A., Kinney A. L., Calzetti D., 1995, AJ, 110, 1071

Couch W. J., Ellis R. S., Sharples R. M., Smail I., 1994, ApJ, 430, 121
Couch W. J., Barger A. J., Smail I., Ellis R. S., Sharples R. M., 1998, ApJ, 497, 188
Crocker A. F., Bureau M., Young L. M., Combes F., 2011, MNRAS, 410, 1197
Davies R. I. et al., 2017, MNRAS, 466, 4917
de Vaucouleurs G., 1977, in Tinsley B. M., Larson Richard B., Gehret D. C., eds, Evolution of Galaxies and Stellar Populations. Yale University Observatory, New Haven, p. 43
Deeley S. et al., 2020, MNRAS, 498, 2372
Deeley S., Drinkwater M. J., Sweet S. M., Bekki K., Couch W. J., Forbes D. A., Dolfi A., 2021, MNRAS, 508, 895
Diamond-Stanic A. M., Rieke G. H., Rigby J. R., 2009, ApJ, 698, 623
Domínguez-Sánchez H., Huertas-Company M., Bernardi M., Tuccillo D., Fischer J. L., 2018, MNRAS, 476, 3661
Domínguez-Sánchez H., Bernardi M., Nikakhtar F., Margalef-Bentabol B., Sheth R. K., 2020, MNRAS, 495, 2894
Dressler A. et al., 1997, ApJ, 490, 577
Dressler A., 1980, ApJ, 236, 351
Eliche-Moral M. C., Rodríguez-Pérez C., Borlaff A., Querejeta M., Tapia T., 2018, A&A, 617, A113
Evans I. N. et al., 2020, in Bulletin of the American Astronomical Society (Meeting Abstracts #235), vol. 52. p. 154.05
Fasano G., Poggianti B. M., Couch W. J., Bettoni D., Kjærgaard P., Moles M., 2000, ApJ, 542, 673
Feldmann R., 2017, MNRAS, 470, L59
Fraser-McKelvie A., Aragón-Salamanca A., Merrifield M., Tabor M., Bernardi M., Drory N., Parikh T., Argudo-Fernández M., 2018, MNRAS, 481, 5580
Giovanelli R. et al., 2005, AJ, 130, 2598
Giovanelli R., Haynes M. P., Chincarini G. L., 1986, ApJ, 300, 77
Gkini A., Plionis M., Chira M., Koulouridis E., 2021, A&A, 650, A75
González-Martín O., Masegosa J., Márquez I., Guainazzi M., Jiménez-Bailón E., 2009, A&A, 506, 1107
Goto T., Yamauchi C., Fujita Y., Okamura S., Sekiguchi M., Smail I., Bernardi M., Gomez P. L., 2003, MNRAS, 346, 601
Gunn J. E., Gott J. R. III, 1972, ApJ, 176, 1
Gürkan G., Hardcastle M. J., Jarvis M. J., 2014, MNRAS, 438, 1149
Haardt F., Maraschi L., 1991, ApJ, 380, L51
Herpich F., Mateus A., Stasińska G., Cid Fernandes R., Vale Asari N., 2016, MNRAS, 462, 1826
Hickox R. C., Alexander D. M., 2018, ARA&A, 56, 625
Houghton R. C. W., 2015, MNRAS, 451, 3427
Ho L. C., 2008, ARA&A, 46, 475
Hubble E. P., 1936, Realm of the Nebulae. Yale University Press, New Haven and London, p. 1–207
Huchra J. P., Geller M. J., Corwin Harold G. J., 1995, ApJS, 99, 391
Jansen F. et al., 2001, A&A, 365, L1
Jarrett T. H. et al., 2011, ApJ, 735, 112
Jones D. H. et al., 2004, MNRAS, 355, 747
Kauffmann G. et al., 2003, MNRAS, 346, 1055
Kauffmann G., Heckman T. M., 2009, MNRAS, 397, 135
Kaviraj S. et al., 2007, ApJS, 173, 619
Kellermann K. I., Condon J. J., Kimball A. E., Perley R. A., Ivezić Ž., 2016, ApJ, 831, 168
Kewley L. J., Dopita M. A., Sutherland R. S., Heisler C. A., Trevena J., 2001, ApJ, 556, 121
Kewley L. J., Groves B., Kauffmann G., Heckman T., 2006, MNRAS, 372, 961
LaMassa S. M., Heckman T. M., Ptak A., Hornschemeier A., Martins L., Sonnentrucker P., Tremonti C., 2009, ApJ, 705, 568
Li C., Kauffmann G., Wang L., White S. D. M., Heckman T. M., Jing Y. P., 2006, MNRAS, 373, 457
Madau P., Dickinson M., 2014, ARA&A, 52, 415
Mapelli M., Rampazzo R., Marino A., 2015, A&A, 575, A16
Maschmann D., Melchior A.-L., 2019, A&A, 627, L3
Maschmann D., Melchior A.-L., Mamon G. A., Chilingarian I. V., Katkov I. Y., 2020, A&A, 641, A171
Mateos S., Alonso-Herrero A., Carrera F. J., Blain A., Severgnini P., Caccianiga A., Ruiz A., 2013, MNRAS, 434, 941
Moore B., Katz N., Lake G., Dressler A., Oemler A., 1996, Nature, 379, 613
Morganti R. et al., 2006, MNRAS, 371, 157
Nelson D. et al., 2019, Comput. Astrophys. Cosmol., 6, 1
Orellana G. et al., 2017, A&A, 602, A68
Overzier R. A., Röttgering H. J. A., Rengelink R. B., Wilman R. J., 2003, A&A, 405, 53
Persic M., Rephaeli Y., 2007, A&A, 463, 481
Poggianti B. M., Smail I., Dressler A., Couch W. J., Barger A. J., Butcher H., Ellis R. S., Oemler Augustus J., 1999, ApJ, 518, 576
Popesso P. et al., 2019, MNRAS, 483, 3213
Postman M., Geller M. J., 1984, ApJ, 281, 95
Querejeta M. et al., 2015, A&A, 579, L2
Radcliffe J. F., Barthel P. D., Thomson A. P., Garrett M. A., Beswick R. J., Muxlow T. W. B., 2021, A&A, 649, A27
Ranalli P., Comastri A., Setti G., 2003, A&A, 399, 39
Renzini A., Peng Y.-J., 2015, ApJ, 801, L29
Rosario D. J., Burtscher L., Davies R., Genzel R., Lutz D., Tacconi L. J., 2013, ApJ, 778, 94
Salim S., Boquien M., Lee J. C., 2018, ApJ, 859, 11
Satyapal S., Vega D., Dudik R. P., Abel N. P., Heckman T., 2008, ApJ, 677, 926
Satyapal S., Secrest N. J., McAlpine W., Ellison S. L., Fischer J., Rosenberg J. L., 2014, ApJ, 784, 113
Schwartz D. A., 2004, Int. J. of Modern Phys. D, 13, 1239
Singh R. et al., 2013, A&A, 558, A43
Spitzer L. Jr, Baade W., 1951, ApJ, 113, 413
Stasińska G. et al., 2008, MNRAS, 391, L29
Stasińska G., Cid Fernandes R., Mateus A., Sodré L., Asari N. V., 2006, MNRAS, 371, 972
Stasińska G., Costa-Duarte M. V., Vale Asari N., Cid Fernandes R., Sodré L., 2015, MNRAS, 449, 559
Stern D. et al., 2012, ApJ, 753, 30
Strauss M. A. et al., 2002, AJ, 124, 1810
Suh H. et al., 2019, ApJ, 872, 168
Suzuki T. L. et al., 2016, MNRAS, 462, 181
Thomas D. et al., 2013, MNRAS, 431, 1383
Tous J. L., 2018, Master's thesis, Dipòsit Digital de la Universitat de Barcelona
Tous J. L., Solanes J. M., Perea J. D., 2020, MNRAS, 495, 4135
Treu T., Ellis R. S., Kneib J.-P., Dressler A., Smail I., Czoske O., Oemler A., Natarajan P., 2003, ApJ, 591, 53
Trouille L., Barger A. J., 2010, ApJ, 722, 212
Vattakunnel S. et al., 2012, MNRAS, 420, 2190
Webb N. A. et al., 2020, A&A, 641, A136
Welch G. A., Sage L. J., 2003, ApJ, 584, 260
Wright E. L. et al., 2010, AJ, 140, 1868
Xiao M.-Y., Gu Q.-S., Chen Y.-M., Zhou L., 2016, ApJ, 831, 63
Xu K., Gu Q., Lu S., Ge X., Xiao M., Contini E., 2022, MNRAS, 509, 1237
York D. G. et al., 2000, AJ, 120, 1579
Yun M. S., Reddy N. A., Condon J. J., 2001, ApJ, 554, 803
Zamfir S., Sulentic J. W., Marziani P., 2008, MNRAS, 387, 856
Zewdie D., Pović M., Aravena M., Assef R. J., Gaulle A., 2020, MNRAS, 498, 4345

SUPPORTING INFORMATION

Supplementary data are available at *MNRAS* online.

PCA_TSP20.txt

Please note: Oxford University Press is not responsible for the content or functionality of any supporting materials supplied by the authors. Any queries (other than missing material) should be directed to the corresponding author for the article.

Table A1. Mean optical spectrum and first five eigenspectra inferred from S0 galaxies with $z \leq 0.1$.

Wavelength [Å]	Mean flux	First eigenspectum	Second eigenspectrum	Third eigenspectrum	Fourth eigenspectrum	Fifth eigenspectrum
3900.3	0.54156	0.02360	−0.00375	−0.01112	−0.02274	−0.03610
3901.2	0.54442	0.02451	−0.00393	−0.01197	−0.02397	−0.03791
3902.1	0.54509	0.02537	−0.00439	−0.01228	−0.02550	−0.04051
3903.0	0.54257	0.02606	−0.00448	−0.01267	−0.02605	−0.04073
3903.9	0.53638	0.02635	−0.00409	−0.01282	−0.02631	−0.04276

Note. This is a sample table consisting of the first 5 rows of data. A machine-readable version of the full table is available online at the CDS website.

APPENDIX A: MEAN OPTICAL SPECTRUM AND MAIN EIGENSPECTRA FROM NEARBY S0 GALAXIES

A data set of N SDSS galaxy spectra can be thought of as a set of flux vectors, $\boldsymbol{f}_i$, in a space of ~ 3800 dimensions or (vacuum) wavelength intervals. Each one of these vectors can be expressed exactly as the sum of a vector of mean fluxes, $\langle \boldsymbol{f} \rangle$, and a linear combination of M orthonormal vectors or eigenspectra, $\boldsymbol{e}_j$, that account for all the variability around the mean, in the form (e.g. Connolly et al. 1995):

$$\boldsymbol{f}_i = \langle \boldsymbol{f} \rangle + \sum_{j=1}^{M} \mathrm{PC}j_i \, \boldsymbol{e}_j \qquad 1 \leq i \leq N, \tag{A1}$$

where the coefficients $\mathrm{PC}j_i \equiv \boldsymbol{f}_i \cdot \boldsymbol{e}_j$ are the projections of each individual spectrum on the new base of principal components, which are arranged in decreasing order of their relative power, i.e. of the amount of the total variance of the data that they explain. Thus, when the main variance of a data set lies in a low-dimensional space, one can get a good visualization of it by truncating the above expansion to the first few eigenvectors. In the present case, we showed in Paper I that near 90 per cent of the sample variance lies in the 2D subspace where we carry out our spectral classification and whose axes are the first two eigenspectra. This is a huge reduction in data size, with a modest loss of information. For those interested in applying this sort of dimensionality reduction to the SDSS galaxy spectra, we provide in Table A1 the mean spectrum and first five eigenspectra inferred from our sample of processed[9] extinction-corrected SDSS spectra of nearby S0 galaxies, with which one can explain more than 96 per cent of the variation in the sample.

[9]As detailed in section 3 of Paper I, to remove any extrinsic source of variability it is necessary to put all the original spectra on an equal basis while preserving their shapes by shifting them to the laboratory rest-frame, and re-binning and normalizing their fluxes.

This paper has been typeset from a TEX/LATEX file prepared by the author.

Part II

INSIGHTS FROM INTEGRAL FIELD SPECTRA

4

STAR-FORMING RINGS

The publications of this part, present the extension of the methodology developed in Tous et al. (2020) to study the spatial distribution of activity in lenticular galaxies. In MaNGA, spectra are obtained with two identical dual-beam BOSS spectrographs, which are an upgraded version of the SDSS' original ones, covering a similar wavelength range with essentially the same resolving power (Smee et al. 2013). Therefore, extending our classification to these data is a natural step.

In Tous et al. (2023), we examine spatially resolved spectroscopic maps in a sample of more than 500 S0 galaxies drawn from MaNGA-DR15 discovering the existence of inner ($\langle R \rangle \sim 1\,R_e$) annular structures betraying ongoing star formation in a good number of these objects ($\sim 30\%$). We study the relation between these, and other, activity patterns – as traced by maps of EW and luminosity in Hα and D4000 spectral index – and the properties of their hosts, including the sign of the radial activity gradient measured within $1.5\,R_e$. The catalogue of ringed S0 galaxies studied in this work (Appendix B), constitutes the largest collection of these objects ever identified using IFS maps.

Gradients are obtained by stacking each galaxy's spaxels into radial bins to determine the spectral profile (i.e., mean flux as a function of galactocentric distance), which is then projected into the plane PC1–PC2. Relying on the linear behaviour exhibited by most of the profiles in such a plane, we further condense the spectral information by replacing the profiles by best-fitting vectors whose orientation indicates the sign of the activity gradient in the galaxies.

SF rings are mostly found in galaxies with a negative activity gradient. The abundance of these rings increases with the mass of their hosts but is uncorrelated with the environment and, although they are present in galaxies of the two main spectral classes, rings are found to be twice as frequent in PS- than in AC-S0s . In agreement with cosmological hydrodynamic simulations from the literature, we attribute these SF rings to mergers but, to explain their lack of correlation with the environment, we conclude that they are possibly associated with annular disc resonances driven by "mini mergers". Such an interaction involves the capture by a S0 of a tiny satellite strongly bound to the lenticular because, otherwise, it could not take place within a galaxy cluster. The fact that the Hα emission in the rings of the AC-S0s is about four times greater than that of the members of the PS class, and that they are mostly coplanar structures, implies that rings should feed mainly on residual gas from their hosts.

The Astrophysical Journal, 942:48 (13pp), 2023 January 1 https://doi.org/10.3847/1538-4357/aca484

The Origin of Star-forming Rings in S0 Galaxies

J. L. Tous[1], H. Domínguez-Sánchez[2,3], J. M. Solanes[1], and J. D. Perea[4]
[1] Departament de Física Quàntica i Astrofísica i Institut de Ciències del Cosmos (ICCUB), Universitat de Barcelona. Martí i Franquès 1, E-08028 Barcelona, Spain
jtous@fqa.ub.edu
[2] Centro de Estudios de Física del Cosmos de Aragón (CEFCA), Plaza San Juan, 1, 44001, Teruel, Spain
[3] Instituto de Ciencias del Espacio (ICE-CSIC), Campus UAB. Can Magrans s/n, E-08193 Barcelona, Spain
[4] Instituto de Astrofísica de Andalucía (IAA-CSIC). Glorieta de la Astronomía s/n, E-18008 Granada, Spain
Received 2022 July 25; revised 2022 November 2; accepted 2022 November 16; published 2023 January 10

Abstract

Spatially resolved integral field spectroscopic maps in a sample of 532 S0 galaxies from the MaNGA survey have unveiled the existence of inner rings ($\langle R\rangle \sim 1\,R_e$) betraying ongoing star formation in a number of these objects. Activity gradients averaged over bins of galactocentric radius up to $\sim$1.5 R_e have been measured in the subspace defined by the first two principal components of the optical spectra of these galaxies. We find that the sign of the gradients is closely related to the presence of such rings in the spectral maps, which are especially conspicuous in the equivalent width of the Hα emission line, EW(Hα), with a fractional abundance—21%–34%—notably larger than that inferred from optical images. While the numbers of S0s with positive, negative, and flat activity gradients are comparable, star-forming rings are largely found in objects for which quenching proceeds from the inside out, in good agreement with predictions from cosmological simulations studying S0 buildup. Assessment of these ringed structures indicates that their frequency increases with the mass of their hosts, that they have shorter lifetimes in galaxies with ongoing star formation, that they may feed on gas from the disks, and that the local environment does not play a relevant role in their formation. We conclude that the presence of inner rings in EW(Hα) is a common phenomenon in fully formed S0s, possibly associated with annular disk resonances driven by weakly disruptive mergers preferentially involving a relatively massive primary galaxy and a tiny satellite strongly bound to the former.

Unified Astronomy Thesaurus concepts: Lenticular galaxies (915); Galaxy spectroscopy (2171); Galaxy structure (622); Galaxy evolution (594)

Supporting material: figure set

1. Introduction

Galaxies of Hubble type S0 (also known as lenticulars) are a heterogeneous population with a wide range of physical properties. They are also the only morphological class that is abundant in both low- and high-density environments, suggesting that different physical mechanisms participate in their formation (e.g., Wilman & Erwin 2012). In recent years, it has become clear, through observations and both semianalytical and numerical modeling, that minor mergers of a disk galaxy with a gas-rich satellite or even major mergers between star-forming (SF) spirals taking place in the field or in small galaxy groups can result in lenticular remnants with a strong structural bulge–disk coupling (Bernardi et al. 2011; Prieto et al. 2013; Querejeta et al. 2015; Tapia et al. 2017; Eliche-Moral et al. 2018; Maschmann et al. 2020). Conversely, there is also the more conventional formation pathway related to dense environments that involves the removal of the intragalactic gas through hydrodynamic processes that, with the help of other mechanisms such as harassment or strangulation (Larson et al. 1980; Nulsen 1982; Moore et al. 1999), is capable of transforming spiral disks infalling into large galaxy aggregations—usually as part of a group—into stellar systems with a lenticular structure (Solanes & Salvador-Sole 1992; Dressler et al. 1997; Fasano et al. 2000; Quilis et al. 2000; Crowl & Kenney 2008; Poggianti et al. 2009; D'Onofrio et al. 2015).

The defining characteristic of S0 galaxies within the disk-galaxy family is the absence of visible spiral arms. However, these objects can show other kinds of dynamical instabilities, such as bars and rings. But just as S0 is the disk-galaxy class where the former features are less abundant and weaker (Aguerri et al. 2009; Wilman & Erwin 2012), the same is not true for galaxy-scale rings, whose fractional abundance is larger among early-type disks, as shown for instance in the statistical study of stellar rings in present-day galaxies by Comerón et al. (2014) based on near-infrared data (see also Fernandez et al. 2021). This negative trend between the frequencies of the two types of transient structural components linked to host morphology, as well as the finding by these and other authors that rings are only partially favored in barred galaxies and not necessarily aligned with bars, suggests that bars and rings may not always be intimately connected, leading to the idea that perhaps not all in-plane rings are disk instability phenomena that originated in bar resonances (Athanassoula et al. 1982; Buta & Combes 1996).

Another relatively novel aspect unveiled by recent studies of S0 galaxies is the finding that they show a duality in their physical properties (Xiao et al. 2016; Fraser-McKelvie et al. 2018; Domínguez-Sánchez et al. 2020). This has been put on firm ground by the statistical analysis of the integrated optical spectra of a sample of more than 68,000 present-day ($z \lesssim 0.1$) lenticulars carried out by Tous et al. (2020; hereafter TSP20) using data from the Sloan Digital Sky Survey (Alam et al. 2015, SDSS-III). The principal component analysis (PCA) of

the SDSS spectra demonstrated that in the PC1–PC2 plane of the first two principal components (PCs) S0 galaxies can be grouped into two main activity classes, named the passive sequence (PS) and the active cloud (AC), separated by a slim dividing zone that constitutes the transition region (TR). Thus, although the majority of the local S0 population belongs to the PS, which conforms to the traditional conception of these objects as quiescent galaxies, approximately the quarter of those found in the AC may show star formation rates (SFRs) and spectral characteristics comparable to those measured in late spirals. This diversity of properties exhibited by S0 galaxies is an expected result in objects that follow the aforementioned multiplicity of formation channels (see also Welch & Sage 2003; Morganti et al. 2006; Crocker et al. 2011; Barway et al. 2013; Deeley et al. 2020). Interestingly, high-resolution far-UV imaging of early-type galaxies from the Hubble Space Telescope/Advanced Camera for Surveys shows that in S0 galaxies with strong UV excess the UV emission is frequently organized in concentric ring- or arm-like structures (Salim and Rich 2010; Salim et al. 2012).

In this work, we apply the same PCA technique of TSP20 to study the spatially resolved optical spectra of a sample of 532 galaxies representative of the local S0 population drawn from the integral field spectroscopic (IFS) survey Mapping Nearby Galaxies at Apache Point Observatory (MaNGA, Bundy et al. 2015; Section 2), with a focus on aspects related to their star formation activity. In Section 4 we provide a way to typify the radial spectral profiles of these objects that in Section 3 are synthesized in the PC1–PC2 subspace, which facilitates their subsequent analysis. The intercomparison of the systematized spectral profiles and several spatially resolved spectral indicators sensitive to the distribution of the dense interstellar gas and the mean age of the stellar component reveals in Section 5 that the typology of the radial gradients of activity in S0 galaxies is closely linked to the presence of SF rings. Aided by this finding and the behavior shown by the fraction of S0 galaxies hosting rings in the equivalent width of Hα emission, EW(Hα), with the global properties of stellar mass and environmental density (Section 6), we postulate in Section 7 that these SF annuli are transient structures mostly driven by scarcely disruptive mergers with tiny mass ratios that could well be significantly less than 1:10. This and other important outcomes of this work are summarized in Section 8. The manuscript also includes two appendices. In Appendix A, we provide a short outline of the PCA methodology and the resulting spectral classes, while in Appendix B, we present the montages of optical images and spectral maps for S0 galaxies with linear PC1–PC2 radial profiles that are published in the online version of the paper, emphasizing those objects harboring an unequivocal ring in the EW(Hα) map. We note that the relatively large number of systems studied, combined with the high rate of detection of SF rings, makes this S0 sample from MaNGA the largest collection of ringed galaxies ever identified in the local universe by spectroscopic observations.

All cosmology-dependent quantities used in the paper assume a flat concordant ΛCDM universe with parameters $H_0 = 70$ km s^{-1} Mpc^{-1} and $\Omega_m = 1 - \Omega_\Lambda = 0.3$.

2. Sample Selection

We use data from the Fifteenth Data Release of the Sloan Digital Sky Surveys (Aguado et al. 2019), which includes the first 4621 MaNGA data cubes on unique galaxies, from the ~10,000 initially planned. This survey provides spatially resolved spectroscopic information on a statistically representative sample of nearby ($\tilde{z} \sim 0.03$) galaxies out to about 1.5 effective radii in the r band, R_e, over the bandpass 3600–10000 Å with a spectral resolving power $R = \lambda/\mathrm{FWHM} \sim 2000$ (Smee et al. 2013) and a spatial resolution of ~1 kpc at the median redshift $\tilde{z}$ of the observations. With the only exception of the total stellar mass M_*, for which we use the estimates listed in the GALEX–SDSS–WISE Legacy Catalog 2 (Salim et al. 2018) derived from UV-to-mid-IR spectral energy distribution fitting, we rely on the physical parameters from the continuum and ionized emission lines provided by the Data Analysis Pipeline (DAP) of MaNGA (Westfall et al. 2019). With them, we build for the target galaxies resolved maps of the flux intensity and EW of their Hα line emission, which in SF galaxies inform, respectively, on the spatial distribution of the ionized gas tracing instantaneous star formation activity and on the specific star formation rate (SSFR), as well as maps of the break at 4000 Å, D4000, which is a proxy for the age of the stellar component and therefore also probes star formation but on longer timescales. Details of the emission-line measurements by the DAP can be found in Westfall et al. (2019). In short, the spaxels are Voronoi binned to reach a signal-to-noise ratio (S/N) of at least 10, and kinematic measurements, including the line-of-sight velocity,[5] are computed. In this work we use the hybrid Voronoi binned maps, HYB10, for which emission-line and spectral-index measurements are performed on the individual spaxels, after subtracting the best-fitting stellar continuum. Likewise, we have retrieved the radius, derived from the semimajor-axis elliptical polar coordinates, in units of the effective radius of the galaxies reported by the NASA-Sloan Atlas catalog (Blanton et al. 2011), $R' = R/R_e$. Throughout this work, we use MARVIN (Cherinka et al. 2019) as a tool to access and manipulate all MaNGA data.

Lenticulars are identified using the deep learning-based morphological classification of Fischer et al. (2019), founded on the methodology detailed in Domínguez-Sánchez et al. (2018), who provide this information for MaNGA galaxies in terms of two parameters: a numerical Hubble stage, T, and the probability, P_{S0}, that an early-type-looking object is truly an S0. After imposing $T \leqslant 0$ and $P_{S0} > 0.7$, we are left with a sample of 648 galaxies that reduce to 532 bona fide S0s, once we remove the problematic cases flagged by the MaNGA data reduction pipeline, as well as those galaxies for which we have detected, after a stringent visual inspection of the SDSS images, a hint of spiral structure, and/or contaminating foreground stars, companion galaxies, or both within MaNGA's field of view.

The PCA-based classification (see Appendix A for details of this methodology) of the selected galaxies has been inferred by cross-matching them with the single-fiber spectral sample of S0 defined in TSP20, while the few objects without a counterpart in this data set have been classified from scratch using the first two PCs of their single-fiber SDSS spectra. This exercise shows that our MaNGA S0 sample has 343 galaxies that are PS members and 150 that belong to the AC. The number of TR objects (39) is not large enough to perform a statistically significant analysis separately for this group, so from now on we will include them under the AC designation, since the behavior of their EW(Hα) profiles is more

[5] The DAP uses a stellar-template library constructed by hierarchically clustering the MILES stellar library (Falcón-Barroso et al. 2011) into a set of 42 composite spectra, termed the MILESHC library, to measure the stellar kinematics; only the first two velocity moments (v and σ_v) are provided.

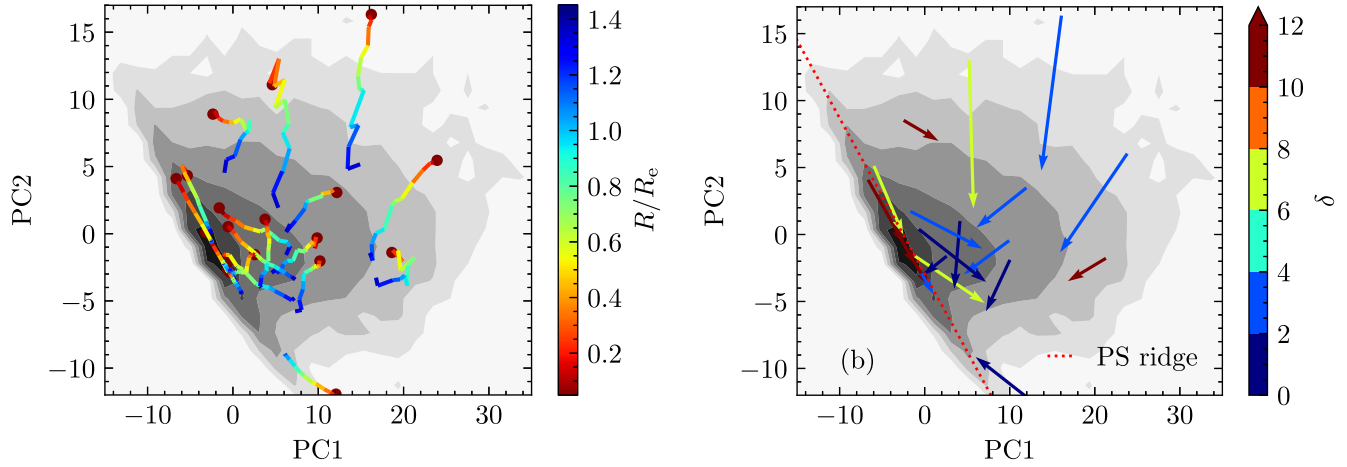

Figure 1. Left: radial profiles of a random subset of S0 galaxies in the subspace defined by the first two PCs of the entire sample. The composite spectra in each radial bin are colored according to the galactocentric distance scaled by the effective radius of the galaxies, with brown dots indicating the position of the central (innermost) bins. Right: vectorization of the spectral profiles. The colors show the value of δ, one of the two parameters used to evaluate its feasibility (see text). The brown arrows identify profiles with $\delta \geqslant 10$, unsuitable for vectorization. The red dotted straight line shows the location of the PS ridge. In both panels, the background grayscale contours represent equally spaced logarithmic densities drawn from the sample of ∼68,000 nearby ($z \lesssim 0.1$) lenticulars explored in TSP20.

similar to that shown by the members of this activity class than that of PS-type objects (see Section 4).

3. Data Cube Processing

To avoid the complications inherent in handling the relatively large number of spaxels in each data cube and the disparity in their areal coverages—the MaNGA integral field units (IFUs) are bundles of between 19 and 127 fibers to optimize the match with the apparent sizes of target galaxies—we choose to stack those with $S/N > 5$ into circularized radial bins in the dimensionless variable R' within the interval [0, 1.5]. Before we proceed with the stacking, the spectra are corrected for Galactic extinction and cleaned from masked regions, glitches, and sky lines, discarding those in which these regions represent more than 10% of the flux array. We also remove the recessional velocity of each galaxy and the mean rotation speed from each spaxel. Finally, we normalize the spectra using Equation [3] from TSP20 and weight them by the S/N of the continuum to generate the mean spectrum of each radial bin, provided that more than 20% of the spaxels in that bin have a spectrum that fulfills the aforementioned quality conditions.

Next, we reduce the multiple dimensions of the flux arrays that construct the composite spectra in each radial bin to their projections into the first two PCs inferred from the global spectra. The left-hand panel of Figure 1 shows the spectral radial profiles obtained by applying this dimensionality reduction to a random subset of our sample of 532 S0 galaxies.

The fact that a great deal of the radial profiles in the PC1–PC2 subspace show an approximate linear behavior allows us to go one step further to simplify the analysis of the MaNGA data without missing essential information. Thus, we have best-fitted all these spectral profiles by means of straight lines that have then been converted into vectors using the projections of the points corresponding to the innermost and outermost radial bins on such lines to set, respectively, the tail and tip of the arrows. However, as shown in Figure 1, there are some vectors, colored in brown in the right-hand panel, that are a poor representation of the spectral radial profiles they intend to replace. To objectively measure the goodness of this approximation and therefore to identify those spectral profiles that can be adequately vectorized, we introduce two empirical parameters: the disorder, δ, that determines the extent to which the projections of the PC1 and PC2 coordinates of the radial bins into the model lines follow the right sequence of radial distances; and the entanglement, ϵ, which is a measure of the lack of linearity shown by the radial profiles in the PC1–PC2 plane inferred from the ratio between the second and the first singular values of the PC1 and PC2 coordinates of the spectral profiles. After some trial and error, we came up with $\delta \geqslant 20$ or ($\delta \geqslant 10$ and $\epsilon \geqslant 0.05$) as the range(s) of these parameters for which vectorization should be avoided. Applying these thresholds, we exclude about 16% of the S0s in our sample, 62 from the PS region and 24 from the AC(+TR) one, which represent ∼18% and 13% of the corresponding subsets. The details of the whole procedure of dimensionality reduction of the MaNGA data cubes and vectorization of the spectral radial profiles will be presented in J. L. Tous et al. (2023, in preparation).

As can be deducted from Figure 2, the removal of the galaxies with nonlinear PC1–PC2 radial profiles from the original data set (empty black histograms) does not introduce meaningful differences in the distributions of effective radius and stellar mass of the reduced sample (green filled histograms). Likewise, this figure shows that, despite spanning the same ranges in these two physical properties, S0 galaxies that belong to the AC class (empty blue histograms) are, on average, slightly smaller and less massive than their PS counterparts (empty red histograms). As expected, no significant biases are observed in the distributions of apparent inclinations. Furthermore, all the spectral images of the S0s with linear spectral profiles extend beyond the FWHM of the point-spread function (PSF), with a median σ_{PSF}/R_{max} of 0.23, and have outermost radial bins that extend to $R'_{max} \sim 1.5$, except for four objects that have $R'_{max} \lesssim 1$.

4. Activity/Star Formation Gradients

To facilitate the analysis of the inner spectral profiles of S0 galaxies, we introduce a new dimension in their classification that accounts for their orientation relative to the PS, the narrow and well-defined band that demarcates the locus of fully

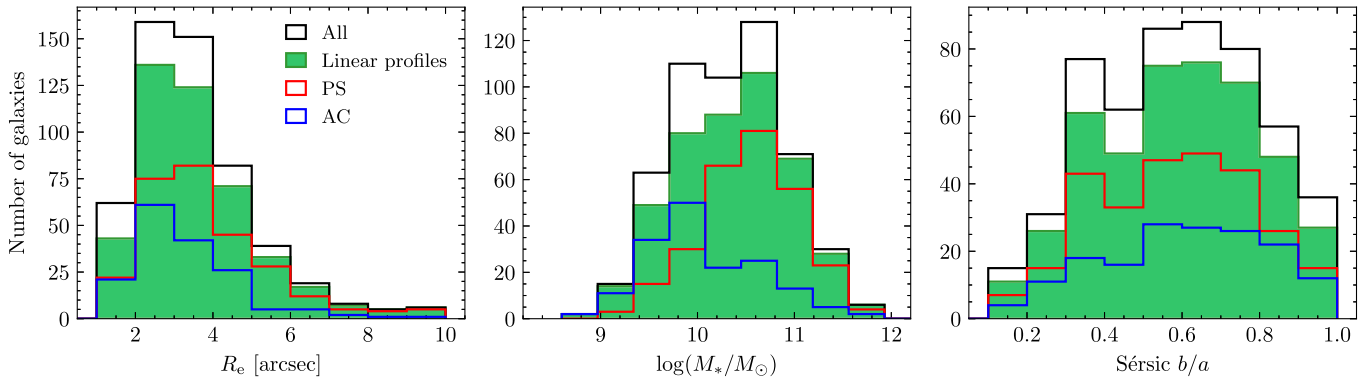

Figure 2. Histograms comparing the effective radius (left), stellar mass (middle), and observed axis ratio (right) of the S0 sample before (empty black histograms) and after (green filled histograms) removing the galaxies with nonlinear PC1–PC2 radial profiles. The red and blue empty histograms show the distributions of these properties for, respectively, the objects of the PS and AC spectral classes with linear profiles.

quiescent galaxies in the PC1–PC2 plane. We know from the work by TSP20 (see also Jiménez-Palau et al. 2022a) that the distance to the main ridge of the PS measured in this subspace shows a strong positive correlation with EW(Hα). Since this last parameter is an observational proxy for the SSFR, the behavior of the spectral profiles with respect to the PS will inform about the sign of the radial gradient of star formation in the target galaxies. We want to see if it bears any relationship with the classes of activity diagnosed by PCA.

This new dimension is the polar angle, θ, of the vectorized spectral profiles measured counterclockwise from the PS ridge (red dotted line in the right-hand panel of Figure 1). We define three orientation tiers. Objects with $5° < \theta < 175°$ are those in which the distance to the PS ridge, and hence the strength of the EW of the Hα line, increase with galactocentric distance, i.e., have positive radial gradients up to $\sim$1.5 R_e. This can be understood as an indication that the star formation activity in these galaxies, irrespective of its global level, is more suppressed in the central regions. Such a group of inside-out (IO) quenched S0s has 113 members (25% of the objects with vectorizable spectral profiles), 71 of these being PS systems (26% of the galaxies of this activity class) and 42 AC (25% of them). There are 116 S0s (26%) with $185° < \theta < 355°$, for which the radial gradient of EW(Hα) is negative. It is remarkable that only nine of the galaxies whose star formation is being suppressed from the outside in (OI) are categorized as PS, while 107 are AC members (3% and 65% of their respective activity classes[6]). The remaining 217 galaxies (201 PS and 16 AC) have $\theta \in [-5°, 5°] \cup [175°, 185°]$ and therefore spectral profiles that run basically parallel to the PS ridge; or, in other words, they have essentially uniform (flat) SSFRs. The vast majority correspond to fully retired objects.

All IO-quenched galaxies show a central depression in the ionization level relative to outer regions of the disk. However, not all members of this class are necessarily centrally quiescent, since for objects of type AC, EW(Hα) of the spaxels located at small galactocentric radii remains, with few exceptions, above 6 Å. For their part, the S0–PS at $R' \lesssim 0.5$ tend to be dominated by low-ionization emission-line regions with values of EW(Hα) below 3 Å that go above this threshold at larger radii. Some of these latter systems may be associated with galaxies with central low-ionization emission-line regions (cLIERs) included in the spatially resolved spectral classification by Belfiore et al. (2017) and with galaxies in a quenching stage of central quiescence identified in the Calar Alto Legacy Integral Field Spectroscopy Area (CALIFA) survey by Kalinova et al. (2021), while others seem to fit better into Kalinova et al.'s category of "nearly retired galaxies," as they show global averages of EW(Hα) equal to or less than 3 Å. On the other hand, our S0–PS with flat spectral profiles resemble the extended LIER (eLIER) and fully retired galaxy classes identified in both works. Surprisingly, we do not find obvious counterparts in these classifications for our S0–AC with OI quenching.

As to the typical value of the average EW(Hα) per galaxy for each one of the six different spectral categories of S0s that result from combining the activity (PS/AC) and quenching (IO/OI/flat) classes, we have, in descending order: $\langle$EW(Hα)$\rangle$ = 31.6 Å for OI+AC lenticulars, 20.0 Å for IO+AC, 8.7 Å for flat+AC, 4.8 Å for IO+PS, 1.8 Å for OI+PS, and 1.6 Å for flat+PS. This shows that all S0–ACs, regardless of their quenching type, can be considered as SF S0s, since their representative values of $\langle$EW(Hα)$\rangle$ are well above the minimum threshold of 6 Å expected when gas excitation is powered by H II regions (e.g., Cid Fernandes et al. 2011). It can also be seen that, within this activity class, the highest SSFRs occur on objects with OI-quenched spectral profiles, which are also the most numerous. This indicates, in good agreement with the findings by Rathore et al. (2022), that the characteristic image of S0–ACs, when considered as a whole, would be that of early-type disks with centrally dominated star formation that reaches values of the SSFRs perfectly comparable to those observed in SF spirals, but that is less extended in galactocentric radius. Furthermore, the general quiescence of the PS lenticulars is confirmed, especially for objects with OI and flat spectral profiles, for which the condition $\langle$EW(Hα)$\rangle < 3$ Å indicates that the source of the ionized gas is likely hot, low-mass, evolved stars, whereas the intermediate emission-line values of the IO-quenched S0–PS could reflect a mixture of ionization sources (Lacerda et al. 2018).

5. Patterns in the Spectral Maps

In this section, we investigate the dominant patterns described by the spatially resolved stellar and ionized gas distributions in S0 galaxies and their possible links with the spectral categories that we have defined in the previous sections. We use for this endeavor maps of the logarithm of the

[6] The fact that about 40% of the few systems tagged TR show OI-quenched spectral profiles corroborates our decision to include them within the AC subset.

EW of the Hα line measured in angstrom and of the flux intensity of this same line in units of 10^{-17} erg cm^{-2} s^{-1} Å^{-1} spaxel^{-1} times the heliocentric redshift squared of the galaxy, so it provides an estimate of the Hα luminosity, $L'(\mathrm{H}\alpha) = kL(\mathrm{H}\alpha)$, except for the constant of proportionality $k = (H_0/c)^2/4\pi$, as well as of the dimensionless D4000 index.

Visual identification of the dominant trends in the spectral maps unveils the existence of a pattern that, although not overwhelmingly prevalent, is quite widespread: the presence of ring-shaped inner structures ($0.5R_e \lesssim R \lesssim 1.5R_e$) in EW(Hα). These spectral rings are also echoed sometimes in the spatial distributions of $L'(\mathrm{H}\alpha)$ and D4000, as well as in the corresponding optical images, although in this latter case with a significantly lower contrast that makes their detection more difficult. To avoid personal bias in ring identification, all the authors of this paper have participated in the visual inspection of the MaNGA spectral maps, after adjusting them to comparable angular sizes. We have followed a scheme in which each of us has independently assigned an integer score from 0 to 2 to the maps depending on whether the presence of a ring is rejected (0), confirmed (2), or doubtful (1), and added the individual scores afterwards. Spectral images are divided into three categories based on the overall ring score (r) they have attained: ringed ($r \geqslant 6$), doubtful ($r = 3$–5), and non-ringed ($r < 3$). Furthermore, to obtain a reliable estimate of the ring abundance in our S0 sample, we have restricted the search to galaxies not highly inclined ($i < 60°$), with linear PC1–PC2 radial profiles, and with a good seeing, a condition that we define as $\sigma_{\mathrm{PSF}}/R_e < 0.6$ after verifying that the removal of galaxies that are small relative to the PSF according to this constraint does not introduce spurious trends either in ring detection or as a function of galaxy size. These additional cuts yield a subset of 275 S0s with essentially the same distributions of effective radii and stellar masses as its parent sample shown by the green histograms of Figure 2, as well as similar fractions of spectral and quenching classes. Still, not all spectral maps in this final high-quality subset show sufficiently continuous spatial coverage to assess the presence of rings. The figures in Table 1 give detailed information about the number of maps of each type that have finally been used.

Applying this strategy, we find that the global fraction of nearby S0s with a ring in EW(Hα) is 0.21, which rises to 0.34 if we include those galaxies for which ring detection has been deemed inconclusive (i.e., with $r \geqslant 3$). These values are substantially larger than the occurrence rate of ∼7% inferred by Deeley et al. (2021) from both simulations and observations. However, we note that in their case, the detection of ringed galaxies was carried out using a single late snapshot from a cosmological run and, observationally, the Hα fluxes. In fact, the near 10% fraction of rings with $r \geqslant 6$ that we infer from our $L'(\mathrm{H}\alpha)$ maps does not stray notably from Deeley et al.'s. As shown in Table 1, EW(Hα) rings are more frequent among the members of the PS class than in S0–ACs, with respective fractions of ∼0.29 and 0.15, assuming again only clear detections. Besides, the mean value of EW(Hα) in the spaxels defining these annular structures in AC systems is about four times larger than in objects of the PS class (we discuss the implications in Section 7). We also find that essentially all S0s with a ring in this spectral index have IO quenching, while more than half of the galaxies with this kind of spectral profile are ringed (85% if we include objects with doubtful rings). In contrast, spectral rings are infrequent in S0 galaxies with either OI-quenched or flat spectral profiles.

Examples of S0 galaxies showing different combinations of quenching and activity classes are provided in Figure 3. As can be seen from this plot and Table 1, the ringed structures are usually more conspicuous in the EW(Hα) maps than in the maps of the other two spectral indices. Examination of the montages of optical images and spectral maps provided in Appendix B shows that most of the resolved $L'(\mathrm{H}\alpha)$ distributions have in common the presence of a peak in the gas density that encompasses the most central spaxels. Nonetheless, in a good number of instances, the values of EW(Hα) achieved in these nuclear gaseous enhancements indicate that they are not forming new stars, but possibly tracing low-ionization emission-line regions fueled by old post-AGB stars (see also, e.g., Figure 3, column (c)). On the other hand, few of the rings with enhanced SSFR detected in the IO-quenched S0–ACs are visible in the associated $L'(\mathrm{H}\alpha)$ maps. In fact, in galaxies of this type, the radial extent of the cold gas tends to lie within the outer boundary of the rings, indicating that the distribution of ionized hydrogen in this area has a strong negative radial gradient (see, e.g., Figure 3, column (d)). In contrast, the stellar populations, as traced by D4000, describe patterns very similar to those found in the EW(Hα) maps, with younger stars concentrating at the location of the SF rings.

The case of MaNGA 9506–1901. Among all the S0s investigated, this object has drawn our attention because its $L'(\mathrm{H}\alpha)$ map shows what resembles a double spiral arm-like feature of ionized hydrogen connected by a similarly intense bar of warm gas. As shown in Figure 4, this is a nearly face-on S0–AC with a global IO-quenched spectral profile that concentrates the most important star formation activity at the ends of the gaseous spiral arms, where the EW(Hα) index reaches peak values that exceed 40 Å. Inspection of the D4000 map suggests that the nebular spiral structure, assuming it behaves as a single body, may be winding in a leading sense. Interestingly, there is no visible sign of the presence of spiral arms or bars in the stellar component of the galaxy in any of the SDSS filters, not even in deeper optical images coming from the Dark Energy Camera Legacy Survey (Dey et al. 2019). Only a faint bluish band is perceived in the optical image along the interior of the IFU's hexagonal boundary that could be spatially correlated with the peripheral zones of enhanced SSFR and younger stellar ages that can be seen, in green/yellow colors, in the corresponding panels of Figure 4. On the other hand, the fact that the central bar-like section of this spectral feature lacks a visible counterpart reinforces the idea that it is a purely gaseous structure not associated with star formation. Early-type galaxies such as this one with eye-catching features of ionized hydrogen have also been documented in other IFS surveys like CALIFA (Gomes et al. 2016). They call for follow-up observations that may end up providing valuable insights for advancing in our understanding of the buildup history of these systems.

6. Ring Fraction versus Global Properties

The next step is to analyze the behavior of the fraction of EW(Hα) rings in relation to two global properties of the studied systems—one internal, the stellar mass, and the other external, the environmental density—that bear a direct relationship with their formation channels. We aim at gathering

Table 1
Number (Fraction) of S0 Galaxies Harboring Rings in Each Type of Spectral Map According to Activity and Quenching Classes

		EW(Hα)						L'(Hα)						D4000					
Spectral Class	Quenching Class	Ringed		Doubtful		Non-ringed		Ringed		Doubtful		Non-ringed		Ringed		Doubtful		Non-ringed	
PS	IO	20	(0.56)	10	(0.28)	6	(0.17)	15	(0.56)	4	(0.15)	8	(0.30)	3	(0.12)	14	(0.54)	9	(0.35)
	OI	0	(0.0)	0	(0.0)	3	(1.0)	0	(0.0)	0	(0.0)	1	(1.0)	0	(0.0)	0	(0.0)	1	(1.0)
	Flat	2	(0.05)	2	(0.05)	34	(0.89)	1	(0.02)	0	(0.0)	42	(0.98)	0	(0.0)	1	(0.01)	108	(0.99)
	All	22	(0.29)	12	(0.16)	43	(0.56)	16	(0.23)	4	(0.06)	51	(0.72)	3	(0.02)	15	(0.11)	118	(0.87)
AC	IO	14	(0.48)	11	(0.38)	4	(0.14)	0	(0.0)	4	(0.15)	23	(0.85)	4	(0.16)	9	(0.36)	12	(0.48)
	OI	1	(0.01)	1	(0.01)	65	(0.97)	0	(0.0)	0	(0.0)	62	(1.0)	0	(0.0)	1	(0.02)	60	(0.98)
	Flat	0	(0.0)	1	(0.14)	6	(0.86)	0	(0.0)	0	(0.0)	8	(1.0)	0	(0.0)	0	(0.0)	9	(1.0)
	All	15	(0.15)	13	(0.13)	75	(0.73)	0	(0.0)	4	(0.04)	93	(0.96)	4	(0.04)	10	(0.11)	81	(0.85)
All	All	37	(0.21)	25	(0.14)	118	(0.66)	16	(0.10)	8	(0.05)	144	(0.86)	7	(0.03)	25	(0.11)	199	(0.86)

Note. Limited to galaxies with vectorizable spectral profiles, non-extreme inclinations ($i \leqslant 60°$), and robust to PSF effects (i.e., $\sigma_{\rm PSF}/R_e < 0.6$).

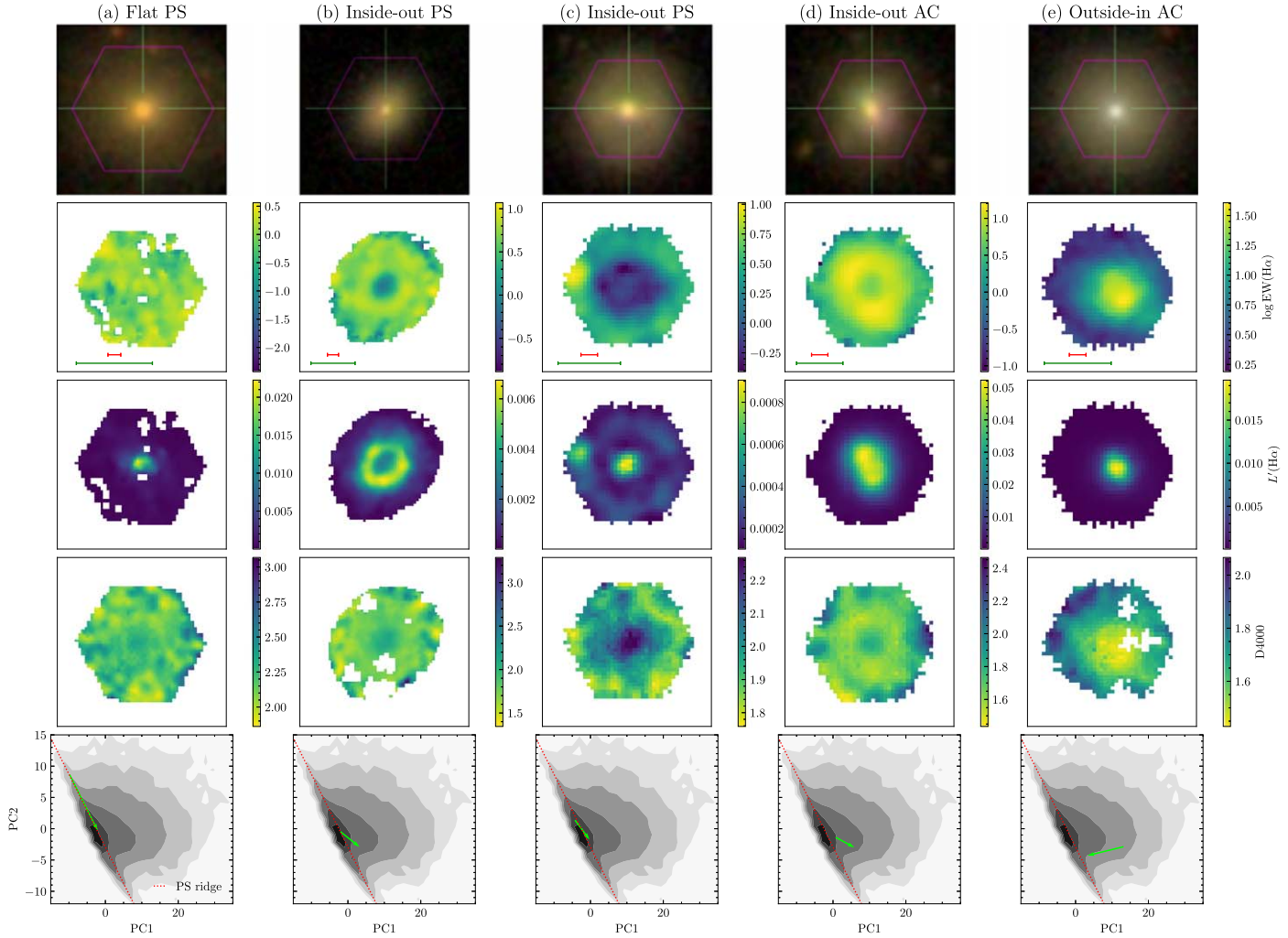

Figure 3. Examples of spectral maps and spectral profiles of S0 galaxies. The second, third, and fourth rows show, in this order, maps of the EW(Hα), L'(Hα), and D4000 spectral indices. Only spaxels with all quality flags equal to zero are drawn. The green and red horizontal lines included in the EW(Hα) panels indicate, respectively, the galaxies' Petrosian half-light diameter in the r band and $2\sigma_{\rm PSF}$. The bottom row shows the vectorized spectral profiles of the galaxies in the PC1–PC2 subspace. The true color images of the galaxies are shown in the first row, with the overlapping violet hexagonal frames depicting the footprint of MaNGA's bundles (images' source: https://data.sdss.org/sas/dr15/manga/). Galaxies in columns (b), (c), and (d) show clear rings in EW(Hα) (i.e., they have ring scores $r \geqslant 6$), whereas no rings are observed for the galaxies in columns (a) and (e) ($r < 3$).

evidence that helps to unveil the role that such fundamental properties play in shaping the rings and to establish later on the relationship that these transient structures may have with the evolutionary histories of the S0 galaxies harboring them—which, as we have seen in the previous section, are almost exclusively those with IO-quenched spectral profiles.

As shown in the top left panel of Figure 5, the fraction of galaxies in our high-quality S0 sample that harbor or likely harbor EW(Hα) rings, $F_{\rm ring}^{\rm WH\alpha}(r \geqslant 3)$, is positively correlated with the measurement of the total stellar mass. It rises monotonically from ∼10%–20% among the S0s in the smallest mass bin ($M_* \leqslant 10^{10}\,M_\odot$) to ∼50%–60% for objects in the more massive one ($M_* \geqslant 10^{11}\,M_\odot$). If the data are partitioned by activity class, this behavior is still maintained. If anything, it might be inferred that the ring fraction for S0–ACs peaks at $M_* \sim 10^{10.5}$–$10^{11}\,M_\odot$. Note, however, that while we have verified using different binning strategies that the observed positive correlation is robust, the quoted fractional abundances of rings are relatively uncertain given the limited size of the subsamples employed (listed in the legend of each panel of the figure). The cumulative frequency plot in the bottom left panel of Figure 5—which allows one to compare the distributions of the number of observations as a function of the stellar mass in a binning-independent manner—confirms that ringed S0 galaxies tend to be more massive than their non-ringed counterparts, regardless of their spectral class. A two-sample Kolmogorov–Smirnov (K-S) test rejects the null hypothesis that ringed and non-ringed subsets arise from the same parent distribution at level $\alpha = 0.01$ for both the PS and AC classes (p-values of 0.01 and 0.0007, respectively). These findings are in line with recent work by Diaz-Garcia et al. (2019), who report, from a subset of the S^{4}G mid-IR sample (Sheth et al. 2010) of nearby disks ($d \lesssim 40$ Mpc) encompassing a similar range of masses, that SF rings are preferentially hosted by massive, gas-poor, centrally concentrated galaxies that are not dominated by dark matter in their innermost regions (see also Section 7).

The influence of the environment is evaluated by means of our own nearest-neighbor (NN) estimator of the local density. It is a parameter based on the distances up to the fifth neighbor measured using a Bayesian metric (see Equations (1) and (2) in TSP20), which is then ranked according to the percentile that each galaxy gets in the deepest volume-limited subset that can

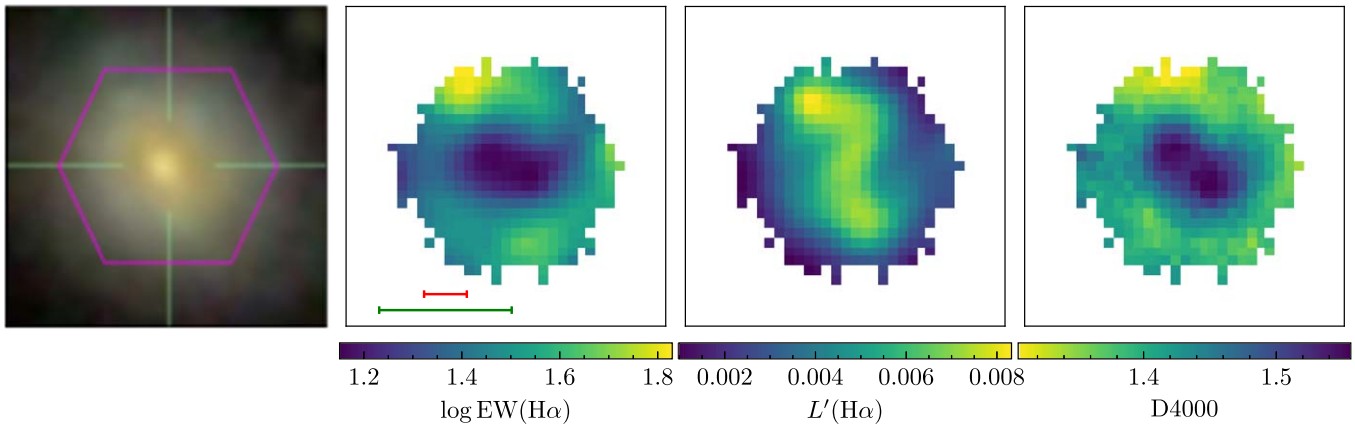

Figure 4. From left to right, optical image and EW(Hα), L'(Hα), and D4000 spectral maps for the IO-quenched S0–AC 9506–1901. The green and red horizontal lines included in the EW(Hα) panel indicate, respectively, the galaxies' Petrosian half-light diameter in the r band and $2\sigma_{\rm PSF}$. Note what appears to be a barred spiral-shaped feature outlined by the dense gas distribution on the Hα luminosity map, which, however, is not evident in the optical image nor in the other two spectral maps. Montages like this one for all the vectorizable galaxies in the MaNGA S0 sample are shown in Appendix B. The ring score of this galaxy in EW(Hα) is $r = 3$.

be defined for it. Prior to running this test, however, we have examined the extent to which its results could be influenced by the observed positive correlation of the ring fraction with stellar mass. With this purpose, we have split our sample into four evenly spaced density percentile intervals centered at 0.125, 0.375, 0.625, and 0.875, and compared the distributions of the stellar mass in them, whose means and standard deviations have turned out to be 10.23 ± 0.52, 10.39 ± 0.47, 10.29 ± 0.63, and 10.29 ± 0.61, respectively. The fact that these values are broadly consistent with each other implies that, at least for the present subset of observations, stellar mass does not correlate with environmental density, and therefore that any trend shown by the fraction of rings as a function of the latter will not be a consequence of its underlying relationship to stellar mass.

As can be seen in the top right panel of Figure 5, the abundance of rings remains constant, within the calculated uncertainties, in the four equal-sized percentile intervals defined above. This result, which is maintained when the PS and AC activity subsets are analyzed separately, also agrees with the findings of Diaz-Garcia et al. (2019), who claim that the galaxies' environs do not play a relevant role in ring formation. To determine the extent to which the procedure applied to probe the environment could be conditioning the outcomes—Díaz-García et al. also use a local NN estimator but relying on three neighbors—we have reevaluated the ring fractions using a more global estimator of environmental density, namely the virial mass, M_{200}, of the host group of the galaxies calculated by Tempel et al. (2017) from the observed velocity dispersion and group extent on the sky (see their Equation (3)), which is available for 94 of the S0s in the high-quality subset. Using this new parameter, after certifying again that our data do not hide a relationship between stellar mass and environment, we still find the ring fraction to be essentially unrelated to the characteristics of the region in which the galaxies reside (crosses in the top right panel of Figure 5). Likewise, the associated cumulative distributions of counts of ringed and non-ringed galaxies with environmental density do not show statistically significant differences, as reflected by the high p-values of 0.996 (PS) and 0.226 (AC) delivered by the K-S test. However, in fairness, we acknowledge that the robustness of all these results is not foolproof, since they are based on a relatively limited number of measurements. Relationships such as those investigated in this section and their dependence on the spectral classification of galaxies will need to be corroborated with the help of data sets that are not only much larger than currently available samples, but that are also highly complete, free from aperture effects, and capable of providing uniform coverage across the full range of stellar environments and masses.

7. A Scenario for the Formation of SF Rings in S0 Galaxies

As commented in the Introduction, star formation in present-day S0 galaxies is observed to be frequently organized in ring-like structures (e.g., Salim et al. 2012). According to the investigation of the formation pathways of S0s by Deeley et al. (2021) from the data generated in the IllustrisTNG-100-1 cosmological simulation (Springel et al. 2018), practically all galaxies of this type experience at some point in their lives a transitional phase in which they host an SF ring. In the simulation, rings always appear related to merger episodes, thereby showing that this mechanism is their major driver in front of other feasible formation channels, such as the inflow of fresh gas through filaments or outflows from active galactic nuclei. Deeley et al. also observe that the onset of SF rings is preceded by the depletion of the gas in the central region of the hosts, and often accompanied by the formation of a stellar bar —or other non-axisymmetric distortion of the gravitational potential set up by the merger itself (see Comerón et al. 2014 and references therein), which indicates that these phenomena are linked for the most part to disk instabilities of the primary galaxy. This agrees with our finding that essentially all our S0s with clear or tentative spectral rings, whether of the AC or PS class, exhibit IO quenching. In this sense, it is hard not to notice that some of our L'(Hα) maps of ringed, IO-quenched S0s (see, for example, the middle panel in Figure 3(c)) bear a close resemblance, if one takes into account the distorting effects of the PSF, with the gas density distribution associated with the coplanar ring formed in the hydrodynamic simulations of mergers of a lenticular galaxy with a small gas-rich satellite by Mapelli et al. (2015, see their Figure 4). The agreement with this latter work also extends to quantitative results, since our finding that EW(Hα) rings are about twice as frequent in PS sources as among AC ones is in good agreement with the shorter lifetimes shown by the simulated gaseous rings in regions of intense star formation because the thermal energy

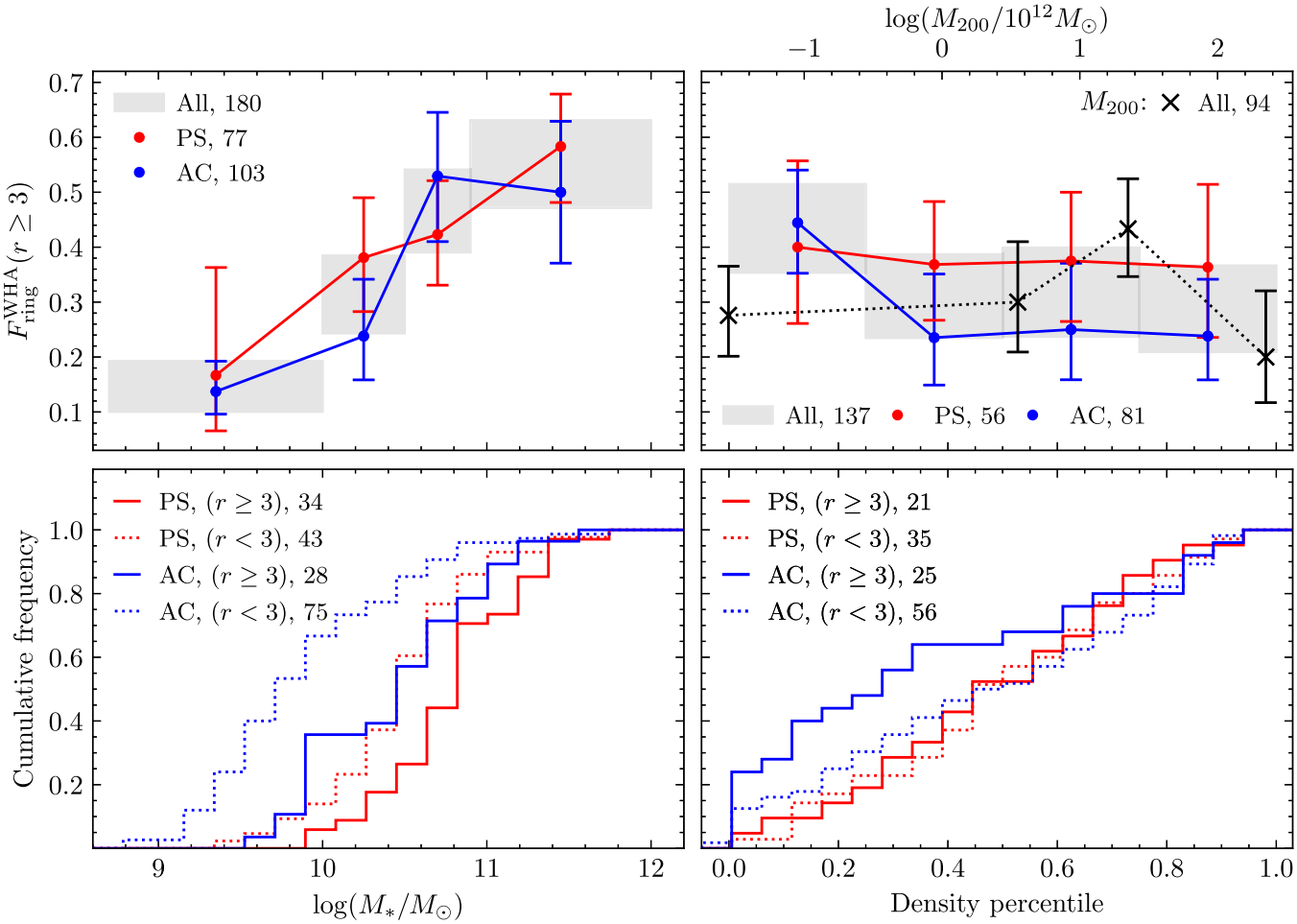

Figure 5. Fractions (top) and cumulative frequencies (bottom) of varying subsets of present-day S0s harboring or likely harboring EW(Hα) rings as a function of their total stellar mass (left) and environment (right). The latter is quantified in the upper panel using two different measures: a ranked density percentile inferred from a nearest-neighbor estimator (colored circles, lower x-axis) and the virial mass M_{200} of the halo hosting the galaxies (black crosses, upper x-axis). The error bars on the fractions show 1σ uncertainties estimated by adopting a Wilson score interval approximation to the binomial error distribution. The number of galaxies in each subset is provided.

released by supernovae explosions easily destroys them. However, unlike what Mapelli et al. suggest with their simulations, the fact that we observe that the Hα emission from the rings of the S0–ACs is about four times higher than that recorded in the rings of S0 categorized as PS (Section 5) implies, provided the gas content of the merged satellites does not correlate with the spectral classification of the central objects, that star formation in these structures is largely fueled by gas remaining in the primary galaxies rather than by gas supplied by the satellites, especially for the S0–ACs. In turn, this result suggests that the Hα rings are very possibly coplanar with the disks and it is therefore consistent with the widely accepted standard theory of ring formation by gas accumulation at bar resonances.

The rest of the results allow us to infer the specifics of the proposed merger scenario for the formation of SF rings in S0 galaxies by showing that such annular structures are more likely to arise in mergers involving a massive primary galaxy closely orbited by a tiny dwarf satellite. It is well known both through simulations (e.g., Villa-Vargas et al. 2010) and observations (e.g., Masters et al. 2012; see also Zhou et al. 2021 and references therein) that the presence of a dissipative gaseous component prevents the formation of disk instabilities, bars, and/or rings, by exchanging energy and angular momentum with the stars. Therefore, it does not seem to be coincidental our finding that the ring fraction increases with the mass of S0 galaxies, reaching its peak around $M_* \sim 10^{10.5}$–$10^{11}\,M_\odot$, a mass scale of the order of the golden mass. The latter is a well-constrained, redshift-independent quantity inferred in theoretical studies of galaxy formation (Dekel & Birnboim 2006; see also Dekel et al. 2019, 2021)—it corresponds to a virial halo mass $M_{\rm vir} \sim 10^{12}\,M_\odot$—that marks a general bimodality in many galaxy properties. In particular, the efficiency of star formation increases progressively as the mass of galaxies approaches this characteristic value, causing the gaseous-to-stellar mass ratio to reach a minimum for golden-mass objects. This would explain the observed tendency of ringed S0s to be more massive than their non-ringed counterparts.

On the other hand, a major merger or a minor one involving a relatively massive satellite could transfer more energy than is required to create a transient instability in a disk marginally stable against developing it. Any resonance that cannot be efficiently damped by the dissipative gaseous component will grow out of control and eventually self-destruct, whereas if the mergers are excessively disruptive, no resonances will be created at all. Furthermore, in a typical merger scenario, the fraction of Hα rings, provided these structures do not last very

long, would be expected to increase with increasing environmental density, peaking at roughly the scales of groups, such as happens with the merger rate efficiency, and then decrease its value in the most overdense regions. However, we have reported evidence for the lack of correlation between the frequency of rings and different metrics that probe the density of the environment. So, for this result to support the picture being built here, it is necessary to assume that the role of satellite is played mostly by tiny dwarf galaxies orbiting in the innermost regions of the halos of the primary galaxies. This should allow the two progenitor galaxies to retain their merging pair status even if the system falls into a densely populated region, and therefore the merger rate efficiency to remain aloof from the physical conditions dictated by a changing local environment. Interestingly, in the example of a typical spiral galaxy transforming into an S0 through multiple merger events shown in the cosmological simulations analyzed by Deeley et al. (2021), it is the merger that takes place at $\sim$7 Ga, involving what is, by far, the smallest satellite that participates in the buildup of this galaxy, the one that triggers the formation of a distinct SF ring (see their Figures 9(a) and (e)). Although we lack enough information to rigorously constrain the mass ratio defining these mini-mergers, we venture to speculate, exclusively on the basis of simulations such as those of Mapelli et al. (2015), that it could well be significantly less than 1:10 and involve star-forming dwarf-galaxy satellites with gas masses of a few times $10^8\,M_\odot$, comparable to those of the Large and Small Magellanic Clouds, which are in the process of falling toward our Galaxy (Besla 2015).

8. Summary and Conclusion

We have studied the spatially resolved optical spectral properties of a sample of 532 lenticular galaxies from the MaNGA survey. The spaxels of the data cubes, once properly corrected and cleaned, have been stacked in radial bins and projected in the plane defined by the first two principal components resulting from the principal component analysis of their single-fiber spectra. The information has been further synthesized by best-fitting these spectral radial profiles by means of straight lines that have been then converted into vectors in the PC1–PC2 plane.

This dimensionality reduction process has allowed us to show that present-day S0s can be classified into three groups according to the sign of the inner radial gradients ($R \lesssim 1.5\,R_e$) of their star formation: galaxies with inside-out quenched radial profiles, systems with outside-in quenching, and galaxies with flat gradients. Regarding the global star formation activity, we have used the Tous et al. (2020) PCA-based diagnostic to divide the galaxies into two main categories: passive sequence and active cloud, encompassing galaxies whose single-fiber spectra are representative, respectively, of passive and active systems, and including in the latter class a few objects with intermediate spectral characteristics assigned by these authors to the transition region.

Visual inspection of the EW(Hα) maps of these galaxies has revealed the existence of a pretty significant fraction of objects hosting inner rings—34% if dubious ringed systems are included—which, however, are generally absent from maps constructed from other spectral indicators of stellar age such as L(Hα) and the D4000 index, as well as in the optical SDSS images. The preferential detection of SF rings by their EW(Hα) emanates not only from the direct relationship between the strength of the Hα emission and the SSFR, but also from the fact the EW provides information on the intensity of the lines normalized to the underlying continuum, thus increasing their contrast in spectral maps. The present sample of S0s constitutes, in fact, the largest collection of ringed galaxies ever identified in the local universe through spatially resolved spectroscopic observations.

The analysis of the relationships of the spectral rings to the physical properties of their host S0 galaxies has produced the following results.

1. In almost all cases, the SF rings are associated with IO-quenched radial profiles of star formation (Table 1). This is in agreement with state-of-the-art cosmological simulations, which show that rings of this type are always related to merger episodes and that their onset is preceded by the depression in the level of star formation in the central region of their host galaxies and frequently linked to other disk instabilities such as bars.
2. The Hα emission in the rings of the S0–ACs is about four times greater than that of the members of the PS class. This suggests that star formation in these rings, especially for objects of the former class, is fueled primarily by gas that still remains in the host galaxies rather than gas provided by the merging satellites. This also suggests that the detected spectral rings are probably mostly coplanar structures.
3. The EW(Hα) rings are found to be about twice as frequent in PS systems as in AC ones (Table 1). This is in line with controlled simulations of ring formation in lenticular galaxies via mergers of small satellites, which show that the more intense the star formation, the more easily these transient structures are destroyed by supernova feedback.
4. Whatever the activity class of the S0s, their ring fraction increases with stellar mass, showing a tentative peak around a mass scale $M_* \sim 10^{10.5}$–$10^{11}\,M_\odot$ of the order of the (golden) mass that marks the maximum of star formation efficiency and the low point of the gaseous-to-stellar mass ratio in galaxies (Figure 5, left-hand panels). Such behavior, which has also been observed in the general galaxy population, can be explained by the well-known fact that disk instabilities have more difficulties forming in the presence of large amounts of gas than in gas-poor systems.
5. There is no statistically significant evidence that the frequency of Hα rings in S0 galaxies correlates with environmental density, which we have measured using two different standard metrics (Figure 5, right-hand panels). This suggests that the formation of SF rings in lenticular galaxies is not ruled by their environment.

Based on these findings, and on the physical conditions necessary for the formation of in-plane SF rings in galaxy disks, we conclude that the presence of annular structures in the EW of the Hα emission line among fully formed S0s is a relatively common phenomenon, possibly originating from disk resonances driven by weakly disruptive mini-mergers, and preferentially involving a relatively massive primary galaxy and a tiny companion strongly bound to the former.

We leave for a future article (J. L. Tous et al. 2023, in preparation) a detailed discussion of how this scenario for ring formation fits into a more extensive and complex picture

describing the multiple formation channels that S0 galaxies seem to follow.

We acknowledge financial support from the Spanish state agency MCIN/AEI/10.13039/501100011033 and by "ERDF A way of making Europe" funds through research grants PID2019–106027GB–C41 and PID2019–106027GB–C43. MCIN/AEI/10.13039/501100011033 has also provided additional support through the Centre of Excellence Severo Ochoa's award for the Instituto de Astrofísica de Andalucía under contract SEV–2017–0709 and the Centre of Excellence María de Maeztu's award for the Institut de Ciències del Cosmos at the Universitat de Barcelona under contract CEX2019–000918–M. J.L.T. acknowledges support by the PRE2020–091838 grant from MCIN/AEI/10.13039/501100011033 and by 'FSE Invests in your future". H.D.S. acknowledges support by the PID2020-115098RJ-I00 grant from MCIN/AEI/10.13039/501100011033. The authors also wish to thank an anonymous referee for comments and suggestions that have helped to improve the presentation of the results.

Appendix A
Classification of S0 Galaxies from the Principal Component Analysis of Their Spectra

In this work, we use the first two eigenspectra derived in the principal component analysis of a sample of 68,043 extinction-corrected single-fiber SDSS optical spectra (TSP20; see also Jiménez-Palau et al. 2022a). Here we provide a brief outline of the method applied and the resulting spectral classes.

A data set of N SDSS galaxy spectra can be thought of as a set of flux vectors, f_i, in a space of ∼3800 dimensions or (vacuum) wavelength intervals. Each one of these vectors can be expressed exactly as the sum of a vector of mean fluxes, $\langle f \rangle$, and a linear combination of M orthonormal vectors or eigenspectra, e_j, that account for all the variability around the mean, in the form (e.g., Connolly et al. 1995)

$$f_i = \langle f \rangle + \sum_{j=1}^{M} \mathrm{PC}j_i e_j \quad 1 \leqslant i \leqslant N, \tag{A1}$$

where the coefficients $\mathrm{PC}j_i \equiv f_i \bullet e_j$ are the projections of each individual spectrum on the new base of principal components arranged in decreasing order of their relative power, i.e., of the proportion of the total variance of the data that they explain. Thus, when the main variance of a data set lies in a low-dimensional space, one can get a good visualization of it by truncating the above expansion to the first few eigenvectors. As we showed in TSP20, once any extrinsic source of variability in the spectra is removed, nearly 90% of the variance in the SDSS sample of S0s lies in the subspace whose axes are the first two principal components, a huge dimensional reduction with a modest loss of information that allows one to carry out the spectral classification of these objects. Furthermore, as we will show in J. L. Tous et al. (2023, in preparation), the first principal components resulting from the PCA of the composite spectra inferred from the MaNGA data cubes are essentially identical to those obtained from the single-fiber spectra. This implies that the spatially resolved spectra have the same main sources of intrinsic variability and can therefore also be classified using the same 2D subspace. The mean optical spectrum of the S0s and the first five eigenspectra inferred from the SDSS data are available in Jiménez-Palau et al. (2022b).

The classification of lenticular galaxies within the PC1–PC2 plane in TSP20 revealed the existence of two clearly distinct regions outlined by subpopulations of S0s with statistically inconsistent physical properties: a very compact and densely populated narrow band that diagonally crosses the PC1–PC2 subspace and a less crowded and much more scattered zone running from the right of it (see also Figure A1). These regions were identified as the "passive sequence" and the "active cloud," because they encompass sources representative, respectively, of passive and active sources. Compared to the S0–PS, which have absorption-dominated spectra, the S0–AC exhibit spectra with significant nebular emission, and on average they are also somewhat less massive, are more luminous but with less concentrated light profiles, possess a younger, bluer, and metal-poorer stellar component, and avoid environments of high galaxy density. These two main areas are separated by a narrow dividing zone, dubbed the "transition region," encompassing objects with intermediate spectral and physical characteristics. This completes a spectral classification for the S0s of the local universe that is reminiscent of the well-known "red sequence–green valley–blue cloud" division applied to the entire galaxy population in color–magnitude diagrams (see Section 5.2 in TSP20 for details).

In Figure A1, we show the projections in the PC1–PC2 subspace of the SDSS optical spectra of the 532 bona fide S0 galaxies that constitute our MaNGA sample. Solid red dots are used to identify PS members, which encompass 64% of the galaxies in the sample, blue dots are for the 29% of the S0s that belong to the AC class, while the remaining 7% of S0s that fall in the TR are drawn using green colored dots (see also Section 2).

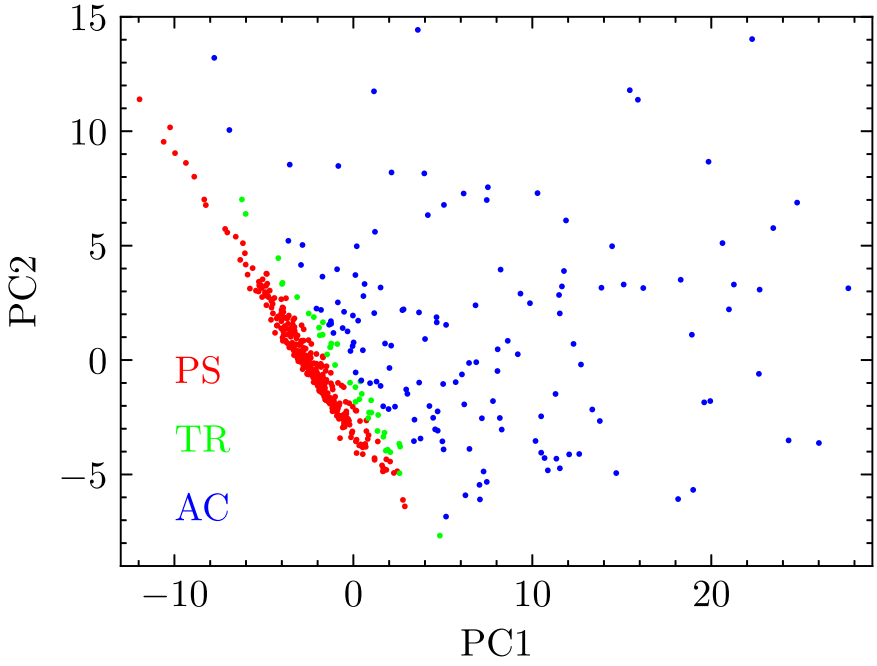

Figure A1. Projections in the PC1–PC2 subspace of the single-fiber SDSS optical spectra of the 532 bona fide galaxies included in our main MaNGA S0 sample. The diagram is subdivided into three distinct regions corresponding to three different spectral classes: passive sequence (PS, red), transition region (TR, green), and active cloud (AC, blue).

Appendix B
Optical Images and Spectral Maps of S0 Galaxies with Linear PC1–PC2 Radial Profiles

In this appendix we show the montages of optical images and spectral maps for S0 galaxies with linear PC1–PC2 radial profiles, emphasizing those objects harboring an unequivocal ring in the EW(Hα) map. The galaxies appear sorted by quenching type (inside out, IO; outside in, OI; and flat, F) and spectral class (passive sequence, PS; active cloud, AC; and transition region, TR).

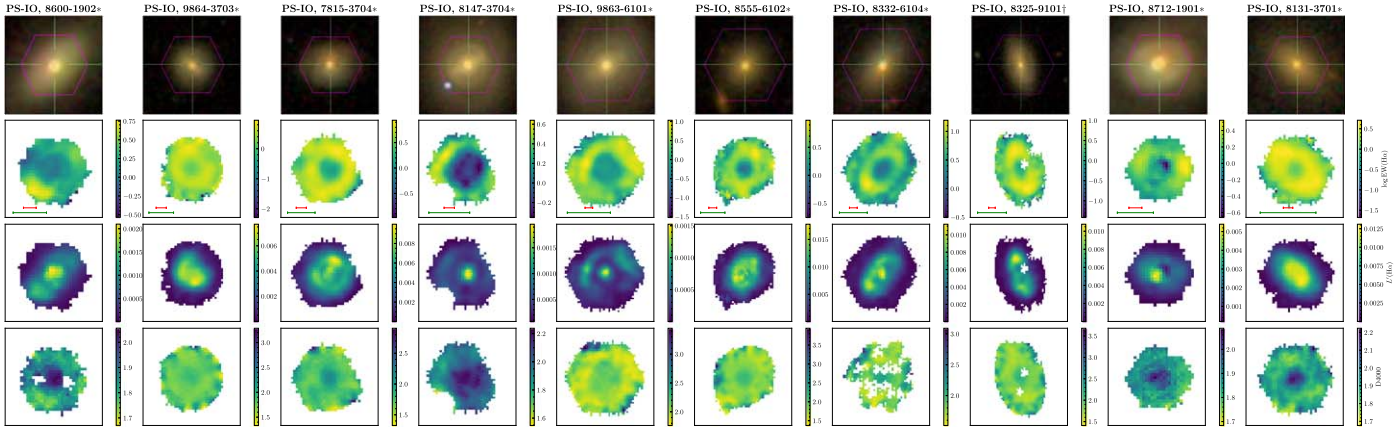

Figure B1. Montages of the optical images and the three spectral maps for all the S0 galaxies with linear PC1–PC2 profiles. The green and red horizontal lines included in the EW(Hα) panels indicate, respectively, the galaxies' Petrosian half-light diameter in the r band and $2\sigma_{\rm PSF}$. An asterisk next to each galaxy's identifier indicates the presence of an unequivocal ring in the EW(Hα) map ($r \geqslant 6$), unless the galaxy is highly inclined ($i > 60°$) or has a poor seeing condition ($\sigma_{\rm PSF}/R_{\rm e} \geqslant 0.6$), in which case a dagger is used.

(The complete figure set (45 images) is available.)

ORCID iDs

J. L. Tous https://orcid.org/0000-0002-1569-0468
J. M. Solanes https://orcid.org/0000-0002-1633-0499
J. D. Perea https://orcid.org/0000-0002-5640-9791

References

Aguado, D. S., Ahumada, R., Almeida, A., et al. 2019, ApJS, 240, 23
Aguerri, J. A. L., Mendez-Abreu, J., & Corsini, E. M. 2009, A&A, 495, 491
Alam, S., Albareti, F. D., Prieto, C. A., et al. 2015, ApJS, 219, 12
Athanassoula, E., Bosma, A., Creze, M., & Schwarz, M. P. 1982, A&A, 107, 101
Barway, S., Wadadekar, Y., Vaghmare, K., & Kembhavi, A. K. 2013, MNRAS, 432, 430
Belfiore, F., Maiolino, R., Maraston, C., et al. 2017, MNRAS, 466, 2570
Bernardi, M., Roche, N., Shankar, F., & Sheth, R. K. 2011, MNRAS, 412, 684
Besla, G. 2015, arXiv:1511.03346
Blanton, M. R., Kazin, E., Muna, D., Weaver, B. A., & Price-Whelan, A. 2011, AJ, 142, 31
Bundy, K., Bershady, M. A., Law, D. R., et al. 2015, ApJ, 798, 7
Buta, R., & Combes, F. 1996, Fund. Cosmic Phys., 17, 95
Cherinka, B., Andrews, B. H., Sanchez-Gallego, J., et al. 2019, AJ, 158, 74
Cid Fernandes, R., Stasińska, G., Mateus, A., & Vale Asari, N. 2011, MNRAS, 413, 1687
Comerón, S., Salo, H., Laurikainen, E., et al. 2014, A&A, 562, A121
Connolly, A. J., Szalay, A. S., Bershady, M. A., Kinney, A. L., & Calzetti, D. 1995, AJ, 110, 1071
Crocker, A. F., Bureau, M., Young, L. M., & Combes, F. 2011, MNRAS, 410, 1197
Crowl, H. H., & Kenney, J. D. P. 2008, AJ, 136, 1623
Deeley, S., Drinkwater, M. J., Sweet, S. M., et al. 2020, MNRAS, 498, 2372
Deeley, S., Drinkwater, M. J., Sweet, S. M., et al. 2021, MNRAS, 508, 895
Dekel, A., & Birnboim, Y. 2006, MNRAS, 368, 2
Dekel, A., Freundlich, J., Jiang, F., et al. 2021, MNRAS, 508, 999
Dekel, A., Lapiner, S., & Dubois, Y. 2019, arXiv:1904.08431
Dey, A., Schlegel, D. J., Lang, D., et al. 2019, AJ, 157, 168
Diaz-Garcia, S., Diaz-Suarez, S., Knapen, J. H., & Salo, H. 2019, A&A, 625, A146
Domínguez-Sánchez, H., Bernardi, M., Nikakhtar, F., Margalef-Bentabol, B., & Sheth, R. K. 2020, MNRAS, 495, 2894
Domínguez-Sánchez, H., Huertas-Company, M., Bernardi, M., Tuccillo, D., & Fischer, J. L. 2018, MNRAS, 476, 3661
D'Onofrio, M., Marziani, P., & Buson, L. 2015, FrASS, 2, 4
Dressler, A., Oemler, A., Jr, Couch, W. J., et al. 1997, ApJ, 490, 577
Eliche-Moral, M. C., Rodriguez-Perez, C., Borlaff, A., Querejeta, M., & Tapia, T. 2018, A&A, 617, A113
Falcón-Barroso, J., Sánchez-Blázquez, P., Vazdekis, A., et al. 2011, A&A, 532, A95
Fasano, G., Poggianti, B. M., Couch, W. J., et al. 2000, ApJ, 542, 673
Fernandez, J., Alonso, S., Mesa, V., Duplancic, F., & Coldwell, G. 2021, A&A, 653, A71
Fischer, J. L., Domínguez-Sánchez, H., & Bernardi, M. 2019, MNRAS, 483, 2057
Fraser-McKelvie, A., Aragón-Salamanca, A., Merrifield, M., et al. 2018, MNRAS, 481, 5580
Gomes, J. M., Papaderos, P., Vílchez, J. M., et al. 2016, A&A, 585, A92
Jiménez-Palau, C., Solanes, J. M., Perea, J. D., del Olmo, A., & Tous, J. L. 2022a, MNRAS, 515, 3956
Jiménez-Palau, C., Solanes, J. M., Perea, J. D., del Olmo, A., & Tous, J. L. 2022b, VizieR On-line Data Catalog: J/MNRAS/515/3956
Kalinova, V., Colombo, D., Sanchez, S. F., et al. 2021, A&A, 648, A64
Lacerda, E. A. D., Cid Fernandes, R., Couto, G. S., et al. 2018, MNRAS, 474, 3727
Larson, R. B., Tinsley, B. M., & Caldwell, C. N. 1980, ApJ, 237, 692
Mapelli, M., Rampazzo, R., & Marino, A. 2015, A&A, 575, A16
Maschmann, D., Melchior, A.-L., Mamon, G. A., Chilingarian, I. V., & Katkov, I. Y. 2020, A&A, 641, A171
Masters, K. L., Nichol, R. C., Haynes, M. P., et al. 2012, MNRAS, 424, 2180
Moore, B., Lake, G., Quinn, T., & Stadel, J. 1999, MNRAS, 304, 465
Morganti, R., De Zeeuw, P. T., Oosterloo, T. A., et al. 2006, MNRAS, 371, 157
Nulsen, P. E. J. 1982, MNRAS, 198, 1007
Poggianti, B. M., Fasano, G., Bettoni, D., et al. 2009, ApJL, 697, L137
Prieto, M., Eliche-Moral, M. C., Balcells, M., et al. 2013, MNRAS, 428, 999
Querejeta, M., Eliche-Moral, M. C., Tapia, T., et al. 2015, A&A, 573, A78
Quilis, V., Moore, B., & Bower, R. 2000, Sci, 288, 1617
Rathore, H., Kumar, K., Mishra, P. K., Wadadekar, Y., & Bait, O. 2022, MNRAS, 513, 389
Salim, S., Boquien, M., & Lee, J. C. 2018, ApJ, 859, 11
Salim, S., Fang, J. J., Rich, R. M., Faber, S. M., & Thilker, D. A. 2012, ApJ, 755, 105
Salim, S., & Rich, R. M. 2010, ApJL, 714, L290
Sheth, K., Regan, M., Hinz, J. L., et al. 2010, PASP, 122, 1397
Smee, S. A., Gunn, J. E., Uomoto, A., et al. 2013, AJ, 146, 32
Solanes, J. M., & Salvador-Sole, E. 1992, ApJ, 395, 91
Springel, V., Pakmor, R., Pillepich, A., et al. 2018, MNRAS, 475, 676
Tapia, T., Eliche-Moral, M. C., Aceves, H., et al. 2017, A&A, 604, A105
Tempel, E., Tuvikene, T., Kipper, R., & Libeskind, N. I. 2017, A&A, 602, A100
Tous, J. L., Solanes, J. M., & Perea, J. D. 2020, MNRAS, 495, 4135
Villa-Vargas, J., Shlosman, I., & Heller, C. 2010, ApJ, 719, 1470
Welch, G. A., & Sage, L. J. 2003, ApJ, 584, 260
Westfall, K. B., Cappellari, M., Bershady, M. A., et al. 2019, AJ, 158, 231
Wilman, D. J., & Erwin, P. 2012, ApJ, 746, 160
Xiao, M.-Y., Gu, Q.-S., Chen, Y.-M., & Zhou, L. 2016, ApJ, 831, 63
Zhou, Z., Ma, J., & Wu, H. 2021, AJ, 161, 260

5 ACTIVITY PROFILES

In our latest paper (Tous et al. submitted), we use the same procedure of Tous et al. (2023) on spatially resolved optical spectra of 1072 S0 galaxies from the final release of MaNGA. The objective is to assess the radial activity configuration of these objects as a function of mass, age, ellipticity and kinematics of the stars, as well as the environment.

Activity profiles are derived by stacking[1] spaxels into radial bins within 1.5 R_e, projecting the resulting spectral profile into the plane PC1–PC2, and using equation 2 from Jiménez-Palau et al. (2022b) to determine the intensity of activity, ΔPS, as a function of galactocentric distance. The sign of their activity gradients, estimated from the orientation of the profiles in the plane PC1–PC2, is compared with the BPT and PCA classifications assigned to their integrated, 3-arcsec spectra, and with their specific star formation rate (SSFR) relative to the main sequence of SF galaxies.

The comparison demonstrates a close correlation between the sign of the radial activity gradient in S0 galaxies and their global activity status. PS lenticulars often show low-level, flat activity profiles, although a significant number of them also show positive activity gradients. Conversely, AC lenticulars generally have negative gradients, usually associated with main sequence SSFRs and, sometimes, with Seyfert emission. A fraction of the AC galaxies also shows radial activity profiles with positive gradients, which become more abundant with increasing stellar mass regardless of environmental density. The median activity profile of the AC lenticulars with negative gradients experiences at all radii a systematic reduction in its activity level with stellar mass, consistent with expectations from the main sequence of SF galaxies. Conversely, PS lenticulars with positive activity gradients show the opposite behaviour. Furthermore, systems whose activity is dominated by star formation are structurally rounder than the rest of S0s, while those classified as Seyfert exhibit higher rotational support.

We also evaluate the consistency of our findings regarding the activity configuration of nearby S0 galaxies with predictions from the literature for the main evolutionary pathways of these objects. All in all, our results seem to align with a scenario where negative and positive activity gradients in S0s may result from rejuvenation by both minor and tiny mergers.

1 I developed the stacking algorithm presented in Section 3.1 of Tous et al. (submitted) years ago as part of my Master's thesis. In Navó et al. (2019), we adapted the algorithm so that it could be applied in the identification of thin absorption lines produced by neutron-capture elements from medium-resolution stellar spectra. The published version of the latter paper is included in Appendix A.

MNRAS 000, 1–20 (2023) Preprint 28 December 2023 Compiled using MNRAS LATEX style file v3.0

The local Universe in the era of large surveys - III. Radial activity profiles of S0 galaxies

J. L. Tous[1,2]★, J. M. Solanes[1,2], J. D. Perea[3] and H. Domínguez-Sánchez[4]
[1]Institut de Ciències del Cosmos (ICCUB), Universitat de Barcelona, Martí i Franquès 1, E-08028 Barcelona, Spain
[2]Departament de Física Quàntica i Astrofísica, Universitat de Barcelona, Martí i Franquès 1, E-08028 Barcelona, Spain
[3]Departamento de Astronomía Extragaláctica, Instituto de Astrofísica de Andalucía, IAA-CSIC, Glorieta de la Astronomía s/n, E-18008 Granada, Spain
[4]Centro de Estudios de Física del Cosmos de Aragón (CEFCA). Plaza San Juan, 1, E-44001, Teruel, Spain

Accepted XXX. Received YYY; in original form ZZZ

ABSTRACT

Spatially resolved MaNGA's optical spectra of 1072 present-day lenticular (S0) galaxies, dimensionally reduced from a principal component analysis (PCA), are used to determine their radial activity structure shaped by any possible nebular ionization source. Activity profiles within 1.5 R_e are examined in tandem with the mass, age, ellipticity and kinematics of the stars, as well as environmental density. Among the results of this comparison, we find that the sign of the radial activity gradient of S0s is tightly related to their PCA classification, BPT designation, and star formation status. PCA-passive lenticulars often show low-level, flat activity profiles, although there is also a significant number of systems with positive gradients, while their less common active counterparts generally have negative gradients, usually associated with high SSFRs and, sometimes, moderate Seyfert emission. A fraction of the latter also shows radial activity profiles with positive gradients, which become more abundant with increasing stellar mass regardless of environmental density. Our analysis also reveals that the subset of active S0s with negative gradients experiences at all galactocentric radii a systematic reduction in its median activity level with stellar mass, consistent with expectations for main sequence galaxies. In contrast, passive S0s with positive gradients show the opposite behaviour. Furthermore, systems whose activity is dominated by star formation are structurally rounder than the rest of S0s, while those classified as Seyfert exhibit higher rotational support. The possibility that negative and positive activity gradients in S0s may result from rejuvenation by two distinct types of minor mergers is raised.

Key words: galaxies: active; galaxies: elliptical and lenticular, cD; galaxies: evolution; galaxies: Seyfert; galaxies: star formation; galaxies: statistics

1 INTRODUCTION

Astronomers have known of the existence of lenticular galaxies (S0s) almost as long as they have known that there are other galaxies besides the Milky Way (Hubble 1926). While it is widely accepted that most spiral galaxies (Sps) emerge from the collapse of primordial vast clouds of gas and dust and subsequent gas-rich mergers that took place in the early Universe (but see Hammer et al. 2009; Graham 2023), and that most elliptical galaxies (Es) have formed from the (often multiple) collisions and mergers of similarly sized galaxies, the formation channel(s) of present-day S0s is (are) still subject to debate. The reason is that, unlike the other two major morphological classes mostly found in specific environments – Sps in the field and Es around clusters and groups of galaxies – S0s are relatively abundant in both low- and high-density regions, which points to a complex evolutionary history that may include various pathways.

Numerical simulations of galaxy interactions show that, in the field or in small groups, S0 galaxies can evolve from mergers, either minor, involving pure discs with small companions, or major between pairs of gas-rich, star-forming (SF) Sps (Querejeta et al. 2015; Tapia et al. 2017; Eliche-Moral et al. 2018), a scenario that is supported by observations such as those analysed in Maschmann et al. (2020). In contrast, physical processes of a complete different nature involving hydrodynamic interactions between the interstellar and intergalactic media (abbreviated ISM and IGM, respectively; Gunn & Gott 1972; Nulsen 1982), probably assisted by other mechanisms such as galaxy harassment or strangulation (Larson et al. 1980; Moore et al. 1999), are expected to transform Sps into S0s mainly within virialised galaxy clusters (e.g. Solanes & Salvador-Sole 1992; Dressler et al. 1997; Fasano et al. 2000; Quilis et al. 2000; Crowl & Kenney 2008; Poggianti et al. 2009; D'Onofrio et al. 2015).

It is also becoming increasingly clear that star formation in early-type galaxies (ETGs) – especially among S0s – is not a stand-alone event. There is, for example, the study by Kaviraj et al. (2007) which, in a sample of ~ 2100 ETGs that combined UV and optical photometry, found traces of recent star formation in around 30 per cent of the galaxies. Likewise, Salim et al. (2012), starting from a small sample of galaxies in the optical red sequence with a strong UV excess but an inactive optical spectrum, determined that galaxy-scale star formation in ETGs is almost exclusively an S0 phenomenon, present in approximately 20 per cent of these objects but practically absent in Es, therefore highlighting the importance of having a disc compo-

★ E-mail: jtous@fqa.ub.edu

nent to enable extended star formation (see also Méndez-Abreu et al. 2019).

The study of the origin of lenticular galaxies has recently been boosted by the incorporation of extensive spectroscopic data, both integrated and spatially resolved. Works based on this type of metric have revealed that the S0s show a significant variance in their structural, kinematic and dynamic properties pointing to a bimodality in this population (e.g. Xiao et al. 2016; Fraser-McKelvie et al. 2018; Domínguez Sánchez et al. 2020; Deeley et al. 2020; Rathore et al. 2022; Coccato et al. 2022), which is problematic to explain by appealing to a single formation channel for these objects. This more than likely multiplicity of evolutionary pathways has also been confirmed by the diverse formative histories associated with galaxies identified with present-day S0s in the newest, state-of-the-art cosmological hydrodynamic simulations that seek to replicate the data provided by large-scale observational studies (e.g. Deeley et al. 2021).

This paper is the third in a series dedicated to investigate S0 galaxies within the local Universe ($z \lesssim 0.1$) from the wealth of information contained in their optical spectra. These works aim to increase understanding of the physical properties of the members of this morphological class that connects the two ends of the Hubble sequence, with the ultimate goal of providing added insight into the possible formation channels followed by these objects. In our first study (Tous et al. 2020; hereafter TSP20), we identified three classes of present-day S0s according to their level of activity[1] from a sample of ∼ 68,000 of these systems. Our classification is based on the clustering shown by these galaxies in the plane defined by the first two eigenvectors derived from the Principal Component Analysis (PCA) of their integrated optical spectra included in the twelve Data Release of the Sloan Digital Sky Survey (SDSS-DR12; Alam et al. 2015). The projections of the individual S0 spectra onto this 2D subspace are distributed in two clearly delineated regions: the most populated one, which we call the passive sequence (PS), is a compact strip that contains systems conforming to the traditional view of these galaxies as inactive objects, while about a quarter of the local S0 population resides in an extended active cloud (AC), formed by systems with significant nebular emission and high specific star formation rates (SSFR) $\sim 10^{-10.3}$ yr^{-1}, similar in some cases to those observed in late Sps. Both areas of the diagram are separated by a narrow dividing zone that constitutes the transition region (TR), inhabited by a small fraction of lenticular galaxies with intermediate spectral properties (see also Section 3.2 in this work).

In a second paper (Jiménez-Palau et al. 2022), we concentrated our efforts on comparing the outcomes of our PCA spectral classifier of S0 galaxies with those delivered by well-known taxonomic paradigms of activity, such as the BPT (Baldwin et al. 1981) and WHAN (Cid Fernandes et al. 2010) diagrams, as well as other conventional activity diagnostics defined in the radio, mid-infrared, and X-ray domains. In this work, we demonstrated that our definition of the PCA spectral classes correlates very strongly with the distance of galaxies to the ridge line of the PS in the PC1–PC2 subspace

$$\mathrm{PC2} = -1.162 \cdot \mathrm{PC1} - 2.932 \,, \tag{1}$$

which is given by the equation:

$$\Delta\mathrm{PS} = \log\left[2.913 + 0.758 \cdot \mathrm{PC1} + 0.652 \cdot \mathrm{PC2}\right] \,, \tag{2}$$

thus reducing in practice the PCA taxonomy to a one-dimensional classifier of activity. In addition to making it possible the compression of the optical spectra of S0 galaxies into a single parameter, this distance is an excellent proxy for the equivalent width (EW) of the Hα emission, to the point that the constant values of ΔPS used to set the PS/TR and TR/AC dividers, 0.23 and 0.44, respectively (see also Fig. 1), bear a one-to-one correspondence with the 3 and 6 Å horizontal demarcations of the EW(Hα) in the WHAN diagram. With regard to the sources of activity, we showed that the AC–S0 subpopulation contains a mixture of SF galaxies (which are the majority) and mostly low-power (i.e. Seyfert 2) AGNs, while LINERs and retired galaxies make up, respectively, the bulk of the TR and PS spectral classes. We also found evidence that most of the nebular emission of Seyfert and LINER S0 systems detected in radio and X-ray is not driven by star birth, and that the dominant ionising radiation for a good number of LINERs could come from post-AGB stars. All these findings inevitably raise questions about the mechanisms that trigger the episodes of activity in lenticular galaxies.

Recently, in Tous et al. (2023), we have made our first attempt to answering these queries, aided by integral field spectroscopic data from 532 S0 galaxies drawn from the first data release of the Mapping Nearby Galaxies at Apache Point Observatory (MaNGA; Bundy et al. 2015) survey. In such work, we have put the focus on aspects exclusively related to star-formation activity and, in particular, to the presence in these galaxies of SF rings in the EW(Hα). Assessment of these ringed structures indicates that they are relatively abundant (∼ 30 per cent on average) in fully-formed S0s, but with a frequency that sharply increases with the mass of the hosts, that they are twice more frequent among the members of the PS class than in AC–S0s, that they likely feed on residual gas from the discs, and that their formation is not influenced by the environment. These results suggest, in good agreement with cosmological simulations, that the formation of these Hα rings is possibly associated with the capture by the S0s of tiny dwarf satellites that closely orbit them.

In this new paper, we aim to characterize in detail the radial structure of activity defined by the baryonic content of lenticular galaxies with the expectation of providing further clues regarding the evolutionary history of this morphological family. For this task, we shall rely again on spatially resolved spectroscopic observations, in this case on a sample of 1072 present-day S0s drawn from the final data release of the SDSS-IV MaNGA survey. In Section 2, we present these spectral data and the ancillary properties that are used throughout this study, while the processing of the MaNGA data cubes is described in Section 3. After identifying the main sources of activity in our S0 sample (Section 4), we determine in Section 5 the typical shapes of the radial activity profiles of the different spectral classes of these systems and examine their relationship with a number of physical magnitudes that are traditionally used to diagnose galaxy evolution. Finally, in Section 6, we review the agreement of our results regarding the activity morphology of nearby S0 galaxies with predictions from the main evolutionary channels of these objects proposed in the literature. Section 7 provides a summary of this work. The manuscript also includes an Appendix A where we test the robustness of our results against morphological contamination.

The values of all cosmology-dependent quantities used in the paper have been calculated by assuming a concordant flat ΛCDM universe with parameters $H_0 = 70$ km s^{-1} Mpc^{-1} and $\Omega_\mathrm{m} = 1 - \Omega_\Lambda = 0.3$.

2 THE DATA

We use the data cubes from the final data release (DR17, Abdurro'uf et al. 2022) of the Mapping Nearby Galaxies at Apache Point Ob-

[1] In all papers that conform to this investigation, activity must be understood in a broad sense that includes ongoing star formation, black hole accretion, and/or any other internal source of ionisation of the IGM.

servatory (MaNGA) survey (Bundy et al. 2015), which is part of the Sloan Digital Sky Survey IV (SDSS, Blanton et al. 2017). This survey provides spatially resolved spectroscopic information up to 1.5 effective radii (R_e) in the r band[2] for a sample of $\sim$ 10000 nearby ($\tilde{z} \sim 0.03$) galaxies observed in the visible (3500 – 10000 Å) with a spectral resolution of $R = \lambda/\mathrm{FWHM} \sim 2000$ (Smee et al. 2013), a spatial resolution of $\sim$ 1 kpc at the median redshift $\tilde{z}$ of the sample. We also use the 2D maps of physical parameters from both the continuum and the ionized emission lines produced by the Data Analysis Pipeline (DAP) of MaNGA (Westfall et al. 2019) through the HYB10-MILESHC-MASTARHC2 analysis approach. We extract from these maps the in-plane disc radial coordinate of the M spaxels of each galaxy in the dimensionless form $R' \equiv R/R_e$, as well as the line-of-sight stellar velocity and velocity dispersion. These data are accessed and manipulated with the aid of the Marvin[3] toolkit (Cherinka et al. 2019).

Lenticular galaxies are selected from the MaNGA Deep Learning Morphological value added catalogue (MDLM-VAC-DR17) of Domínguez Sánchez et al. (2022). Following this work, our S0 sample is defined from the numerical Hubble stage, T, the probability that a galaxy is of late-type, P_{LTG}, and the probability that an early-type looking object is truly an S0, P_{S0}, by applying the conditions $T < 0.5$, $P_{\mathrm{LTG}} < 0.5$, and $P_{\mathrm{S0}} > 0.5$. These restrictions are fulfilled by 1283 galaxies, which reduce to 1072 once we remove a few problematic cases flagged by the MaNGA Data Reduction Pipeline (DRP), as well as those galaxies for which we detect, after a careful visual inspection of the SDSS colour images, a hint of spiral structure, and or contaminating foreground stars, companion galaxies, or both within the MaNGA's field of view.

The global activity status of each one of the S0s, which we define by their spectral class, is determined from our own PCA-based classification (see also Section 3.2). For most galaxies, we are able to directly use the class assigned in TSP20 from their distance to the ridge of the passive sequence (ΔPS; see eqs. (1) and (2)) measured in the latent space produced by the first two principal components (PC) of the single-fibre SDSS spectra of the present-day S0 galaxy population. However, there are 128 galaxies in our current sample that are not included in the SDSS Legacy Survey or that, although they are part of it, have not received a spectral classification because of problems with their single-fibre spectra (e.g. an excessive number of masked regions). For these objects, we first synthesize their integrated spectra by emulating the three-arcsecond aperture of the SDSS fibres from the MaNGA data cubes and then project the synthetic spectra onto the PC1–PC2 subspace to determine the spectral class. We have verified that the results of this work do not change if these 128 galaxies are excluded. By proceeding in this way, we find that our MaNGA S0 sample contains a total of 781 galaxies of the PS spectral class, 199 of the AC class, and 92 TR objects (see Table 1).

The spectral information is extended with several physical magnitudes that are relevant for the aims of this work. Thus, we include for a great deal of the MaNGA S0s the values of their local environmental density estimated in TSP20. They consist on the percentile associated to this property when it is calculated from the average projected distance between a galaxy and its first five neighbours with recessional velocities less than 1000 km s^{-1} from it in the deepest volume-limited region that can be defined for the central object in the $z < 0.1$ subset of the SDSS Legacy Survey (see eqs. (1) and (2) in this work). We also retrieve, for most galaxies, their global stellar mass, M_*, and star formation rate (SFR) by crossmatching our dataset with the GALEX-SDSS-WISE Legacy Catalog 2 (GSWLC-2; Salim et al. 2018a), while the luminosity- and mass-weighted mean ages of the stellar populations are obtained from the MaNGA Pipe3D value added catalogue for those galaxies with a null QCFLAG (Sánchez et al. 2016a,b, 2022). The best estimates of the apparent axis ratio b/a in the r band, taken from the latest version of the PyMorph photometric catalogue (Domínguez Sánchez et al. 2022), are used to determine the ellipticity of each galaxy, defined as $\varepsilon = 1 - b/a$. Finally, we infer for all our galaxies their observed projected stellar angular momentum per unit mass, λ_{R_e}, by adopting the definition introduced by Emsellem et al. (2007):

$$\lambda_{R_e} = \frac{\sum_{j=1}^{M_e} R_j F_j |V_j|}{\sum_{j=1}^{M_e} R_j F_j \sqrt{V_j^2 + \sigma_j^2}}\,, \tag{3}$$

where F, V, and σ are, respectively, the flux, and the stellar rotational velocity and velocity dispersion corrected for instrumental resolution of the jth spaxel, and the sum runs over the M_e spaxels within elliptical isophotes of mean radius $R = a\sqrt{1-\varepsilon}$ out to 1 R_e.

3 DATA CUBE PROCESSING

Next, we proceed to divide the MaNGA data cubes into annuli by grouping the individual spectra of the spaxels into ten circularized radial bins defined in terms of the dimensionless variable R' (assigned to each spaxel by the DAP) using steps of $0.15R'$ within the interval $[0, 1.5]$.

3.1 Build-up of the radial composite spectra

In order to stack the spectral information of the spaxels included within a radial bin, we follow a method that is an adaptation of the one used in Navó et al. (2019; see also Mas-Ribas et al. 2017). To begin with, we exclude from the stacking any spaxel with S/N < 5. Next, for those spaxels above this limit, we mask any problematic flux element flagged by the MaNGA's DRP, as well as those flux elements in wavelength ranges that are usually affected by sky lines. Nonetheless, we have observed that unrealistic flux values sometimes escape detection by these filters and end up contributing to the final composite spectrum. Although only about one per cent of the processed spaxels contain one or more glitches, they can greatly influence the PCA. To limit as much as possible the presence of these false emission lines, we apply the following procedure to identify and mask them:

(i) For a given spectrum, the maximum flux value is determined every 50 consecutive elements of the flux vector.

(ii) From the distribution of maximum flux values, a threshold is established above of which any flux value will be considered as a potential glitch candidate. The threshold is defined as the sum of the third quartile and 10 times the interquartile range (IQR) of the distribution of maximum flux values. The arbitrary factor multiplying the IQR has been chosen to make the threshold lay above most of the actual strong emission lines.

(iii) To ensure that any real emission line is not being masked,

[2] Although $\sim 1/3$ of the MaNGA galaxies are covered up to $2.5\,R_e$, in this work we restrict the analysis to the information contained within $1.5\,R_e$ to maximise sample size.

[3] https://sdss-marvin.readthedocs.io/en/stable/

the candidate glitches are cross-checked against an extensive list of known emission lines[4].

(iv) Candidate glitches are considered true glitches either if they are located at a distance larger than 3 Å from any of the known emission lines, or if they are near a known emission line but have a maximum flux value which is at least 1.2 times larger than the highest of the peak value of the fluxes of the lines [O III] λ 4960, [O III] λ 5008, H β, H α, or [N II] λ 6585 of the same spectrum.

Any spaxel that after this second filtering step has more than 10 per cent of its flux elements masked is also discarded. Retained spectra are then corrected for Galactic dust reddening using a standard Fitzpatrick (1999) dust extinction model. To do so, we determine the total extinction at V, A_V, by renormalizing the extinction coefficient of each object in the g band listed in the NASA-Sloan Atlas catalog (Blanton et al. 2011) by the factor $R_V/R_g = 0.82$. Individual spectra are subsequently shifted to the laboratory rest-frame through the following expression that removes the recessional velocity of each galaxy and the mean rotation speed from each spaxel: $\log \lambda_r = \log \lambda_o - \log(1+z) - \log(1+v/c)$, where λ_r and λ_o are, respectively, the rest-frame and observed wavelengths, while v is the rotational velocity of the spaxel. The flux and associated error vectors are re-binned by interpolating into new intervals with the same constant logarithmic spacing of 0.0001 of the original spectra.

Then, we determine the normalization factor for each individual spectrum, which for a given galaxy is defined as

$$n_j = \sum_{i=1}^{N_j^c} \frac{f_{ij}}{N_j^c} \, , \tag{4}$$

where f_{ij} is the ith flux element or wavelength bin of the jth spaxel of the galaxy, f_j, and the summation runs over the N_j^c flux elements of this spaxel included in the four rest-frame wavelength intervals 4200 – 4300, 4600 – 4800, 5400 – 5500, and 5600 – 5800 Å that are good representatives of the continuum (Dobos et al. 2012). Besides, to weight each spaxel in a manner that penalizes the noisiest ones, we also compute the S/N of the continuum,

$$w_j = n_j \left(\sum_{i=1}^{N_j^c} \frac{e_{ij}^2}{N_j^c} \right)^{-1/2} \, , \tag{5}$$

where e_{ij} is the error associated with the ith flux element of the spectrum of the jth spaxel and the summation runs over the same wavelength intervals defined for equation (4). Note that N_j^c may differ from one individual spectrum to another depending on the number of masked flux elements that fall on the adopted continuum regions. Spaxel spectra with more than 20 per cent of masked flux values within these intervals are discarded too.

Finally, we derive the composite spectrum for the kth radial bin of a galaxy by means of the equation

$$\bar{f}_k = \sum_{j=1}^{M_k} w_j \frac{f_j}{n_j} \left(\sum_{j=1}^{M_k} w_j \right)^{-1} \, , \tag{6}$$

where the summation runs over the M_k spaxels included in this radial bin. We restrict this calculation to radial bins for which at least 20 per cent of their spaxels have spectra that meet the aforementioned quality conditions.

After applying this stacking process, the total spectral information of all the galaxies in our sample is stored in a single large matrix that contains, for each galaxy, $k \leq 10$ rows or elements of the radial composite spectra and $\sim$ 3300 columns, one per each flux element of the radial flux arrays.

3.2 Dimensionality reduction through PCA

To facilitate the interpretation of the information encoded in the radial spectra of galaxies, we now proceed to radically reduce their dimensionality but keeping most of the variance contained in the original 2D arrays. As was done in the two previous papers of this series (TSP20, Jiménez-Palau et al. 2022), as well as in Tous et al. (2023), to accomplish this we apply a multivariate analysis statistical technique known as PCA. In short, this information compression method transforms the original flux arrays by rotating the N-dimensional space defined by their flux elements into a new orthogonal coordinate system whose eigenvectors are both oriented along the directions in which the variance of the data is maximized and ranked in decreasing order according to the fraction of the total variance they encapsulate. This allows one to replace the initial highly-dimensional space with a low-dimension space defined by a few first eigenvectors or principal components using the tuples of scalars that result from projecting the original spectra onto such eigenvectors[5] with a minimal loss of information (see TSP20 for more information on this technique).

As in TSP20, we restrict the current analysis to the first two principal components, since they already offer a very complete description of the variance of the spectra of present-day S0 galaxies. Unsurprisingly, the representation we obtain of the MaNGA's radial composite spectra in the PC1–PC2 subspace defined by TSP20 bears a great similarity to that inferred in this previous work from a much larger sample of single-fibre SDSS spectra of nearby S0s ($z \lesssim 0.1$). As shown in Fig. 1, we have, on one hand, a narrow and densely populated diagonal band delineated by the clustering of the projections of fully passive spectra from objects that belong to the PS class. This region is characterized by a sharp linear ridge that crosses the subspace from small/large values of PC1/PC2 to larger/smaller values, and that sets the zero point that we use for the spectral classification of the S0s (see also Jiménez-Palau et al. 2022). On the other hand, a much more dispersed group of data can be observed to the right of the passive sequence, which extends over a large area of the subspace. This cloud of points encompasses all the radial composite spectra that exhibit emission lines – the relevance of which progressively increases as they move away from the PS ridge – and which are all part of the AC class. Between these two main areas of the diagram, it is possible to identify, in a very narrow strip that runs parallel to the PS ridge, spectra of the TR class, with intermediate characteristics from those of the two previous groups.

Our PCA-based taxonomy of galaxy spectra has several advantages compared to more traditional procedures, among them the fact that it is a versatile methodology applicable to any galaxy, irrespective of its activity level. In contrast, common diagnostics in the literature like the BPT and WHAN diagrams, rely on the flux (ratios) of a few specific emission lines (H α, H β, [N II], [O III], ...), making them less effective for classifying spectra with low signal-to-noise ratios or

[4] Retrieved from http://astronomy.nmsu.edu/drewski/tableofemissionlines.html conveniently converted from air to vacuum wavelengths as stated in https://www.sdss4.org/dr17/spectro/spectro_basics/.

[5] By abuse of language, the term principal component is often used interchangeably both for the eigenvectors and for the scalar coefficients associated with the projections of the data on them.

lacking these lines, as in classical ETGs. Since our approach utilizes the entire optical spectrum, it also eliminates the need for continuum subtraction, for which there is no standardised procedure. Furthermore, our spectral classification stems from purely mathematical arguments derived from the observed distribution of the principal components in the latent space, avoiding the necessity for a priori assumptions about the physics of galaxies to define model-based or theoretically motivated dividers. And while the quantities derived from PCA are not necessarily physical parameters, this method allows us to explore whether it is possible to characterize gas ionization in galaxies more optimally than through the physical properties used in emission-line-based diagnostics. As discussed in Section 4, our analysis yields indicators that are effective proxies for well-known specific sources of gas ionisation.

In comparing the outcomes from the PCA of the MaNGA and SDSS spectra of S0 galaxies, it is important to remark that the direction of the PS ridge (equation (1) and dashed line in Fig. 1) has not changed. Although the instrument used in obtaining the spectra of both samples is the same, as it is the way of presenting the data to the PCA, the differences in the spatial coverage of the observations, in the dynamic range of the targeted objects, and even in the methodology and strictness adopted in the morphological identification of the S0s, will necessarily translate into a different covariance matrix and result in the reorientation of the orthogonal base of eigenvectors derived from the PCA decomposition of the MaNGA data. However, the contribution to the total variance of these factors is expected to be quite moderate and have a minimum impact on the firsts principal components. In fact, we have verified that the reorientation of the MaNGA's eigenbasis hardly affects the first two principal components, and therefore neither does it affect the projections of its spectra on said axes, the changes only beginning to be noticeable from the third component. This invariance is also transferred to the PS ridge lines deduced from the MaNGA and SDSS spectra which, calculated in the same PC1–PC2 plane, have orientations that differ by less than one degree and intercepts that differ by just one tenth. Thus, the use in this work of the same PC1–PC2 subspace, PS ridge line, and ΔPS demarcations defined in Jiménez-Palau et al. (2022) to classify the radial composite spectra of the MaNGA S0 sample is fully justified.

3.3 Vectorization of the projected spectra

The fact that a large part (∼ 87 per cent) of the sample variance of the radial spectral profiles is captured by their first two principal components allows us to carry out the analysis of the MaNGA's spectra using their set of projections in the more convenient PC1–PC2 latent space[6], where such profiles are much easier to handle and interpret. Moreover, the approximate linear behaviour shown by most of these strings of PC1 and PC2 components makes it possible to further streamline their analysis without missing essential information. This additional simplification consists in approximating the PC1–PC2 representations of the radial profiles with best-fitting straight lines, which are then converted into vectors using the projections of the PC1–PC2 coordinates of the innermost and outermost radial bins of the spectra on such lines to set, respectively, the tail and tip of the arrows. To objectively identify the few profiles that do not admit a good vectorization (see, e.g., the profile in Fig. 2 associated with a brown vector in the right-hand panel), we have computed two ad-hoc parameters that measure the goodness of such representation. The

[6] The first five eigenvectors, including the two that define this PC1–PC2 latent space, are publicly available in Jiménez-Palau et al. (2022).

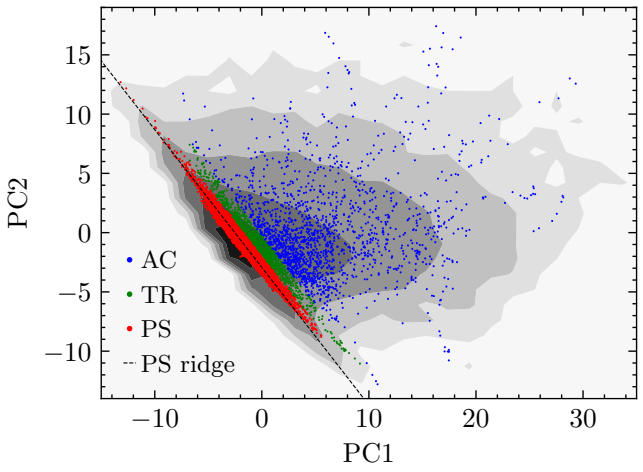

Figure 1. PC1 and PC2 components of the radial composite spectra of the 1072 lenticular galaxies included in our MANGA S0 sample projected onto the eigenbasis defined in TSP20 from a sample of more than 68,000 SDSS spectra of present-day ($z \lesssim 0.1$) S0s. The greyscale contours represent equally spaced logarithmic densities of the projections inferred in that work. The radial elements of the composite spectra that belong to the PS ($\Delta\mathrm{PS} < 0.23$), the TR ($0.23 \leq \Delta\mathrm{PS} < 0.44$) and the AC ($\Delta\mathrm{PS} \geq 0.44$) are drawn, respectively, as red, green and blue dots. The black dashed line shows the ridge of the PS given by equation (1).

first one is called the disorder, since it determines the extent to which the projections of the PC1 and PC2 coordinates of the radial bins of a spectrum into the fitted straight line follow the right sequence of radial distances,

$$\delta = \left(\sum_{k=0}^{9} (p_k - k)^2 \right)^{-1/2} , \qquad \{p_k \in \mathbb{Z} \mid 0 \leq p_k \leq 9\} , \tag{7}$$

where p_k is the position of the kth radial bin within the vector components. The second parameter, which we call the entanglement, provides a measure of the degree of linearity of the radial spectral profiles in the PC1–PC2 plane from the ratio between the second and the first singular values, i.e.

$$\epsilon = \frac{\sigma_2}{\sigma_1} , \tag{8}$$

of the 10×2 matrix, M, whose rows are the PC1 and PC2 coordinates of the radial bins of a profile. The singular values are found by diagonalizing $M^T M$:

$$M^T M = V(\Sigma^T \Sigma)V^T , \tag{9}$$

where V is a 2×2 matrix whose columns are the eigenvectors of $M^T M$ and the non-zero elements of the 10×2 rectangular diagonal matrix Σ are the square roots of the non-zero eigenvalues, λ_i, of $M^T M$, so $\sigma_i = \sqrt{\lambda_i}$ with $i = 1, 2$. After some experimentation, we have decided to restrict the vectorization to those profiles that have either $\delta < 7$ for any ϵ or $\delta < 10$ and $\epsilon < 0.06$. About 90 per cent of the galaxies in our sample show radial spectral profiles that are linear according to these criteria. The results of our analysis do not vary if other sensible combinations of upper bounds for these two parameters are considered instead.

The vectorization of the composite radial spectra facilitates their division into separate categories according to their orientation relative to the main ridge of the PS, i.e. according to the sign of the radial gradient of their activity. The latter is given by the polar angle, θ,

Table 1. Number and fraction of S0 galaxies included in the different subsamples considered in this work.

Spectral class	All[a]	W. linear profiles[b]	Outside in[b]	Inside out[b]	Flat[b]
Passive sequence	781 (0.73)	688 (0.73)	31 (0.05)	177 (0.26)	480 (0.70)
Active cloud	199 (0.19)	188 (0.83)	148 (0.79)	30 (0.16)	10 (0.05)
Transition region	92 (0.09)	84 (0.72)	32 (0.38)	27 (0.32)	25 (0.30)
All	1072 (1.0)	960 (0.90)	211 (0.22)	234 (0.24)	515 (0.54)

In parentheses are the fractions of galaxies (^{a}) in each spectral class and (^{b}) with linear profiles in the same spectral class.

of the associated vectors measured counterclockwise from the ridge line. We define three orientation tiers:

- galaxies with $5° < \theta < 175°$, which correspond to objects whose activity grows inside out (IO) up to $\sim 1.5R_e$, i.e. that show a positive radial gradient of activity within this galactocentric radius;
- galaxies with $185° < \theta < 355°$, for which the gradient of activity is negative as it grows outside in (OI)[7]; and
- galaxies with $\theta \in [-5°, 5°] \cup [175°, 185°]$, whose radial activity profiles run essentially parallel to the PS ridge and that, therefore, exhibit a null or flat (F) activity gradient.

As shown in Table 1, the majority (70 per cent) of the PS lenticulars in our sample whose composite radial spectra support vectorization show F-type profiles, while 26 per cent of such systems have IO activity gradients and only a few objects (5 per cent) OI gradients. In the case of the AC class, galaxies with OI gradients clearly dominate (79 per cent), while those with F profiles are in the minority (5 per cent). And for TR class objects, the signs of the radial activity gradients are approximately evenly distributed, although with a slight prevalence of those of type OI. Vice versa, by reading the table from the point of view of the gradients, one can see that 70 per cent of the galaxies with OI activity profiles belong to the spectral class AC, while up to 93 per cent of those with F profiles are PS systems and only less than 2 per cent objects of the AC class. Finally, $\sim$ 3 out of every 4 positive activity gradients (i.e. IO profiles) occur in PS–S0s.

We note that we have chosen not to impose cuts on inclination or apparent size of galaxies relative to the point spread function (PSF) within our S0 sample, after verifying that including objects with extreme values of these observational parameters ($i > 70°$, $\sigma_{PSF}/R_e > 0.5$) does not bias our analysis. While applying these additional selection criteria would result in the exclusion of a non-negligible number of galaxies ($\sim$ 8 and 16 per cent, respectively), the fact that our approach relies on both the sign of activity gradients rather than their specific numerical values, along with the strict angular boundaries we apply to identified a gradient as flat, effectively mitigates the flattening in the radial profiles that oversampled and highly inclined objects can induce. In any case, a thorough examination of the outcomes both before and after implementing the aforementioned cuts to the data, using the same battery of empirical tests outlined in Appendix A, confirms that retaining such galaxies in the sample does not compromise the main findings and conclusions of this study.

[7] Note that these designations may not necessarily indicate inside-out or outside-in quenching, a common terminology used to state that the cessation of star formation progresses from the centre to large radii or vice versa.

4 ACTIVITY PROFILES OF S0 GALAXIES

In this section, we use the PC1 and PC2 coordinates of the radial spectral profiles of our S0 galaxies to derive their corresponding ΔPS profiles in order to infer how activity modulates with galactocentric distance in these objects. Fig. 3 shows the interquartile range of the distributions of the ΔPS profiles for each of the three spectral classes of S0s. Leaving aside the shapes of the corresponding median profiles (solid curves), which are perfectly explained by the data listed in Table 1, a first result that emerges from this graph is that, within the range of galactocentric distances examined by MaNGA, the local estimates of the spectral class of most S0s agree with the global spectral class deduced from their respective 3-arcsec-single-fibre SDSS spectra, regardless of the physical sources of the activity. This is true for nearly 95 per cent of the PS-class galaxies, about 75 per cent of the AC–S0s, and 50 per cent of the TR members, a more than considerable proportion given the narrow range of ΔPS values that define this latter class.

Another interesting result shown in Fig. 3 is that the median radial spectral profile of the subset of AC–S0s assembled from galaxies classified as SF in a classical BPT diagram (dot-dashed blue curve) remains at all radii above, not only of the median profile of the AC subset as a whole, but also of that inferred from their counterparts classified as Seyfert (dotted blue curve), including the innermost region. This suggests that the highest values of ΔPS in present-day S0s will be normally achieved by objects that are actively forming stars (but see next section). However, it must be kept in mind that ΔPS is a *mathematical* parameter sensitive to any type of nebular ionization source that has its reflection in the optical spectra of galaxies, be it ongoing star formation, accretion into central supermassive black holes (SMBH), photoionizing radiation from post-AGB stars, or wind-driven shocks in the ISM. Therefore, before proceeding further, it is important that we gather all the information that can help us identify the main physical mechanisms contributing to ΔPS in each of the three spectral classes of lenticular galaxies.

With this aim, we show in the background of the four panels of Fig. 4 the bivariate distribution of the ΔPS values of the sample of single-fibre S0 spectra studied in TSP20 as a function of their separation from the MS of SF galaxies, ΔMS, using as zero point the ridge line of the star formation peak (cf Renzini & Peng 2015):

$$\Delta\mathrm{MS} = \log\left[\frac{\mathrm{SFR}}{\mathrm{M}_\odot\ \mathrm{yr}^{-1}}\right] - 0.76\log\left[\frac{M_*}{\mathrm{M}_\odot}\right] + 7.6\ . \quad (10)$$

The panels include the ΔPS-based demarcations of our three spectral classes, as well as the same ΔMS dividers used by Bluck et al. (2020) for the general population of galaxies, which we use to assign different statuses to the S0s according to the value of this parameter, that is a measure of the SSFR. We have also overlaid on each panel coloured hexagonal cells that show, from left to right and top to bottom, the distributions of the S0s in that sample classified by Thomas

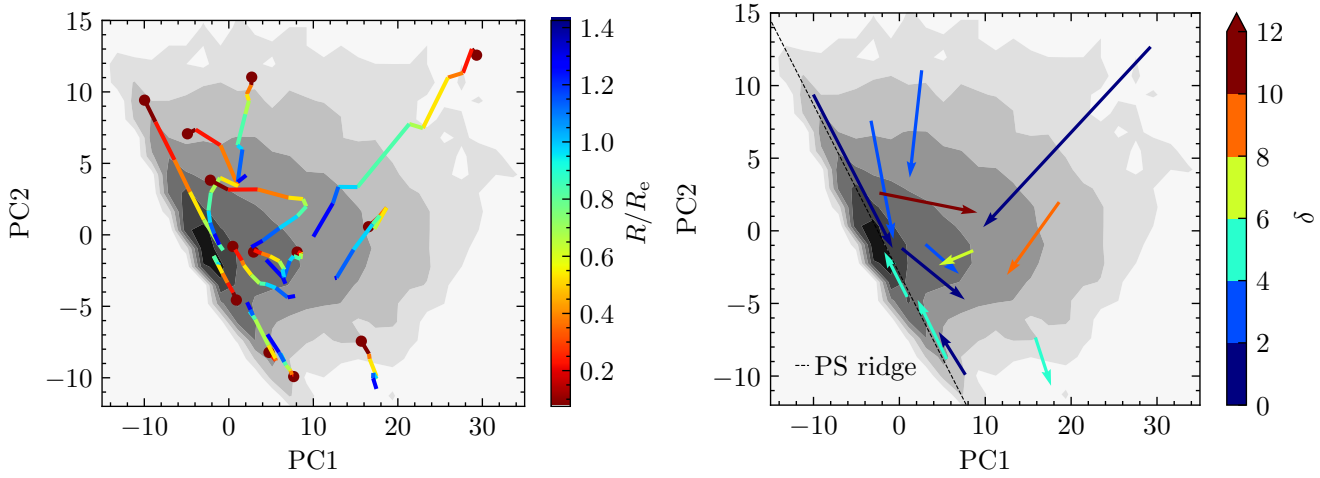

Figure 2. *Left:* radial profiles of a small random subset of the MaNGA S0 sample in the subspace of the first two PCs defined in TSP20 for nearby lenticulars. The composite spectra in each radial bin are coloured according to the galactocentric distance of the bin scaled by the effective radius of the galaxies, with brown dots indicating the position of the central (innermost) bins. *Right:* vectorization of the spectral profiles in the left panel. The colours show the value of δ, one of the two parameters used to evaluate its feasibility (see text). The brown arrow identifies one profile with $\delta \geq 10$, unsuitable for vectorization. The black dotted line shows the PS ridge. In both panels, the greyscale contours are the same as Fig. 1.

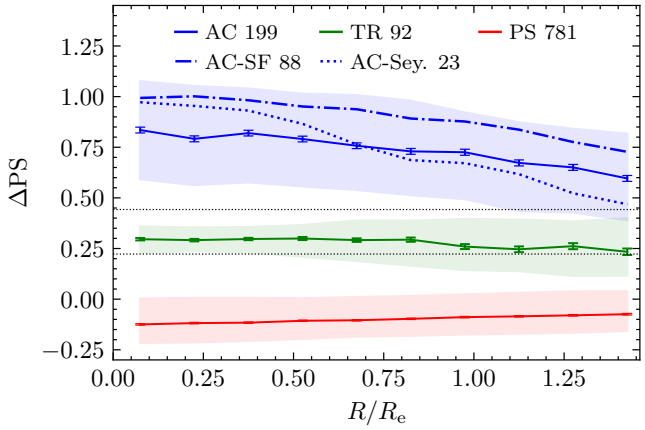

Figure 3. Median radial ΔPS profiles of 1072 present-day S0s observed by MaNGA segregated with respect to spectral class into passive sequence (PS; red), transition region (TR; green), and active cloud (AC; blue) systems. Error bars correspond to the 1σ scatter of the median. Shaded regions show the interquartile range of the profile distribution within each radial bin. For the AC subset, we also show the spectral profiles of galaxies classified by Thomas et al. (2013) as star forming (SF, blue dash-dotted line) and Seyfert (Sey., blue dotted line). The figures in the legend report the total number of objects considered in deriving the statistics for each subset. The horizontal dotted lines, located at 0.23 and 0.44 in ΔPS, indicate the boundaries of the TR as defined in Jiménez-Palau et al. (2022).

et al. (2013), using the standard N II–BPT line-ratio diagnostic, as SF, Seyfert, or LINER, while the fourth panel shows the distribution of those S0s identified as 'blank' because their emission lines were unavailable. Unsurprisingly, the latter are objects that in our PCA-based taxonomic paradigm are included in the PS spectral group and that, for the most part, have negative, uncorrelated ΔPS and ΔMS values, as well as a quiescent status regarding the star formation. On the other hand, the vast majority of both SF- and Seyfert-type lenticulars are found within the AC class. Unlike the above, in the present case both types of objects show a strong positive linear correlation between their values of ΔPS and ΔMS, especially those belonging to the SF category, which, in agreement with the work of Jiménez-Palau et al. (2022), are also by far the most abundant within the AC subpopulation. However, it can be observed that when the AGN activity dominates, star formation tends to be somewhat less important, suggesting negative feedback. In addition, while the maxima of the distributions of both BPT types lie in the MS, Fig. 4 shows that the most active of the AC–S0s are SF objects that extend into the starburst (SB) region, while the least active of these systems are distributed along the green valley (GV), even penetrating, more clearly when it comes to Seyfert-type galaxies, the quiescent (Q) zone. We find up to nine MaNGA S0s located in this sparsely populated Q–AC sector of the diagram, all but one with OI-type spectral profiles, i.e. ΔPS profiles with negative radial gradients, which could be the result of combining a weak central AGN with little or no extended star formation. Meanwhile, the distribution of the LINER S0s runs throughout the three activity regimes, but showing a tendency to concentrate in the vicinity of the PS with their peak straddling the PS–TR divide. In regard to the star formation, these are galaxies located mainly in the GV, although there are also a fair amount of quiescent objects and some in the MS as well.

Likewise, although most of the 'blank' S0s are, as it could not be otherwise, passive, quiescent galaxies, it can be observed that some of them reach the GV, and a few even the MS. Within this last subset, we find lenticulars with relatively high SSFRs ($\gtrsim 10^{-11}$ yr^{-1}), as well as distributions of stellar mass and stellar mass-to-light ratio in the r-band centred at slightly smaller values than the bulk of the PS population. From the spectral point of view, these are passive objects whose optical spectrum has a fairly blue continuum, lacks obvious emission lines and shows strong Balmer absorption lines. These characteristics are found in the galaxies that populate the lower half of the PS ridge (see, for instance, panels d and e of fig. B1 in TSP20). We suspect that these PS–S0s located in the MS are probably mostly post-starburst E+A galaxies (Dressler & Gunn 1992). This is, in fact, what seems to emerge from the PC1–PC2 diagram of Fig. 5, where we draw the location of the single-fibre SDSS spectra of the sample of E+A galaxies studied by Greene et al. (2021). Remarkably, almost one third of this E+A sample lies within the 90 per cent contour of

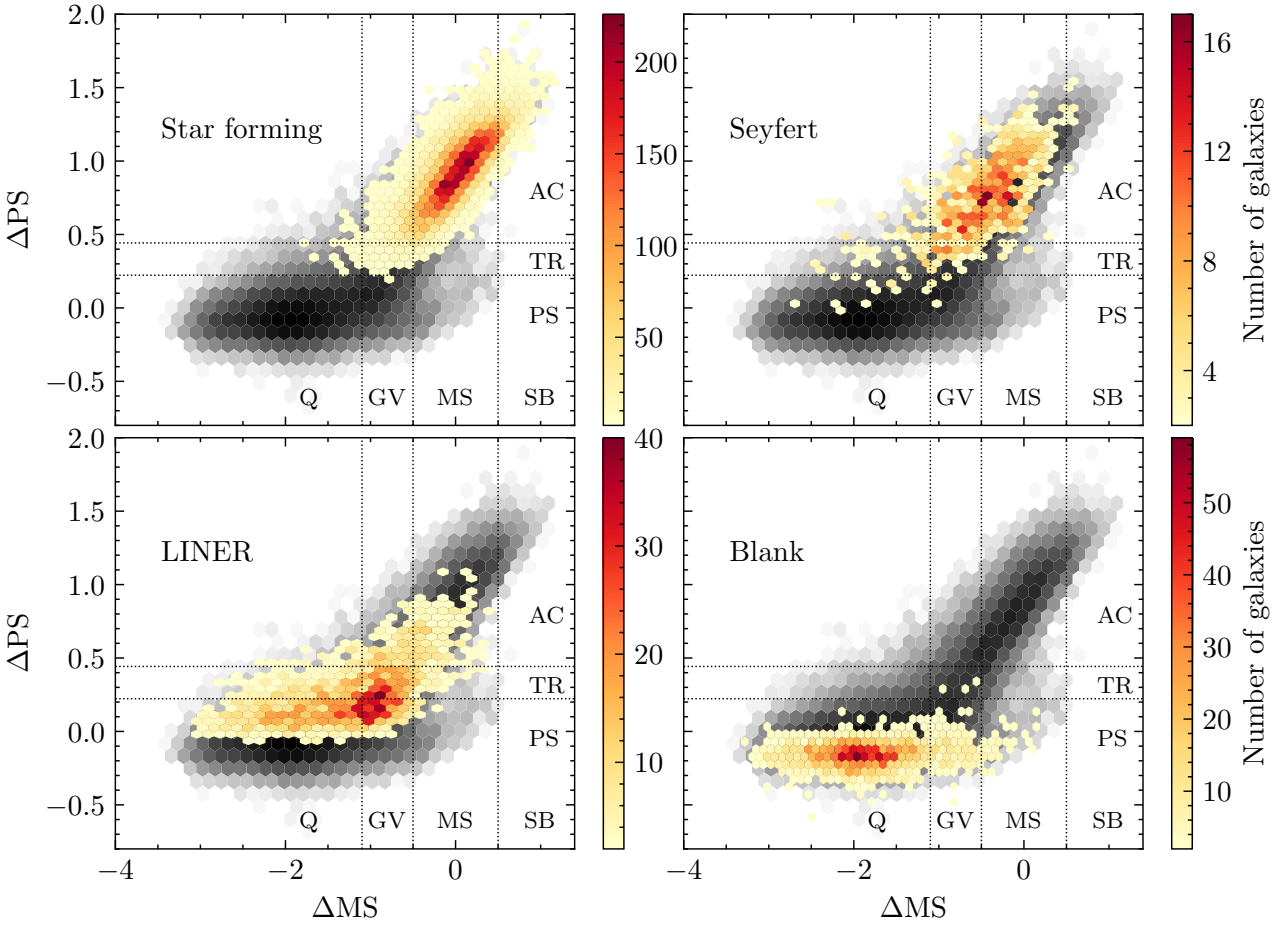

Figure 4. Distance to the ridge of the passive sequence (ΔPS) vs distance to the MS of SF galaxies (ΔMS) for the sample of ∼ 68, 000 S0s studied in TSP20. The grey-shaded background binned into hexagonal pixels shows the distribution of the full sample, the darker the tones the higher the number density. Overlaid coloured hexagonal pixels show the distributions of those lenticulars from this dataset classified by Thomas et al. (2013) as star forming (upper-left panel), Seyfert (upper-right), LINER (bottom-left), or Blank, i.e. without a BPT (Baldwin et al. 1981) classification due to the lack of emission lines (bottom-right). In the first three panels only objects with an amplitude-over-noise > 2 in the four emission lines [O III] λ 5008, Hβ, H α, and [N II] λ 6585 have been considered. The horizontal dotted lines show the demarcations of our three spectral classes, from top to bottom, active cloud (AC), transition region (TR), and passive sequence (PS), whereas the vertical dotted lines divide the galaxies, from left to right, into quiescent (Q), green valley (GV), main sequence (MS), and starburst (SB) systems.

the peak density of the distribution of the MaNGA PS–S0s that are classified in the MS (inner red curve), while only three of them fall outside the 10 per cent boundary of this distribution (outer red curve). The presence of E+A galaxies within the SF MS might initially appear paradoxical, as their lack of emission line indicators suggests little-to-no ongoing star formation. However, this apparent contradiction can be reconciled by considering that the values of the SSFR are inferred over a specific timescale. In particular, the SSFRs derived in this work from Salim et al.'s (2018b) data account for the star formation activity over the past 100 Myr.

We complete this subsection by showing in Fig. 6 the distributions of the galaxies of the MaNGA S0 sample in the ΔMS–ΔPS plane according to the sign of their activity gradient. This plot shows, on one hand, that there is a clear link between the peak density of the three distributions and the star formation status of the galaxies. Thus, it can be seen that while OI-type profiles occur in S0s with highly diverse but positively correlated levels of activity and star formation, the bulk of these objects populates the MS–AC sector of the subspace. Likewise, among lenticular galaxies with IO activity profiles, PS class objects abound, which can nevertheless show in some cases levels of star formation typical of the MS, so the peak of this distribution is located at the top of the GV–PS sector. For their part, virtually all galaxies with F gradients are Q–PS systems that have stopped forming stars and show no other signs of activity. Note that this relationship between the star formation status of S0s and the sign of their radial gradient of activity is a more than remarkable result, because the former is inferred via equation 10 from two observables, SFR and M_*, retrieved from the GSWLC-2 catalogue, where they were determined by multi-SED fitting, while the shapes of the ΔPS profiles come from a completely independent PCA carried out on the MaNGA data cubes. On the other hand, Fig. 6 also reveals that the distributions of the activity gradients substantially overlap with the distributions corresponding to the activity classes inferred from the conventional N II–BPT diagnostic. Since the first of these distributions present a high degree of mutual overlap in the ΔMS–ΔPS plane, the existence of a common ground in said subspace between BPT types and the sign of activity gradients does not guarantee per se that both classifications are closely related. Even so, we find that 78 per cent of the SF and Seyfert S0s have OI profiles – actually all but one of the Seyfert show this type of profile –, while 73 per cent of those that do not fit in

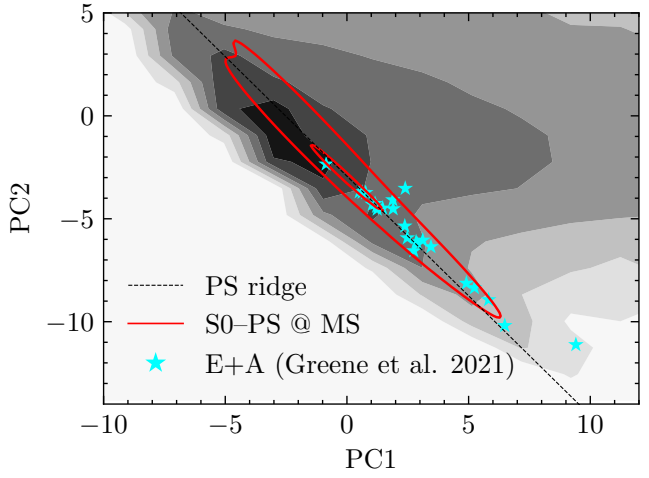

Figure 5. Location of the SDSS spectra of the sample of E+A galaxies (cyan stars) studied by Greene et al. (2021) in the PC1–PC2 plane defined in Tous et al. 2020 for present-day S0 galaxies. The red contours enclose 10 per cent (inner) and 90 per cent (outer) of the probability of finding MaNGA PS–S0 systems included in the MS of SF galaxies. The dashed line shows the ridge of the PS given by equation (1). The greyscale contours in the background are the same as Fig. 1.

any of the BPT categories according to Thomas et al. (2013) due to the lack of emission lines have flat ΔPS profiles. Only in the case of LINER S0s do we obtain a somewhat more balanced distribution of activity morphologies: 49 per cent F, 30 per cent IO, and 22 per cent OI. However, a good number of them (49) are included in our spectral class PS. Inspection of their M_* and EW(Hα) distributions shows that virtually all (48) have $M_*/M_\odot \geq 10^{10}$ and EW(Hα) ≤ 3. And what is most interesting, all but 3 LINER S0s with an optical spectrum of the PS class possess either IO (15) or F (31) radial activity profiles. Such features lead us to argue, in agreement with the findings in Jiménez-Palau et al. (2022), that any trace of emission displayed by these systems will most likely be powered not by nuclear accretion, but by photoionisation by very hot post-AGB stars of any diffuse gas they withheld (e.g. Cid Fernandes et al. 2010). Again, these are results that can be described as remarkable, since the radial gradient of ΔPS does not play any role in the BPT classification (or lack thereof), which is based on the integrated optical spectra of galaxies.

5 ACTIVITY PROFILES VS PHYSICAL PROPERTIES

Here, we offer an overview of the relationship of the radial distribution of the activity in the different spectral types of present-day S0s with several physical properties that act as hallmarks of galaxy formation mechanisms.

5.1 Total stellar mass and local density of the environment

The stellar mass is quite possibly the key intrinsic property in the evolution of galaxies. To assess its relationship with the radial run of activity in S0 galaxies, we have represented in the top nine panels of Fig. 7 the median ΔPS profiles of the three spectral types of these objects (i.e. AC/TR/PS) arranged in three rows according to the sign of the gradient and in three columns corresponding to M_* grouped in disjoint bins. As this figure shows, the largest subgroup within

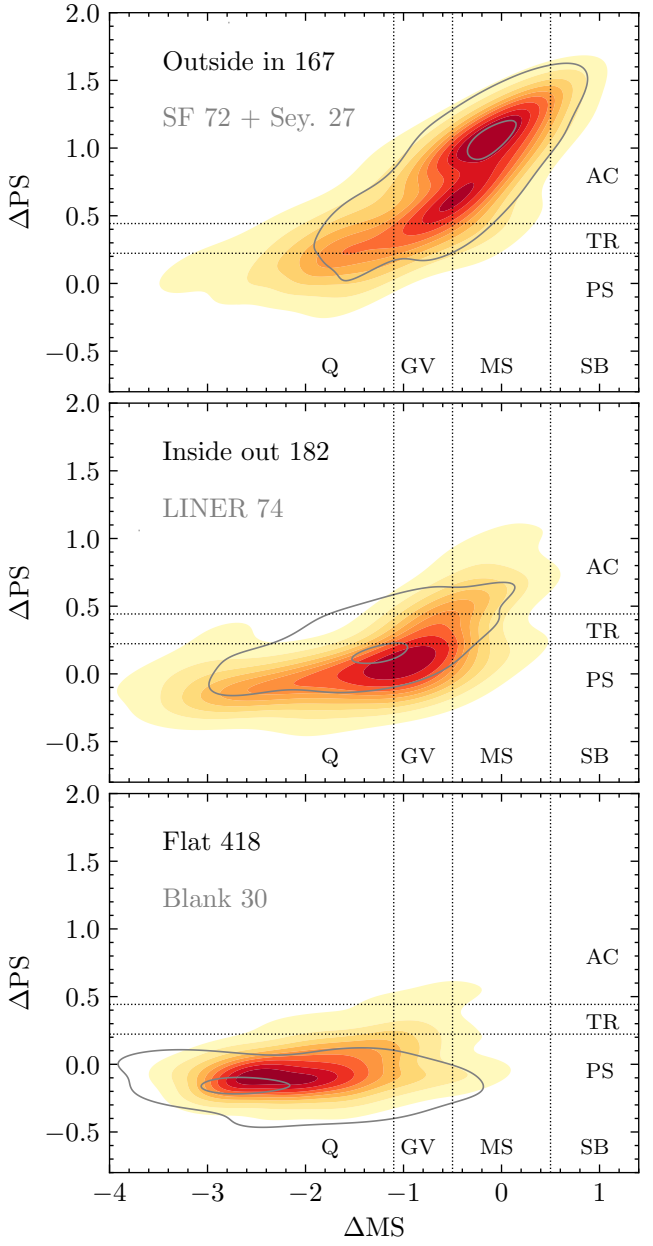

Figure 6. Kernel density estimates of the distributions in the ΔPS–ΔMS diagram of the MaNGA S0 sample divided into three groups according to the sign of the radial gradient of activity, from top to bottom panels: OI, IO and F. The intensity of the coloured contours positively correlates with the number density of data points. The grey contours on top of the distributions enclose 10 per cent (inner) and 90 per cent (outer) of the probability of finding MaNGA S0s classified by Thomas et al. (2013) as SF or Seyfert (top panel), LINER (middle panel), or that could not be classified because their emission lines were unavailable (bottom panel). Subset sizes are indicated next to each label. The horizontal and vertical dotted lines show the same demarcations as Fig. 4

the S0s of the AC class (blue solid curves and/or associated shaded regions) is that of low-M_* objects with OI quenched activity profiles, while their PS counterparts (red solid curves and/or associated shaded regions) prefer higher masses and F activity profiles. Conversely, TR lenticulars (green solid curves and/or associated shaded regions) are relatively evenly distributed, both in terms of M_* and the sign of the

activity gradient. Using as reference the median radial profiles of all galaxies with the same gradient and class of activity calculated ignoring the division in mass (dashed curves), we can also observe in Fig. 7 that the characteristic level of activity of the AC galaxies with OI profiles decreases at all galactocentric radii as M_* increases. This bearing is produced by the progressive reduction of the SSFR with mass in the SF S0s included within this class (see the blue dot-dashed curves in the panels of the top row), a result that is in good agreement with the findings of e.g. Belfiore et al. (2018) for the general disc-galaxy population. For their part, the Seyfert-type S0s show a more erratic relationship with M_* (blue dotted curves, but note the small number of these objects) which makes their entire median activity profile to run clearly below that of the SF in the lowest-mass bin ($M_*/M_\odot < 10^{10}$) and, instead, reverse this trend at intermediate and high masses. In the same way, one can also see that the negative gradients of the median ΔPS profiles of the AC:OI–S0s also tend to become steeper with mass. This effect, combined with the gradual reduction in activity intensity, causes much of this profile to penetrate deeply into the TR in the highest mass range. Despite the smallness of the subsamples, the above trends can also be guessed in the characteristic profiles of PS–S0s with OI activity gradients (red curves in the upper row of panels of Fig. 7).

Focussing on the median ΔPS profiles of type IO included in the second row of panels of Fig. 7, those associated with PS systems also show a progressive steepening of the – in this case positive – gradient with M_*, their level of activity increases instead of decreasing. This leads the outermost section of this profile to cross, in the high-mass bin, the upper boundary of the PS class and enter the TR. Regarding the AC:IO profiles, the most remarkable feature is not so much related to their shape but to the fact that their fractional abundance within this spectral class, contrary to what happens with those with OI gradients, increases with M_*. A similar result, but restricted to the quenching of star formation, has been reported by Lin et al. (2019) for the general population of emission-line galaxies.

Probably due to their intermediate spectral classification, the different types of TR profiles exhibit a somewhat less defined trends with mass, although with a certain preference to imitate those from their PS counterparts. As shown by the green profiles in the upper subset of nine panels of Fig. 7, the outer parts of these profiles usually go into one of the adjacent spectral regions, AC or PS depending on the positive or negative sign of the gradient, respectively, while the strength of the activity does not seem to follow a defined pattern. As for the S0s with F-type profiles, represented in the third row of panels, no significant variations with M_* are observed in any of the spectral classes, the most notorious result being that, independently of the value of this variable, $\gtrsim$ 75 per cent of the PS:F–S0s have profiles with ΔPS < 0 in the entire explored range of galactocentric distances.

A similar procedure is applied to determine the part played by the density of the environment, the most important external factor when talking about evolution, in the activity profiles of S0 galaxies. To this effect, we show in the last three rows of panels in Fig. 7 the distributions of the ΔPS profiles of each activity class divided into three blocks, or terciles, according to the rank reached by the best estimate of the local density for each galaxy: columns T1, T2 and T3, from lowest to highest. Here too, galaxies with the same type of activity gradient are depicted in the same row. It can be seen, that the median profiles of the AC and TR activity classes exhibit behaviours with increasing local density that, to some extent, are not too different from those they showed with increasing mass. If anything, the reduction in the strength of activity of the AC:OI profiles (first row of the lower subset of nine panels in Fig. 7) is now less progressive and pronounced. This is so to the point that the median ΔPS profile in the third density tercile barely penetrates the TR in the densest environments, in this case probably due to the greater relative contribution to the activity level of the entire AC subset, both in number and magnitude, of the Seyfert S0s against the SF S0s. On the other hand, the median TR–S0 profiles with a non-null gradient are characterized by penetrating at high R, and regardless of environmental density, into the adjacent spectral zones, reproducing the same behaviour observed with M_*. Meanwhile, the typical profiles of the PS:IO–S0s (second row of the lower subset of panels) do not show significant variations with the environment, remaining always entirely within their activity class, although for the few AC–S0s with IO gradients the average level of activity does seem to increase slightly with density. This would come to confirm that, unlike the M_*, the density of neighbouring galaxies does not play a relevant role in the existence of IO profiles in S0s, which are usually associated with SF rings (Tous et al. 2023; see also Section 6.2.2). We also observe in the bottom row of Fig. 7 that the F-type profiles classified according to this extrinsic variable, in complete agreement with the results derived from the sampling based on M_*, are those that display a more neutral behaviour for all spectral classes. And there is also coincidence in the fact that in all density ranges the entire profiles of around three out of four PS:F systems exhibit negative ΔPS values.

The information conveyed by Fig. 7 is complemented by Fig. 8, which shows the empirical cumulative distribution functions (CDFs) of M_* (left column of panels) and environmental density (right column of panels), corresponding to the subsamples of each type of activity gradient, both divided into activity classes and aggregated. The upper-left panel reveals that within the lenticulars of the AC class there is a large difference between the CDFs of galaxies with OI and both IO and F gradients, the latter two being notably more massive in statistical terms. Comparison of the mass distribution of the subsample of OI gradients with the other two via a two-sample Kolmogorov-Smirnov (KS) test shows, however, a statistically significant difference only with respect to the IO subsample, for which the test returns a low p-value ($<< 0.05$), indicating that it is very unlikely that the masses of the AC:IO–S0s arise from the same parent distribution than those of the corresponding OI subset. For the AC:F subset, its small size (9 galaxies) prevents the KS test from giving a significant result. Nonetheless, we go on to obtain highly significant differences in all cases when these comparisons involve those AC:OI with an SF BPT-classification, something that also occurs when the Seyfert and SF subsets are compared to each other. This allows us to objectify the fact that the latter have the smallest masses of all S0s.

For the lenticulars of the PS class significant differences are also found between the CDF of the IO profiles and those of the other two types of gradient (third panel), although in this case the order of the median values of the mass is reversed, so the PS:IO–S0s are now somewhat less massive than the rest on average. In contrast, and also likely due to the relative smallness of the different subsamples, we find no statistically meaningful differences among the CDFs of the three types of gradients within the TR population (second panel). On the other hand, the larger size of the samples of the aggregated distributions that are obtained by not partitioning the data into activity classes and that we have depicted in the bottom-left panel of Fig. 8, makes them all significantly different from each other according to the two-sample KS test. The order of the three subsets ranked by the average M_* of their member galaxies is OI, IO and F, from lower to higher.

On the other hand, the shapes of the CDFs of the local density percentile shown in the upper-right panel of Fig. 8 hint at the possibility

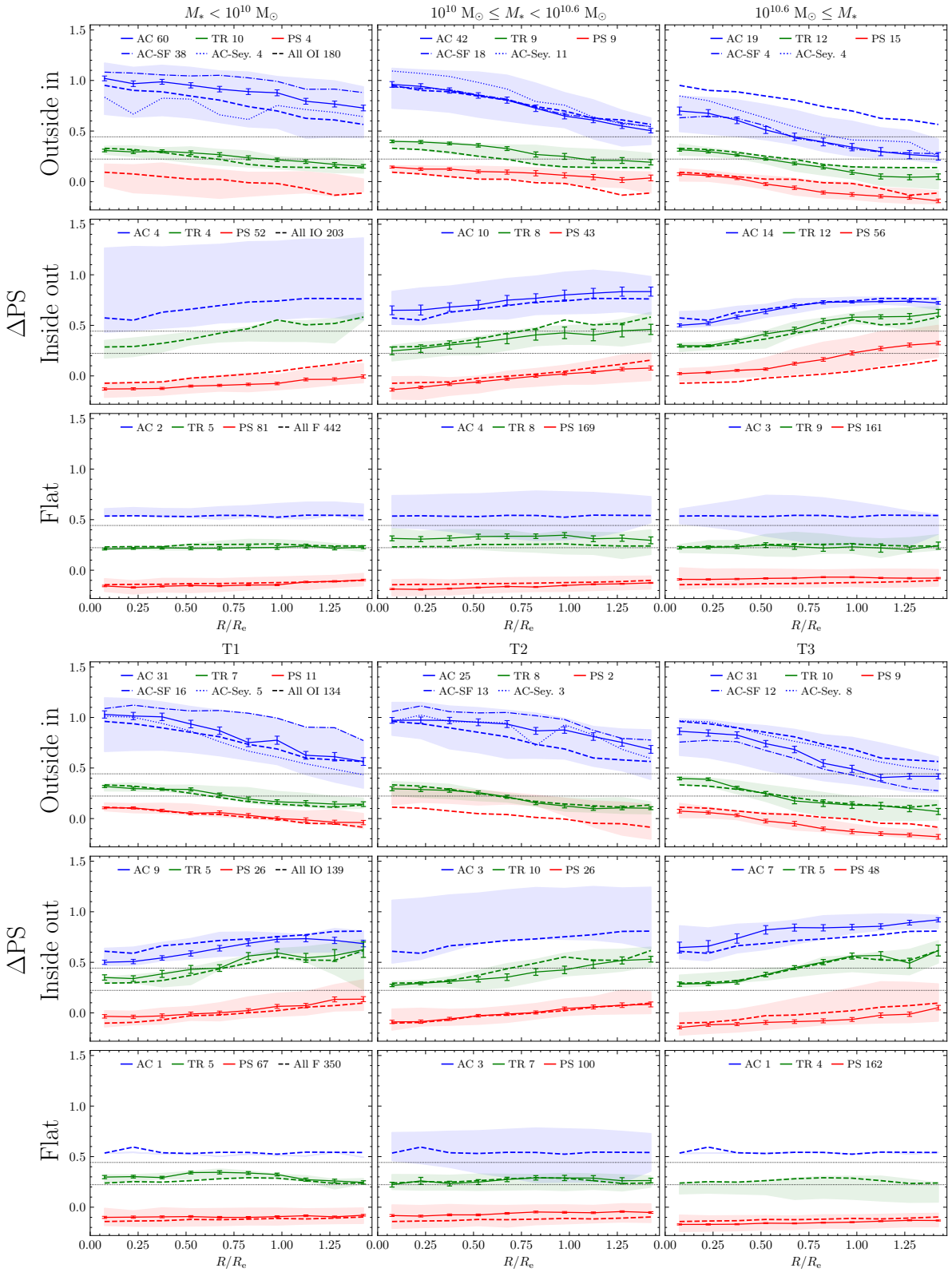

Figure 7. *First three rows of panels:* median radial ΔPS profiles and 1σ uncertainty (solid curves and error bars) of present-day AC (blue), TR (green) and PS (red) S0 galaxies divided into three bins of M_* and by the sign of their radial gradient of activity: OI (top), IO (middle), and F (bottom). Shaded regions show the interquartile range of the profile distribution for samples with more than four objects; otherwise, they show the total area encompassed by all the available profiles. For the AC:OI subset, we also show the spectral profiles of galaxies classified by Thomas et al. (2013) as star forming (SF, blue dash-dotted line) and Seyfert (Sey., blue dotted line). The median radial profile of all galaxies of each spectral class with the same activity gradient irrespective of M_* (dashed curves) is repeated along the panels of the same row for reference. The horizontal dotted lines are the boundaries of the TR zone. The numbers of objects used in deriving the statistics of each subset are indicated in the legends. *Last three rows of panels:* as upper rows, but grouping the radial profiles into terciles of local density, T1, T2 and T3, which roughly correspond to low-, medium- and high-density environments.

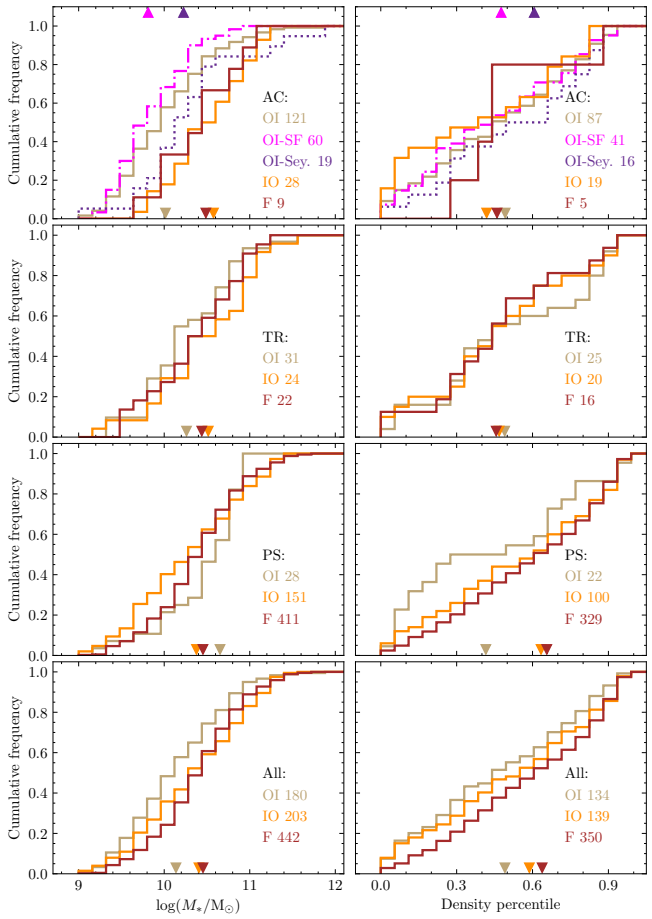

Figure 8. *Left panels:* cumulative distribution functions of M_* for the different types of activity profiles of the MaNGA S0 galaxies. The solid lines show outside in (OI, light brown), inside out (IO, orange) and flat (F, brown) gradients. Each panel depicts the CDFs segregated by activity class, from top to bottom: active cloud (AC), further divided into galaxies with a SF (dash-dotted line) and Seyfert (dotted line) status assigned by Thomas et al. (2013), transition region (TR), and passive sequence (PS), respectively, while the bottom panel shows aggregate results. The filled triangles indicate the medians of each CDF. The size of each subset is shown in the legend next to the profile labels. *Right panels:* as the panels on the left, but using as random variable the percentile corresponding to the local density of the environment (see Section 2).

that the AC:IO–S0s are somewhat more abundant in low-density galaxy environments than their OI counterparts and, especially, than the F ones, which almost completely avoid the first density tercile (but beware of the small number of galaxies (5) of this subclass). Nevertheless, and in accordance with the similarity shown by the median values, none of the observed differences turns out to be statistically significant, not even if we involve the AC:OI SF and Seyfert in the comparisons – even though the latter show a clear predilection for residing in denser environments. In the case of the PS–S0s (third panel) it is the CDF of the OI profiles that is positively skewed with respect to the other two distributions, although according to the two-sample KS test, only the comparison between the OI and F subsamples of these passive systems yields a statistically significant difference. And just as it happens with the mass, we cannot reject either for the TR galaxies (second panel) the null hypothesis that the three subsamples of gradients come from the same parent distribution of local galaxy densities. The similarities between the CDFs of M_* and environmental density also extend to the ascending ordering of the median values of the samples of the aggregate profiles, which for this extrinsic variable is again OI, IO and F. In this case, however, the differences among the CDFs of the aggregated profiles (bottom-right panel of Fig. 8) turn out to be statistically significant only between the OI and F subsets.

5.2 Stellar ages and kinematics

We now turn to investigating if there is any connection between the radial gradients of activity of S0 galaxies and the ages and kinematics of their stellar populations.

To delve into the dependence with stellar age, we apply the same methodology used in Fig. 8, so we compare in Fig. 9 the CDFs of the mean stellar age of S0s weighted with both luminosity (left column of panels) and mass (right column of panels) for the different activity gradients. As before, the upper three panels collect from top to bottom the results corresponding to the AC, TR and PS classes of activity, respectively, while the lower ones show aggregated results. In the case of the luminosity-weighted ages, the spectral class AC is, as would be expected, the one that harbours, regardless of the sign of the gradient, the youngest stellar population on average, followed by the TR systems and then the PS systems. In this panel, the most discrepant and significantly different CDF corresponds to the Seyfert AC:OI subgroup, which contains the galaxies with the oldest luminosity-weighted stellar populations within this spectral class. This result agrees perfectly with the idea, already expressed in Section 4, that the presence of an AGN has a negative impact on the SFRs of the S0s. Fig. 9 also shows that, in each of the three spectral classes, lenticular galaxies with IO activity gradients harbour fractions of younger stars – which are the ones that dominate the optical spectrum – somewhat larger than those of the other two types of profiles, which translates into significant discrepancies with the CDFs of both when applying the two-sample KS test. This finding implies that the relative contribution of recent star formation to overall activity, regardless of its level, is more important in S0 galaxies with IO profiles than in their OI and F counterparts. Only in the bottom panel depicting the cumulative histograms of the integrated light-weighted mean ages, all three gradients show distinctly segregated CDFs which in this case are ranked OI, IO and F from lowest to highest ages. This apparent development in the sequence of ages of the stellar populations simply takes account of the fact that the bulk of S0s with OI profiles are SF galaxies of the AC class, while most systems with both IO and F activity gradients belong to the quiescent PS class, just as shown in Fig. 6.

The CDFs of the mass-weighted mean stellar ages of the MaNGA S0s are depicted in the right column of panels of Fig. 9. In addition to an overall increase in the ages, explained by the fact that mass-weighted values are a good proxy for the integrated star formation history of galaxies and, therefore, of the actual average age of their stellar populations, we can now verify that the distributions are, in general, much more similar to each other within a given spectral class (note the different scale of the abscissae with respect to the left column). The only exceptions are the Seyfert AC:OIs, which again host stellar populations significantly older than their SF AC, IO and F counterparts, and the PS:IOs, for which the p-values from the KS test suggest that their mass-weighted stellar ages could come from a slightly younger parent population than that of the other S0s belonging to this passive subset. The broad homogeneity shown by the characteristic stellar ages of S0s regardless of their level of activity gives way in the last panel to small, but statistically signifi-

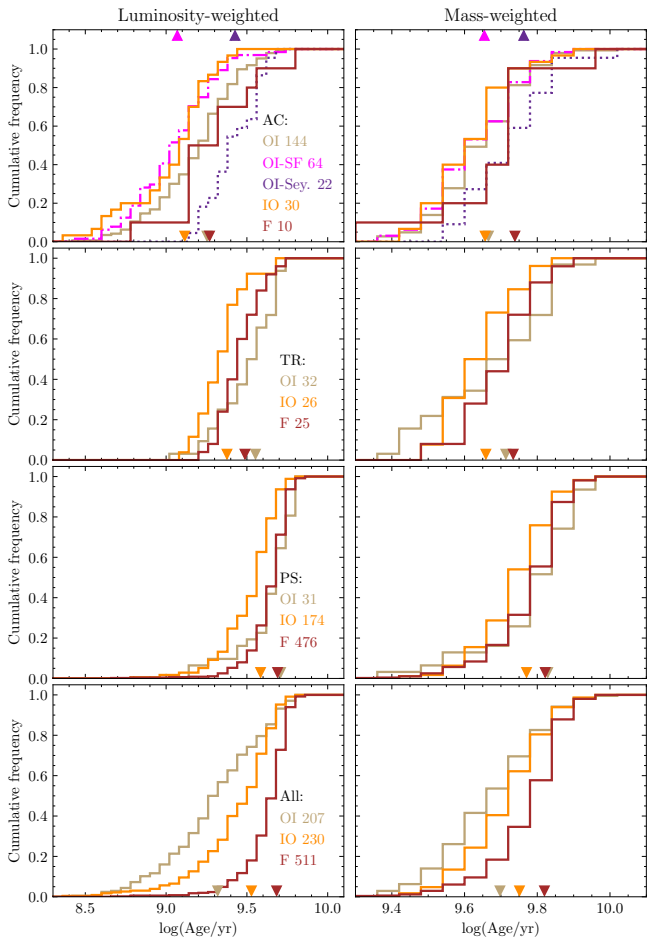

Figure 9. As Fig. 8 but using as random variables the luminosity-weighted age (left panels) and mass-weighted age (right panels) of the stellar populations.

cant differences in the aggregated CDFs, which reproduce the same arrangement of median ages OI < IO < F observed in the corresponding light-weighted measurements. The correlation of the sign of the activity gradients with the SSFRs (Fig. 6) tells us that this sequence is due to the fact that we are dealing with old galaxies that harbour different fractions of *newly formed* stars. Indeed, the results of this particular analysis provide a strong argument in favour of considering active S0s to arise primarily from the rejuvenation of their passive counterparts. However, as will be discussed later (Section 6), some of our findings also support, or do not contravene, the fading of Sps as a viable explanation for the existence of AC–S0s.

To investigate possible dependences of the radial gradients of activity with the stellar kinematics of S0s, we resort to examining the bivariate distributions of the central values of the stellar spin parameter, λ_{R_e}, defined in Section 1, and the overall observed ellipticity, ε, for the various subsets of these galaxies that we have defined along this work. Fig. 10 compares the kernel density estimates of four of these distributions in the $(\lambda_{R_e}, \varepsilon)$ diagram: the S0s with OI or F activity gradients and those identified as SF or Seyfert by Thomas et al. (2013) within the AC:OI subclass[8]. To guide the eye, we have included in all four panels curves showing the theoretical relationship expected from the dynamical modelling of isotropic regular rotators (top dashed line), as well as from those obeying the lineal relation between anisotropy and ellipticity given by (cf Cappellari et al. 2007) $\beta = 0.7\varepsilon_{\rm intr}$ (bottom solid line), in both cases for galaxies seen edge-on[9]. Randomly oriented real fast rotators are expected to broadly form an envelope to the left and above this latter line, which acts as an empirical boundary for anisotropic rotators structurally flattened by rotation, while counter-rotating disc galaxies will tend to fall below it. Besides, we have added in the lower-left corner of each individual diagram a box providing the best empirical separation between fast and disc-less slow rotators, as given by equation (19) in Cappellari (2016), and that encloses mainly, but not all, E galaxies.

Despite the large scatter usually associated with individual measurements, diagrams based on stellar kinematics do a rather good job separating the two main groups of fast and slow rotators when they are applied to the general galaxy population (e.g. Emsellem et al. 2007). However, the sensitivity of these plots becomes rather limited when it comes to detecting differences among members of the family of fast rotators, especially if they are of the same Hubble type, as in the present case. Nevertheless, as depicted in the top panels of Fig. 10, the $(\lambda_{R_e}, \varepsilon)$ diagrams of the two aggregate distributions of the OI and F gradients, reveal some eye-catching differences that are also broadly replicated by the distributions of their main spectral contributors, the activity classes AC and PS, respectively. Thus, while both distributions cover quite similar ranges of the parameter space and tend to avoid the region associated with slow rotators (see also Appendix A), their shapes are clearly distinct. In the case of the OI subset (left panel), much like the AC, the data shows a single peak centred on top of the upper guide line, in the region of the diagram bounded by the coordinates $0.15 \lesssim \varepsilon \lesssim 0.35$ and $0.3 \lesssim \lambda_{R_e} \lesssim 0.5$, accompanied by traces of a possible secondary peak at higher values of both ε and λ_{R_e} (see below and Appendix A). On the other hand, the F subset (right panel), as well as the PS, showcase a clearly bimodal distribution, with the maxima relatively close to each other and located between the two divide lines in a region where ε ranges from ~ 0.2 to 0.55 and where the modal values of λ_{R_e}, as happens with the OI and AC subsets, remain centred around 0.4, which is typical of nearby lenticular systems (Cappellari 2016). For their part, the IO and TR subsets, in which GV galaxies abound, exhibit essentially unimodal distributions with maxima located approximately between those of the extreme cases depicted in the plot. Objective comparison of all these distributions using a 2D KS test[10], shows that the differences between the OI (AC) and F (PS) subsets are in fact significant.

To investigate the origin of the above discrepancies, we have also inferred the distributions of anisotropies of the two main contributors to the AC:OI subgroup of S0s. As can be seen in the lower-left panel of Fig. 10, the distribution of the AC:OI lenticulars classified as SF only presents minor differences with respect to that of all OI systems,

[8] To make this plot more compact, the diagram corresponding to the IO activity gradients, which depicts an intermediate behaviour between the OI and F cases, has not been included. Nor are the diagrams of the AC, TR and PS spectral classes shown, since they do not provide relevant new information. All of them are, however, discussed in the text.

[9] A rigorous application of this anisotropy diagram and the different guide lines adopted assumes that the summation (3) used to calculate λ_{R_e} is not spatially limited and that the value of ε is intrinsic and constant with radius. However, the fact that we are only interested in an internal comparison between different S0 subsets, whose unknown selection functions are expected to be uncorrelated with projection effects, allows us to carry it out directly using the observational estimates of both parameters.

[10] The PYTHON implementation of this test is available at `https://github.com/syrte/ndtest` (not to be confused with the two-sample KS test used above to compare pairs of CDFs).

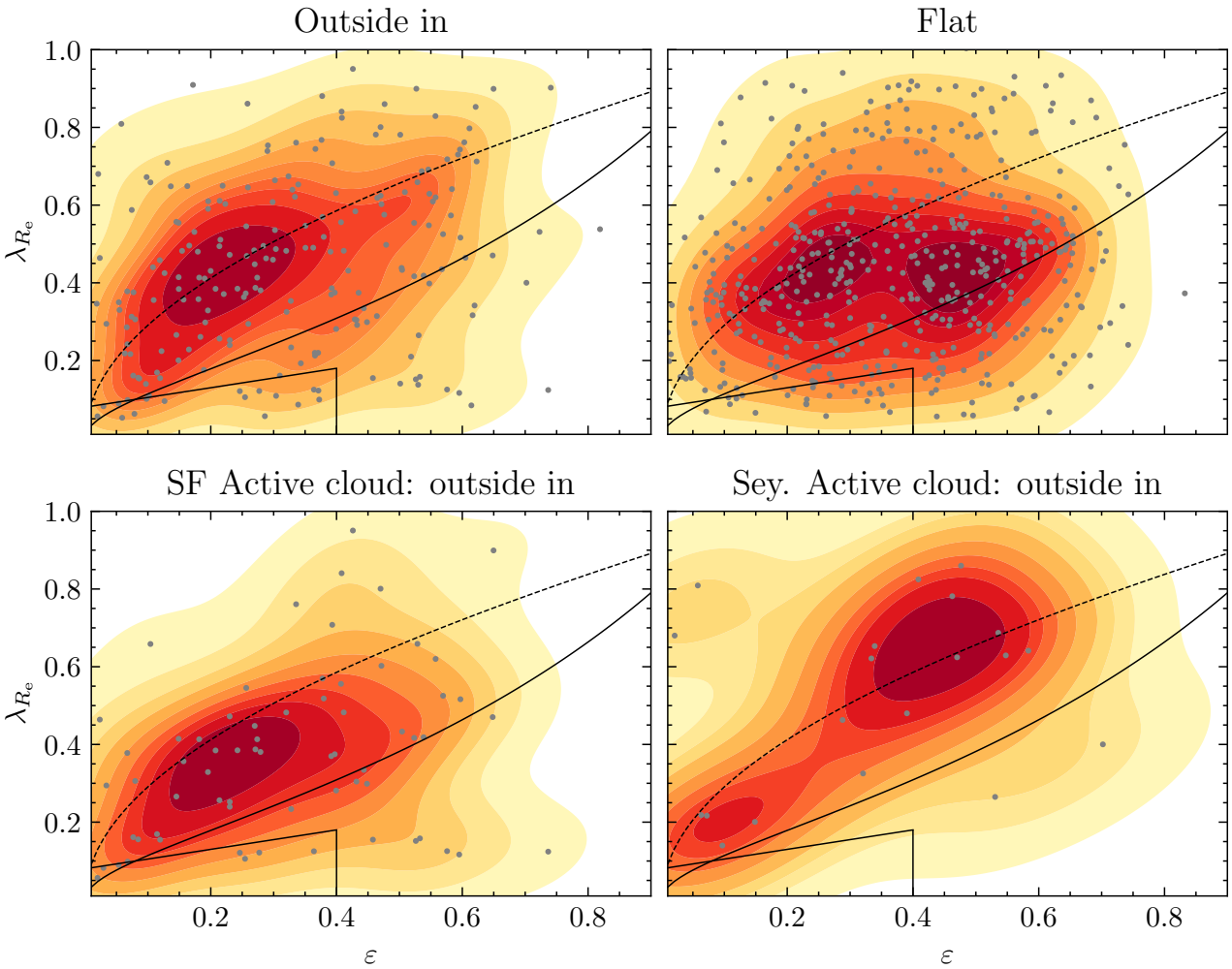

Figure 10. Kernel density estimates of the distributions of the MaNGA S0 galaxies with OI or F activity gradients in the $(\lambda_{R_e}, \varepsilon)$ diagram (top panels), and of those members of the AC:OI subset classified as SF or Seyfert by Thomas et al. (2013) (bottom panels). The darker the colour, the higher the number density of data points. The grey dots show the individual values. The luminosity-weighted averaged projected specific angular momentum of the galaxies, λ_{R_e}, is calculated from equation (3). The black curves, the same in all panels, indicate the theoretical relations expected for oblate edge-on models of regular rotators that are either isotropic, $\beta = 0$ (top dashed lines), or have an anisotropy $\beta = 0.7\varepsilon_{\rm intr}$ (bottom solid lines). The small boxes in the lower-left corner provide the best empirical fast/slow rotator divide, as given by equation (19) in Cappellari (2016).

which are specified in a slight displacement of the maximum towards lower values of λ_{R_e} and the total absence of evidence of a second peak, something that is not unexpected given that these objects are the most abundant in this type of gradient. By contrast, the distribution of the Seyfert S0s with AC:OI profiles in the lower-right panel shows a small peak near the origin and a primary maximum notably shifted towards higher values, not only of ε, which now overlap with those of the second maximum of PS:F systems, but also of λ_{R_e}, that exceed those typical of the S0 population. This suggests that within S0s, AGN episodes take place preferentially in galaxies that have more rotational support than most. Although the small size of our Seyfert's subset (21 objects) limits the robustness of this latter result, we note that del Moral-Castro et al. (2020) have recently reached a similar conclusion based on an analysis of the dimensionless stellar spin parameter too, but applied to isolated Sa–Sbc type discs (see also Section 6.1).

6 DISCUSSION

In this section, we aim to assess the alignment between the predictions of the main evolutionary channels for local S0s and the results of our analysis on their activity profiles, particularly highlighting the role played by hydrodynamic interactions and gravitational encounters in the formation of these objects.

6.1 Activity driven by hydrodynamics

Hydrodynamic mechanisms, exemplified by ram pressure stripping (RPS; Gunn & Gott 1972) and accompanying transport processes like turbulent viscous stripping (Nulsen 1982; Roediger & Hensler 2005), entail high-speed interactions between the galaxies' ISM and a dense and hotter IGM, two conditions that are met in large aggregations of these objects. Candidate S0 galaxies that may have acquired their morphology by this mean are former spiral galaxies that transitioned after falling into a cluster or a rich group, preferably during the making of these systems (Solanes et al. 2016).

IGM-ISM interactions in galaxies primarily result in the removal,

occurring on time-cales of $\sim$ 1–2 $\times$ 10^9 yr (Lotz et al. 2019), of both the cold atomic gas in the discs and the surrounding hotter gas reservoir (strangulation), leading to an overall outside-in reduction in star formation activity and a potential localized increase in the SFR at the ISM-IGM interface, with the complete transformation into an S0 necessitating of a subsequent galaxy-wide structural rearrangement induced either externally or by the sweeping gas itself (Lee et al. 2022). While the gravitational field of massive galaxies may be strong enough to retain some neutral gas in their central regions or to reaccrete a certain fraction of the displaced ISM, in small galaxies the stripping of the H I may be total and irreversible, which may accelerate their transition to quiescence (see Boselli et al. 2022 and references therein). Conversely, the impact of RPS on the nuclear activity of galaxies remains unclear. Some authors regard clusters as a hostile environment for AGNs (e.g. Dressler et al. 1985; Lopes et al. 2017; Mishra & Dai 2020), whilst others argue that hydrodynamic interactions could actually enhance the feeding of the central SMBHs (e.g. Ricarte et al. 2020; Peluso et al. 2022).

This scenario certainly calls for S0s with OI profiles (and possibly F profiles too). As shown by Fig. 7, the level of activity of galaxies with this type of gradient diminishes with increasing stellar mass and/or environmental density, leading to significantly reduced ΔPS values in the outer radial bins. This trend is accompanied by a rise in the relative abundance of PS (and TR) OI lenticulars at the expense of systems featuring an AC:OI configuration, which generally tend to be less massive and younger, especially those classified as SF (Figs. 8 and 9). The substantial difference in typical masses is precisely what prevents the former from being broadly considered as the result of the fading of the latter. Figure 11 complements previous plots by contrasting summarized stellar mass distributions across three local density terciles (left panel) and vice versa, density percentile distributions across three stellar mass bins (right panel), with spectra categorized solely by gradient type to ensure a reliable statistical analysis. While it is obvious that in the second panel the differences between the distributions are less pronounced, they still allow us to discern certain trends, such as, for instance, that the central part of the distribution of local densities for galaxies exhibiting OI gradients (depicted by light brown boxes) undergoes a slight shift toward higher values as mass increases. This indicates a tendency for the most massive S0s with this activity profile to be more commonly found in densely populated regions.

Despite the lack of significant variations in the ΔPS profiles of the Seyfert AC–S0s with the local density, our finding that Seyfert S0s tend to be more massive, elongated and rotationally supported than their SF counterparts (see Fig. 10), can still be seen as evidence favourable to the contribution of RPS to AGN activity. A similar result regarding the larger values of λ_{R_e} shown by AGNs is reported in del Moral-Castro et al. (2020) for isolated Sps. These authors attribute their outcome either to an internal angular momentum redistribution between the gas and the baryons remaining in the disc promoted by bars or other large-scale disc instabilities (e.g. spiral arms), or to external gas directly supplied to the central region of the galaxies through gas-rich minor mergers. Nevertheless, neither of these two scenarios appears well-suited for our Seyfert S0s, as they lack spiral arms, exhibit on average a low probability of bars in the MDLM-VAC-DR17 catalogue, and tend to inhabit rich environments (as indicated in the upper-right panel of Fig. 8). Therefore, to embrace the idea that the evolutionary path of certain Seyfert S0 may be related to RPS, it is necessary to consider other alternatives, such as collisions between the IGM and any residual ISM that may remain in the disks of these galaxies. This could potentially reduce the angular momentum of the latter, causing the inflow of a part of it towards the centre and consequently triggering nuclear activity.

6.2 Activity driven by gravity

Lately, minor merger events are frequently invoked as drivers of both extended star formation activity in S0 galaxies located in the field or in small groups (e.g. Fraser-McKelvie et al. 2018; Deeley et al. 2020; Rathore et al. 2022; Coccato et al. 2022; Maschmann et al. 2022), and localized star formation in inner Hα rings (Tous et al. 2023). The prevalence of these SF rings in diverse environments, including dense regions, suggests that they may originate from mergers with tiny neighbour dwarfs, as these are the only satellites capable of remaining trapped in the potential well of primaries during their infall into more massive haloes. Given that differences in the mass ratios of the merging galaxies may be associated with differences in the structure of activity induced in the remnants, we discuss below regular minor mergers and less conventional captures of small dwarf satellites, or mini mergers, separately.

6.2.1 Minor mergers

In a recent study, Rathore et al. (2022) concluded that the most plausible explanation for their observation, where more than half of the galaxies in a sample of 120 low-mass S0s with global SSFRs akin to SF Sps display signs of galaxy interactions, is rejuvenation through minor mergers. The central dominance of star formation in their SF lenticular galaxies aligns them well with our AC:OI–S0s, which not only feature activity profiles with the appropriate shape, but also exhibit star formation levels comparable to those observed in MS LTGs (see Fig. 6). Considering that our ΔPS parameter serves as a reliable proxy for the SSFR in SF systems (Fig. 4), one can observe that the parallelism with the SF S0s studied by Rathore et al. further encompasses the dependence of the SSFR radial profiles on M_* (compare the first row of panels in our Fig. 7 with their fig. 7). Negative gradients are evident in both studies that become more pronounced as mass increases. These authors also find that although the SF S0s and Sps show similar SSFRs in their central regions, the radial gradients of the latter are positive on average. This reveals important differences with respect to the structural component, bulb or disc, respectively, which concentrates most of the star formation (see also González Delgado et al. 2016). Additionally, the younger typical ages of the stellar populations of our AC:OI–S0s (Fig. 9), along with their greater structural roundness and slightly more pressure-supported discs (Fig. 10), are characteristics that fit perfectly into a rejuvenation scenario driven by minor mergers.

As Fig. 11 illustrates, the stellar mass distributions of S0s with OI activity gradients, primarily associated with the AC spectral class, exhibit a bias toward lower masses in the first two terciles of local density. Notably, in the second density tercile, where minor mergers are expected to be frequent, there is no overlap between the interquartile range of the OI subset (depicted by light brown boxes in the left panel) and those of the other two gradient types. If these galaxies originate from rejuvenated PS lenticulars with F or IO profiles, the relative paucity of high-mass OI systems at low and intermediate environmental densities might suggest that minor mergers are particularly effective in rejuvenating low-mass passive S0s. This could be attributed to the higher ratio of residual gas to stars expected in these objects compared to their more massive counterparts. For the latter, the most likely outcome of such interactions would be a SF ring localized in the inner region of the disc, giving rise to an IO

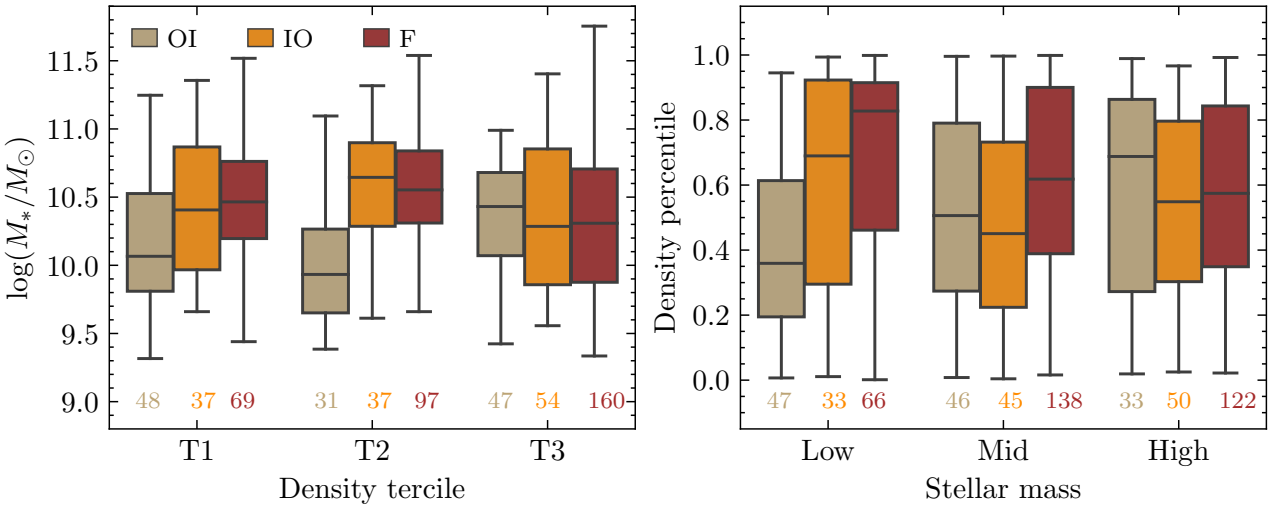

Figure 11. Box plots summarizing the aggregate distributions of stellar mass for the OI, IO and F types of the radial gradient of activity in each of the three terciles of environmental density (*left panel*) and, vice versa, of the density percentile of such gradients in the three bins of stellar mass defined in Fig. 7 (*right panel*). The figures underneath each box show the number of objects included in the different subsamples.

activity profile (see Section 6.2.2). As discussed in the preceding section, some high-mass AC:OI–S0s might originate from alternative mechanisms, such as RPS.

S0s can also form in one of the last steps of a chain of sequential minor mergers that feed the main progenitor and gradually change its morphology from a late spiral to an ETG system, as in the stream-driven merger scenario for galaxy formation discussed in Dekel et al. (2009). This form of evolution differs from the more dramatic impact of major mergers, which can produce more radical alterations of morphology, and it aligns well with the concept of hierarchical bulge growth described by Bournaud et al. (2007). It is also the preferred scenario by Maschmann et al. (2022) to explain the central star-formation enhancements observed in a large sample of double-peak (DP) emission-line bulge-dominated LTGs, Sas and S0s identified from the SDSS. As noted by these authors, the possible merger-induced central star formation in DP galaxies occurs without a simultaneous increase in AGN activity.

One of the ways in which minor mergers involving gas-rich satellites can lead to the transition of Sps into S0s is by inducing galaxy-wide suppression of star formation. As revealed in the simulations conducted by Osman & Bekki (2017), the existence of counter-rotating gas in stellar discs has the potential to weaken or entirely inhibit gas density-enhancing structures like spiral arms and bars. In these circumstances, star formation is severely suppressed and can only proceed at a rate considerably lower than in co-rotating discs with comparable gas density. Notably, we find that the median SFR of the AC:OI–S0s located in the 'counter-rotation zone' of the anisotropy diagram (i.e., below the $\beta = 0.7\varepsilon_{\rm intr}$ guideline) in the bottom-left panel of Fig. 10 is slightly lower than that of galaxies situated above it: $\log(\mathrm{SFR}/(M_\odot\ \mathrm{yr}^{-1})) = -0.58$ vs -0.44, respectively. Although this might be an overly simplistic approach to evaluate the feasibility of this scenario, the scant inferred difference still corresponds with the results of the simulations performed by Osman & Bekki, suggesting that a small fraction of our S0 galaxies could have followed this formation route. On the other hand, dry minor mergers may trigger morphological quenching (Martig et al. 2009), a concept that involves the cessation of star formation in discs that become stable against fragmentation into bound gas clumps in galaxies that transition to a spheroid-dominated state after merging.

Late, gas-rich mergers with lower mass ratios (i.e., intermediate and/or major mergers) are more likely to give instead completely ellipsoidal SF systems, akin to the 15 blue SF elliptical galaxies identified by Lacerna et al. (2020) in a sample of 343 objects of this morphology also extracted from the MaNGA survey. These SF ETGs exhibit younger stellar ages, lower metallicities, and essentially flat median SSFR profiles up to 1.5 $R_{\rm e}$. Although the limited number of such objects complicates the identification of general evolutionary trends, the authors of the study propose that these galaxies could be the result of recent wet mergers that rejuvenate intermediate- and low-mass classical Es in low or average density environments (see also Thomas et al. 2010). This idea represents a natural extension of the formation scenario proposed for our AC:OI–S0s, in which the mergers would be energetic enough to disrupt any preexisting disc and the initial mass of the satellite large enough to allow a substantial fraction of its core to reach the innermost regions of the primary (Walker et al. 1996). The flatness observed in the SSFR radial gradients of the SF Es could then be a consequence of an increased central star formation that spans a significant portion of the remnants.

6.2.2 *Mini mergers*

Numerical simulations aimed at investigating the formation histories of lenticular galaxies, such as those conducted by Deeley et al. (2021), reveal that most S0s formed through mergers undergo a phase wherein they develop a transient SF ring, typically lasting $\sim$ 1–2 Gyr. These rings consistently emerge in connection with minor merger events, their onset being preceded by the exhaustion of the gas in the central region of the hosts. They are often accompanied by the formation of a stellar bar or another non-axisymmetric gravitational distortion of the disc, signifying their close association with the central galaxy and, consequently, their coplanarity. Our examination of this phenomenon using MaNGA data, as detailed in Tous et al. (2023), has revealed that the existence of inner ($\langle R\rangle \sim 1\,R_{\rm e}$) SF rings in S0 galaxies is largely associated with an IO configuration of their activity gradients. Additionally, our study has confirmed the ubiquity of these rings, particularly among massive S0s, with fractional abundances reaching $\sim$ 50 per cent independently of both their

spectral type (AC or PS) and environmental density. Drawing from these findings, we deduced that the minor mergers responsible for the formation of these SF rings probably involve tiny satellites closely bound to the primary galaxy.

Regarding the possibility that these small satellite captures could also drive AGN activity, simulations such as those conducted by Mapelli et al. (2015), which explore the build up of gas rings in S0s through minor mergers of mass ratio ∼ 1:20, show that while much of the stars and gas initially bound to the satellites are scattered into the halo of the central galaxy, a small fraction of their material can be channelled towards its nucleus. However, it is important to note that in these simulations satellites were also modelled as disc galaxies equipped with a stellar bulge. In a mini-merger scenario, where most merging satellites are expected to have a more diffuse stellar structure of the Irr or Sph type, they are less likely to reach the host's nucleus before being fully disrupted, unless their initial orbit is well aimed towards this region (Kendall et al. 2003).

Our analysis of the IO radial activity profiles aligns seamlessly with the scenario outlined above. The second and fifth rows of panels in Fig. 7 show that the median IO profiles exhibit a more pronounced S-shape with increasing stellar mass, a behaviour that becomes less prominent when these profiles are represented as a function of environmental density. There is also the substantial overlap shown by the interquartile ranges of the mass distributions of the IO and F subsets across all density intervals (depicted, respectively, by the orange and brown boxes in Fig.11), which supports the notion that the former could be rejuvenated versions of the latter. The rejuvenation scenario is further supported by the observation that, within each spectral class, the stellar populations of S0s with IO profiles exhibit statistically younger luminosity-weighted ages than those of the other gradients (see the left panels of Fig. 9). However, the fact that, as shown in Fig.6, lenticulars with this type of activity profile typically reside in the green valley (GV), suggests that these rejuvenation events trigger localized, bursty star formation episodes that significantly increase the SFRs of the galaxies, but have a less pronounced effect on their SSFRs compared to S0s with OI profiles.

6.3 Is the PS:F subset the S0s' graveyard?

The relatively short-lived and transient nature of both the rejuvenation and fading phenomena implies that all the evolutionary pathways of S0s are expected to eventually lead to quiescent systems characterized by a fundamentally bland activity profile. In our classification system, these features correspond to S0s of spectral class PS and F-type gradients. Consequently, it is natural to expect that this subset of galaxies has properties compatible with the notion of attractors of evolutionary histories.

Certainly, the PS:F subset stands out as the largest within the MaNGA sample (Table 1). This, coupled with the observation that these galaxies also host the oldest stellar populations (Fig. 9), indicates that they are the most prevalent and enduring state among present-day S0s. Furthermore, the distribution of their stellar masses spans the entire range of values seen in the other subsets, while the frequency distribution of their environmental densities encompasses all percentile ranks (Figs. 8 and 11). To all this must be added the fact that the PS:F systems are the only ones that show a distinctly bimodal distribution in the $(\lambda_{R_e}, \varepsilon)$ diagram (Fig. 10), with two peaks that differ basically in the value of the ellipticity. Assuming that the positioning of galaxies in this diagram reflects the evolutionary path they have followed, the mode centred on the lowest value of ε would be associated with galaxies that, after attaining the S0 status, have undergone one or more transient episodes of rejuvenation during which their SFRs have been considerably intensified (as evident from the comparable positions of the left-hand peak and the peak of the SF AC subset). Our study's findings suggest that minor mergers could be the most effective catalysts for these periods of heightened activity. Such mergers would result in rounder objects by triggering disc instabilities and heating, although, as deduced from the anisotropy diagrams, they would barely impact the rotational support of the primary galaxy. On the other hand, the right-hand mode would correspond to galaxies that have experienced a less eventful formative history, in which once they have become fully-formed S0s have not subsequently suffered significant structural and dynamic alterations.

7 SUMMARY AND CONCLUSION

We have studied the radial activity profiles up to 1.5 R_e of 1072 present-day S0 galaxies drawn from the SDSS-IV MaNGA survey as a function of their mass, age, structure and kinematics, and density of their environment to see how they fit with the different evolutionary histories proposed for these objects. The activity profiles have been obtained after a process of dimensionality reduction consisting in projecting the composite spectra that result from stacking the spaxels of the data cubes, grouped in radial bins, into the PC1–PC2 space defined by their first two principal components, which encompass most of the variance of the whole sample of spectra. In this latent space, three zones or spectral classes can be distinguished that correlate with the level of activity of the galaxies and that we identify as the passive sequence (PS class), the active cloud (AC), and the intermediate transition region (TR). Near 90 per cent of the PC1–PC2 representations of the radial profiles are well approximated by straight lines, which has facilitated the division of the above spectral classes into outside-in (OI), inside-out (IO) and flat (F) categories according to, respectively, the negative, positive and null value of the radial activity gradient. The introduced classifications based on the ΔPS parameter, as well as on its radial gradient, provide a unified picture of the spectral information of S0 galaxies in the optical range with respect to their overall activity level and, in combination with more physical quantities and line diagnostics, help to interpret key trends in these systems. Next, we provide a summary of the main findings of this study.

- The gradients of the radial activity profiles of S0s show a close relationship with their spectral class, BPT type and SSFR.
- PS–S0s very often exhibit low-level, F-type activity gradients as well as a significant number of IO profiles, while in a substantial fraction of AC–S0s activity increases OI. F activity gradients in AC lenticulars and OI in PS systems are uncommon.
- Most SF and Seyfert S0s are AC systems that preferentially show OI activity gradients, while a good number of LINER S0s fall in our PS spectral class. The fact that the vast majority of the latter show F or IO activity gradients suggests that they are weakly-active systems likely powered by post-AGB stars. Among the S0s with a PS status, we also identify 9 objects with E+A-type spectra located in the MS of star formation.
- A significant portion of S0s in the MS exhibit negative activity gradients, whereas among the quiescent ones, the majority have flat gradients. Positive activity gradients are frequently observed in GV objects.
- The significance of recent star formation in relation to overall activity is greater in S0 galaxies displaying IO profiles compared to their OI and F counterparts, irrespective of the activity level.
- Among low-mass AC–S0s, the highest levels of activity correspond to objects classified as SF. However, the progressive reduction

of the SSFR with stellar mass makes Seyfert S0s to become the most active systems at intermediate and high masses. We also observe that star formation tends to be less intense when AGN activity dominates, which suggests negative feedback.

- The greatest abundance of SF AC–S0s compared to those classified as Seyfert leads to the decrease of the activity level in this spectral class with stellar mass at all galactocentric radii, an effect that is particularly noticeable in galaxies with OI activity profiles. This behaviour, which is consistent with the SSFR–M_* relationship defining the MS, is however inverted in the PS–S0s with IO profiles, pointing to a faster increase of the star formation efficiency with stellar mass in these latter objects than in typical SF galaxies.
- The ratio between positive and negative activity gradients in AC–S0s increases with stellar mass.
- The relationship between the median level of the activity profiles of S0 galaxies and the local density of their environment is, in general, less clear-cut than with stellar mass, showing only indications in the highest density bin of a slight suppression of the intensity in the AC:OI systems and of a similarly light increase in it in the few objects of this same spectral class with IO gradients that inhabit these richer environments.
- The bivariate distributions of S0s in the $(\lambda_{R_e}, \varepsilon)$ anisotropy diagram show that AC:OI systems classified as SF are rounder and slightly more pressure supported, and their Seyfert counterparts more rotationally supported, than the bulk of the local population of these objects. For its part, the distribution of PS–S0s is bimodal, with a peak centred around values typical of lenticular systems, along with another one that roughly aligns with that of the SF subset.

The approach followed in this work is complementary to those followed in similar efforts that focus on the spatial gradient of properties exclusively related to star formation. While the results of our analysis are compatible with the different evolutionary scenarios proposed in the literature for fully-formed S0s, they also reveal a certain tendency to identify gravitational encounters, more specifically, two different types of dry minor mergers, as the primary actors, even in rich environments, at the expense of more traditional mechanisms involving hydrodynamic interactions.

In forthcoming papers, we will extend this methodology to the entire Hubble sequence while incorporating information about the third principal component. The latter, in addition to increasing the fraction of explained sample variance, will allow us to self-consistently disentangle star formation from both nuclear accretion and photoionization by post-AGB stars in any galaxy from a sample of spatially resolved spectra, thus avoiding the use of external activity diagnostics to identify the source of ionization.

ACKNOWLEDGEMENTS

We acknowledge financial support from the Spanish state agency MCIN/AEI/10.13039/501100011033 and by 'ERDF A way of making Europe' funds through research grants PID2019–106027GB–C41 and PID2019–106027GB–C43. MCIN/AEI/10.13039/501100011033 has also provided additional support through the Centre of Excellence Severo Ochoa's award for the Instituto de Astrofísica de Andalucía under contract SEV–2017–0709 and the Centre of Excellence María de Maeztu's award for the Institut de Ciències del Cosmos at the Universitat de Barcelona under contract CEX2019–000918–M. J.L.T. acknowledges support by the PRE2020–091838 grant from MCIN/AEI/10.13039/501100011033 and by 'ESF Investing in your future'. H.D.S. acknowledges support by the PID2020-115098RJ-I00 grant from MCIN/AEI/10.13039/501100011033 and from the Spanish Ministry of Science and Innovation and the European Union - NextGenerationEU through the Recovery and Resilience Facility project ICTS-MRR-2021-03-CEFCA. This project makes use of the MaNGA-Pipe3D dataproducts. We thank the IA-UNAM MaNGA team for creating this catalogue, and the Conacyt Project CB-285080 for supporting them.

DATA AVAILABILITY

This research has made prominent use of the following databases in the public domain: the SDSS Science Archive Server (`https://data.sdss.org/sas/`), the VizieR Online Data Catalog J/MNRAS/515/3956 (`https://cdsarc.cds.unistra.fr/viz-bin/cat/J/MNRAS/515/3956`) and the GSWLC-2 catalogue (`https://salims.pages.iu.edu/gswlc/`).

REFERENCES

Abdurro'uf et al., 2022, ApJS, 259, 35
Alam S., et al., 2015, ApJS, 219, 12
Baldwin J. A., Phillips M. M., Terlevich R., 1981, PASP, 93, 5
Belfiore F., et al., 2018, MNRAS, 477, 3014
Blanton M. R., Kazin E., Muna D., Weaver B. A., Price-Whelan A., 2011, AJ, 142, 31
Blanton M. R., et al., 2017, AJ, 154, 28
Bluck A. F. L., et al., 2020, MNRAS, 499, 230
Boselli A., Fossati M., Sun M., 2022, A&ARv, 30, 3
Bournaud F., Jog C. J., Combes F., 2007, A&A, 476, 1179
Bundy K., et al., 2015, ApJ, 798, 7
Cappellari M., 2016, ARA&A, 54, 597
Cappellari M., et al., 2007, MNRAS, 379, 418
Cherinka B., et al., 2019, AJ, 158, 74
Cid Fernandes R., Stasińska G., Schlickmann M. S., Mateus A., Vale Asari N., Schoenell W., Sodré L., 2010, MNRAS, 403, 1036
Coccato L., Fraser-McKelvie A., Jaffé Y. L., Johnston E. J., Cortesi A., Pallero D., 2022, MNRAS, 515, 201
Crowl H. H., Kenney J. D. P., 2008, The Astronomical Journal, 136, 1623
D'Onofrio M., Marziani P., Buson L., 2015, Frontiers in Astronomy and Space Sciences, 2
Deeley S., et al., 2020, MNRAS, 498, 2372
Deeley S., Drinkwater M. J., Sweet S. M., Bekki K., Couch W. J., Forbes D. A., Dolfi A., 2021, MNRAS, 508, 895
Dekel A., et al., 2009, Nature, 457, 451
Dobos L., Csabai I., Yip C.-W., Budavári T., Wild V., Szalay A. S., 2012, MNRAS, 420, 1217
Domínguez Sánchez H., Bernardi M., Nikakhtar F., Margalef-Bentabol B., Sheth R. K., 2020, MNRAS, 495, 2894
Domínguez Sánchez H., Margalef B., Bernardi M., Huertas-Company M., 2022, MNRAS, 509, 4024
Dressler A., Gunn J. E., 1992, ApJS, 78, 1
Dressler A., Thompson I. B., Shectman S. A., 1985, ApJ, 288, 481
Dressler A., et al., 1997, ApJ, 490, 577
Eliche-Moral M. C., Rodríguez-Pérez C., Borlaff A., Querejeta M., Tapia T., 2018, A&A, 617, A113
Emsellem E., et al., 2007, MNRAS, 379, 401
Fasano G., Poggianti B. M., Couch W. J., Bettoni D., Kjærgaard P., Moles M., 2000, ApJ, 542, 673
Fitzpatrick E. L., 1999, PASP, 111, 63
Fraser-McKelvie A., Aragón-Salamanca A., Merrifield M., Tabor M., Bernardi M., Drory N., Parikh T., Argudo-Fernández M., 2018, MNRAS, 481, 5580
González Delgado R. M., et al., 2016, A&A, 590, A44

Graham A. W., 2023, MNRAS, 522, 3588
Greene O. A., Anderson M. R., Marinelli M., Holley-Bockelmann K., Campbell L. E. P., Liu C. T., 2021, ApJ, 910, 162
Gunn J. E., Gott J. Richard I., 1972, ApJ, 176, 1
Hammer F., Flores H., Puech M., Yang Y. B., Athanassoula E., Rodrigues M., Delgado R., 2009, A&A, 507, 1313
Hubble E., 1926, Contributions from the Mount Wilson Observatory / Carnegie Institution of Washington, 324, 1
Jiménez-Palau C., Solanes J. M., Perea J. D., del Olmo A., Tous J. L., 2022, MNRAS, 515, 3956
Jiménez-Palau C., Solanes J. M., Perea J. D., del Olmo A., Tous J. L., 2022, VizieR Online Data Catalog, p. J/MNRAS/515/3956
Kaviraj S., et al., 2007, ApJS, 173, 619
Kendall P., Magorrian J., Pringle J. E., 2003, MNRAS, 346, 1078
Lacerna I., Ibarra-Medel H., Avila-Reese V., Hernández-Toledo H. M., Vázquez-Mata J. A., Sánchez S. F., 2020, A&A, 644, A117
Larson R. B., Tinsley B. M., Caldwell C. N., 1980, ApJ, 237, 692
Lee J. H., Lee M. G., Mun J. Y., Cho B. S., Kang J., 2022, The Astrophysical Journal Letters, 931, L22
Lin L., et al., 2019, The Astrophysical Journal, 872, 50
Lopes P. A. A., Ribeiro A. L. B., Rembold S. B., 2017, MNRAS, 472, 409
Lotz M., Remus R.-S., Dolag K., Biviano A., Burkert A., 2019, MNRAS, 488, 5370
Mapelli M., Rampazzo R., Marino A., 2015, A&A, 575, A16
Martig M., Bournaud F., Teyssier R., Dekel A., 2009, ApJ, 707, 250
Mas-Ribas L., et al., 2017, ApJ, 846, 4
Maschmann D., Melchior A.-L., Mamon G. A., Chilingarian I. V., Katkov I. Y., 2020, A&A, 641, A171
Maschmann D., Melchior A.-L., Combes F., Mazzilli Ciraulo B., Freundlich J., Halle A., Drabent A., 2022, A&A, 664, A125
Méndez-Abreu J., Sánchez S. F., de Lorenzo-Cáceres A., 2019, MNRAS, 488, L80
Mishra H. D., Dai X., 2020, AJ, 159, 69
Moore B., Lake G., Quinn T., Stadel J., 1999, MNRAS, 304, 465
Navó G., Tous J. L., Solanes J. M., 2019, A&A, 631, A93
Nulsen P. E. J., 1982, MNRAS, 198, 1007
Osman O., Bekki K., 2017, MNRAS, 471, L87
Peluso G., et al., 2022, ApJ, 927, 130
Poggianti B. M., et al., 2009, ApJ, 697, L137
Querejeta M., et al., 2015, A&A, 579, L2
Quilis V., Moore B., Bower R., 2000, Science, 288, 1617
Rathore H., Kumar K., Mishra P. K., Wadadekar Y., Bait O., 2022, MNRAS, 513, 389
Renzini A., Peng Y.-j., 2015, ApJ, 801, L29
Ricarte A., Tremmel M., Natarajan P., Quinn T., 2020, ApJ, 895, L8
Roediger E., Hensler G., 2005, Astronomy & Astrophysics, 433, 875
Salim S., Fang J. J., Rich R. M., Faber S. M., Thilker D. A., 2012, ApJ, 755, 105
Salim S., Boquien M., Lee J. C., 2018a, ApJ, 859, 11
Salim S., Boquien M., Lee J. C., 2018b, ApJ, 859, 11
Sánchez S. F., et al., 2016a, Rev. Mex. Astron. Astrofis., 52, 171
Sánchez S. F., et al., 2016b, Rev. Mex. Astron. Astrofis., 52, 171
Sánchez S. F., et al., 2022, ApJS, 262, 36
Smee S. A., et al., 2013, AJ, 146, 32
Solanes J. M., Salvador-Sole E., 1992, ApJ, 395, 91
Solanes J. M., Perea J. D., Darriba L., García-Gómez C., Bosma A., Athanassoula E., 2016, MNRAS, 461, 321
Tapia T., Eliche-Moral M. C., Aceves H., Rodríguez-Pérez C., Borlaff A., Querejeta M., 2017, A&A, 604, A105
Thomas D., Maraston C., Schawinski K., Sarzi M., Silk J., 2010, MNRAS, 404, 1775
Thomas D., et al., 2013, MNRAS, 431, 1383
Tous J. L., Solanes J. M., Perea J. D., 2020, MNRAS, 495, 4135
Tous J. L., Domínguez-Sánchez H., Solanes J. M., Perea J. D., 2023, ApJ, 942, 48
Walker I. R., Mihos J. C., Hernquist L., 1996, ApJ, 460, 121
Westfall K. B., et al., 2019, AJ, 158, 231
Xiao M.-Y., Gu Q.-S., Chen Y.-M., Zhou L., 2016, ApJ, 831, 63

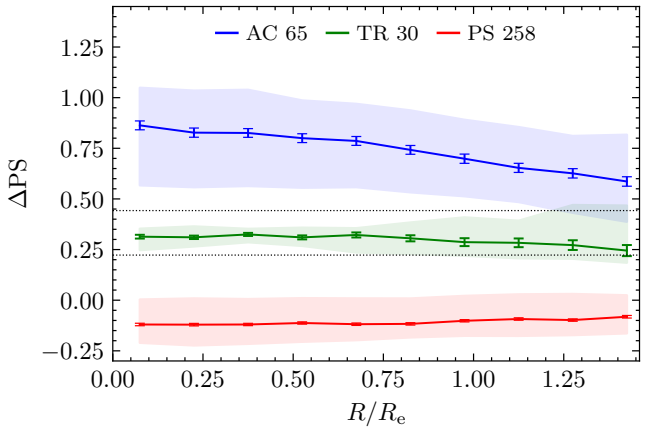

Figure A1. As Fig. 3 but for the reduced sample of S0s defined with a stricter morphological selection criteria (see text for details) and without including the spectral profiles of AC galaxies classified as SF and Seyfert.

del Moral-Castro I., et al., 2020, A&A, 639, L9

APPENDIX A: ROBUSTNESS OF THE RESULTS AGAINST MORPHOLOGICAL CONTAMINATION

In this appendix, we test the robustness of our results against biases caused by uncertainties in the selection of the lenticular morphology. As explained in Section 2, to identify the S0s studied in this work we have adopted the selection criteria $T < 0.5$, as well as the probabilities $P_{\rm LTG} < 0.5$ and $P_{\rm S0} \geq 0.5$ recommended in the Deep Learning-based morphological catalogue of Domínguez Sánchez et al. (2022). Additionally, we have thoroughly reviewed the SDSS images to eliminate spiral contaminants that might have bypassed these filters. However, it is important to note that when probabilities are close to the limits mentioned above, the likelihood that a galaxy is an S0 becomes comparable to the likelihood that it is actually an elongated E or an Sp with faint spiral arms. To evaluate the effects of this potential bias in our results, we now increase the priority given to purity over completeness in our data by placing yet more stringent constraints on the sample selection. Thus, we have repeated our analysis on a subsample of MaNGA S0 galaxies obtained by replacing the conditions stated above by the more restrictive selection criteria $P_{\rm LTG} < 0.3$ and $P_{\rm S0} \geq 0.7$. We consider this approach to be preferable to other options, such as adopting a minimum value in the specific angular momentum and ellipticity of the galaxies to minimise the presence of E systems, since measurements of these two magnitudes are affected by large uncertainties, or imposing an upper limit on the inclination or on the SSFR that minimises contamination by SF Sps, but that could also remove S0s with significant star formation.

After applying the above stricter selection criteria to the MaNGA catalogue, we are left with a sample of 353 S0s. The significantly smaller size of this dataset (contains about one third of the original S0s) makes it impossible to repeat each and every one of the analyses carried out in the main text of this work, but it does allow us replicating an important part of them, enough to confirm that the results obtained with the original sample are not affected by any substantial morphological bias.

Thus, as shown by Fig. A1, the median radial ΔPS profiles of the different spectral classes inferred from the reduced sample of S0s turn out to be nearly identical to those derived in Section 4 for

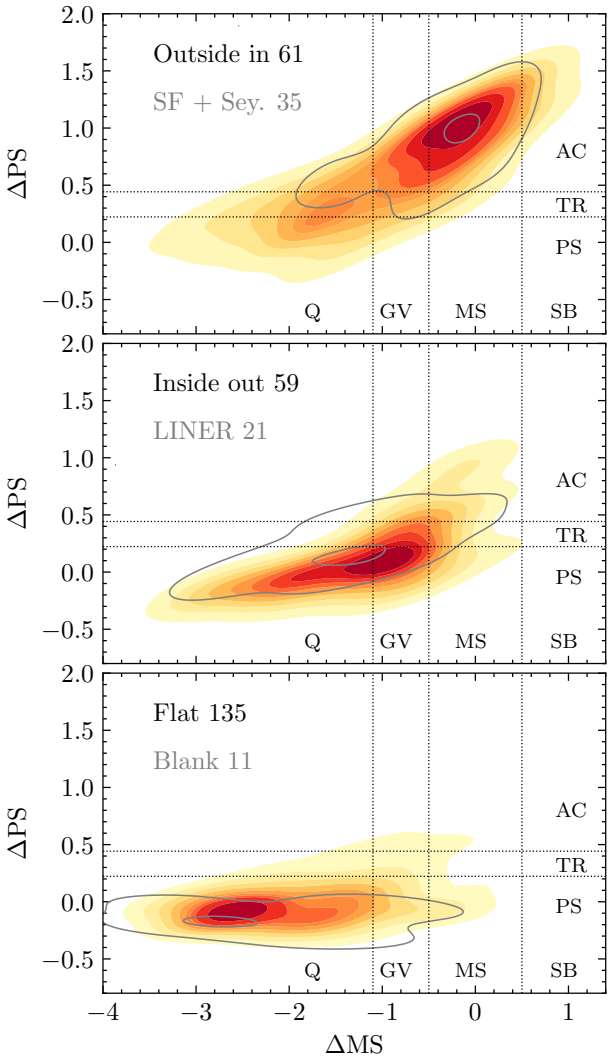

Figure A2. As Fig. 6 but for the reduced sample of S0s defined with a stricter morphological selection criteria (see text for details).

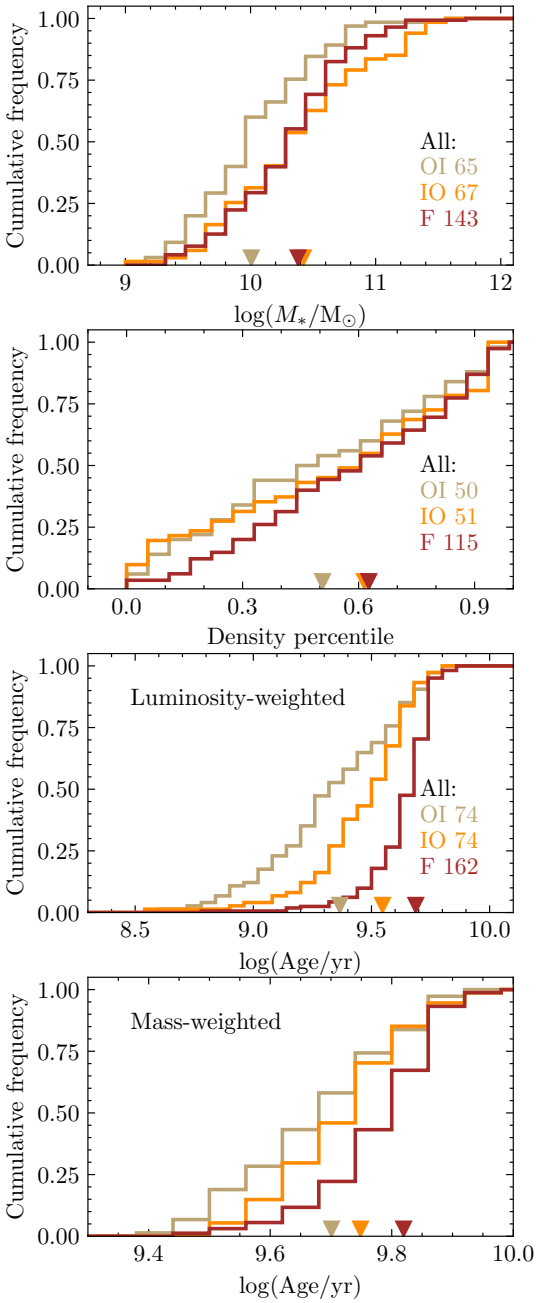

Figure A3. *From top to bottom:* cumulative distribution functions of the stellar mass, local density of the environment expressed by percentiles, and luminosity- and mass-weighted ages for the reduced sample of S0s defined with a stricter morphological selection criteria (see text for details). The histograms represent the CDFs of galaxies with outside in (OI, light brown), inside out (IO, orange), and flat (F, brown) activity gradients. The inverted filled triangles show the medians of these CDFs. The size of each subset is indicated in the legend next to the profile labels. To be compared with the bottom panels of Figs. 8 and 9.

the initial sample and depicted in Fig. 3. Likewise, the ΔMS–ΔPS diagrams in Fig. A2 reveal that the tight relationships between the distributions of activity gradients, spectral and BPT classes, and star formation status of the galaxies featured in Fig. 6 also continue to hold perfectly. The aggregated CDFs of stellar mass, environmental density, and luminosity- and mass-weighted stellar ages of the different activity gradients depicted in the four panels of Fig. A3 maintain clear consistency with their corresponding previous results as well (see the bottom panels of Fig. 8 and 9), thus preserving the hierarchy of the mean values of these variables established by the original data in Section 5. In the same way, the general shapes of the aggregated bivariate distributions of the different spectral classes and gradient types in the $(\lambda_{R_e}, \varepsilon)$ diagram are also preserved. This allows us to identify in the two upper panels of Fig.A4 the same trends between the observed ellipticity and specific angular momentum of stars shown by the more complete samples of S0s with OI and F activity gradients represented in Fig.10. Additionally, the significant reduction in the number of galaxies due to the more stringent morphological selection reveals an interesting effect related to the kinematics of these objects. As the lower panels of Fig. A4 show, this 'morphological cleaning' has a particularly noticeable impact in the region of slow rotators, which reduce their presence in the new sample to only 2.5 per cent, when before this fraction was around 6 per cent. This supports Cappellari (2016)'s claim that slowly rotating E galaxies can be differentiated from S0 galaxies using just their images.

This paper has been typeset from a TEX/LATEX file prepared by the author.

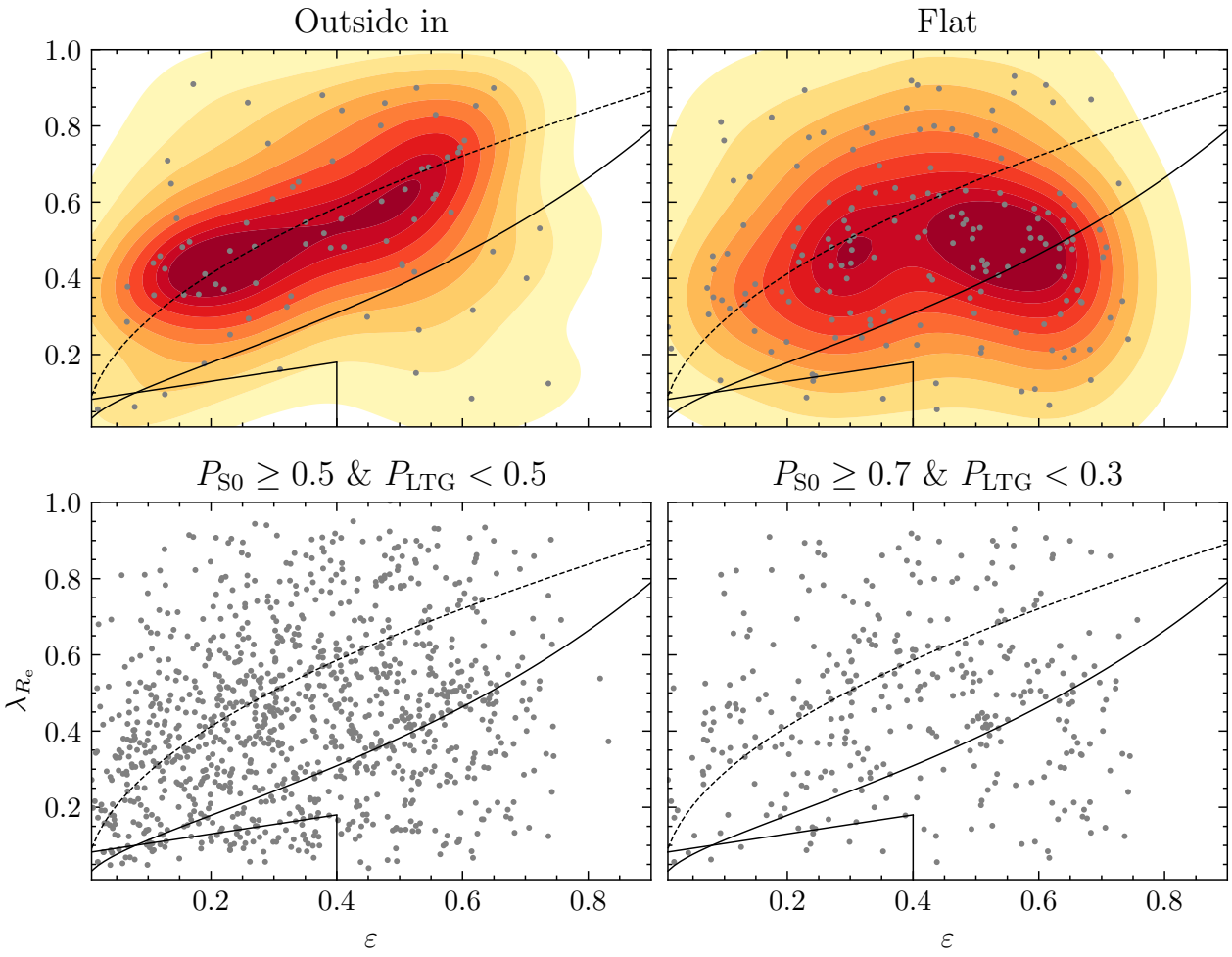

Figure A4. Upper panels are as the upper panels of Fig. 10 but for the reduced sample of S0s defined with a stricter morphological selection criteria (see text for details). Lower panels show the individual $(\lambda_{R_{\rm e}}, \varepsilon)$ values for the 1072 S0s studied in this work (left) and for the 373 S0s in the reduced sample (right). Comparison of the two scatter diagrams demonstrates that the data loss experienced by the reduced sample is considerably greater around the slow rotator area than in the rest of the diagram.

Part III

SUMMARY OF RESULTS AND FUTURE PROSPECTS

6

SUMMARY OF RESULTS AND FUTURE PROSPECTS

Galaxy evolution is a complex journey that transcends a linear progression from the Big Bang to the present day. Numerous physical mechanisms likely contribute to the formation and evolution of galaxies over their lifespans. Confirming the hierarchical paradigm embraced by contemporary theories of galaxy formation, this thesis provides insights that highlight the importance of mergers in the continued evolution of S0-classified galaxies. This importance persists even after these galaxies have adopted their characteristic lenticular shape, as mergers, mostly minor, may contribute to their rejuvenation, thus countering the impact of cluster regions which tend to suppress their star formation.

For the first time, with this thesis, the entire optical spectrum of lenticular galaxies has been used to attempt to constrain their formation pathways. As a purely mathematical procedure, the PCA has liberated us from relying on preconceived ideas about the physics of the galaxies we have investigated. While it may be an atypical approach, as it diverges from the norm of directly working with physical quantities, we have enjoyed the opportunity to interpret the outcomes of our analysis with absolute freedom. In addition, it has enabled us to explore the possibility of characterising S0 galaxies more effectively than if we had followed a more traditional, but at the same time more constrained, procedure. Given the advent of exhaustive galaxy surveys, the timing of this thesis is ideal for actively contributing to building a comprehensive picture of these unique galaxies through the examination of their optical spectra.

6.1 SUMMARY OF MAIN RESULTS AND CONCLUSIONS

Next, I summarize the main results and conclusions derived from the analysis of both single-fibre and integral field spectra of lenticular galaxies.

- The PCA of optical spectra of S0 galaxies presented in Tous et al. (2020; Chapter 2) allows identifying two main, distinct spectral classes within the main galaxy sample of the SDSS. About 70% of S0s, characterized by spectra without emission lines, belong to the PS class, while another 25% show active spectra and belong to the AC class. In comparison to PS, AC-S0s are, on average, slightly less-massive, exhibit SFRs comparable to those observed in LTGs, and avoid high-galaxy-density regions.

- In Jiménez-Palau et al. (2022b; Chapter 3) we demonstrate that the strong correlation between the EW(Hα) and the separation of any spectrum from the PS ridge line in the plane PC1–PC2 translates into a good correspondence between the boundaries of our spectral classes and the demarcations along the vertical axis of the WHAN diagram. Additionally, our findings indicate that most of the nebular emission of Seyfert and LINER S0s detected in radio and X-ray is not driven by star formation.

- The analysis of IFS data from MaNGA presented in Tous et al. (2023; Chapter 4) reveals that coplanar SF rings are relatively abundant in present-day S0 galaxies. Rings are twice as frequent in PS- as in AC-S0s, they are mainly associated with a positive radial gradient of activity, their frequency increases with the mass of the hosts but is uncorrelated with the environment, and they likely feed on residual gas from the disc. With this thesis, we release the complete version of the largest catalogue of ringed galaxies ever identified through spatially resolved spectra (Appendix B).

- As demonstrated in Tous et al. (submitted; Chapter 5), the radial activity gradient of S0s is tightly related to their PCA classification, BPT designation, and star formation status. PS lenticulars typically show flat profiles associated with low-levels of activity, while lenticulars of the AC class often show negative activity gradients, primarily attributed to enhanced central star formation. Positive activity gradients are frequently observed in green valley S0s, mainly from the PS class.

Our results are a robust statistical confirmation of the existence of more than one class within the S0 morphological family and indicate that star formation is not a rare phenomenon in fully-formed S0 galaxies. The clear segregation to low-density environments of the active class, and the relatively similar distributions of stellar mass exhibited by the two main spectral classes, suggests that environment plays a more important role than mass in quenching the star formation of the local S0 population.

The coincidence of the spectral class demarcations with the horizontal WHAN dividers provides physical meaning to the PCA classification derived in Tous et al. (2020). The nebular emission lines, together with the shape of the stellar continuum, represent a large portion of the information contained within the galaxy spectra, and precisely this has been captured by the first principal components. However, the mixing of activity sources identified in Jiménez-Palau et al. (2022b) within the same spectral class, indicates that the variance due to different ionization mechanisms could still be encoded in higher order principal components (see Section 6.2).

Cosmological hydrodynamic simulations show that SF rings in disc galaxies can result from mergers. The fact that we observe SF rings in *fully-formed* S0s suggests that they are likely the outcome of galaxy rejuvenation (Mapelli et al. 2015), rather than the final stages of recently transformed S0s that are quenching inside out after a merger (Deeley et al. 2021). The characteristics of rings observed in real lenticulars as described in Tous et al. (2023), suggest that they probably feed on gas from the host and that the interaction should be a "mini merger", involving the capture by the S0s of tiny neighbouring satellites. The two conditions are required to explain both the high intensity of activity observed in the rings and their occurrence even within large galaxy aggregations. On the other hand, the battery of formation mechanisms presented in Section 1.2 suggests that negative activity gradients could be a common feature in lenticulars observed at the later stages of their morphological transformation. However, the observation of enhanced star formation in the central part of disc galaxies often coincides with clear signs of a recent gravitational interaction (e. g., Maschmann et al. 2020, 2022) that could betray, instead, rejuvenation in fully-formed S0s (Rathore et al. 2022).

Although the results presented in Tous et al. (submitted) cannot be used to rule out either possibility, they seem to tip the scale in favour of the rejuvenation scenarios. Galaxies with negative activity gradients fit within the "mini merger" scenario showing in addition, within each spectral class, statistically younger stellar populations than those of the other gradient types. Moreover, the high SSFRs that characterize the lenticulars with negative activity gradients, which are typical of SF main sequence galaxies, indicate that these systems are not fading but, instead, have been probably rejuvenated. Either way, the PS spectral class with a null activity gradient seems to be the finish line where, sooner or later, all fully-formed lenticular galaxies arrive.

6.2 FUTURE PROSPECTS

At several points in this thesis it has been mentioned that the third principal component, PC3, can be used to identify the ionization source. This is so because this component is characterized by an essentially flat continuum and several ionization lines, among which there are five out of the six lines used in the BPT digrams: Hα, Hβ, [O III], [N II], and [S II] (see figure 2 in Tous et al. 2020). Thus, by incorporating the third principal component, our spectral classification system should provide a much more complete picture of activity in S0 galaxies in the optical domain. This statement is illustrated by the updated version of our PCA classification provided in Fig. 2, which introduces the ΔPS–PC3 diagram (Tous et al. in preparation).

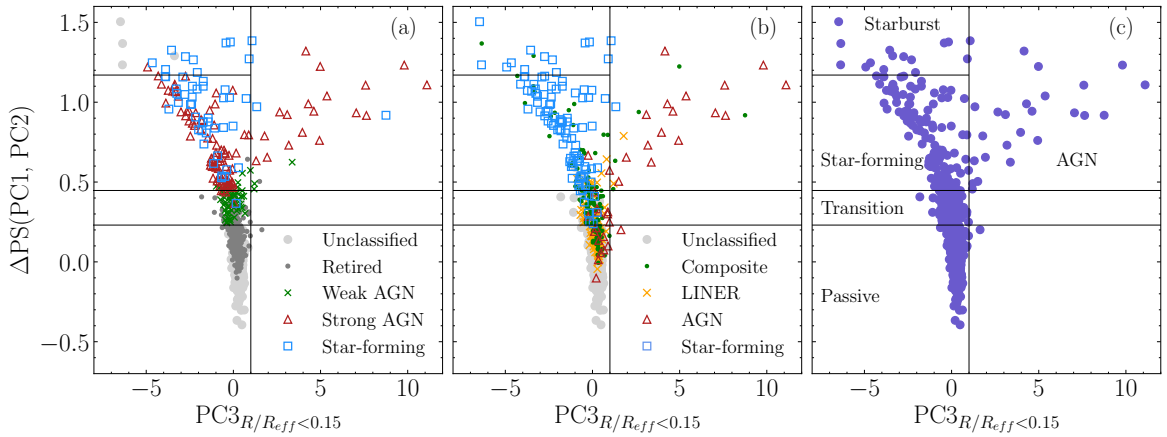

Figure 2: Distribution of 937 S0s in the ΔPS-PC3 diagram classified using the WHAN (a), the BPT (b), and the PCA (c) schemes. The two lower horizontal lines correspond to the PS/TR/AC class dividers derived in Jiménez-Palau et al. (2022b), while the vertical line has been introduced to distinguish the regions where galaxies cluster depending on whether the dominant ionization source is star formation or AGN. The upper-left corner contains galaxies with strong emission lines (EW(Hα)$\geqslant$ 100 Å) likely associated with a starburst. Note the segregation of the WHAN classes: retired, weak AGN and strong AGN/star-forming along ΔPS (a); and the BPT classes: star-forming/LINER and AGN along PC3 (b).

This diagram condensates along the vertical axis the information of the first two principal components through ΔPS (equation 2 from Jiménez-Palau et al. 2022b), exploiting its good correspondence with the horizontal dividers of the WHAN diagram (panel a of Fig. 2, see also figure 7 in Jiménez-Palau et al.). On the horizontal axis, PC3 acts like the BPT diagrams, segregating the ionization sources when the spectra of the central region of the galaxies ($R/R_{eff} < 0.15$) are projected (panel b of Fig. 2). Note that, while the latter two narrow-line systems discriminate about 45% and 60% of S0s, respectively, the PCA classifier includes any galaxy, regardless of its activity level, as it relies on information from the full optical spectrum rather than solely on the flux of a few emission lines. Our idea for the nearby future is to exploit the full potential of our updated PCA classifier, as shown in panel c of Fig. 2, and extend it to the rest of the Hubble tuning fork diagram.

Finally, this thesis has awakened my interest in knowing more about galaxy rejuvenation. All the processes that can transform a spiral galaxy into a lenticular are somehow related to the suppression of star formation. In a quiescent galaxy, the disc instabilities that would typically lead to the formation of spiral arms grow uncontrollably and self-destruct due to a lack of SF regions where the gas collides and dissipates the excess of energy. However, as we have demonstrated, a quarter of the present-day population of lenticular galaxies exhibits ongoing star formation, yet shows no signs of spiral arms. Thus, understanding the existence of these objects depends, to

a great extent, on our knowledge of the mechanisms of galaxy rejuvenation.

There are several tests that could help to prove the two scenarios of rejuvenation through mergers that we have proposed. For example, we could study the relation between the different radial activity configurations and merger signatures like double-peak spectra or kinematic misalignments. Determining the metallicity of the SF rings could be used to rule out an external origin of the ionized gas from cosmic filaments or low-metallicity, dwarf satellites. Nevertheless, the most conclusive evidences might come from directly studying the molecular gas, which is the raw material of star formation. Despite their quiescent status, ETGs may retain some of this gas that, if it is compressed – for example by the shocks produced in a galaxy merger – and reaches a sufficiently high density, could reignite the star formation. But, is the gas reservoir in quiescent galaxies enough to account for the observed rejuvenation associated with the different activity configurations? Or is an external supply needed? To answer these questions, first I will need to acquire new skills to explore lenticular galaxies in the radio domain.

Part IV

APPENDIX

A

STACKING OF SPECTRA: IDENTIFYING STARS ENRICHED IN NEUTRON-CAPTURE ELEMENTS

Stacking techniques have been extensively used in astronomy since the advent of photographic plates. The philosophy is to accumulate light from a target source and use the randomness of noise to increase the S/N in the output data. The stacking procedure described in Section 3.1 of Tous et al. (submitted; Chapter 5) was developed several years ago to study the mean spectrum of S0 galaxies in low- and high-density environments during my Master's thesis (Tous 2018).

In Navó et al. (2019), the stacking procedure is adapted to derive reference spectra for a sample of around 70,000 F- and G-type stars in 215 plates from the segue2 and segcluster programs of the Sloan Extension for Galactic Understanding and Exploration (SEGUE) survey (Yanny et al. 2009). Integrated flux differences with respect to the reference spectra are computed for each individual star at five fine absorption lines of europium. Stars are then ranked by their likelihood of having enhanced content of this heavy element, identifying as such those scoring in the upper 2.5%. We then identify those plates with at least three positive detections, which is the minimum number required, in the present work, to consider that this part of the Galaxy would merit being explored in the search for n-capture enriched stars.

We find that only one plate among 202 in the segue2 program meets the minimum criteria, while up to four of the 13 plates in the segcluster program contain multiple stars enriched n-capture elements. These findings are consistent with the expectation that most targets included in the tiles of the latter program, which are specifically directed at both globular and open star clusters, should be stars created in a common formative environment; while the presumably disparate birthplaces of the objects observed in the segue2's tiles should contribute to blur any signature that might exist from past heavy-element nucleosynthesis events in the targeted regions of our Galaxy. Of especial interest are the NGC 5053 and M 3 globular clusters. With ten or more objects potentially rich in heavy elements, they are the two stellar systems of the segcluster program with the highest fractions of r-process enriched stars: 7% and 15%, respectively. We provide a table with the SDSS identifiers and basic information of the 43 candidate stars rich in r-process elements that have been detected in these five plates.

Our method enables a fast and reliable detection of the fine absorption lines produced by heavy elements in stellar spectra with a resolution unsuitable to approach this problem in a traditional way.

A&A 631, A93 (2019)
https://doi.org/10.1051/0004-6361/201936324

Astronomy & Astrophysics

A statistical method for the identification of stars enriched in neutron-capture elements from medium-resolution spectra

G. Navó[1,2], J. L. Tous[1,2], and J. M. Solanes[1,2]

[1] Departament de Física Quàntica i Astrofísica, Universitat de Barcelona, C. Martí i Franquès, 1, 08028 Barcelona, Spain
e-mail: gerrinp@gmail.com
[2] Institut de Ciències del Cosmos (ICCUB), Universitat de Barcelona, C. Martí i Franquès, 1, 08028 Barcelona, Spain

Received 16 July 2019 / Accepted 24 September 2019

ABSTRACT

We present an automated statistical method that uses medium-resolution spectroscopic observations of a set of stars to select those that show evidence of possessing significant amounts of neutron-capture elements. Our tool was tested against a sample of ~70 000 F- and G-type stars distributed among 215 plates from the Galactic Understanding and Exploration (SEGUE) survey, including 13 that were directed at stellar Galaxy clusters. Focusing on five spectral lines of europium in the visible window, our procedure ranked the stars by their likelihood of having enhanced content of this atomic species and identifies the objects that exhibit signs of being rich in neutron-capture elements as those scoring in the upper 2.5%. We find that several of the cluster plates contain relatively large numbers of stars with significant absorption around at least three of the five selected lines. The most prominent is the globular cluster M 3, where we measured a fraction of stars that are potentially rich in heavy nuclides, representing at least 15%.

Key words. nuclear reactions, nucleosynthesis, abundances – line: identification – methods: statistical

1. Introduction

Metals in stars today are a snapshot of the metals in the interstellar medium (ISM) at the time and place where stars were born. While element synthesis is reasonably well understood from the primordial lightest elements up to the iron peak via fusion reactions that take place in the stellar interiors, explaining the origin of elements that are heavier than iron remains one of the major challenges in modern astrophysics. In order to accomplish this, it is essential to gather detailed and accurate information on the stellar abundances of the elements in question.

Since the binding energy per nucleon only increases until ^{62}Ni (though it is generally believed that ^{56}Fe is more common than nickel isotopes), heavier elements present in ancient halo stars, the ISM, dust grains, meteorites, and on Earth cannot be produced in a fusion process and must form by reactions of neutron (n) capture usually followed by a β^- decay (most commonly) or β^+ decay, which have the generic form:

$$^{A}_{Z}X + n \rightarrow {}^{A+1}_{Z}X + \gamma, \tag{1}$$

$$^{A+1}_{Z}X \rightarrow {}^{A+1}_{Z+1}X + e^- + \bar{\nu}_e \quad \text{if } \beta^-, \tag{2}$$

or

$$^{A+1}_{Z}X \rightarrow {}^{A+1}_{Z-1}X + e^+ + \nu_e \quad \text{if } \beta^+, \tag{3}$$

where A and Z are the mass number and the atomic number of the nuclide, respectively.

The two predominant n-capture mechanisms are the *s*-process and the *r*-process, which are from slow and rapid neutron capture, respectively (Burbidge et al. 1957; Meyer 1994; Sneden & Cowan 2003). In *s*-process reactions, the characteristic time of β-decay, τ_β (Eqs. (2) and (3)), is short compared to the neutron capture time (Eq. (1)), τ_n, that is $\tau_\beta \ll \tau_n$, creating elements close to the floor of the valley of stability, which is formed by long-lived heavy nuclides (Busso et al. 1999; Sneden et al. 2008; Heil et al. 2009; Käppeler et al. 2011). Instead, in *r*-process reactions the time related to β-decay is large compared to the neutron capture time, $\tau_\beta \gg \tau_n$, allowing the capture of several neutrons before the nuclei have time to undergo radioactive decay (Reifarth 2010; Thielemann et al. 2011; Arnould et al. 2007). As a result, the *r*-process typically synthesizes the heaviest isotopes of every heavy element.

While τ_β only depends on the nuclear species, τ_n hinges on the neutron flux involved. The *s*-process takes place within stars, particularly during He-burning. Therefore, it can occur in the He-shell flashes of asymptotic giant branch (AGB) stars or in the He-burning cores of massive stars ($M > 12\,M_\odot$) where new heavy elements are synthesized through the capture of free neutrons by preexisting heavy nuclei. This mostly arises in iron isotopes that are left, for instance, by a previous stellar generation (Lugaro et al. 2003; Karakas et al. 2012; Battistini & Bensby 2016; Goriely & Siess 2018; Limongi & Chieffi 2018). Thus, the observation of an overabundance of *s*-process elements in low-mass halo stars that cannot produce them is nowadays explained by the transfer from a more massive companion, currently a white dwarf, that has gone through some of these He-burning phases (see e.g., the review by Sneden et al. 2008 and references therein). Due to the relatively low neutron densities involved in this process (~10^8 cm^{-3}; Busso et al. 1999), typically several decades can pass between consecutive neutron captures.

On the other hand, although the astrophysical sources of the *r*-process are still not definitively identified, it is well known that this is a primary process that only occurs in environments with extremely large neutron densities (~10^{20}–10^{28} cm^{-3} depending on the source consulted, e.g., Kratz et al. 2007; Frebel & Beers 2018; Liccardo et al. 2018), meaning that it cannot occur in stellar interiors. The huge densities involved also imply, contrary to

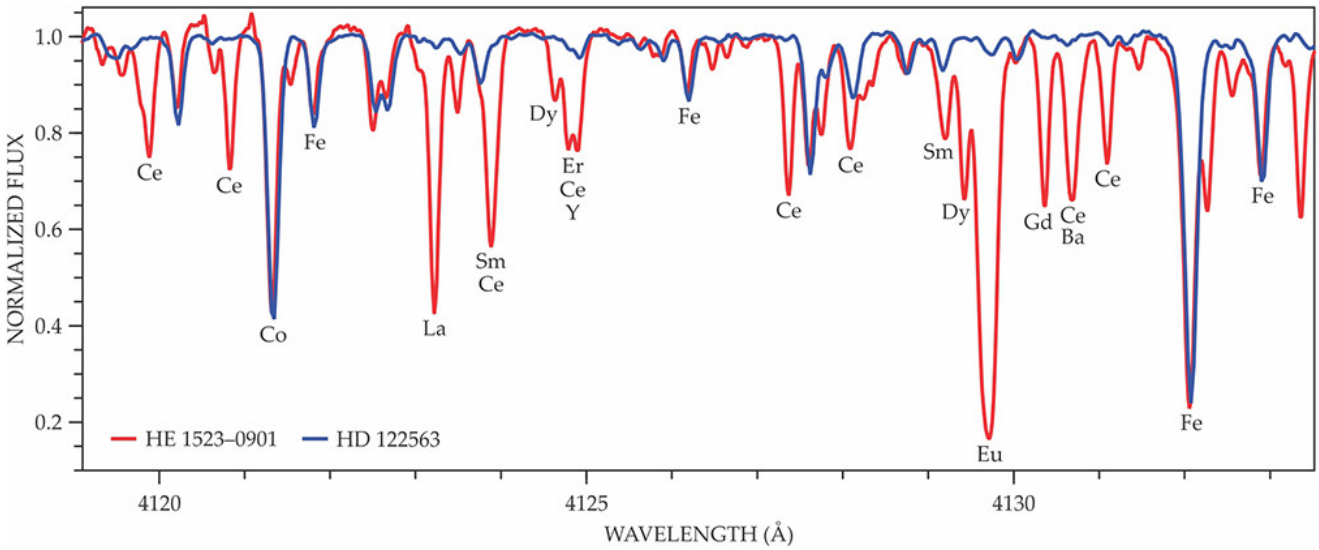

Fig. 1. High-resolution spectra of two stars: HD 122563 (blue) and HE 1523−0901 (red). While the former star has low abundances of *r*-process elements, the latter is the richest object in these elements ever found in the Galaxy's halo. It is important to note that the spectrum of HE 1523−0901 shows a large number of strong absorption lines from lanthanides such as lanthanum (La), cerium (Ce), samarium (Sm) and europium (Eu), which produces the most intense absorption line at 4129.70 Å. (Reproduced from Frebel & Beers 2018, with the permission of the American Institute of Physics).

the *s*-process, that the *r*-process can itself create free nucleons as well as the heavy seeds (iron-peak nuclei) that are required to build heavier elements.

Traditionally, the most probable site for the *r*-process has been assumed to be the large regions swept by the ejecta (i.e., neutrino winds) of core-collapse supernovae (SNII; Burbidge et al. 1957; Woosley et al. 1994; Cowan & Thielemann 2004; Thielemann et al. 2018). However, theoretical models that rely on this mechanism have difficulties in explaining the observed, very low abundance of *r*-process nuclides in the interstellar medium, as well as the required high density of free neutrons in the ejected material.

Another possible, presumably less uniformly distributed, source of neutron-rich matter are binary neutron star (NS–NS) mergers (Freiburghaus et al. 1999; Komiya & Shigeyama 2016; Kasen et al. 2017; Naiman et al. 2018). The feasibility of this scenario was recently confirmed in 2017 when the gravitational waves coming from the LIGO/Virgo Event GW170817 were used to identify the location of a kilonova[1] whose rapidly expanding ejecta revealed spectral features consistent with the presence of high-opacity lanthanides (Pian et al. 2017; Arcavi et al. 2017; Smartt et al. 2017). Assuming the solar *r*-process abundance pattern for the ejecta, current Galactic chemical evolution models suggest that this NS–NS merger event may have generated between 1–5 Earth masses of europium (Eu) and 3–13 Earth masses of gold (Argast et al. 2004; Côté et al. 2018). This is a much higher yield of heavy materials than in typical SNII, which compensates for their alleged greater rarity. More importantly, the range of the cosmic NS–NS merger rate estimated by LIGO/Virgo, although still poorly constrained, is consistent with the range required by these models to explain the nucleosynthesis of heavy elements in the Milky Way.

Very recently, collapsars – the supernova-triggering collapse of rapidly spinning, massive stars into black holes – have also been suggested to explain the presence of heavy elements in the stars that formed early in the history of the universe. This rare type of supernovae can occur shortly after the first stars begin to form and they are expected to be even more prolific producers of *r*-process elements than NS–NS mergers (Siegel et al. 2019). All of these findings are shifting the focus from SNII to both binary NS mergers and collapsars as the primary *r*-process sites in the universe.

The aim of this work is to provide a tool to locate regions of our Galaxy that show signs of being rich in n-capture elements, such as those arising from the *r*-process mentioned above. For this purpose, we use the complete spectral sample from the Sloan Extension for Galactic Understanding and Exploration (SEGUE) survey collected under the program names segue2 and segcluster during the first and second extensions of the Sloan Digital Sky Survey that was made available for its eighth Data Release (SDSS-III DR8; Yanny et al. 2009; Eisenstein et al. 2011). The segue2 program plates contain spectra for approximately 119 000 stars, and the program focuses on the in situ stellar halo of the Galaxy at distances between 10 and 60 kpc. Among the different target types included in this survey, there are blue horizontal branch stars, F and G main-sequence stars, and K- and M-giants. On the other hand, the segcluster program consists of 13 plates specifically targeted on known globular or open clusters. We aim to search for the presence of neutral or singly ionized Eu in the spectra of these stars since this element is one of the best indicators of enrichment by rapid n-capture reactions (Argast et al. 2004). In particular, Eu is an element synthesized practically on its totality through the *r*-process (97% at solar metallicity according to Burris et al. 2000) that has several strong absorption lines in the part of the electromagnetic spectrum falling within the wavelength coverage of SEGUE. Fig. 1 illustrates the major differences that can result in a small range of visible wavelengths between an n-capture-rich star and one that is not when they are observed with a very high-resolution spectrometer.

This article is organized as follows. In Sect. 2 we describe our data sample and the analysis performed. In Sect. 3 we briefly

[1] A rapidly fading optical-infrared transient powered by the radioactive decay of n-rich species synthesized in NS–NS mergers.

discuss the results obtained. Finally, in Sect. 4 we present the main conclusions of this work.

2. Methodology

2.1. The data

The spectra range of SEGUE is from 385 nm to 920 nm, with an average spectral resolution of $R \equiv \lambda/\Delta\lambda \sim 2000$ (4 km s^{-1}). Although it does not allow one to resolve the usually very thin lines corresponding to atomic electronic transitions, it is, however, good enough to make the application of the statistical procedure that we describe in this article feasible. The SEGUE sample consists primarily of two surveys, SEGUE-1 and SEGUE-2, which in turn encompass several programs that vary in their observational focus. Each program consists of a number of different plates or tiles, each covering an area of 7 deg^2 and containing 640 fibers. The segue2 program mainly focuses on the distant northern Galactic halo region. It consists of 202 tiles that encompass a total sky area of 1317 deg^2 and spectroscopically observe a total of 118 151 unique stars up to a magnitude of $g = 19$. The segue2 "blind" plates contain stars that are likely heterogeneous in terms of their chemical abundances because of the mixing that results from the high proper motions, which are characteristic of this structural component. In contrast, the segcluster program focuses on regions dominated by open and globular clusters, that is, on collections of stars that are expected to be more chemically homogeneous because they contain numerous objects that have been gravitationally bound since the day they were born.

In this work, we analyze the subset of high-quality, high signal-to-noise ratio (S/N) spectra (see next section) of ~70 000 stars of F and G spectral types. In fact, the adopted dataset is heavily biased against G-type stars. Therefore, we were forced to limit the application of our statistical procedure to the warmest objects (subclasses G0–G2) of G-type stars. This constraint was far from an inconvenience and was actually beneficial for this analysis since we excluded the coolest G-type objects, which are also the most likely to be affected by absorption lines from diatomic molecules (CH, CN) in the spectral region studied. Depending on the intensity of these lines, they could potentially lead to false detections, something that might happen if our method is applied to the colder K- and M-type stars.

2.2. Spectral analysis

Our methodology essentially consists of first averaging the spectra for all of the stars with the same spectral type and then comparing each individual spectrum with the inferred mean to identify the most discordant ones (i.e., the most flux deficient) in several narrow spectral bands that encompass certain strong absorption lines of n-capture elements. The averaging process is based on the algorithm described in detail by Mas-Ribas et al. (2017; see references therein), which we modified in order to adapt it to our needs. We began by shifting each spectrum to the laboratory rest-frame. Because the binning in wavelength has a constant logarithmic dispersion, the correction is given by $\log \lambda_r = \log \lambda_o - \log(1+z)$, where λ_r is the rest-frame wavelength and λ_o is the observed one. After this correction, we rebinned the flux and its error by interpolating into pixels with a constant logarithmic spacing of 0.0001, so the resolution of the original spectra was preserved along the full visible range[2]. Next, we removed the pixels whose errors are set to infinity from the spectra as well as those that have the mask bit `BRIGHTSKY` activated[3]. Any spectrum containing more than 50% of problematic pixels was discarded from the sample. Furthermore, we also discarded from the analysis those spectra in which the most immediate neighborhood of the lines selected to probe the presence of n-rich species (see below) was not free of anomalies. This neighborhood is formed by the twenty pixels located to the left and right of the central pixel of these lines (i.e., the interval $\lambda_{i-20} \leq \lambda_i \leq \lambda_{i+20}$, with λ_i the pixel containing the wavelength of any line of interest).

Then, we used the tool iSpec (Blanco-Cuaresma et al. 2014; Blanco-Cuaresma 2019) for each spectrum, j, that fit the criteria just mentioned to determine both its S/N, s_j, and normalized flux, f_j (for the continuum normalization we used a spline of second degree every 5 nm that ignores any region with strong lines). Finally, the normalized spectra having an $S/N \geq 10$ were stacked together as the weighted average

$$\bar{f}_i = \frac{\sum_j s_j \cdot f_{ij}}{\sum_j s_j}, \tag{4}$$

where $\bar{f}_i$ is the mean normalized flux at pixel i. The error assigned to the mean fluxes is simply the sample standard deviation of the composite spectrum at each pixel:

$$\sigma_{\bar{f},i} = \sqrt{\frac{\sum_j \left(f_{ij} - \bar{f}_i\right)^2 \cdot s_j}{\sum_j s_j}}. \tag{5}$$

To minimize the chances of making erroneous identifications, we chose a total of five lines of two different species of the r-process element Eu that are among the strongest lines of this element in the visible window. There are three intense lines of Eu I, as well as two Eu II resonance lines that are also among the most intense of this species, all of them located near the UV-Blue end of this window (see Kramida et al. 2018 and references therein). In order to detect the lines, we have taken into account that SEGUE's spectra have been obtained using a medium-resolution instrument with a spectral resolution of about two angstroms in the range of wavelengths of interest. This means that, in practice, the fluxes of the narrow, sub-angstrom-wide lines produced by heavy nuclides (see Fig. 1) end up distributed among several pixels around the peak[4]. This makes them both wider and weaker and increases the likelihood that they would blend with adjacent lines. The absorption lines that we wish to detect are expected, therefore, to show up in the SDSS data as moderately deep depressions of the continuum that spread over a few angstroms. The different absorption lines adopted and the spectral ranges assigned for their detection are both listed in Table 1.

With all of this in mind, we devised a strategy to find candidate stars rich in n-capture elements, which consists in computing the differences between the fluxes of each individual stellar spectrum and the average spectrum of the corresponding spectral class calculated within four-Å-wide spectral ranges around the adopted lines (see Table 1). The differences for each spectral range were then ranked in increasing order and those included in the upper 2.5% were considered to be indicators of the existence of an enhancement in the corresponding species. We also imposed that for a star to be considered a potential candidate

[2] http://www.sdss.org/dr12/spectro/spectro_basics/

[3] See SDSS bitmasks at http://www.sdss.org/dr12/algorithms/bitmasks/#SPPIXMASK.

[4] Pixel size at ~4000 Å is a bit less that one Å.

Table 1. Strongest lines from Eu in optical window and assigned spectral ranges for detection (see text).

Nuclide	Spectral line (Å)	Spectral range (Å)
Eu I	4594	4592–4596
	4627	4625–4629
	4661	4659–4663
Eu II	4129	4127–4131
	4205	4203–4207

rich in n-capture elements, it must have produced positive results in the overabundance of these elements in the majority fraction of the selected spectral regions, that is, in at least three of the five[5] Eu lines. The final step consisted of identifying the SEGUE plates that contain the highest number of stars with these characteristics. The idea behind this procedure is that we expect metal enrichment, especially when it is driven by rapid n-capture in spatially localized events, to manifest itself clearly in specific regions of the Galaxy, such as the star clusters targeted by the segcluster program where most objects share a common origin. Likewise, we hope that finding evidence of localized enrichment in heavy nuclides will be more difficult in the segue2 plates, since they include Galactic halo field stars with disparate formation histories.

At this point, it also has to be borne in mind that some of the electronic transitions that we aim to detect produce absorption lines that are known to be ill-suited for equivalent-width analysis. This is because they can blend with nearby lines from lighter metal species and/or by molecular band regions that also lead to difficulties in placing the continuum (e.g., Koch & Edvardsson 2002; Roederer & Lawler 2012; Siqueira Mello et al. 2012; Battistini & Bensby 2016). Certainly, these factors can make the detection of such lines in individual stellar analyses very challenging (even from very high-resolution and S/N observations), which critically limits their usefulness as estimators of the abundance of n-capture elements. We want to emphasize, however, that the effects of crowding are taken into account in our methodology. This is so because it relies on the identification of the most statistically significant deviations in the fluxes from the spectral regions around lines of n-rich elements, which are self-consistently synthesized by averaging the spectra from thousands of similar Galactic halo stars that have been observed with the same instrument. This should also account for possible affectations related to hyperfine splitting due to the presence of different isotopes. In addition, the robustness of this procedure was boosted by introducing the requirement that, for a star to be considered an n-capture-rich candidate, it must present simultaneous indications of flux deficits in the mayority of the lines of interest. In any event, in an effort to be conservative, we subdivided our candidate stars into primary and secondary candidates, according to whether or not they show a significant flux deficit in the spectral ranges that are associated with at least one of the Eu absorption lines at 4129 Å and 4594 Å, which are two of the most frequently used indicators of the abundance of *r*-process elements in the visible spectral range because of their strength and lack of significant blending (see e.g., Fig. 1).

[5] This number and the minimum rank for detection were adopted interdependently to avoid selecting too many or too few candidate stars. We verified, however, that the results of the present analysis remain essentially unchanged as long as the values of these two parameters are kept within reasonable bounds.

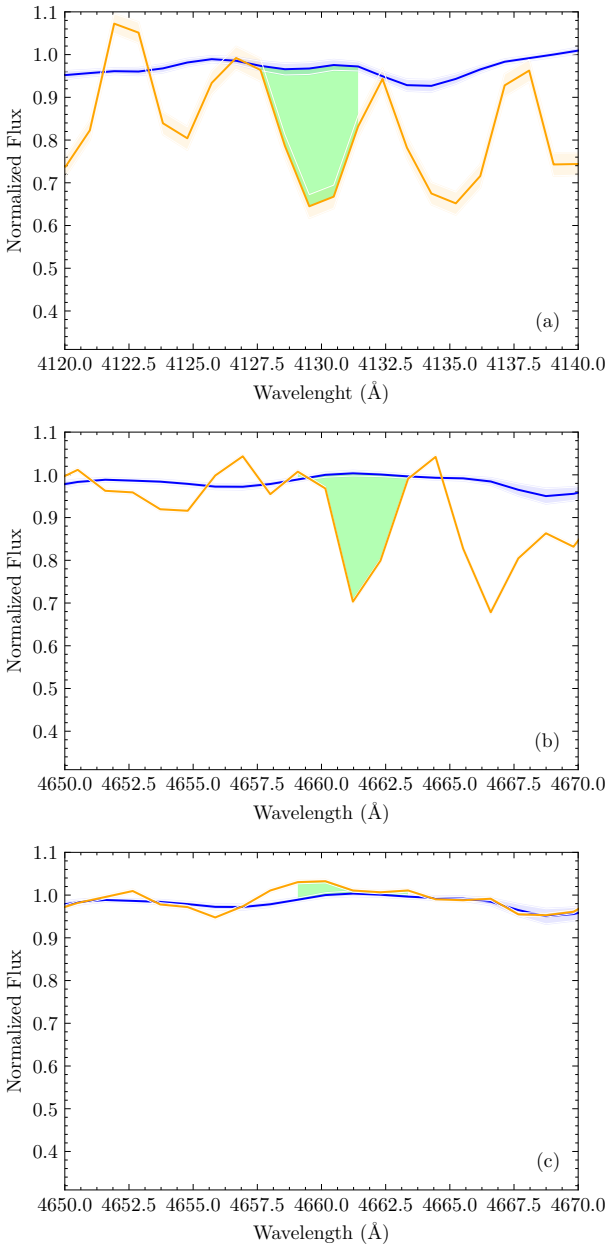

Fig. 2. Comparison of certain observed lines in F5 stars (orange curves) with average flux inferred from whole spectral class (blue curves). The lighter bands surrounding the fluxes show their associated uncertainties, while the green colored areas identify the integrated flux differences that we attribute to lines from Eu. *Panel a*: F5 star (`specobjID` = 3719984370237415424) that shows a substantial flux deficit compared to the mean in the 4127–4131 Å wavelength range that encompasses an important line of Eu II (see Table 1). *Panel b*: another F5 star (`specobjID` = 2786716958031191040) also showing a significant flux deficiency in the 4659–4663 Å range, which is the interval of wavelengths where one expects to find a strong Eu I line. In both cases the stars have been identified as positive detections. In contrast, *panel c* shows a third F5 star (`specobjID` = 3002850987342928896) that does not show evidence for the existence of this latter line in absorption, which classifies it as a non-detection.

Figure 2, provides a graphical example of the sort of spectral features with which our method operates. In the top and middle panels of the plot, we include two F5 stars whose stellar spectra show large deficits with respect to the average flux of this spectral class within the spectral ranges that delineate

Table 2. SEGUE plates with at least three candidate stars rich in n-capture elements.

SEGUE program	Plate ID	l (°)	b (°)	Cluster ID	$N_{\geq 3}$	N_3	N_4	N_5	Q	F_r
Segue2	3304	132.06	62.00	–	3	3	0	0	0.1	0.08
Segcluster	2667	132.82	10.94	M 67	6	4	2	0	0.5	0.03
	1961	54.00	−35.43	M 2	6	4	1	1	0.3	0.03
	2476	199.03	17.01	NGC 5053	10	8	2	0	0.3	0.07
	2475	42.31	78.70	M 3	18	13	4	1	0.2	0.15

the Eu II line at 4129 Å and the Eu I line at 4661 Å, which are represented by solid green areas. In both cases the flux differences within the corresponding spectral ranges fall into the upper 2.5% and, therefore, are classified as potential detections of these species. This situation clearly contrasts with the bottom panel, where we show the spectrum of another F5 star that, instead of showing a significant decrease in the intensity within the spectral window associated with the Eu I 4661 Å line, presents a slight increase with respect to the mean, which classifies it as a non-detection. Next, we present and comment on the results obtained after applying our methodology to identify stars rich in n-capture elements to the collections of spectra gathered in the segue2 and segcluster samples.

3. Results

The application of the statistical procedure described in the previous section led us to detect a total of 67 *r*-process-rich candidates in the different tiles that make up the segue2 and segcluster programs. Forty-three of these objects (39 primary and 4 secondary) are distributed in the five plates that we include in Table 2 where we list the plate ID (in Col. 2), the galactic coordinates of its center in degrees (Cols. 3 and 4), and the name of the targeted cluster (Col. 5) for those belonging to the segcluster program. These plates correspond to regions of the sky that include at least three positive detections, which is the minimum number required, in the present work, to consider that this part of the Galaxy would merit being explored in the search of n-capture enriched stars. As expected, all but one of these plates are devoted to star clusters. Besides, the only field halo (segue2) plate in this list contains the lowest total number of stars with an enhanced content in heavy elements in at least three lines, $N_{\geq 3}$ (Col. 6). Table 2 also reports the number of stars per plate whose spectrum produces evidence that is favorable to the existence of significant amounts of elements arising from n-capture nucleosynthesis in exactly $l = 3$, 4, and 5 of the narrow spectral ranges investigated and given by N_3, N_4, and N_5 (Cols. 7–9)[6], respectively. The last two columns of Table 2 provide information about the fraction of stars within each plate whose spectrum complies our quality requirements (see Sect. 2.2), which is defined by the ratio

$$Q \equiv \frac{\#\,\text{high-quality spectra}}{\#\,\text{spectroscopic targets}}, \tag{6}$$

and the frequency of candidate stars per plate

$$F_r \equiv \frac{\#\,\text{spectra rich in n-capture elements}}{\#\,\text{high-quality spectra}}. \tag{7}$$

The comparison of the values reported for the last relation with its probability distribution function (PDF) inferred from the whole dataset allows one to observe their extreme nature: while the median of the PDF is $\tilde{F}_r = 0.0$ (and the mean is $\langle F_r \rangle = 0.004$) all of the frequencies listed are well within its upper decile ($F_r > 0.014$). Therefore, these figures can be considered as a piece of evidence that lends support to the claim that the selected plates are directed at locations in the Galaxy where there is an overabundance of stars rich in *r*-process elements. We note that four of these five plates sample areas of the sky containing collections of stars with a contemporary origin and that, therefore, are expected to have a similar chemical composition. On the other hand, the fact that the plates with the highest numbers of candidate stars (IDs 2475 and 2476) show Q values very close to the average of the whole set, $\langle Q \rangle \simeq 0.2$, excludes the possibility that the number of these stars found in a plate depends on the fraction of spectra analyzed. It should be added that even if we only consider the candidate stars contained in these five plates, the probability of obtaining 43 positive signals from a sample of 70 000 stars by chance is extremely low (in the order of 10^{-57}, or 10^{-45} if we count the 39 primary detections)[7]. It is also important to note that eleven of the 43 candidate stars show indications of a heavy nuclide boost in four lines and two of them in all of the five lines (see Table 2). This reinforces the robustness of the detections. All of these very strong objective arguments confirm a posteriori the correct functioning of our method and, therefore, make us particularly confident in our identification, via SEGUE's spectra, of regions of our Galaxy that are potentially rich in n-capture-enhanced stars. The SDSS spectroscopic identifiers (`specobjID`), together with the spectral subclasses and metallicities (the latter are taken from Lee et al. 2008) of all candidate stars enriched in Eu detected in the plates discussed above, can be found in Table A.1.

4. Conclusions

We have developed an automated statistical approach to identify stars containing enhanced contents of neutron-rich nuclei that use spectra whose resolution is not optimal to adequately detect from single observations the very thin absorption lines produced by this kind of elements. To illustrate how our methodology actually works, we focused on measuring the integrated flux within windows of a few angstrom wide around three lines of Eu I and two of Eu II that fall within the visible spectrum, subsequently identifying the strongest flux deficiencies found in these narrow spectral ranges with the presence of absorption features linked to these elements. For a star to be considered rich in heavy elements, we require it to test positive in at least three of the five lines investigated.

[6] $N_{\geq 3} = N_3 + N_4 + N_5$.

[7] These estimates are based on a binomial distribution with a probability p of success (i.e., detecting three or more lines on a star by chance) equal to 1.6025×10^{-5}, so the expected number of chance detections in a sample of $n \simeq 70\,000$ stars would be $\sim 1 \pm 1$.

The performance of the procedure has been tested against a sample of around 70 000 high-quality, medium-resolution optical spectra from F- and G-type stars observed within 215 plates belonging to two programs of the SDSS/SEGUE survey. We find that there is only one plate among the 202 of the segue2 program that reaches the minimum required content of three candidate stars enriched in n-capture elements. In contrast, it is found that up to four of the 13 plates of the segcluster program contain between six and eighteen stars where n-rich nuclei are plentiful. These findings are consistent with the expectation that most targets included in the tiles of the latter program, which are specifically directed at both globular and open star clusters, should be stars created in a common formative environment; while the presumably disparate birth places of the objects observed in the segue2's tiles should contribute to blur any signature that might exist from past heavy-element nucleosynthesis events in the targeted regions of our Galaxy. For those readers interested in deciphering the site and origin of the n-capture processes, we provide a table listing the spectral SDSS identifiers and other basic information about the 43 candidate stars rich in *r*-process elements (distinguishing primary and secondary) that have been detected in these five plates.

Highlights of the numerical results obtained include the ten or more objects that are potentially rich in heavy elements found in each one of the NGC 5053 and M 3 globular clusters, which are the two stellar systems observed in the segcluster program with the highest fractions of *r*-process enriched stars: 7% and 15%, respectively. These results, however, exclusively report on the presence of stars with extreme photospheric abundances of heavy elements within their spectral class. Nevertheless, they do not indicate what could be the particular values of such abundances, neither in absolute terms nor normalized to the stars' metallicities, which are normally inferred from the Fe abundance. Since the latter, despite being subsolar in all cases, span quite a large range (from [Fe/H] $\simeq -0.45$ to -2.5; see Table A.1), it seems reasonable to expect that both the selected stars and their host systems can also end up showing substantial variations in the abundance ratios of heavy nuclides. Thus, on one end, only one of the six stars rich in *r*-process elements located in the region of the open star cluster M 67 is truly metal-poor ([Fe/H] $\lesssim -1$). At the other end, there are the plates M 2, NGC 5053, and M 3, which show fractions of objects with abundances of Fe below 10% of 4/6, 8/10, and 9/10, respectively (for the last fraction we are considering only the stars with known metallic content), which would confirm that globular clusters are one of the best astrophysical sites to find stars with enhanced levels of n-capture elements.

In summary, we devised a fast and reliable automated procedure that enables the detection of the fine absorption lines that are produced by heavy elements in stellar spectra by using data from large surveys whose spectral resolution is too coarse to approach this problem in a traditional way. Thus, our method can help, for instance, future high-resolution stellar spectral abundance surveys that search for clues as to the astrophysical origin of the *r*-process nuclides by facilitating the identification of the sites where it should be possible to find a good number of stars that exhibit enhancement in such elements. This would avoid the time-consuming searches through thousands of candidates that are currently being carried out to find these precious objects in the Galactic halo. Ultimately, this is about contributing to the collection of a more complete inventory of n-capture-enhanced stars that increases our understanding of the synthesis of heavy elements and that sheds more light on the formation history of galaxies from the chemical evolution of their stellar populations.

Acknowledgements. The authors are grateful to an anonymous referee whose comments have prompted us to improve our methodology and its presentation, as well as better emphasize the reliability of the results. We also warmly thank Jaime Perea and María Asunción del Olmo for interesting discussions and useful advice about spectra normalization. J. L. T. and J. M. S. acknowledge financial support from the Spanish AEI and European FEDER funds through the research project AYA2016-76682-C3. Additional funding has been provided by the State Agency for Research of the Spanish MCIU through a "Center of Excellence María de Maeztu" award to the Institut de Ciències del Cosmos of the University of Barcelona.

References

Arcavi, I., Hosseinzadeh, G., Howell, D. A., et al. 2017, Nature, 551, 64
Argast, D., Samland, M., Thielemann, F.-K., & Qian, Y.-Z. 2004, A&A, 416, 997
Arnould, M., Goriely, S., & Takahashi, K. 2007, Phys. Rep., 450, 97
Battistini, C., & Bensby, T. 2016, A&A, 586, A49
Blanco-Cuaresma, S. 2019, MNRAS, 486, 2075
Blanco-Cuaresma, S., Soubiran, C., Heiter, U., & Jofré, P. 2014, A&A, 569, A111
Burbidge, E. M., Burbidge, G. R., Fowler, W. A., & Hoyle, F. 1957, Rev. Mod. Phys., 29, 547
Burris, D. L., Pilachowski, C. A., Armandroff, T. E., et al. 2000, ApJ, 544, 302
Busso, M., Gallino, R., & Wasserburg, G. J. 1999, ARA&A, 37, 239
Côté, B., Fryer, C. L., Belczynski, K., et al. 2018, ApJ, 855, 99
Cowan, J. J., & Thielemann, F.-K. 2004, Phys. Today, 57, 47
Eisenstein, D. J., Weinberg, D. H., Agol, E., et al. 2011, AJ, 142, 72
Frebel, A., & Beers, T. C. 2018, Phys. Today, 71, 30
Freiburghaus, C., Rosswog, S., & Thielemann, F.-K. 1999, ApJ, 525, L121
Goriely, S., & Siess, L. 2018, A&A, 609, A29
Heil, M., Juseviciute, A., Käppeler, F., et al. 2009, PASA, 26, 243
Käppeler, F., Gallino, R., Bisterzo, S., & Aoki, W. 2011, Rev. Mod. Phys., 83, 157
Karakas, A. I., García-Hernández, D. A., & Lugaro, M. 2012, ApJ, 751, 8
Kasen, D., Metzger, B., Barnes, J., Quataert, E., & Ramirez-Ruiz, E. 2017, Nature, 551, 80
Koch, A., & Edvardsson, B. 2002, A&A, 381, 500
Komiya, Y., & Shigeyama, T. 2016, ApJ, 830, 76
Kramida, A., Ralchenko, Y., Reader, J., & NIST ASD Team 2018, NIST Atomic Spectra Database (version 5.6.1), https://physics.nist.gov/asd
Kratz, K.-L., Farouqi, K., Pfeiffer, B., et al. 2007, ApJ, 662, 39
Lee, Y. S., Beers, T. C., Sivarani, T., et al. 2008, AJ, 136, 2022
Liccardo, V., Malheiro, M., Hussein, M. S., Carlson, B. V., & Frederico, T. 2018, Eur. Phys. J. A, 54, 221
Limongi, M., & Chieffi, A. 2018, ApJS, 237, 13
Lugaro, M., Herwig, F., Lattanzio, J. C., Gallino, R., & Straniero, O. 2003, ApJ, 586, 1305
Mas-Ribas, L., Miralda-Escudé, J., Pérez-Ràfols, I., et al. 2017, ApJ, 846, 4
Meyer, B. S. 1994, ARA&A, 32, 153
Naiman, J. P., Pillepich, A., Springel, V., et al. 2018, MNRAS, 477, 1206
Pian, E., D'Avanzo, P., Benetti, S., et al. 2017, Nature, 551, 67
Reifarth, R. 2010, J. Phys. Conf. Ser., 202, 012022
Roederer, I. U., & Lawler, J. E. 2012, ApJ, 750, 76
Siegel, D. M., Barnes, J., & Metzger, B. D. 2019, Nature, 569, 241
Siqueira Mello, C., Barbuy, B., Spite, M., & Spite, F. 2012, A&A, 548, A42
Smartt, S. J., Chen, T. W., Jerkstrand, A., et al. 2017, Nature, 551, 75
Sneden, C., & Cowan, J. J. 2003, Science, 299, 70
Sneden, C., Cowan, J. J., & Gallino, R. 2008, ARA&A, 46, 241
Thielemann, F. K., Arcones, A., Käppeli, R., et al. 2011, Nucl. Phys., 66, 346
Thielemann, F.-K., Isern, J., Perego, A., & von Ballmoos, P. 2018, Space Sci. Rev., 214, 62
Woosley, S. E., Wilson, J. R., Mathews, G. J., Hoffman, R. D., & Meyer, B. S. 1994, ApJ, 433, 229
Yanny, B., Rockosi, C., Newberg, H. J., et al. 2009, AJ, 137, 4377

Appendix A: SDSS/SEGUE stars potentially rich in *r*-process elements

Table A.1. Spectroscopic identifier, spectral subclass and metallicity of stars with likely enhancement of neutron-rich elements that are located in SEGUE plates listed in Table 2.

Plate ID	Cluster ID	SpecobjID	Subclass	[Fe/H]	l	Spectral lines detected
3304	–	3719984370237415424	F5	–	3	Eu Iλ4594; Eu IIλ4129,4205
		3719973924876951552	F5	−1.240	3	Eu Iλ4594; Eu IIλ4129,4205
		3720148197469954048	F5	−1.668	3	Eu Iλ4594,4627,4661
2667	M 67	3002942521685941248	F2	−1.519	3	Eu Iλ4594,4627; Eu IIλ4205
		3002810305412701184	F5	−0.841	3	Eu Iλ4661; Eu IIλ4129,4205
		3002885072203389952	F9	−0.449	3	Eu Iλ4594,4627,4661
		3002824049308048384	G2	−0.463	3	Eu Iλ4594,4661; Eu IIλ4205
		3002777320063867904	F9	−0.774	4	Eu Iλ4627,4661; Eu IIλ4129,4205
		3002878750011530240	F9	−0.841	4	Eu Iλ4594,4661; Eu IIλ4129,4205
1961	M 2	2208063770381622272	F9	−0.519	3	Eu Iλ4594; Eu IIλ4129,4205
		2208000273585118208	F9	−0.650	3	Eu Iλ4594,4627; Eu IIλ4205
		2207981856765352960	F9	−1.721	3	Eu Iλ4627,4661; Eu IIλ4129
		2207959591654890496*	G2	−1.790	3	Eu Iλ4627,4661; Eu IIλ4205
		2208003297242094592	G2	−1.534	4	Eu Iλ4627,4661; Eu IIλ4129,4205
		2208044803806043136	F5	−2.530	5	Eu Iλ4594,4627,4661; Eu IIλ4129,4205
2476	NGC 5053	2787852478346009600*	F2	−2.230	3	Eu Iλ4627,4661; Eu IIλ4205
		2787767541072763904	F5	−1.052	3	Eu Iλ4594,4627,4661
		2787760669125090304	F9	−1.078	3	Eu Iλ4594,4627,4661
		2787743351816952832	F5	−1.062	3	Eu Iλ4594,4661; Eu IIλ4129
		2787843132497173504	G0	−1.817	3	Eu Iλ4661; Eu IIλ4129,4205
		2787852203468102656	G2	−2.113	3	Eu Iλ4627,4661; Eu IIλ4129
		2787789256427412480	G2	−1.812	3	Eu Iλ4627,4661; Eu IIλ4129
		2787840108840197120	F9	−0.823	3	Eu Iλ4594,4627; Eu IIλ4205
		2787877492235541504	F9	−0.691	4	Eu Iλ4594,4627,4661; Eu IIλ4205
		2787754072055323648	G2	−1.198	4	Eu Iλ4594,4627,4661; Eu IIλ4205
2475	M 3	2786624599054457856*	F9	−0.588	3	Eu Iλ4627,4661; Eu IIλ4205
		2786709261449796608	F9	–	3	Eu Iλ4594,4627; Eu II 4205
		2786609755647482880	F9	–	3	Eu Iλ4627; Eu II 4129,4205
		2786707062426541056	F9	–	3	Eu Iλ4594; Eu IIλ4129,4205
		2786708436816075776	F9	–	3	Eu Iλ4594; Eu IIλ4129,4205
		2786700190478867456*	F5	–	3	Eu Iλ4627,4661; Eu IIλ4205
		2786633944903293952	G2	–	3	Eu Iλ4594,4661; Eu IIλ4129
		2786630646368410624	F9	–	3	Eu Iλ4594,4661; Eu IIλ4129
		2786611954670738432	F9	−1.213	3	Eu Iλ4594,4661; Eu IIλ4129
		2786730152170724352	G0	−1.837	3	Eu Iλ4594,4661; Eu IIλ4205
		2786726029002120192	F9	−1.229	3	Eu Iλ4594,4627,4661
		2786658409037011968	F5	−1.368	3	Eu Iλ4594,4627,4661
		2786681773659102208	F9	−1.475	3	Eu Iλ4627,4661; Eu IIλ4129
		2786704863403285504	F5	−1.615	4	Eu Iλ4594,4627,4661; Eu IIλ4129
		2786753516792814592	F2	−1.698	4	Eu Iλ4594,4627,4661; Eu IIλ4205
		2786720531443981312	F2	−1.621	4	Eu Iλ4594,4627,4661; Eu IIλ4129
		2786716958031191040	F5	−2.056	4	Eu Iλ4594,4627,4661; Eu IIλ4129
		2786636418804456448	F9	–	5	Eu Iλ4594,4627,4661; Eu IIλ4129,4205

Notes. Secondary candidates (i.e., lacking both the Eu I 4594 Å and the Eu II 4129 Å lines) are identified with an asterisk.

B

CATALOGUE OF STAR-FORMING RINGS IN LENTICULAR GALAXIES

This appendix contains the catalogue of SF rings in S0 galaxies from MaNGA-DR15 with linear PC1–PC2 radial profiles built in Tous et al. (2023).

B.1 THE RING CATALOGUE

To create the catalogue, we inspected the MaNGA's maps of EW and luminosity (L′) in Hα, and D4000 shown in Section B.2. The maps were divided into three categories based on the overall ring score (r) they were attributed: ringed ($r \geqslant 6$), doubtful ($r = 3-5$), and non-ringed ($r < 3$). Furthermore, to obtain a reliable estimate of the ring abundance in our S0 sample, we restricted the search to good quality maps from galaxies not highly inclined ($i < 60°$), with linear PC1–PC2 radial profiles, and with a good resolution, a condition that we define, in terms of apparent size of galaxies relative to the point spread function (PSF), as $\sigma_{PSF}/R_e < 0.6$ (see Chapter 4 for more details on the identification).

Below, it is shown the tabular version of the ring catalogue, where galaxies appear sorted in decreasing order of the ring score attributed to the map of EW(Hα). The catalogue contains 7 columns for 446 galaxies with the following information:
Column 1: MaNGA PLATE-IFU.
Column 2: flag indicating if the inclination and/or spatial resolution of a galaxy are adequate for ring identification (0); otherwise, 1: high inclination, 2: bad resolution, 3: both bad conditions are met.
Column 3: PCA spectral class.
Column 4: profile type where IO, F, and OI correspond, respectively, to positive, null, and negative activity gradients.
Columns 5-7: ring score attributed to the map of equivalent width and luminosity in Hα, and D4000 spectral index, where −999 indicates that the corresponding maps were not used in the identification.

Table 1: Spectral and gradient class, and ring score in S0s from MaNGA.

PLATE-IFU	Flag	Spectral class	Gradient class	Ring score		
				EW(Hα)	L′(Hα)	D4000
8721-3701	0	AC	IO	8	0	3
9487-6101	0	AC	IO	8	0	0
8600-1902	0	PS	IO	8	-999	-999

Table 1: Cont.

PLATE-IFU	Flag	Spectral class	Gradient class	Ring score		
				EW(Hα)	L′(Hα)	D4000
9095-3701	0	AC	IO	8	5	7
9864-3703	0	PS	IO	8	2	2
7815-3704	0	PS	IO	8	8	3
8147-3704	0	PS	IO	8	-999	-999
8462-3704	0	AC	IO	8	0	2
9863-6101	0	PS	IO	8	8	6
8446-3704	0	AC	IO	8	0	5
8555-6102	0	PS	IO	8	1	3
8150-6104	0	TR	IO	8	-999	-999
8332-6104	0	PS	IO	8	6	-999
8325-9101	1	PS	IO	8	5	4
8462-3701	0	PS	F	8	6	0
9182-6101	0	PS	IO	7	8	5
8567-3701	0	AC	IO	7	2	5
8623-3701	0	PS	IO	7	7	1
8131-3701	0	PS	IO	7	0	6
8323-3702	0	PS	IO	7	8	5
7972-3702	1	PS	IO	7	-999	-999
8323-3703	0	AC	IO	7	1	4
8319-3703	0	AC	IO	7	2	7
9196-6101	0	PS	IO	7	6	5
8996-9102	0	PS	IO	7	8	4
9485-6101	0	PS	IO	7	-999	-999
8978-6104	0	AC	IO	7	2	-999
9500-6104	0	AC	IO	7	0	1
8978-9102	0	PS	IO	7	8	2
8978-1901	0	PS	F	7	0	0
8712-1901	0	PS	IO	7	-999	-999
8312-12704	0	AC	OI	6	0	-999
9035-12703	1	AC	IO	6	1	0
8315-3701	0	PS	IO	6	3	5
8482-3703	1	PS	IO	6	6	4
8550-12702	1	PS	IO	6	4	4
9872-3704	0	TR	IO	6	1	6
7964-12702	0	PS	IO	6	7	3

Table 1: Cont.

PLATE-IFU	Flag	Spectral class	Gradient class	Ring score		
				EW(Hα)	L′(Hα)	D4000
8158-12702	0	PS	IO	6	3	5
8984-3704	1	PS	IO	6	3	1
9035-3704	0	TR	IO	6	4	7
9033-6101	1	PS	IO	6	3	1
8313-6103	0	AC	IO	6	3	4
8983-6104	0	PS	IO	6	2	4
7964-6104	0	PS	IO	6	5	-999
8138-6102	1	TR	F	6	5	0
7977-3704	0	PS	IO	5	8	3
8077-12703	1	PS	IO	5	2	-999
8982-1901	0	PS	IO	5	8	6
8257-1902	0	PS	IO	5	2	3
8626-3701	0	PS	IO	5	-999	-999
8459-3702	0	AC	IO	5	0	4
8447-3703	0	AC	IO	5	0	3
7990-3704	0	PS	IO	5	6	1
9869-6103	1	AC	IO	5	1	0
9485-6104	0	TR	IO	5	4	5
9000-1902	2	AC	F	5	0	0
8137-6104	0	PS	F	5	1	0
8325-3704	0	TR	IO	4	0	1
9509-1901	0	AC	IO	4	1	2
9024-12701	0	PS	IO	4	8	4
8625-12701	1	PS	IO	4	1	0
8483-1901	2	TR	IO	4	1	1
8612-1902	1	TR	IO	4	2	3
8258-1902	0	TR	IO	4	2	-999
9195-1902	2	AC	IO	4	0	3
7975-1902	1	PS	IO	4	1	3
8311-3704	0	PS	IO	4	6	4
9872-1902	0	TR	F	4	0	0
9047-3704	1	AC	IO	4	0	2
9502-6101	1	AC	OI	4	0	1
8999-6102	1	PS	IO	4	1	1
8616-9101	0	AC	IO	4	0	1

Table 1: Cont.

PLATE-IFU	Flag	Spectral class	Gradient class	Ring score		
				EW(Hα)	L′(Hα)	D4000
9507-9102	0	PS	IO	4	3	2
8936-9102	1	PS	IO	3	2	3
9506-1901	0	AC	IO	3	1	3
8450-1902	1	TR	IO	3	1	2
8555-1902	0	PS	IO	3	0	2
9490-3701	0	TR	IO	3	0	0
9181-3701	0	AC	IO	3	0	1
9196-3702	0	AC	IO	3	0	0
8623-6101	1	PS	IO	3	2	1
8440-6103	0	AC	OI	3	0	0
9509-9101	0	PS	IO	3	5	3
8939-12705	1	PS	F	3	0	0
8450-9102	0	AC	IO	3	6	3
8720-3702	0	PS	F	3	-999	0
8567-3702	1	PS	F	3	0	0
8311-12702	1	PS	F	3	0	0
8150-12701	1	AC	F	3	0	0
8982-1902	1	AC	IO	2	0	-999
8989-3701	0	PS	IO	2	-999	-999
7992-6103	0	AC	OI	2	0	0
9506-1902	0	TR	OI	2	-999	-999
9045-1901	2	PS	IO	2	1	2
9485-3703	0	AC	IO	2	0	1
8143-6101	0	AC	OI	2	0	0
8146-1902	0	AC	OI	2	0	0
8465-1902	0	TR	F	2	0	0
8244-3701	0	PS	F	2	0	0
9872-3701	1	AC	OI	1	0	0
8149-3703	0	AC	OI	1	0	0
8997-3703	0	TR	OI	1	0	0
8443-3702	0	TR	OI	1	0	1
9497-3702	0	AC	OI	1	0	1
8985-3702	0	AC	OI	1	0	0
7975-3701	1	AC	OI	1	1	0
8947-3701	1	AC	OI	1	0	0

Table 1: Cont.

PLATE-IFU	Flag	Spectral class	Gradient class	Ring score		
				EW(Hα)	L′(Hα)	D4000
8252-3704	0	AC	OI	1	0	0
8992-1902	0	PS	IO	1	0	1
8939-1902	0	AC	OI	1	0	0
9183-12705	2	AC	OI	1	0	0
8461-12703	1	AC	IO	1	1	-999
8550-12701	0	PS	IO	1	-999	-999
9487-3703	1	AC	OI	1	0	0
8138-1901	1	AC	IO	1	1	0
9034-6101	1	AC	OI	1	0	0
9184-6103	1	TR	IO	1	0	0
8132-1902	0	PS	F	1	-999	0
8312-6102	0	AC	F	1	0	0
8133-9101	0	AC	IO	1	-999	-999
8932-6104	0	TR	OI	1	0	0
8615-6103	0	AC	OI	1	0	0
8602-6104	0	AC	OI	1	0	0
9048-6101	1	AC	OI	1	0	0
9487-6103	1	AC	OI	1	0	0
8618-3704	0	AC	OI	0	0	0
8263-3704	0	TR	OI	0	1	0
8977-3704	0	AC	OI	0	0	0
8138-3704	0	AC	OI	0	0	0
8456-3704	0	AC	OI	0	-999	-999
8996-3704	0	AC	OI	0	0	0
8323-3704	0	AC	OI	0	0	0
8978-3704	0	AC	OI	0	0	0
8940-6101	1	AC	OI	0	0	0
8249-3704	0	AC	OI	0	-999	-999
8933-3704	0	AC	OI	0	0	0
9183-6101	0	AC	OI	0	0	0
8458-6101	1	AC	OI	0	0	0
8442-3704	0	AC	OI	0	0	0
8715-6101	0	AC	OI	0	0	0
9870-6101	0	AC	OI	0	0	0
9035-6101	0	AC	OI	0	0	0

Table 1: Cont.

PLATE-IFU	Flag	Spectral class	Gradient class	Ring score		
				EW(Hα)	L′(Hα)	D4000
8717-6101	1	PS	OI	0	-999	-999
9490-3704	0	AC	OI	0	0	0
8568-3703	0	AC	OI	0	0	0
9049-3704	0	AC	OI	0	0	0
8623-6102	1	PS	OI	0	-999	-999
8606-3702	1	PS	IO	0	-999	-999
8945-3702	2	AC	OI	0	0	0
8335-3702	1	AC	OI	0	0	0
8727-3702	0	AC	OI	0	0	0
8485-3701	0	AC	OI	0	0	0
8979-3701	1	AC	OI	0	0	0
8948-3702	0	PS	IO	0	-999	-999
8263-3701	1	AC	OI	0	0	0
8483-3704	1	AC	OI	0	0	0
8995-3703	1	TR	OI	0	0	0
8931-3703	0	AC	OI	0	0	0
8313-3703	0	AC	OI	0	0	0
8250-3703	2	AC	OI	0	0	1
9883-3703	0	PS	OI	0	0	0
8249-3703	0	AC	OI	0	0	1
8592-1902	0	PS	F	0	0	0
8464-6101	0	AC	OI	0	0	0
8255-3703	0	AC	OI	0	0	0
8077-6102	1	AC	OI	0	0	0
8945-3703	0	AC	F	0	0	0
9028-3702	1	PS	F	0	0	0
9025-3704	1	PS	F	0	0	0
9000-6101	0	PS	F	0	0	0
8996-3701	1	PS	F	0	0	0
8993-3703	0	PS	F	0	0	0
8992-3701	0	PS	F	0	0	0
8980-12703	0	PS	F	0	0	0
8945-1901	0	PS	F	0	0	0
9035-9101	1	PS	F	0	0	0
8941-3704	1	PS	F	0	0	0

Table 1: Cont.

PLATE-IFU	Flag	Spectral class	Gradient class	Ring score		
				EW(Hα)	L′(Hα)	D4000
8941-3701	0	PS	F	0	0	0
8725-3704	0	PS	F	0	0	0
9026-3701	0	AC	OI	0	0	0
8720-1901	0	AC	F	0	0	0
8719-1902	0	PS	F	0	0	0
8626-6103	1	PS	F	0	0	0
9034-1902	0	PS	F	0	0	0
9041-6101	0	PS	F	0	0	0
7962-6102	0	AC	IO	0	0	0
9865-3704	1	PS	F	0	0	0
8718-6102	1	AC	OI	0	0	0
8135-6104	1	PS	IO	0	-999	-999
8241-9102	1	AC	OI	0	0	0
8078-9102	1	AC	OI	0	-999	-999
9864-9102	0	AC	OI	0	0	0
9881-3703	0	PS	F	0	0	0
9876-1902	0	PS	F	0	0	0
9509-3704	0	PS	F	0	0	0
9045-3701	0	PS	F	0	0	0
9509-1902	2	PS	F	0	0	0
9486-3704	0	PS	F	0	0	0
9193-1901	1	PS	F	0	0	0
9183-3702	2	PS	F	0	0	0
9095-3704	0	PS	F	0	0	0
9088-3703	1	PS	F	0	0	0
9085-12704	0	PS	F	0	0	-999
8255-3701	0	AC	OI	0	0	0
8154-3701	1	AC	F	0	0	0
9485-3701	1	AC	OI	0	0	0
8450-1901	0	AC	OI	0	0	0
8443-6104	1	PS	F	0	0	0
8449-1902	1	TR	F	0	0	0
8461-1902	1	TR	F	0	0	0
8547-3702	0	TR	F	0	0	0
8550-3703	1	PS	F	0	0	0

Table 1: Cont.

PLATE-IFU	Flag	Spectral class	Gradient class	Ring score		
				EW(Hα)	L′(Hα)	D4000
8553-1902	0	PS	F	0	0	0
8554-1902	0	PS	F	0	0	0
8567-3704	0	PS	F	0	0	0
8442-1901	3	AC	OI	0	0	0
8141-1901	0	AC	OI	0	0	4
9488-1901	0	TR	OI	0	-999	-999
9501-1901	0	AC	OI	0	0	0
8625-1901	0	AC	OI	0	0	0
8444-1901	0	AC	OI	0	0	0
8252-3701	1	TR	OI	0	-999	-999
8443-3701	1	PS	F	0	0	0
8318-6103	1	PS	F	0	0	0
8318-1902	0	PS	F	0	0	-999
8137-3701	0	PS	F	0	0	0
9486-1901	0	TR	IO	0	0	0
7990-12705	0	PS	F	0	0	0
7992-3701	0	PS	F	0	0	0
8084-1902	0	TR	F	0	0	0
8134-6102	0	PS	F	0	0	0
8137-1901	1	TR	F	0	0	0
8143-1902	0	PS	F	0	0	0
8318-1901	1	PS	F	0	0	0
8611-3701	0	PS	F	0	0	0
8154-3704	1	PS	F	0	0	0
8244-3703	0	PS	F	0	0	0
8253-1901	0	PS	F	0	0	0
8253-1902	1	PS	F	0	0	0
8311-1901	0	PS	F	0	0	0
8143-1901	0	AC	OI	0	0	0
8485-1901	2	AC	OI	0	0	0
8567-1901	1	PS	IO	0	-999	-999
8274-1902	0	PS	IO	0	0	2
8711-1902	1	AC	OI	0	0	0
8943-1901	1	AC	OI	0	0	1
9026-1902	0	TR	OI	0	-999	-999

Table 1: Cont.

PLATE-IFU	Flag	Spectral class	Gradient class	Ring score		
				EW(Hα)	L′(Hα)	D4000
8937-1902	1	TR	OI	0	-999	-999
8241-1902	1	AC	OI	0	0	0
9028-1902	0	AC	OI	0	0	0
8616-1902	0	PS	OI	0	-999	-999
8155-1902	0	AC	OI	0	0	0
8615-1902	0	AC	OI	0	0	0
8718-1902	1	AC	OI	0	0	0
8259-1902	0	AC	OI	0	0	0
8333-1902	0	AC	OI	0	0	0
8250-1902	0	PS	OI	0	-999	-999
8978-1902	0	PS	IO	0	-999	-999
8552-3701	0	AC	OI	0	0	0
8455-1902	1	AC	OI	0	0	0
9869-1902	3	AC	OI	0	0	1
8140-1902	2	AC	OI	0	0	0
8135-1901	2	AC	OI	0	0	0
8588-1901	2	AC	OI	0	0	0
8459-1901	0	AC	OI	0	0	0
8983-1901	0	TR	OI	0	0	0
8486-1901	0	AC	OI	0	0	1
8147-1902	0	AC	OI	0	0	0
8081-1901	1	AC	OI	0	0	0
8461-1901	1	AC	OI	0	0	1
8258-1901	0	AC	OI	0	0	0
9195-1901	0	AC	OI	0	0	0
8081-1902	0	AC	OI	0	0	0
9865-1902	1	TR	OI	0	-999	-999
8990-1902	1	AC	OI	0	0	0
9048-1902	0	AC	OI	0	0	0
9181-1902	0	AC	OI	0	0	0
8613-3701	0	PS	F	0	0	3
9088-3702	0	PS	IO	-999	-999	1
7964-3703	1	PS	IO	-999	-999	1
9863-6103	1	PS	IO	-999	-999	0
9085-6101	0	PS	IO	-999	-999	-999

Table 1: Cont.

PLATE-IFU	Flag	Spectral class	Gradient class	Ring score		
				EW(Hα)	L′(Hα)	D4000
9033-3702	1	AC	IO	-999	-999	0
9002-6103	0	PS	F	-999	-999	0
9183-12701	1	PS	IO	-999	-999	-999
8949-12705	1	PS	IO	-999	-999	-999
9047-3701	0	TR	F	-999	-999	0
8987-1902	1	PS	F	-999	-999	-999
8996-1902	1	PS	F	-999	-999	-999
8999-12702	0	PS	F	-999	-999	0
9002-6101	0	PS	F	-999	0	0
9026-12701	0	PS	F	-999	-999	0
9026-9102	0	PS	F	-999	0	0
9029-1901	0	PS	F	-999	-999	0
9029-3704	0	PS	F	-999	-999	0
9029-6101	0	PS	F	-999	-999	0
9033-3701	1	PS	F	-999	-999	0
9038-3704	0	PS	F	-999	-999	0
9039-12702	0	PS	F	-999	-999	0
9041-3703	1	PS	F	-999	-999	0
9047-1902	2	PS	F	-999	-999	0
9049-1902	2	PS	F	-999	-999	-999
9049-3703	1	PS	F	-999	-999	0
9050-1902	1	PS	F	-999	-999	0
8984-3702	0	PS	F	-999	-999	0
8984-3701	0	PS	F	-999	-999	0
8980-6103	0	PS	F	-999	-999	0
8947-3702	1	PS	F	-999	-999	0
8934-6101	1	PS	F	-999	-999	3
8935-1901	1	PS	F	-999	-999	0
8935-3702	1	PS	F	-999	-999	0
8937-6104	0	PS	F	-999	-999	0
8942-12701	0	PS	F	-999	0	0
8945-3701	1	PS	F	-999	-999	0
8945-6102	1	PS	F	-999	-999	0
8947-6102	1	PS	F	-999	-999	0
8979-12704	1	PS	F	-999	-999	-999

Table 1: Cont.

PLATE-IFU	Flag	Spectral class	Gradient class	Ring score		
				EW(Hα)	L′(Hα)	D4000
8949-1902	1	PS	F	-999	-999	-999
8949-3702	0	PS	F	-999	-999	0
8949-6103	0	PS	F	-999	-999	0
8950-12704	0	PS	F	-999	-999	0
8950-1902	0	PS	F	-999	-999	0
8950-6104	0	PS	F	-999	-999	-999
8977-1902	1	PS	F	-999	-999	0
9088-1902	0	PS	F	-999	-999	0
9181-1901	0	PS	F	-999	-999	0
9193-3703	0	PS	F	-999	-999	0
8567-3703	0	PS	OI	-999	-999	-999
8985-9101	0	PS	IO	-999	-999	-999
8466-6102	0	PS	OI	-999	-999	-999
7495-3704	0	PS	OI	-999	-999	-999
9037-3704	0	PS	IO	-999	-999	-999
8256-3703	0	PS	OI	-999	-999	-999
9510-3703	0	PS	IO	-999	-999	-999
8486-3703	0	PS	IO	-999	-999	-999
9193-3702	0	PS	IO	-999	-999	-999
9891-9102	0	PS	F	-999	-999	0
8937-3702	1	PS	IO	-999	-999	-999
7962-3701	1	PS	IO	-999	-999	-999
7991-1902	0	PS	IO	-999	-999	-999
8485-1902	1	PS	IO	-999	-999	-999
8941-1902	0	PS	IO	-999	-999	-999
8933-1902	0	PS	IO	-999	-999	-999
9876-1901	0	PS	F	-999	-999	-999
8933-9102	0	PS	IO	-999	-999	-999
9888-6104	0	PS	F	-999	-999	0
9193-6103	0	PS	F	-999	-999	0
9505-1902	2	PS	F	-999	-999	0
9487-1902	0	PS	F	-999	-999	0
9492-3704	1	PS	F	-999	-999	0
9493-3703	0	PS	F	-999	-999	0
9497-3704	1	PS	F	-999	-999	0

Table 1: Cont.

PLATE-IFU	Flag	Spectral class	Gradient class	Ring score		
				EW(Hα)	L′(Hα)	D4000
9497-6103	0	PS	F	-999	-999	0
9500-1902	2	PS	F	-999	-999	0
9501-3702	0	PS	F	-999	-999	0
9505-6101	0	PS	F	-999	-999	0
9881-12703	0	PS	F	-999	-999	0
9863-3704	0	PS	F	-999	-999	0
9864-12705	1	PS	F	-999	-999	0
9864-1902	2	PS	F	-999	0	0
9864-6102	0	PS	F	-999	0	0
9865-6104	0	PS	F	-999	-999	0
9869-6104	1	PS	F	-999	-999	0
9876-3704	1	PS	F	-999	-999	0
8934-1901	1	PS	F	-999	-999	0
8934-12704	0	PS	F	-999	-999	0
8933-3701	1	PS	F	-999	-999	0
8274-1901	0	PS	F	-999	-999	0
8241-1901	1	PS	F	-999	-999	0
8244-6104	0	PS	F	-999	-999	0
8247-1902	0	PS	F	-999	-999	0
8255-1902	0	PS	F	-999	-999	0
8259-3701	0	PS	F	-999	-999	0
8261-9101	1	PS	F	-999	-999	0
8262-6103	1	PS	F	-999	-999	0
8311-1902	1	PS	F	-999	-999	0
8146-3703	0	PS	F	-999	-999	0
8312-1902	0	PS	F	-999	-999	-999
8315-1901	0	PS	F	-999	-999	0
8315-1902	0	PS	F	-999	-999	-999
8315-9101	0	AC	F	-999	0	0
8317-3703	1	PS	F	-999	-999	0
8318-3701	1	PS	F	-999	-999	0
8319-3702	0	PS	F	-999	0	0
8156-1901	2	PS	F	-999	-999	0
8143-3701	0	PS	F	-999	-999	0
8323-6102	0	PS	F	-999	-999	0

Table 1: Cont.

PLATE-IFU	Flag	Spectral class	Gradient class	Ring score		
				EW(Hα)	L′(Hα)	D4000
8077-3703	1	PS	F	-999	-999	0
10001-1902	0	PS	F	-999	-999	0
10001-3701	2	PS	F	-999	-999	0
10001-6103	0	PS	F	-999	-999	0
7957-6103	0	PS	F	-999	-999	0
7962-1901	0	PS	F	-999	-999	0
7962-3703	0	PS	F	-999	-999	0
7972-1901	3	PS	F	-999	-999	0
8080-1901	2	PS	F	-999	-999	0
8141-3704	1	PS	F	-999	0	0
8086-3701	0	PS	F	-999	-999	0
8131-3702	0	PS	F	-999	-999	0
8133-1902	3	PS	F	-999	-999	0
8133-6104	1	PS	F	-999	-999	-999
8134-3703	1	PS	F	-999	-999	0
8134-3704	1	PS	F	-999	0	0
8141-3703	0	PS	F	-999	-999	0
8320-6103	1	PS	F	-999	-999	0
8332-6101	1	PS	F	-999	-999	0
8933-1901	1	PS	F	-999	-999	0
8718-3701	0	PS	F	-999	-999	0
8603-3702	1	PS	F	-999	-999	0
8611-1901	0	PS	F	-999	-999	0
8616-6101	1	PS	F	-999	-999	0
8623-1901	1	PS	F	-999	-999	0
8711-1901	2	PS	F	-999	-999	0
8711-9101	0	PS	F	-999	-999	0
8713-3703	0	PS	F	-999	0	0
8720-9102	1	PS	F	-999	-999	0
8568-3702	1	PS	F	-999	-999	0
8724-6104	1	PS	F	-999	0	-999
8726-6104	1	PS	F	-999	-999	-999
8727-1901	0	PS	F	-999	-999	0
8931-1901	0	PS	F	-999	-999	0
8931-3702	1	PS	F	-999	-999	0

Table 1: Cont.

PLATE-IFU	Flag	Spectral class	Gradient class	Ring score		
				EW(Hα)	L′(Hα)	D4000
8932-1902	1	PS	F	-999	-999	0
8932-6101	0	PS	F	-999	-999	0
8595-9102	0	PS	F	-999	-999	0
8568-1902	0	PS	F	-999	0	0
8333-1901	0	PS	F	-999	-999	0
8455-3703	0	PS	F	-999	-999	0
8338-3701	0	PS	F	-999	-999	0
8341-1901	0	PS	F	-999	-999	0
8444-3703	0	PS	F	-999	-999	0
8445-1901	3	PS	F	-999	-999	0
8445-6101	0	PS	F	-999	-999	0
8447-9101	1	PS	F	-999	-999	0
8453-3701	1	PS	F	-999	-999	0
8458-1902	0	PS	F	-999	-999	0
8554-1901	0	PS	F	-999	-999	0
8461-3701	1	PS	F	-999	-999	0
8481-3703	1	PS	F	-999	-999	0
8482-6104	0	PS	F	-999	-999	-999
8486-3702	1	PS	F	-999	0	0
8486-6103	0	PS	F	-999	-999	0
8552-1901	0	PS	F	-999	-999	0
8553-6104	1	PS	F	-999	-999	-999
8442-6104	0	PS	F	-999	-999	0

B.2 OPTICAL IMAGES AND SPECTRAL MAPS OF LENTICULAR GALAXIES

Here we show the montages of optical images and spectral maps for S0 galaxies with linear PC1–PC2 radial profiles, emphasizing those objects harbouring an unequivocal ring in the EW(Hα) map. The galaxies appear sorted by gradient class (inside out, IO; outside in, OI; and flat, F) and spectral class (passive sequence, PS; active cloud, AC; and transition region, TR).

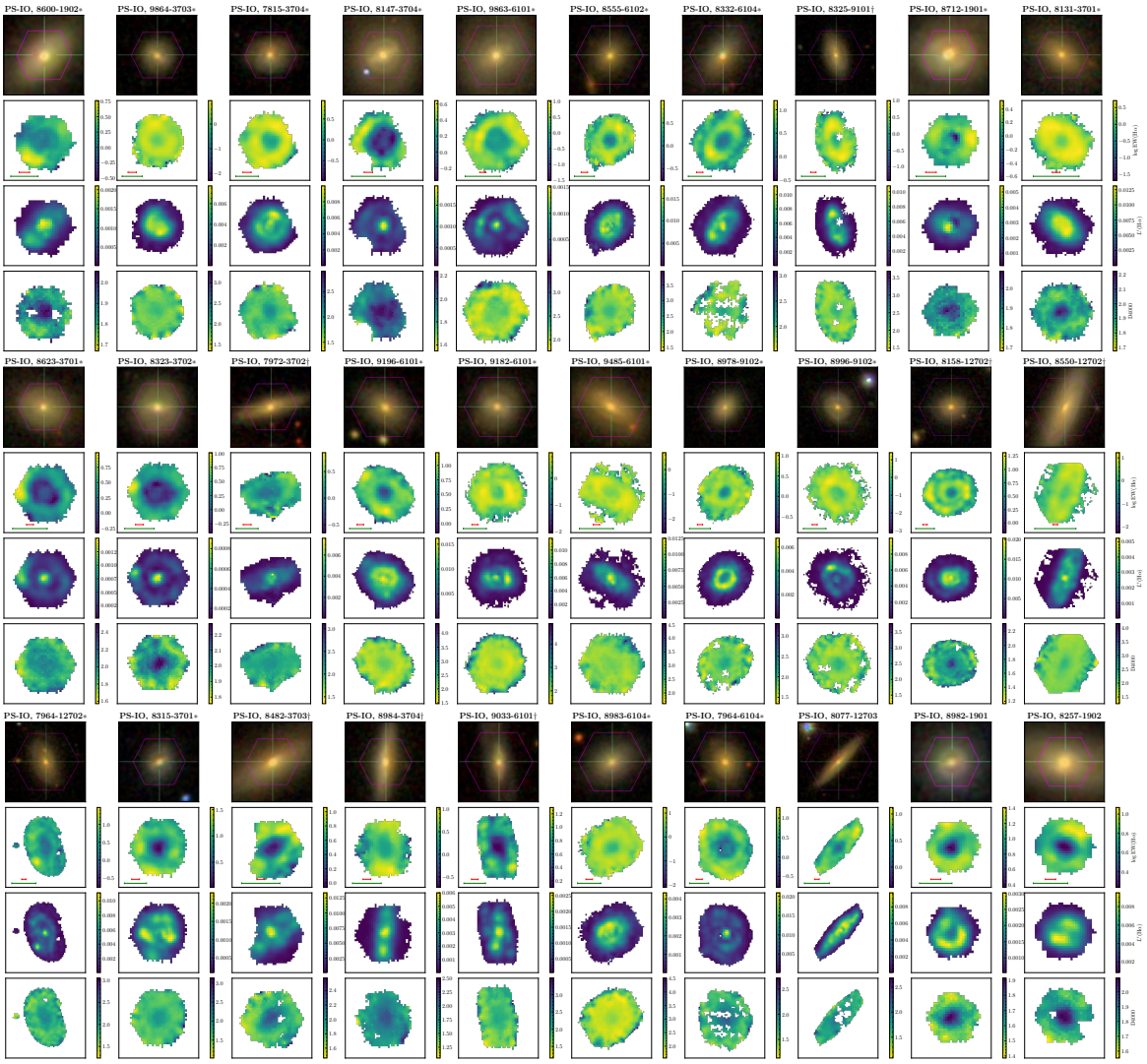

Figure 1: Montages of the optical images and the three spectral maps for all the S0 galaxies with linear PC1–PC2 profiles. The green and red horizontal lines included in the EW(Hα) panels indicate, respectively, the galaxies' Petrosian half-light diameter in the r band and $2\,\sigma_{PSF}$. An asterisk next to each galaxy's identifier indicates the presence of an unequivocal ring in the EW(Hα) map ($r \geqslant 6$), unless the galaxy is highly inclined ($i > 60°$) or has a poor seeing condition ($\sigma_{PSF}/R_e \geqslant 0.6$), in which case a dagger is used.

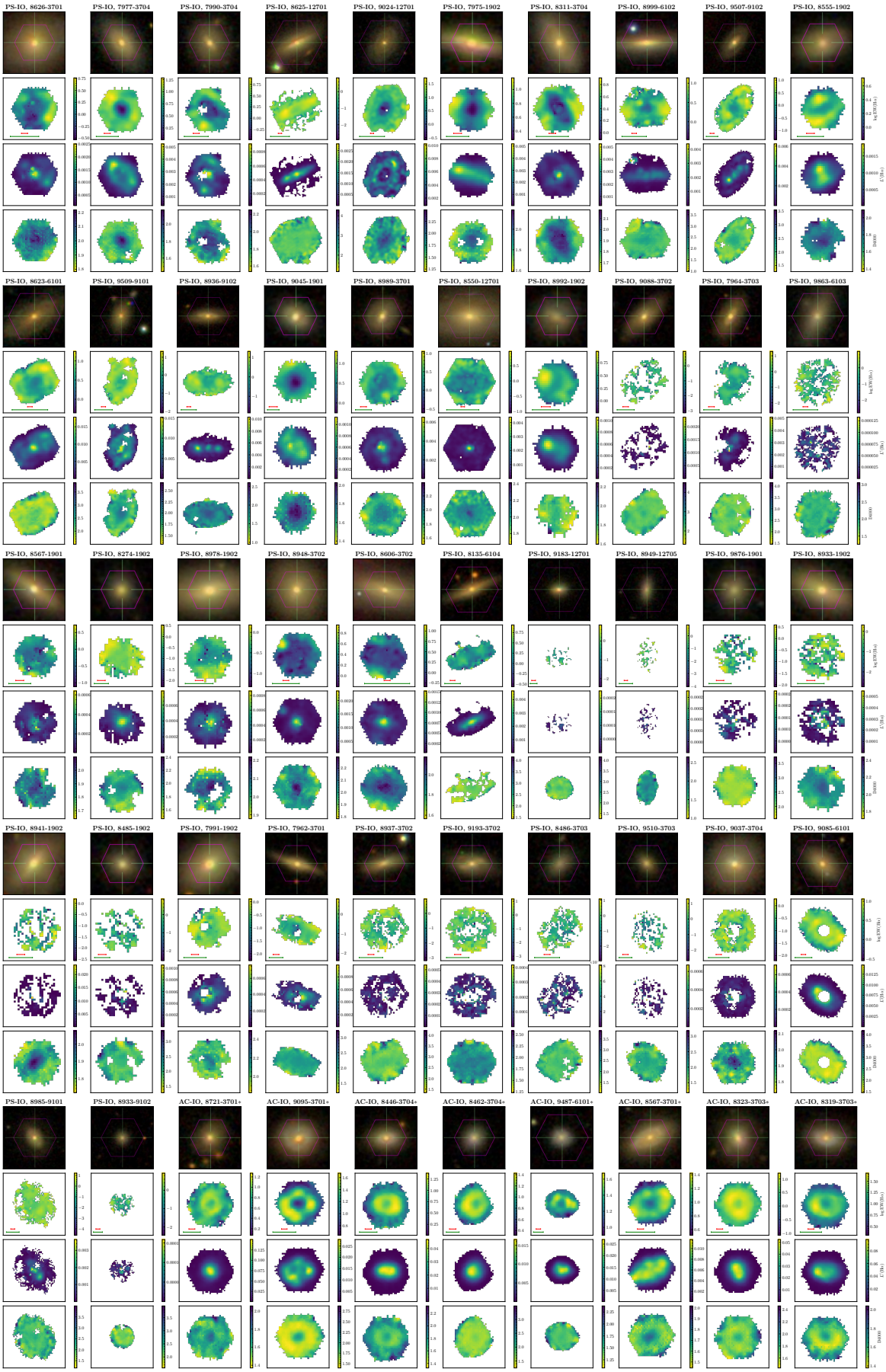

Figure 1: Cont.

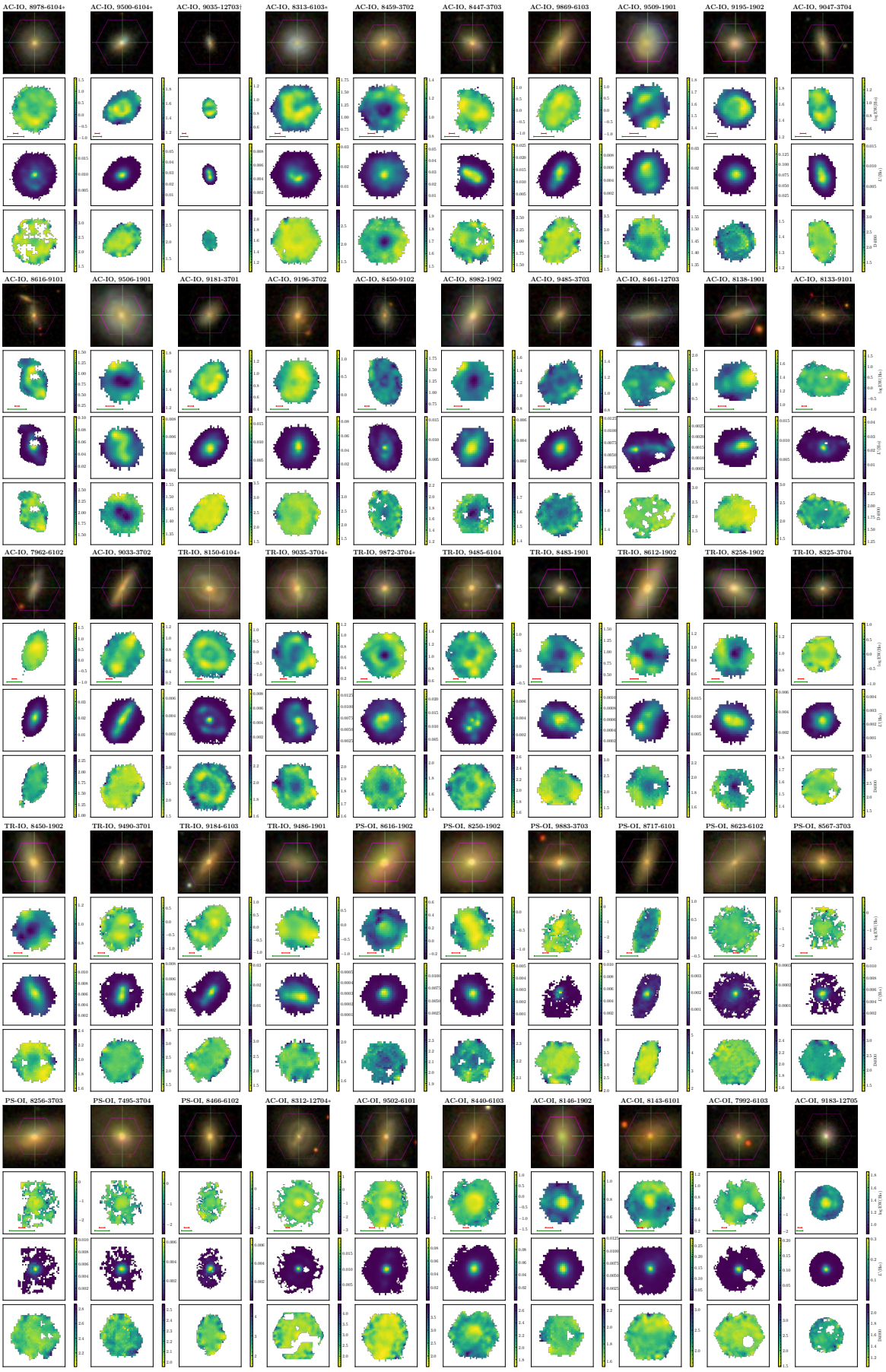

Figure 1: Cont.

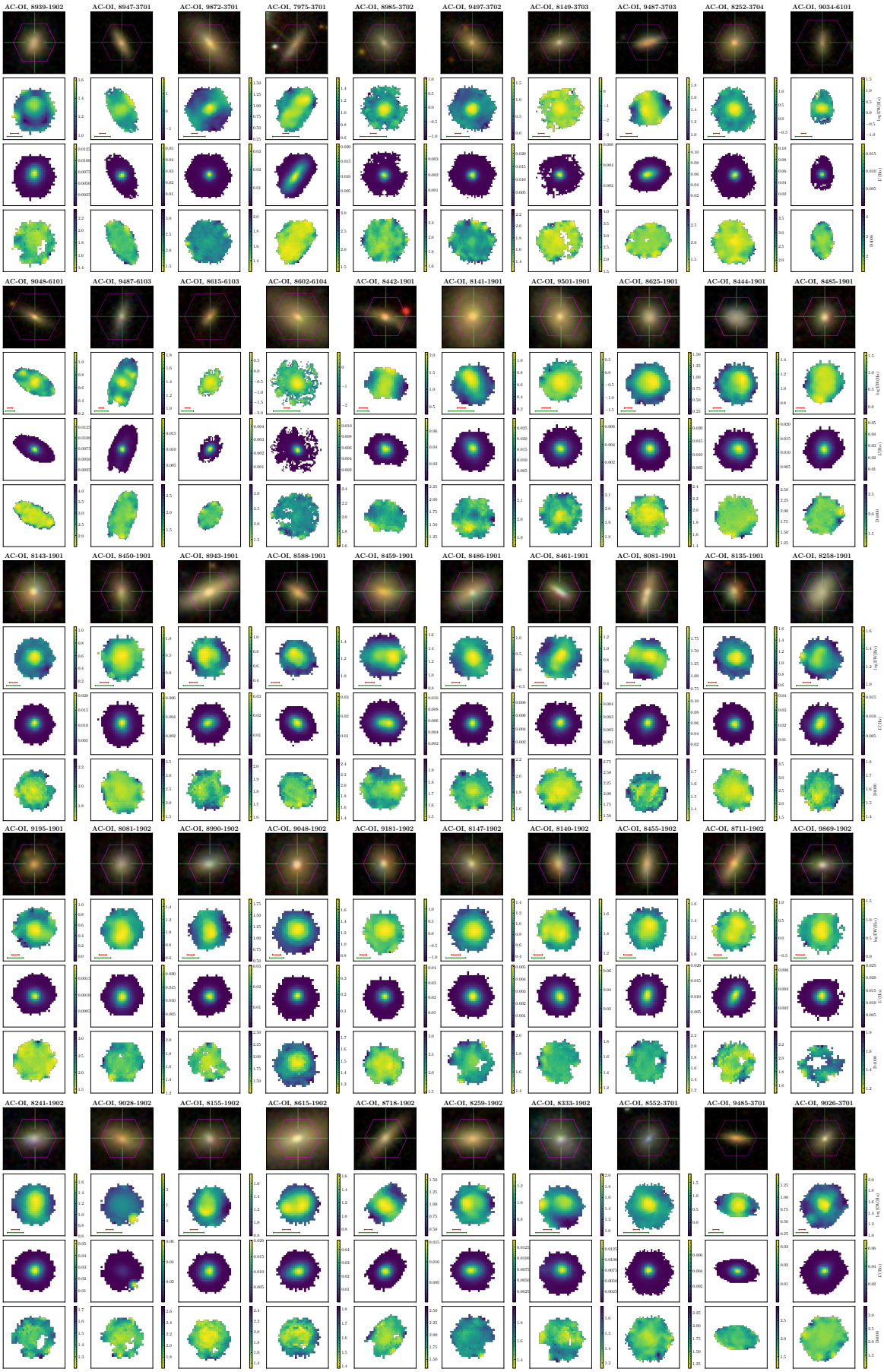

Figure 1: Cont.

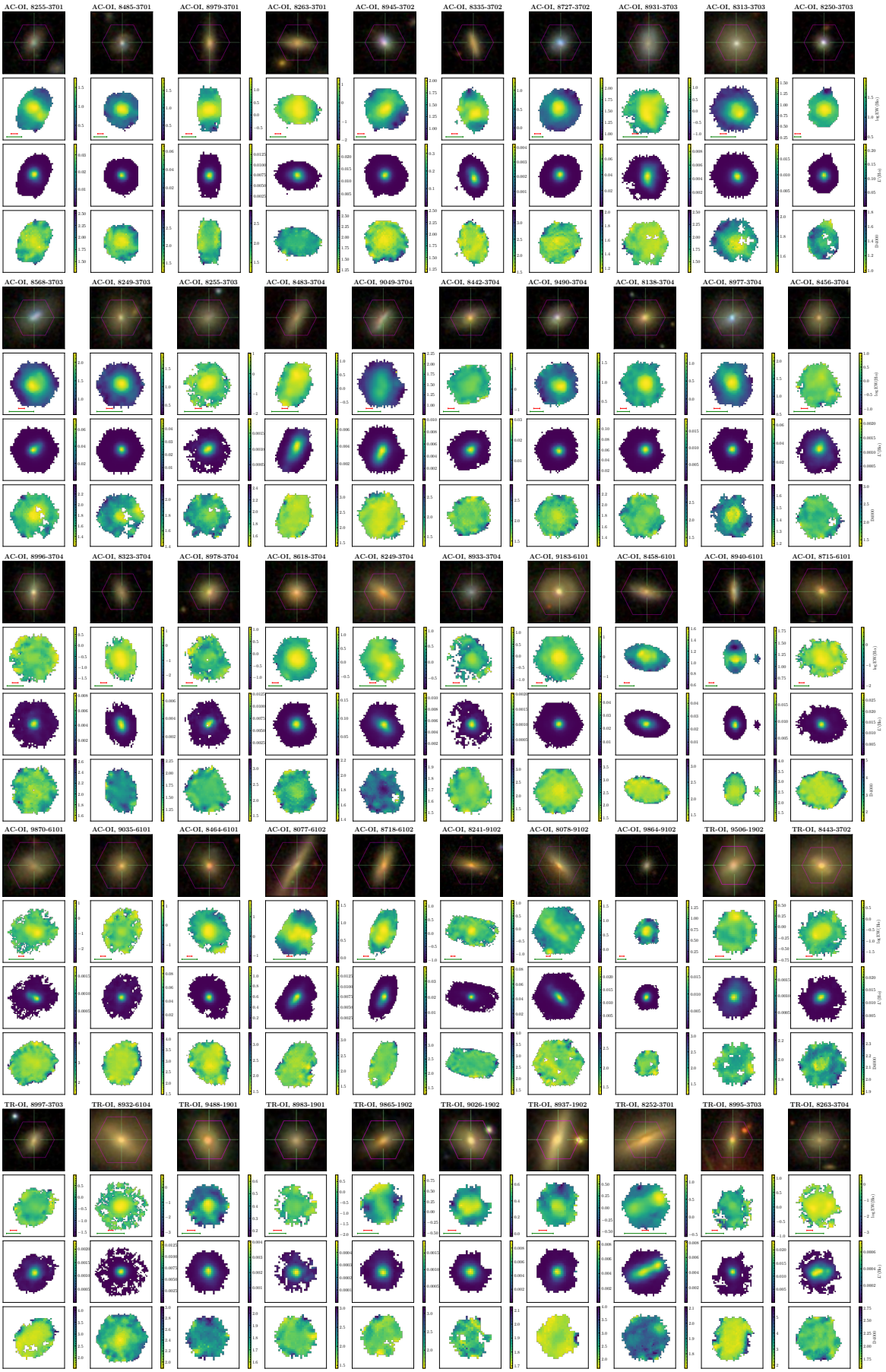

Figure 1: Cont.

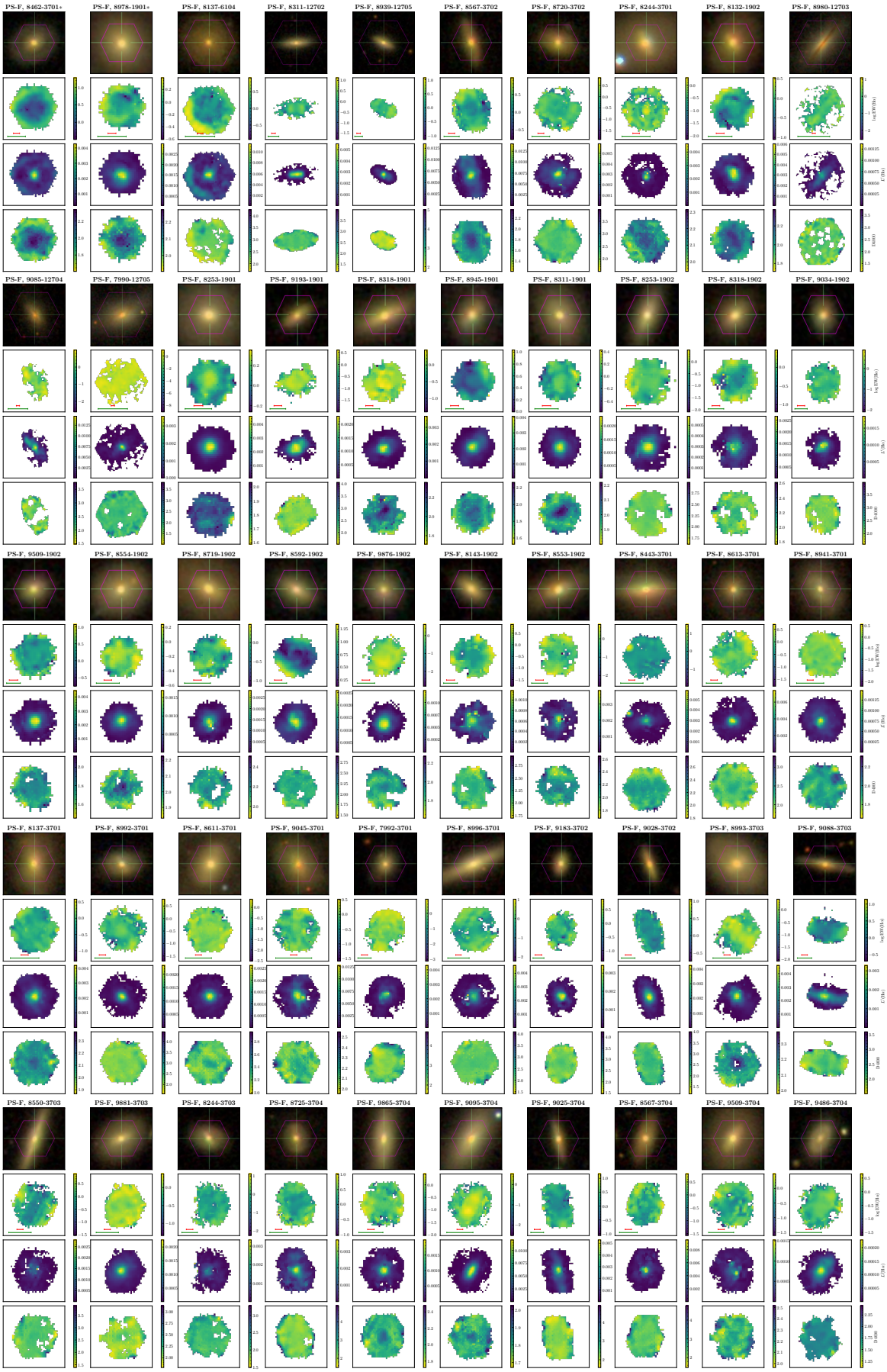

Figure 1: Cont.

Figure 1: Cont.

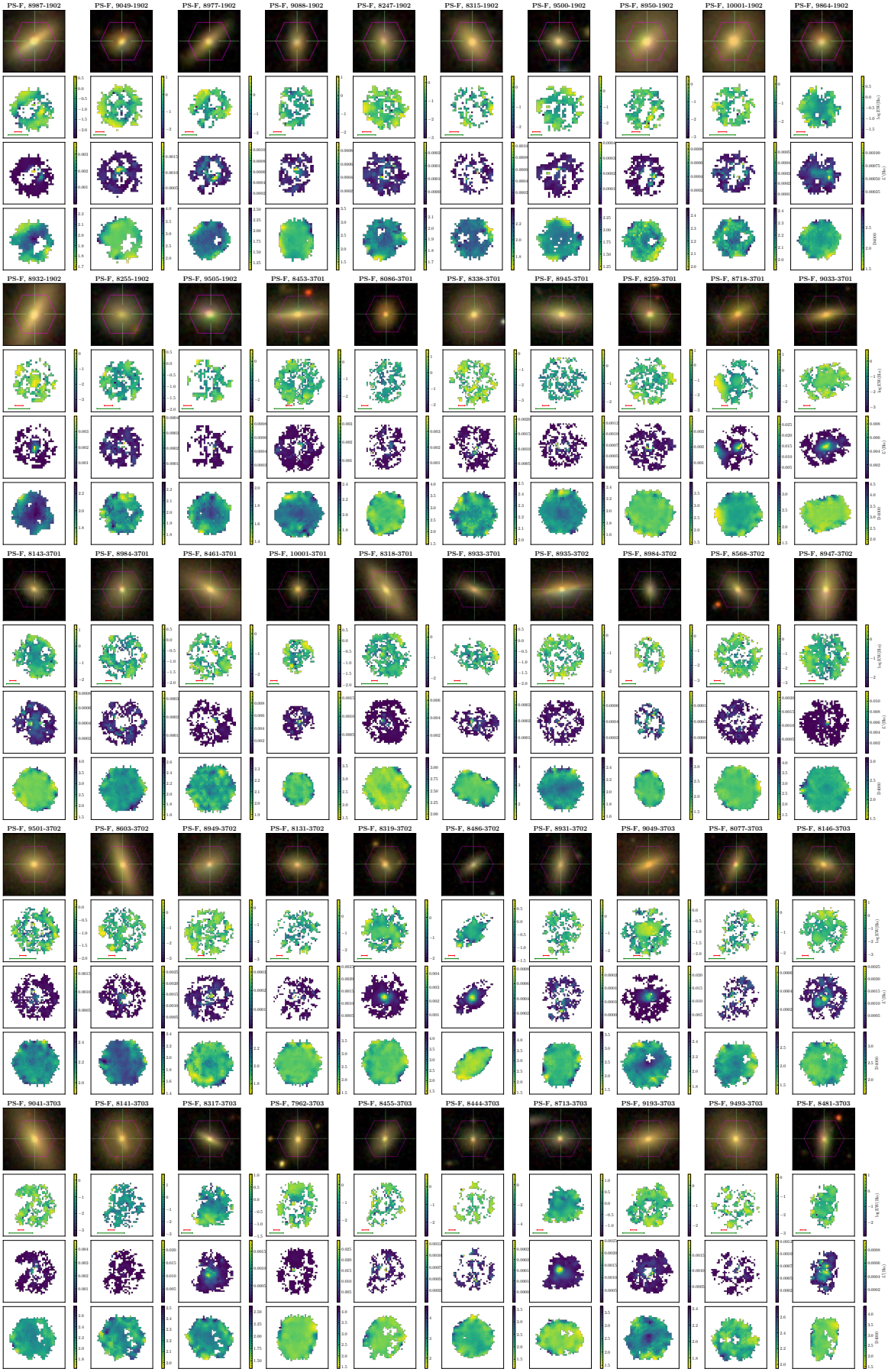

Figure 1: Cont.

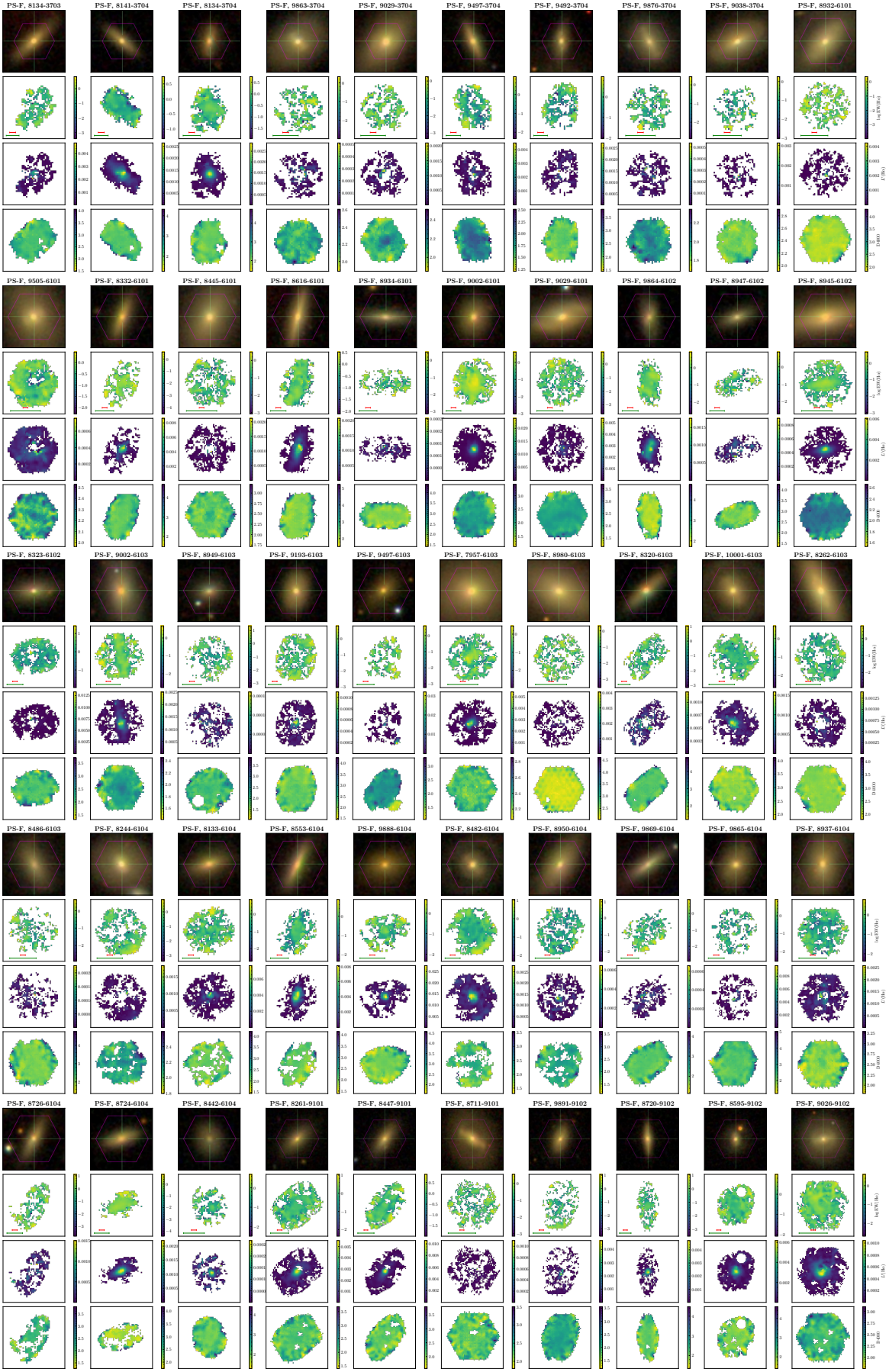

Figure 1: Cont.

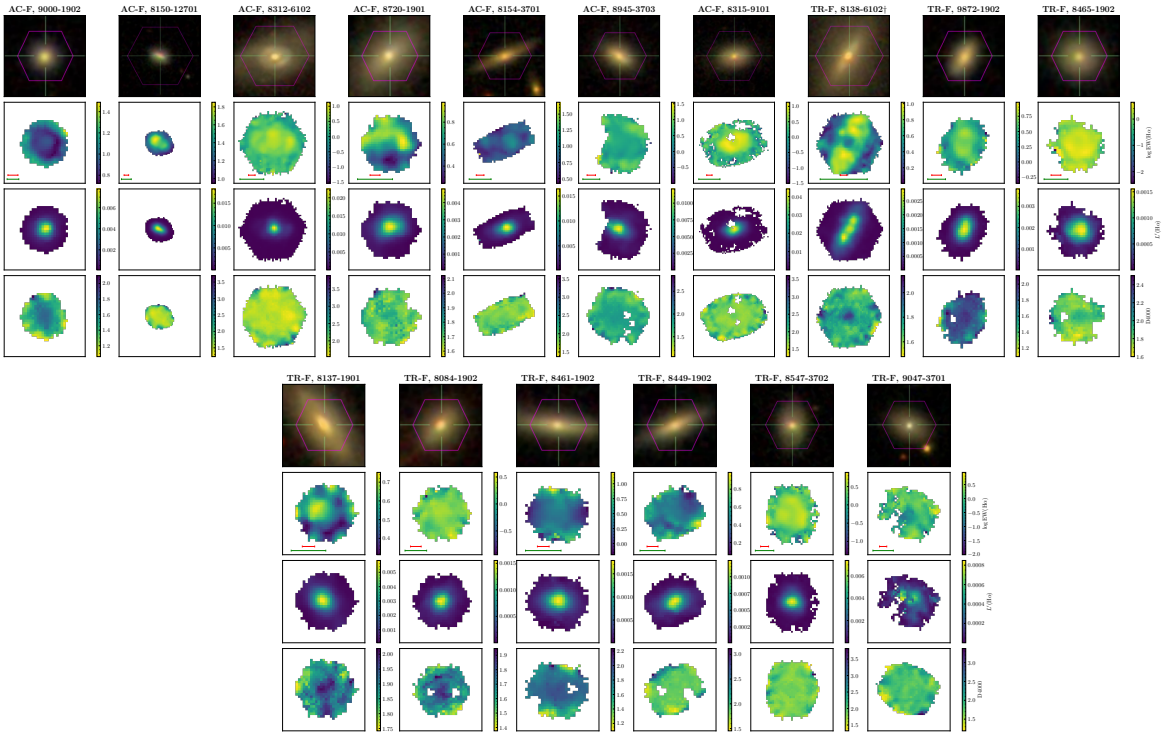

Figure 1: Cont.

ACRONYMS

Note: this list refers to acronyms used in the Introduction, the individual chapter introductions, the Summary of results and future prospects, and the Catalogue of star-forming rings in lenticular galaxies. Acronyms used in each individual publication are defined within the corresponding paper.

AC active cloud
AGN active galactic nuclei
BOSS Baryon Oscillation Spectroscopic Survey
BPT Baldwin, Phillips and Terlevich
DES Dark Energy Survey
DR data release
ETG early type galaxy
EW equivalent width
ICM intracluster medium
IFS integral field spectroscopy
IGM intergalactic medium
ISM interstellar medium
LINER low-ionization nuclear emission-line region
LTG late type galaxy
MGS main galaxy sample
MaNGA Mapping Nearby Galaxies at Apache Point Observatory
MOS multi-object spectroscopy
PCA principal component analysis
PC principal component
PS passive sequence
PSF point spread function
RPS ram pressure stripping
SDSS Sloan Digital Sky Survey
SEGUE Sloan Extension for Galactic Understanding and Exploration
S/N signal-to-noise ratio
SFR star formation rate
SSFR specific star formation rate
SSP single stellar population

SAMI	Sydney-AAO (Australian Astronomical Observatory) Multi-object Integral field spectrograph
SF	star-forming
TR	transition region

BIBLIOGRAPHY

Note: the bibliography listed below refers to citations in the Introduction, the individual chapter introductions, the Summary of results and future prospects, and the Catalogue of star-forming rings in lenticular galaxies. Citations in each individual publication are listed within the corresponding paper.

Abadi M. G., Moore B., Bower R. G., 1999, MNRAS, 308, 947

Abazajian K. N., et al., 2009, ApJs, 182, 543

Abdurro'uf et al., 2022, ApJs, 259, 35

Adelman-McCarthy J. K., et al., 2006, ApJS, 162, 38

Aguado D. S., et al., 2019, ApJS, 240, 23

Alam S., et al., 2015, ApJS, 219, 12

Allen J. T., et al., 2015, MNRAS, 446, 1567

Bacon R., et al., 2010, in McLean I. S., Ramsay S. K., Takami H., eds, Society of Photo-Optical Instrumentation Engineers (SPIE) Conference Series Vol. 7735, Ground-based and Airborne Instrumentation for Astronomy III. p. 773508 (arXiv:2211.16795), doi:10.1117/12.856027

Baldwin J. A., Phillips M. M., Terlevich R., 1981, PASP, 93, 5

Barway S., Wadadekar Y., Vaghmare K., Kembhavi A. K., 2013, MNRAS, 432, 430

Becker R. H., White R. L., Helfand D. J., 1995, ApJ, 450, 559

Bekki K., Couch W. J., 2011, MNRAS, 415, 1783

Bertola F., Buson L. M., Zeilinger W. W., 1992, ApJ, 401, L79

Bianchi L., Shiao B., Thilker D., 2017, ApJS, 230, 24

Boselli A., Fossati M., Sun M., 2022, A&ARv, 30, 3

Brownson S., Maiolino R., Tazzari M., Carniani S., Henden N., 2019, MNRAS, 490, 5134

Bundy K., et al., 2015, ApJ, 798, 7

Butcher H., Oemler Jr. A., 1978, ApJ, 219, 18

Cappellari M., et al., 2011a, MNRAS, 413, 813

Cappellari M., et al., 2011b, MNRAS, 416, 1680

Chen Y.-M., et al., 2016, Nature Communications, 7, 13269

Cheng T.-Y., et al., 2021, MNRAS, 507, 4425

Chisholm J., Tremonti C. A., Leitherer C., Chen Y., 2017, MNRAS, 469, 4831

Cid Fernandes R., Stasińska G., Schlickmann M. S., Mateus A., Vale Asari N., Schoenell W., Sodré L., 2010, MNRAS, 403, 1036

Coccato L., et al., 2020, MNRAS, 492, 2955

Coccato L., Fraser-McKelvie A., Jaffé Y. L., Johnston E. J., Cortesi A., Pallero D., 2022, MNRAS, 515, 201

Comerón S., et al., 2014, A&A, 562, A121

Couch W. J., Ellis R. S., Sharples R. M., Smail I., 1994, ApJ, 430, 121

Couch W. J., Barger A. J., Smail I., Ellis R. S., Sharples R. M., 1998, ApJ, 497, 188

DESI Collaboration et al., 2016, arXiv e-prints, p. arXiv:1611.00036

Davis T. A., et al., 2011, MNRAS, 417, 882

Dawson K. S., et al., 2016, AJ, 151, 44

Deeley S., et al., 2020, MNRAS, 498, 2372

Deeley S., Drinkwater M. J., Sweet S. M., Bekki K., Couch W. J., Forbes D. A., Dolfi A., 2021, MNRAS, 508, 895

Domínguez Sánchez H., Huertas-Company M., Bernardi M., Tuccillo D., Fischer J. L., 2018, MNRAS, 476, 3661

Domínguez Sánchez H., Bernardi M., Nikakhtar F., Margalef-Bentabol B., Sheth R. K., 2020, MNRAS, 495, 2894

Domínguez Sánchez H., Margalef B., Bernardi M., Huertas-Company M., 2021, MNRAS,

Dressler A., 1980, ApJ, 236, 351

Dressler A., et al., 1997, ApJ, 490, 577

Eisenstein D. J., et al., 2011, AJ, 142, 72

Eliche-Moral M. C., Rodríguez-Pérez C., Borlaff A., Querejeta M., Tapia T., 2018, A&A, 617, A113

Euclid Collaboration et al., 2022, A&A, 662, A112

Evans I. N., et al., 2020, in Bulletin of the American Astronomical Society (Meeting Abstracts #235), Vol. 52, No. 1. p. 154.05

Fasano G., Poggianti B. M., Couch W. J., Bettoni D., Kjærgaard P., Moles M., 2000, ApJ, 542, 673

Fischer J. L., Domínguez Sánchez H., Bernardi M., 2019, MNRAS, 483, 2057

Fluetsch A., et al., 2019, MNRAS, 483, 4586

Fraser-McKelvie A., Aragón-Salamanca A., Merrifield M., Tabor M., Bernardi M., Drory N., Parikh T., Argudo-Fernández M., 2018, MNRAS, 481, 5580

Gavazzi G., Consolandi G., Pedraglio S., Fossati M., Fumagalli M., Boselli A., 2018, A&A, 611, A28

Giovanelli R., Haynes M. P., Chincarini G. L., 1986, ApJ, 300, 77

Goto T., Yamauchi C., Fujita Y., Okamura S., Sekiguchi M., Smail I., Bernardi M., Gomez P. L., 2003, MNRAS, 346, 601

Gunn J. E., Gott J. Richard I., 1972, ApJ, 176, 1

Helmboldt J. F., Walterbos R. A. M., Goto T., 2008, MNRAS, 387, 1537

Hopkins P. F., Cox T. J., Hernquist L., Narayanan D., Hayward C. C., Murray N., 2013, MNRAS, 430, 1901

Houghton R. C. W., 2015, MNRAS, 451, 3427

Hubble E. P., 1926, ApJ, 64, 321

Hubble E. P., 1936, Realm of the Nebulae

Jansen F., et al., 2001, A&A, 365, L1

Jimenez-Palau C., Solanes J. M., Perea J. D., Del Olmo A., Tous J. L., 2022a, VizieR Online Data Catalog, p. J/MNRAS/515/3956

Jiménez-Palau C., Solanes J. M., Perea J. D., del Olmo A., Tous J. L., 2022b, MNRAS, 515, 3956

Kannappan S. J., Fabricant D. G., 2001, AJ, 121, 140

King A., Pounds K., 2015, ARA&A, 53, 115

Larson R. B., Tinsley B. M., Caldwell C. N., 1980, ApJ, 237, 692

Lintott C. J., et al., 2008, MNRAS, 389, 1179

Lotz M., Remus R.-S., Dolag K., Biviano A., Burkert A., 2019, MNRAS, 488, 5370

Mapelli M., Rampazzo R., Marino A., 2015, A&A, 575, A16

Maschmann D., Melchior A.-L., Mamon G. A., Chilingarian I. V., Katkov I. Y., 2020, A&A, 641, A171

Maschmann D., Melchior A.-L., Combes F., Mazzilli Ciraulo B., Freundlich J., Halle A., Drabent A., 2022, A&A, 664, A125

Merluzzi P., Busarello G., Dopita M. A., Haines C. P., Steinhauser D., Bourdin H., Mazzotta P., 2016, MNRAS, 460, 3345

Moore B., Katz N., Lake G., Dressler A., Oemler A., 1996, Nature, 379, 613

Muratov A. L., Kereš D., Faucher-Giguère C.-A., Hopkins P. F., Quataert E., Murray N., 2015, MNRAS, 454, 2691

Nair P. B., Abraham R. G., 2010, ApJs, 186, 427

Navó G., Tous J. L., Solanes J. M., 2019, A&A, 631, A93

Nulsen P. E. J., 1982, MNRAS, 198, 1007

Peng Y., Maiolino R., Cochrane R., 2015, Nature, 521, 192

Peterson J. R., Fabian A. C., 2006, Phys. Rep., 427, 1

Poggianti B. M., Smail I., Dressler A., Couch W. J., Barger A. J., Butcher H., Ellis R. S., Oemler Augustus J., 1999, ApJ, 518, 576

Postman M., Geller M. J., 1984, ApJ, 281, 95

Querejeta M., et al., 2015, A&A, 579, L2

Quilis V., Moore B., Bower R., 2000, Science, 288, 1617

Raimundo S. I., Malkan M., Vestergaard M., 2023, Nature Astronomy, 7, 463

Rathore H., Kumar K., Mishra P. K., Wadadekar Y., Bait O., 2022, MNRAS, 513, 389

Rizzo F., Fraternali F., Iorio G., 2018, MNRAS, 476, 2137

Roediger E., Hensler G., 2005, Astronomy & Astrophysics, 433, 875

Sánchez S. F., et al., 2012, A&A, 538, A8

Sandage A., 1961, The Hubble Atlas of Galaxies

Sarzi M., et al., 2006, MNRAS, 366, 1151

Silva-Lima L. A., Martins L. P., Coelho P. R. T., Gadotti D. A., 2022, A&A, 661, A105

Skrutskie M. F., et al., 2006, AJ, 131, 1163

Smee S. A., et al., 2013, AJ, 146, 32

Spitzer Lyman J., Baade W., 1951, ApJ, 113, 413

Springel V., et al., 2018, MNRAS, 475, 676

Strauss M. A., et al., 2002, AJ, 124, 1810

Tapia T., Eliche-Moral M. C., Aceves H., Rodríguez-Pérez C., Borlaff A., Querejeta M., 2017, A&A, 604, A105

The Dark Energy Survey Collaboration 2005, arXiv e-prints, pp astro–ph/0510346

Tous J. L., 2018, Dipòsit Digital de la Universitat de Barcelona, http://hdl.handle.net/2445/147221

Tous J. L., Solanes J. M., Perea J. D., 2020, MNRAS, 495, 4135

Tous J. L., Domínguez-Sánchez H., Solanes J. M., Perea J. D., 2023, ApJ, 942, 48

Vega-Ferrero J., et al., 2021, MNRAS, 506, 1927

Vera M., Alonso S., Coldwell G., 2016, A&A, 595, A63

Webb N. A., et al., 2020, A&A, 641, A136

Willett K. W., et al., 2013, MNRAS, 435, 2835

Wright E. L., et al., 2010, AJ, 140, 1868

Xiao M.-Y., Gu Q.-S., Chen Y.-M., Zhou L., 2016, ApJ, 831, 63

Yanny B., et al., 2009, AJ, 137, 4377

York D. G., et al., 2000, AJ, 120, 1579

van de Voort F., Quataert E., Hopkins P. F., Faucher-Giguère C.-A., Feldmann R., Kereš D., Chan T. K., Hafen Z., 2016, MNRAS, 463, 4533

FUNDING ACKNOWLEDGEMENTS

The author acknowledges financial support by the PRE2020-091838 grant from the Spanish state agency MCIN/AEI/10.13039/501100011033 and by 'ESF Investing in your future'. The author also acknowledges financial support from MCIN/AEI/10.13039/501100011033 and by 'ERDF A way of making Europe' funds through grants PID2019-106027GB-C43, PID2019-106027GB-C41, and also from the state agency and European FEDER funds through the grant AYA2016-76682-C3. MCIN/AEI/10.13039/501100011033 has provided additional support through the Centre of Excellence María de Maeztu's award for the Institut de Ciències del Cosmos at the Universitat de Barcelona under contract CEX2019-000918-M.

Final Version as of December 29, 2023 (`classicthesis` version 4.2).